Hierarchical Nanoporous Solid Base Catalysts for Biodiesel Synthesis

Julia J. Woodford

Submitted for the degree of
Doctor of Philosophy

Cardiff University
Chemistry Department
2013

Abstract

The discovery of alternative solid base catalysts to replace homogeneous catalysts currently used in the industrial synthesis of biodiesel could remove the need for atom and energy inefficient routes to the desired biofuel product, and allow for the possibility of a continuous production process.

Hydrotalcites have shown promise as catalysts in the transesterification of triglycerides with methanol to form biodiesel; however their activity is hampered by slow diffusion of the bulky triglycerides through the microporous hydrotalcite structure and poor accessibility of the active sites. This thesis has examined the synthesis of hydrotalcites via novel routes in an attempt to improve base site accessibility to triglycerides feedstocks in order to enhance catalytic performance. Macropore introduction into MgAl hydrotalcites helps to overcome mass transport limitations and increase their activity 10-fold for the transesterification of olive oil. Hydrotalcites prepared on an alumina support through a novel grafting and hydrothermal protocol form well-ordered crystallites on the high surface area oxide support. The resulting hydrotalcite-coated aluminas exhibit activities comparable to macroporous hydrotalcites of similar Mg:Al stoichiometries. Hydrotalcites prepared on alumina-grafted SBA-15 and macroporous-mesoporous SBA-15 employing the same grafting and hydrothermal synthesis are also extremely active in triglyceride transesterification, with the hierarchical macroporous-mesoporous outperforming the purely mesoporous SBA-15 support.

Comparative studies on non-porous solid bases derived from nanocrystalline MgO reveal that Cs doping via co-precipitation confers superior activity for tributyrin transesterification. X-ray absorption spectroscopy has been applied to probe the local chemical environment of Cs atoms within such Cs-doped MgO, and the catalytically active phase identified as $Cs_2Mg(CO_3)_2(H_2O)_4$. Cs-MgO is an order of magnitude more active for the transesterification of bulky triglycerides and olive oil than the undoped, parent MgO nanocrystals.

List of Contents

Chapter 5 - Hydrotalcite supported on mesoporous and macro-mesoporous silica...180

List of Abbreviations

ALD	Atomic layer deposition
at%	Atomic percent
B20	Blend of biodiesel with petroleum diesel where 20% is biodiesel
BET	Brunauer-Emmet-Teller
BJH	Barrett, Joyner and Halenda
C4 TAG	Triglyceride with fatty acid chain length of 4 carbons (tributyrin)
C8 TAG	Triglyceride with fatty acid chain length of 8 carbons (tricaprylin)
C12 TAG	Triglyceride with fatty acid chain length of 12 carbons (trilaurin)
C18 TAG	Triglyceride with fatty acid chain length of 18 carbons (triolein)
C*X*	Carbon chain where *X* denotes number of carbons in chain
ConvHT	2:1 Mg:Al ratio conventional hydrotalcite
CVD	Chemical vapour deposition
DAG	Diacyl glyceride
DCM	Dichloromethane
DFT	Density functional theory
DTA	Differential thermal analysis
EDX	Energy dispersive X-rays
EXAFS	Extended X-ray absorption fine structure
FAME	Fatty acid methyl ester
FID	Flame ionisation detector
FWHM	Full width half maximum
GC	Gas chromatography
GC-MS	Gas chromatography-mass spectrometry
GHG	Greenhouse gas
HK	Horvath-Kawazoe
HPR	High pressure rehydrated
HT	Hydrotalcite
LDH	Layered double hydroxide
LPR	Liquid phase rehydration
MacroHT	2:1 Mg:Al ratio macroporous hydrotalcite

MAG	Monoacyl glyceride
MB	Methyl butyrate
MC	Methyl caprylate
ML	Methyl laurate or monolayer
MM	Macro-mesoporous
MO	Methyl oleate
MS	Mass spectrometer
NMR	Nuclear magnetic resonance
OOP	Oleic-oleic-palmitic triglyceride
PS	Polystyrene
RPM	Revolutions per minute
RT	Room temperature
SBA-15	Mesoporous silica with uniform hexagonal pores of diameter 5-15nm
SEI	Secondary electron imaging
SEM	Scanning electron microscopy
TAG	Triacyl glyceride
TEM	Transmission electron microscopy
TGA	Thermal gravimetric analysis
TOF	Turn over frequency
TPD	Temperature programmed desorption
VPR	Vapour phase rehydration
wt%	Weight percent
WtW	"Well-to-wheel"
XANES	X-ray absorption near edge structure
XAS	X-ray adsorption spectroscopy
XPS	X-ray photoelectron spectroscopy
XRD	X-ray diffraction

Acknowledgements

This thesis would not have been possible without the help and support of many people, to whom I am extremely grateful.

Many thanks to Professor Adam Lee and Dr Karen Wilson for supervising and guiding me through this PhD. Your support, particularly throughout the last year, has been greatly appreciated. I thank the EPSRC for funding this project, and also the School of Chemistry at Cardiff University, for providing me with the facilities to carry out my research.

Several of the results in this thesis were obtained with the assistance of some very helpful people. Thank you to Dr Jean-Philippe Dacquin, for his helpful support throughout my first year, and for carrying out TEM analysis for me. Thank you to Dr Christopher Parlett for preparing one of my catalyst supports, and for helping me with XRD and porosimetry analysis when I couldn't get into the lab. Also many thanks for coming in on a weekend to help me set up my preparations, all of your guidance has been invaluable. Thanks go to Gianantonio Cibin, the beamline scientist at Diamond who helped in obtaining our EXAFS data.

To all of the past and current members of the Cardiff Surface Chemistry and Catalysis group, thank you for the giggles, the gossip and the nights out! A special thank you to Christine, for lots of cups of tea and for putting the world to rights with me many times, and Chris, for always having a helpful idea when I needed one! I feel truly lucky to have met such good friends.

To all of my other friends, particularly Grace up in Yorkshire, thank you for not letting me give up and run back home when things have been tough!

To my fantastic Mum and Dad. You have been there for me from the start and I wouldn't be here if it wasn't for your unwavering support. You have never stopped believing in me and your encouragement from an early age has given me the confidence to do this. Words can't really express my gratitude for all you have

done for me. To my brother Peter, for all of your support and for being my best friend for as long as I can remember, thank you.

To Paul, my wonderful fiancé, who I absolutely could not have done this without. Your constant support has been incredible. You have been there for me through all of the ups and downs, and there have been plenty of both! Sharing my life with you is the most wonderful experience and I am so excited as to what the future might bring. With you at my side anything is possible. I love you so much.

Finally, to my son Lewis. Your smiles and cuddles never fail to make my day. Thank you for changing my world and giving everything a greater meaning.

DECLARATION

This work has not been submitted in substance for any other degree or award at this or any other university or place of learning, nor is being submitted concurrently in candidature for any degree or other award.

Signed …………………………………(candidate) Date …………………........

STATEMENT 1

This thesis is being submitted in partial fulfillment of the requirements for the degree of PhD

Signed ……………………………… (candidate) Date …………………………

STATEMENT 2

This thesis is the result of my own independent work/investigation, except where otherwise stated. Other sources are acknowledged by explicit references. The views expressed are my own.

Signed …………………………………(candidate) Date ………………………

STATEMENT 3

I hereby give consent for my thesis, if accepted, to be available for photocopying and for inter-library loan, and for the title and summary to be made available to outside organisations.

Signed …………………………...…… (candidate) Date ……………..................

Some of the research reported in this manuscript has been published in peer reviewed journal articles, which are referenced below:

J. J. Woodford, J.-P. Dacquin, K. Wilson and A.F. Lee, Better by design: nanoengineered macroporous hydrotalcites for enhanced catalytic biodiesel production, *Energy & Environmental Science,* 2012, **5**, 6145-6150

J.J. Woodford, C.P. Parlett, J.-P. Dacquin, G. Cibin, A. Dent, J. Montero, K. Wilson and A.F. Lee, Identifying the active phase in Cs-promoted MgO nanocatalysts for triglyceride transesterification, *Journal of Chemical Technology and Biotechnology,* Accepted Article

Chapter 1

Introduction

1.1 Fossil fuels and alternative fuel sources

Concerns over dwindling oil reserves and rising CO_2 emissions, from fossil fuel consumption and associated climate change, are driving the need for alternative renewable energy sources.[1] Out of the three fossil fuels: coal, natural gas and crude oil, it is crude oil which is in shortest supply, with a reserves to production ratio of 54.2 years in 2012.[2] Therefore, development of alternatives to oil based fuels such as petrol, diesel and other transportation fuels is a priority. The most readily implemented (and low cost) solutions for transportation are those based upon liquid fuels derived from biomass.[3, 4] These include bioethanol, vegetable and plant oils, biogas and biodiesel, which can all be acquired or manufactured from sustainable sources.[5]

1.2 Biodiesel

Biodiesel is a clean-burning, non-toxic fuel derived from plant or algal oils and animal fats, which is viewed as a viable alternative (or additive) to current petroleum-derived diesel.[6, 7] In 2010, biodiesel production peaked in Europe at 9.57 million tonnes, a 5.5 % increase on 2009 figures.[8]

1.2.1 Physical properties of biodiesel

Commercial biodiesel is synthesised via the liquid base catalysed transesterification of the C14-C20 triglyceride (TAG) components of natural fats or oils (of vegetable or animal origin) with C1-C2 alcohols,[9-12] into their respective fatty acid methyl esters (FAMEs) which constitute biodiesel, together with glycerol by-product.[13] While the use of higher (e.g. C4) alcohols is also possible,[14] and offers some advantages of producing a less polar and corrosive FAME[15] with reduced cloud and pour points,[16] the current high cost of longer chain alcohols, and difficulties associated with separating the FAME product from un-reacted alcohol and glycerol remain problematic. **Figure 1.1** shows the reaction scheme for the transesterification of triglycerides to form biodiesel.

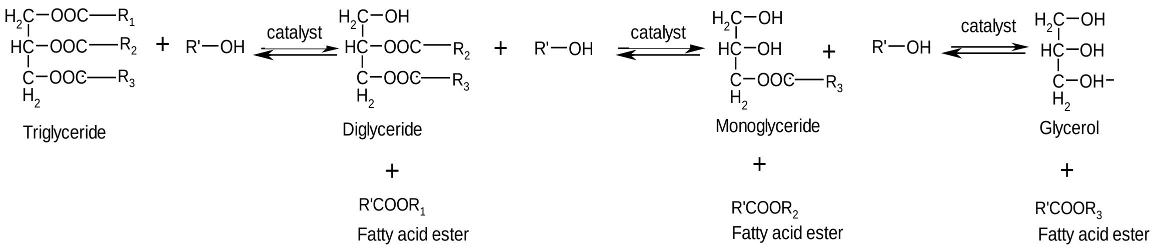

Figure 1.1. Reaction scheme showing the transesterification of triglycerides to form the fatty acid methyl ester (FAME) biodiesel product.

Biodiesel fuel can contain different FAME species depending on the feedstock used in the synthesis. The 5 most dominant fatty acids in the composition of FAME derived from plant oils and animal fats are palmitic acid (16:0), stearic acid (18:0), oleic acid (18:1), linoleic acid (18:2), and linolenic acid (18:3),[17] where the first number of the two in brackets separated by a colon relates to the carbon chain length of the fatty acid, and the second gives the number of carbon-carbon double bonds in the chain. Biodiesel has very similar properties to conventional diesel, and so can be used as blends with conventional diesel in current diesel engines with little or no modification.[18] **Table 1.1** gives some typical properties of biodiesel as a class, compared to those of petroleum diesel, however the exact properties of the biodiesel depends on the composition of the oil or fat it has been derived from.

Table 1.1. Typical properties of biodiesel compared to petroleum diesel.[17]

	Petroleum Diesel	Biodiesel (FAME)
Carbon, wt%	86.8	76.2
Hydrogen, wt%	13.2	12.6
Oxygen, wt%	0.0	11.2
Specific gravity	0.85	0.88
Cetane number	40-45	45-55
T_{90} / °C	300-330	330-360
Viscosity / mm^2s^{-1}@40°C	2-3	4-5

Biodiesel has a higher oxygen content than petroleum diesel, and a lower hydrogen and carbon content, resulting in a 10 % lower mass energy content. However, due to biodiesel's higher fuel density, its volumetric energy content is only about 5–6 % lower than petroleum diesel. Typically, biodiesel has a higher molecular weight than petroleum diesel, which is reflected in slightly higher distillation temperatures, as measured by T_{90}. The cetane numbers of most biodiesel fuels are higher than for petroleum diesel, due to the presence of mainly straight chain esters. The viscosity of most biodiesel fuels is also significantly higher than petroleum diesel, often two fold.[17] In terms of emissions, the high oxygen content of biodiesel helps to complete combustion and lower CO emissions compared to petroleum diesel.[19] Biodiesel also produces less sulfur dioxide[20] than conventional diesel. Emissions from prototype vehicles using biodiesel were found to contain 94 % less carcinogenic particulate matter than petroleum-based diesel engines.[4, 21]

1.2.2 Biodiesel feedstocks

There is a lot of debate surrounding the use of feedstocks which could be used as food crops, such as soybean oil and rapeseed oil, to produce first generation biodiesel. Not only is this less economically viable, but using these crops and the land they are grown on to make biodiesel, rather than food crops, will increase food prices and limit availability. To be sustainable, so called 'second generation' biodiesel should be sourced from alternative non-food plants such as *Jatropha curcas*[22, 23] or *Miscanthus*, images of which are shown in **Figure 1.2**.

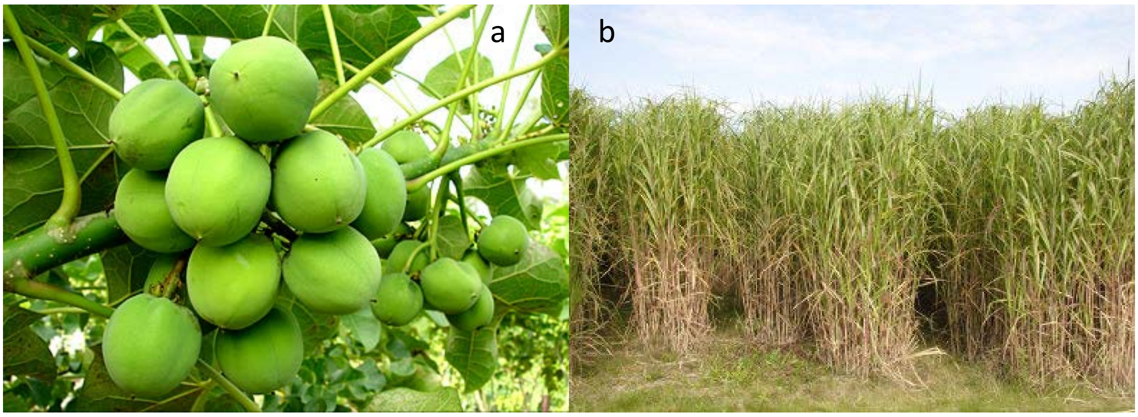

Figure 1.2. Images of non-edible plant oil feedstocks showing a) *Jatropha Curcas* seeds and b) a *Miscanthus* crop.[24, 25]

1.2.2.1 Non-edible plant feedstocks

Non-food crops are unsuitable for human consumption or animal feed, and have comparable or even higher oil yields and lower resource consumption than conventional food crops.[26] This makes them good candidates for a more sustainable biodiesel production in terms of efficient use of resources, less interaction with food crops and a lower environmental impact.[27, 28] *Jatropha Curcas* is the most widely investigated non edible feedstock for biodiesel production. It is a drought resistant perennial with toxic seeds and oil due to the presence of phorbol esters.[7] It grows well in poor soil, meaning it can be grown on what would otherwise be barren wasteland,[29] therefore it does not require farm land which could otherwise be used for growing food crop, and may also provide a solution for the production of biodiesel in developing countries such as India. The resulting biodiesel properties are comparable to that of conventional diesel and all fall within the European and American biodiesel quality standards.

1.2.2.2 Non-edible animal fats

Animal fats such as beef tallow, pork lard and chicken fat are by-products of the food processing industry, and are considered non-edible for human consumption. They generally represent low value feedstocks for biodiesel production due to the high percentage of saturated fatty acids (around 40 % in beef tallow, compared to 14 % in soybean oil),[30] therefore giving the resulting biodiesel a high melting point, making it unsuitable for use in cold climates. There is also a bio-safety issue relating to the use of animal fats from contaminated animals.[31] Greene and co-workers[32] have highlighted the future research needs for ensuring the bio-safety of biodiesel produced from animal waste from cradle to grave.

1.2.2.3 Used cooking oils

Used cooking oils (UFO) are of great interest as a feedstock for biodiesel, as huge quantities are available throughout the world from restaurants and households. There are potentially serious environmental problems linked to the disposal of waste cooking oils, which could be resolved by their proper utilisation and management as a diesel fuel.[33] Their use reduces the cost of biodiesel production; however there are issues with the quality of the used cooking oil feedstock. The physical and chemical properties depend on those of the fresh cooking oil, and the used cooking oil may contain a lot of impurities such as water and free fatty acids,[34] which will require pre-treatment prior to transesterification.

1.2.2.4 Algal feedstocks

There is growing interest in the use of oil triglycerides derived from microorganisms such as algae or fungi, which potentially offer biodiesel yields >100 times those attainable per hectare from plant feedstocks.[35, 36] Microalgae are sunlight driven cell organisms which convert atmospheric CO_2 via photosynthesis into a range of chemical metabolites, including oil.[37, 38] They are often cultivated in open raceways, an image of which can be seen in **Figure 1.3**, as these are cheaper to build and operate than closed photo bio-reactors. A paddlewheel re-circulates the biomass in its water and nutrients, and CO_2 can be pumped through the system to improve aeration and mixing, increase CO_2 consumption, and enhance algal biomass growth.[39] There are major limitations with the use of algal feedstocks. Economically, the biodiesel production process cannot compete to any using waste oils and fat as the feedstock. There is also the issue of contamination in open-pond systems.[36] Recent studies have shown transesterification can be performed using the whole organism, rather than extracting the algal oil.[40] This, along with genetic engineering to increase oil content, could in the future lead to an economically viable biodiesel production process using algal feedstocks.

Figure 1.3. Image of an algal raceway.[41]

1.2.2.5 Effect of biodiesel feedstock on CO_2 emissions

The choice of feedstock can have a large effect on the environmental impact of biodiesel produced. Land use change has to be taken into account; deforestation in order to clear space for biodiesel crops results in far greater net CO_2 emissions. Yan and co-workers[3] conducted a study in which they compared "well-to-wheel" (WtW) greenhouse gas (GHG) emissions per vehicle kilometre travelled for various fuels in China. The CO_2 emissions taken from this study for rapeseed and *Jatropha* feedstocks in B20 blends, grown in an area that was previously either forest or grassland, compared to petroleum diesel, can be seen below in **Figure 1.4.**

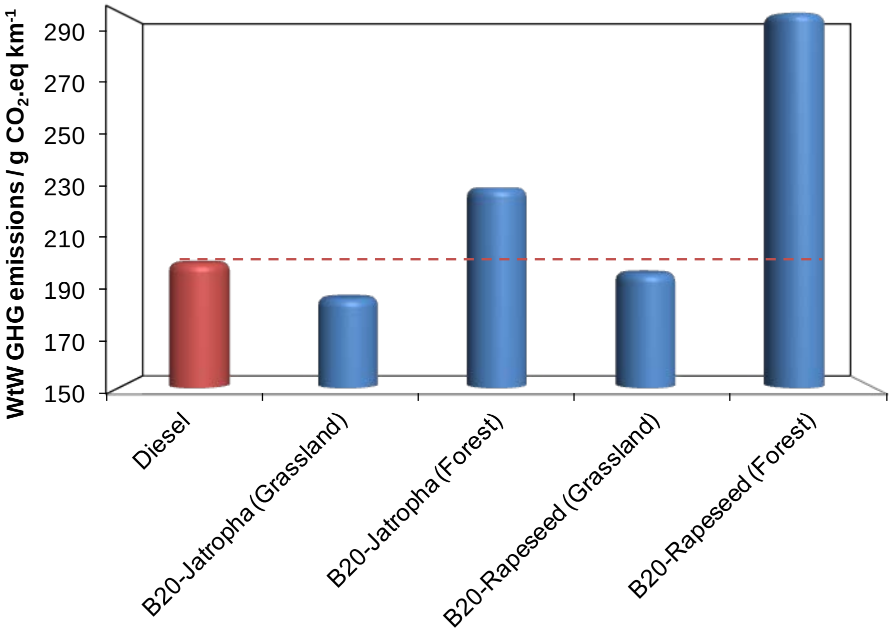

Figure 1.4. WtW fossil fuel use and GHG emissions ‘per vehicle kilometre travelled’ for fuels in China.[3]

B20 blends of *Jatropha* and rapeseed have lower CO_2 emissions overall than petroleum diesel when grown on grassland. However, if deforested areas are used to prepare these crops, the net CO_2 emissions are much higher, and substantially greater than those of petroleum diesel. The CO_2 emissions for B20-*Jatropha* could be lowered significantly if the feedstocks were grown on marginal cropland or degraded land because of the potential soil carbon sequestration, rendering this feedstock the most favourable in terms of lowest CO_2 emissions.

1.3 Current problems in the industrial synthesis of biodiesel

Liquid bases such as Na or K alkoxide or hydroxide are commonly used in the industrial synthesis of biodiesel.[42] However, extraction of pure biodiesel and removal of Na(K) hydroxide or alkoxide catalysts is problematic due to saponification and emulsification,[4] but essential to prevent corrosion of vehicle fuel tanks and injector systems.[43] Associated quenching and processing steps to remove the base also contaminates the glycerol by-product with alkali salts and water, rendering it unusable directly as a commodity chemical. The development of alternative solid acid[44-47] or solid base[48-50] catalysts, which are easily separated from the biodiesel and glycerol products, has thus been the subject of intensive academic and commercial research.[51, 52] Heterogeneous catalysts offer facile product separation, eliminating quenching steps as well as permitting process intensification via continuous biodiesel production.[10, 53]

1.4 Solid acid catalysts for biodiesel synthesis

A range of solid acids have been examined for their activity in the synthesis of biodiesel, for example sulfated zirconia,[54-56] sulfonic acid functionalised silicas,[57] heteropolyacids[58, 59] and zeolites.[60, 61] Solid acids show lower activity in the direct transesterification of oils into biodiesel than solid bases,[46] requiring higher temperatures to reach acceptable conversions. However, their ability to esterify free fatty acids means that they can cope well with unrefined oils containing 2-6 wt% free fatty acids.[46] It would be beneficial to pre-treat feedstocks with a solid acid catalyst to esterify the free fatty acids first, before transesterifying with a solid base, as this would remove the need for separation and neutralisation steps.[62]

Commercial sulfonic resins are acid catalysts which are classified according to the polymer backbone, either polystyrene (Amberlyst® resins) or perfluorinated alkanes (Nafion® resins). Lopez and co-workers investigated the use of Amberlyst®-15 and Nafion® NR50 as solid acid catalysts in the transesterification of triacetin.[63, 64] After 8 hours at 60 ºC with a methanol: oil ratio of 6:1 and 2 wt% catalyst, the Amberlyst-15 showed the highest activity, converting 79 % of the triacetin.

Mesoporous silicas such as SBA-15 can be functionalised with phenyl or propyl sulfonic acid groups to form a solid acid catalyst.[47, 57, 65] Mbaraka and co-workers[57] reported activities comparable to those of commercial ion exchange resins Nafion® NR50 and Amberlyst®-15 when testing sulfonic acid functionalised mesoporous silicas in the esterification of palmitic acid. The phenylsulfonic acid functionalised silicas showed greater activity than their propylsulfonic acid functionalised counterparts, which agrees with their corresponding acid strengths.

There have been several studies carried out on the use of sulfated zirconia (SO_4/ZrO_2) as an acid catalyst in the synthesis of biodiesel, due to its strong acidity and regeneration capacity.[54-56] Lopez and co-workers[63] showed that at 60 ºC SO_4/ZrO_2 performed better than sulfuric acid for TAG transesterification, allowing for the possibility of replacing its homogeneous counterpart. Sulfated zirconia was tested as a catalyst in the transesterification of coconut oil by Jitputti and co-workers.[66] An 80.6 % FAME yield was obtained after 4 hours at 200 ºC and a 6:1 methanol: oil ratio.

Heteropolyacids, for example $H_3PW_{12}O_{40}$, have flexible structures and tuneable acidity,[53] with enough acid strength to allow low temperature transesterification. The structure consists of 4 Keggin units surrounding crystalline water, as illustrated in **Figure 1.5**.

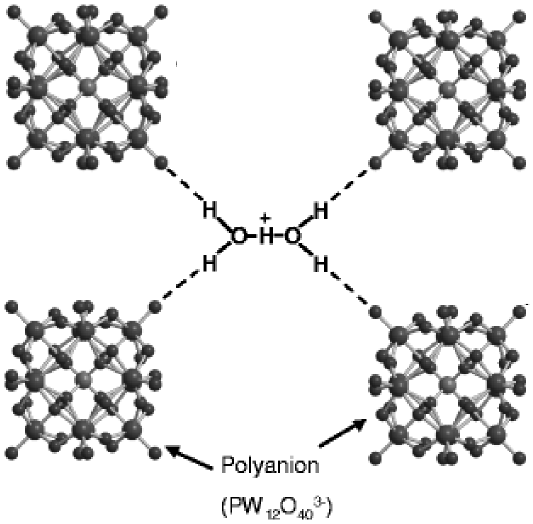

Figure 1.5. The structure of $H_3PW_{12}O_{40}$, showing the 4 Keggin units surrounding crystalline water, $H_5O_2^+$.[67]

However, heteropolyacids are soluble in polar media[68] and therefore cannot be used directly for biodiesel synthesis. Ion-exchanged Keggin type phosphotungstic acids[69] can remove this problem as the Cs^+ and NH_4^+ doped variants are insoluble in water.[70] $Cs_xH_{(3-x)}PW_{12}O_{40}$ shows high activity for fatty acid methyl ester (FAME) production during palmitic acid esterification.[44] Narasimharao and co-workers[44] reported that when $x = 2.3$, the Cs doped heteropolyacid catalyst converted 100 % of the palmitic acid after 6 hours at 60 ºC, with a 30:1 methanol: oil ratio and 1.9 wt% catalyst. The selectivity to methyl palmitate was greater than 98 %.

1.5 Solid base catalysts for biodiesel synthesis

Solid base catalysts generally show higher activity than solid acids in the transesterification of triglycerides to form biodiesel, and are particularly ideal when transesterifying high purity oil feedstocks with low free fatty acid content. Solid base catalysts such as hydrotalcites,[48, 71] alkaline earth oxides[49, 50, 72-74] and alkali-doped mesoporous silicas[75] have all been reported to show good activities for TAG transesterification.

1.5.1 Hydrotalcites

Hydrotalcites (HTs) are a class of naturally occurring materials possessing layered double hydroxide structures,[12, 76] with the general formula $[M(II)_{1-x}M(III)_x(OH)_2]^{x+}(A^{n-}{}_{x/n})\cdot mH_2O$,[9] where $0.17<x>0.33$. MgAl HTs comprise positively charged brucite-like layers, due to substitution of Mg^{2+} with Al^{3+} cations, charge-balanced by interlayer anions A^{n-}.[77] The Mg:Al ratio in the hydrotalcite can be varied within the defined values for x, altering the basicity. The basicity increases with increasing Mg:Al ratio, enhancing the activity of the catalyst in the transesterification of triglycerides.[48] Carbonate is commonly found in the interlayer space of the as-prepared hydrotalcites, although intercalation of sulfate[78], nitrate[79] and various organic anions[80] have been reported. The hydrotalcite structure is shown in **Figure 1.6.**

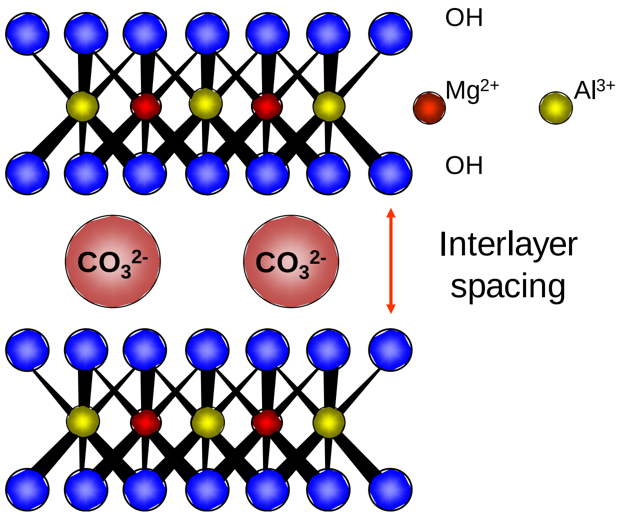

Figure 1.6. General structure of an MgAl hydrotalcite.

Hydrotalcites are used as catalysts but they have also found use in many other applications, such as in flame retardants, antacids or as catalyst supports.[76] They also have good anion exchange capacity[81], and are therefore used in applications such as the removal of anions from wastewater supplies.[82]

The hydrotalcite as it is prepared, with interlayer carbonate anions, is not active as a catalyst in the transesterification of triglycerides. On calcination, the carbonate is removed and the hydrotalcite loses its layered double hydroxide structure, forming a mixed metal oxide, which does show activity in the transesterification reaction.[83] Xie and co-workers[84] tested a 3:1 Mg:Al calcined hydrotalcite in the transesterification of soy bean oil and reported conversions of 67 % after 9 hours at 60 ºC, with a methanol: oil ratio of 15:1 and 7.5 wt% catalyst.

If the hydrotalcites are exposed to water vapour after calcination, the layered double hydroxide structure can be reformed in a process dubbed “The Memory Effect”,[85] the interlayer carbonate anions replaced with hydroxide anions. These rehydrated hydrotalcites have Brønsted base sites incorporated into the interlayer space,[86] and have shown greater activity than Lewis base site containing calcined hydrotalcites in the aldol condensation of benzaldehyde with acetone,[87] Michael addition reactions,[88] and the transesterification of methyl oleate with glycerol.[89] Xi and Davis[51] reported 80 % tributyrin conversion for a 4:1 Mg:Al rehydrated hydrotalcite over 400 minutes at 60 ºC, with a methanol: oil ratio of 30:1 and only 0.06 wt% catalyst. They showed that the Brønsted base sites of the Mg:Al hydrotalcite are active in the presence of water.

However, significant hydration resulted in rapid deactivation. This was thought to be due to butyric acid, formed by ester hydrolysis, blocking the active base sites.

The vast majority of synthetic hydrotalcite catalysts are prepared via co-precipitation using caustic pH regulators which result in residual alkali contamination[90] and associated complications arising from leaching and homogeneous contributions to biodiesel production,[91, 92] in addition to their corrosive impact. To combat this problem, Cantrell and co-workers[48] reported an alkali-free route to prepare hydrotalcites using ammonia and ammonium carbonate. They showed increasing activity of the hydrotalcites in the transesterification of tributyrin with increasing Mg:Al ratio, the most active 2.93:1 Mg:Al catalyst converting around 75 % of the tributyrin after 3 hours at 60 ºC, with a 30:1 methanol: oil ratio and 1.6 wt% catalyst.

Currently, the commercial application of hydrotalcites to bio-derived oils is hampered by narrow interlayer spacings which restrict diffusion of bulky/unsaturated TAGs within crystallites.[48, 51, 52]

1.5.2 Alkaline earth oxides

Alkaline earth oxides, for example CaO and MgO, possess a rock-salt structure with alternating metal cations and oxygen anions. The basicity of alkaline earth oxides can arise in various ways.[93] Defects in the lattice, such as cationic vacancies (**Figure 1.7a**) or step and edge sites, can occur as the surface reconstructs during annealing,[94] providing lower co-ordinate anion sites with higher basicity.

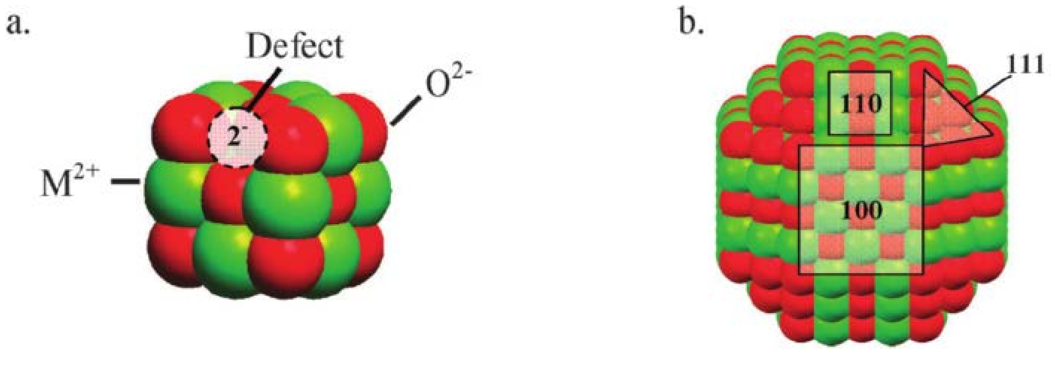

Figure 1.7 a) Cationic defect site and **b)** (100), (110) and (111) surface terminations in an alkaline earth oxide crystal, taken from Wilson and co-workers.[53]

Alkaline earth oxides have three common surface terminations: (100), (110), and (111), as shown in **Figure 1.7b**. The nature of the exposed planes can also affect the basicity of the alkaline earth oxide. Both the (100) and (110) surfaces are defined by Tasker[95] as type I surfaces, for which the surface layer is a charge neutral array of equal numbers of cations and anions.[96] The (100) plane is the most thermodynamically stable as the relaxed terminated surface results in a nearest neighbour Mg-O interatomic distance of 2.11 Å, which is relatively unperturbed from the bulk. For the (110) surface, two pairs of Mg-O atoms are relaxed to interatomic distances of 2.11 Å and 2.02 Å, respectively, creating a higher energy surface.[96] The least energetically stable, type III polar (111) surface consists of alternating oxide anion and metal cation layers, with the oxide layer thermodynamically favourable on exposure to air, giving this plane the highest electron density. Therefore, the basicity of the planes increases in the order (100) > (110) > (111).[97] An alkaline earth oxide exposing more of the electron rich planes, along with a greater number of defect sites, would have a higher Lewis basicity and show higher activity. Verziu and co-workers[98] compared microcrystalline MgO with nanoparticulate MgO prepared in different ways in the transesterification of sunflower oil. They found that the nanoparticulate MgO catalysts all outperformed the microcrystalline catalyst, but that also the nanoMgO catalyst consisting of (111) exposed planes had higher activity than the catalysts with (110) or (100) exposed facets, in accordance with the higher Lewis basicity for this plane.

CaO has been widely studied as a catalyst in the transesterification reaction.[99-102] Verziu and co-workers[103] report conversions of 92 % when testing thermally activated microcrystalline CaO in the transesterification of sunflower oil at 75 °C, after 2 hours reaction with a 4:1 methanol: oil ratio and 1.4 wt% catalyst. However, some leaching of Ca^{2+} from the CaO lattice does occur under reaction conditions, this homogeneous contribution leading to problems with separation of the alkali metal from the biodiesel product.

1.5.3 Alkali metal doping of alkaline earth oxides

Doping alkaline-earth oxides with alkali metals offers a route to achieving even higher catalytic transesterification rates, through the resulting enhancement of surface basic properties.[104] Ito and co-workers[105] found that doping magnesium oxide with Li^+ rendered it more active for the oxidative dimerisation of methane than an undoped oxide. It was hypothesised that Li^+ doping led to the generation of more O^{2-} anionic base sites on the oxide surface, increasing the Lewis basicity. Hargreaves and co-workers[106] also studied lithium doped MgO, and reported that alkali metal ion incorporation into the oxide lattice produced potentially more electron rich corner sites, point defects and step sites, enhancing the catalytic activity.

It has been suggested that Li^+ dopants subsequently preferentially coordinate to these highly active corner and step sites upon thermal processing, modulating the anticipated enhanced basicity.[104] Larger alkali cations are predicted unable to coordinate to these sites due to their greater ionic radii, leaving them available for reaction.[107, 108] Instead, they can donate electrons to the magnesium oxide lattice, which are trapped at oxygen vacancies, giving rise to electron rich sites, called F-centres. Matsuhashi and co-workers[107] hypothesised that it was these sites which resulted in the highly basic properties of the doped magnesium oxide, and the high catalytic activity observed in base-catalysed reactions.

Montero and co-workers[109] reported on the enhanced catalytic activity of MgO in the transesterification of tributyrin (a short chain C_4 model triglyceride) with methanol, via Cs doping using a co-precipitation method, however the nature of the active phase, and broader application of this catalyst to biodiesel synthesis remains unclear.

1.5.4 Supported alkali metals/alkaline earth oxides

Supporting metal nanoparticles or metal oxides on high surface area materials is a well reported way of reducing the cost and increasing their stability as catalysts.[110] The high surface area support allows good dispersion of a small amount of the catalytically active metal,[111-113] and easy recovery of the metal catalyst after reaction. Supports are a good way of minimising mass transfer limitations for heterogeneous catalysts in liquid phase reactions,[114] by providing greater accessibility through the existence of pores where metal particles can be anchored.[115] Common support materials include silica,[116] alumina,[117, 118] zirconia,[119] ceria[120] and titania.[121] SBA-15 belongs to a family of ordered mesoporous silicas. Its high surface area, tuneable pore structure and thermal and chemical stability make it an ideal candidate as a catalyst support.[122, 123] Samart and co-workers[124] achieved conversions of 95% in the transesterification of soybean oil when using 15 wt% CaO supported on mesoporous silica at 60 ºC after 8 hours with 5 wt% catalyst and a 16:1 methanol: oil ratio.

Alkali metals supported on alumina have been studied as catalysts in the transesterification of triglycerides.[125-128] Xie and co-workers[129] loaded KI onto alumina and found on activation, high activities were obtained in the transesterification of soybean oil. The basicity is thought to arise from the K_2O formed during calcination, along with surface Al-O-K groups formed by salt-support interactions. At 35 wt% KI loading on alumina, 96 % conversion was achieved after 8 h at methanol reflux, with 2.5 wt% catalyst and a 15:1 methanol: oil ratio. Vyas and co-workers[130] tested 35 wt% KNO_3 supported on alumina in the transesterification of *Jatropha* oil. After calcination at 500 ºC, the catalyst converted 84 % of the *Jatropha* oil after 6 h reaction at 70 ºC, with a methanol: oil ratio of 12:1 and 6 wt% catalyst. However, there are concerns in the literature over leaching of the alkali metal from these supported catalysts, and therefore the high activities reported may be partially due to homogeneous activity.[131, 132]

Umdu and co-workers[133] tested CaO, both pure and supported, on alumina, in the transesterification of algal lipids to form biodiesel. They found that the unsupported CaO was not active, however the supported catalysts did show activity. This was due to the much smaller particle size of the CaO when formed on the support, ~5 nm as supposed to 164 nm for pure CaO, as well as the high dispersion of the CaO over the alumina support.

1.6 Porosity in catalysis

Pore networks in catalysts and their supports allow for the mass transport of substrates to active sites within the catalyst bulk, and therefore play a vital role in the activity of catalytic materials. Depending on the average pore diameters, materials can either be defined as microporous (pore size < 2 nm), mesoporous (2-50 nm) or macroporous (> 50 nm).[134]

1.6.1 Microporous materials

Among the family of microporous materials, the best known members are zeolites, aluminosilicates which have a narrow and uniform micropore size distribution due to their crystallographically defined pore system. Their structure consists of silica and alumina tetrahedra, linked at the corners via a common oxygen atom, resulting in an inorganic macromolecule with a 3D framework.[135] The framework, which has an overall negative charge due the presence of AlO_2^- tetrahedra, contains regular microporous channels with a diameter up to 1 nm, which house water molecules and charge balancing cations. Two examples of zeolite structures can be seen in **Figure 1.8**.

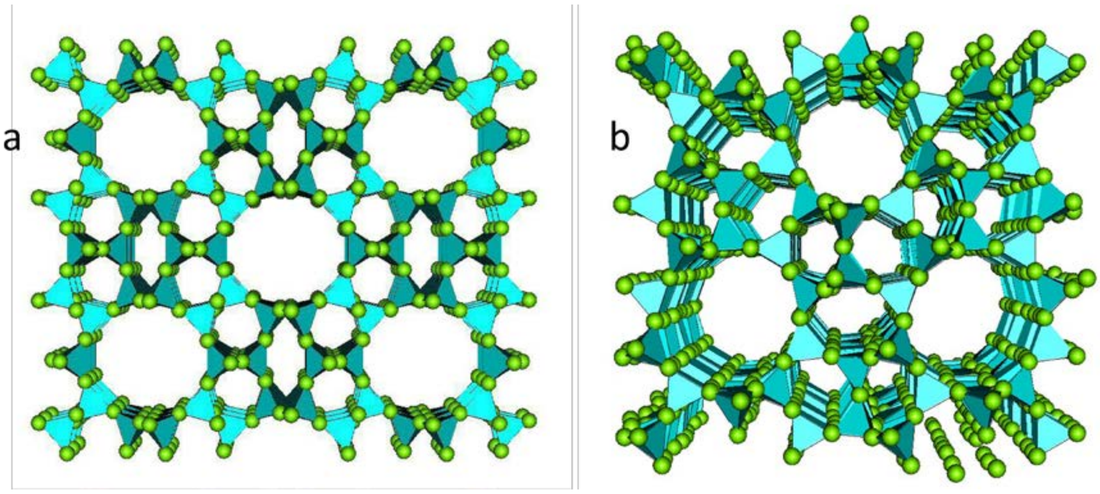

Figure 1.8. Examples of different zeolite structures: a) zeolite Theta-1 and b) zeolite ZSM-5, showing the microporous channels.[136]

Zeolites are the catalyst of choice for the cracking of crude oil, a process vital for the large scale generation of commodity compounds.[137] However, their microporous nature means that there are mass transport limitations due to slow diffusion of the bulky substrates through the narrow pore channels, and therefore problems arise from coking and pore blockage. Therefore cracking reactors must operate with a fluidised catalyst regenerator unit. Air is used to burn off the coke from spent catalysts, and the hot regenerated zeolite is circulated back to the reactor. The incorporation of larger pore networks could enhance their activity and remove the need for this regeneration step.

1.6.2 Mesoporous materials

In liquid phase catalysis, mesoporous catalysts and/or supports can be used to minimise the diffusion limitations commonly observed for microporous materials. In the case of zeolites discussed in the previous section, preparing a hierarchical material which contains a secondary mesopore structure, such as H-β-zeolite, can lead to enhanced activity in fluid catalytic cracking compared to conventional zeolites.[138, 139 140]

In 1992, Mobil Oil Corporation discovered the ordered mesoporous silica, MCM-41; with a hexagonal array of unidimensional mesopores and a narrow pore size distribution.[141, 142] MCM-48 and MCM-51, which have cubic and lamellar mesostructures respectively, were also reported in these early publications. The three different types of mesopore structure are illustrated below in **Figure 1.9**.

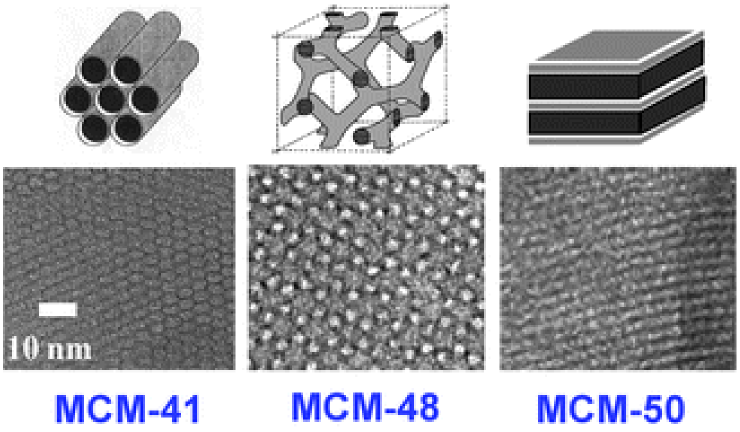

Figure 1.9. Diagrams and TEM images showing the hexagonal, cubic and lamellar pore structures of the MCM-41, MCM-48 and MCM-50 mesoporous silicas respectively.[143]

The MCM family of silicas are prepared using ionic surfactants. However, there has been a large amount of research into the generation of mesoporous solids. By altering the silica source, the synthesis conditions and the type of surfactant used as a template many different types of mesoporous silica can be prepared.[144] SBA-15, a 2D non-interconnected hexagonal mesoporous material exhibiting *p6mm* pore symmetry, with pore diameters between about 6 and 15 nm, is prepared through liquid crystal templating using a Pluronic® surfactant. The ethylene oxide units of the Pluronic®

polymer and the cationic silicate species favourably interact to form the mesostructured assembly. Within the same family, SBA-16 and KIT-6 have 3D interconnected pore structures with $Im\overline{3}m$ and $Ia\overline{3}d$ symmetry respectively. The high surface areas, tuneable pore structures and thermal/chemical stability [123] of the SBA family,[145, 146] in particular SBA-15/16, and KIT-6 [147, 148] make them choice support materials. These architectural variations combined with their chemical inertness relative to reducible supports [149] and weak metal interactions,[150, 151] are beneficial in the role of catalyst support. Significant enhancements in in-pore accessibility can be achieved via the use of 3D interconnected mesopore architectures over 2D ones, for example by stabilising high active site dispersion,[111] or enhancing reagent diffusion during catalytic reactions when bulky substrates are employed.[152]

Mesoporous silicas have been widely investigated as catalysts in cracking and hydrocracking reactions. Al can be substituted into the silica framework to increase the acidity of the catalyst. Al containing MCM-41 has shown substantial cracking activity for palm oil, with conversions of 80-90 wt% and high selectivity to liquid hydrocarbons obtained[153]. Sulfated zirconia can also be supported in the SBA-15 pore network. Garg and co-workers[154] tested sulfated zirconia supported on SBA-15 at different weight percentages as catalysts for the cracking of cumene. The 35 wt% sulfated zirconia on SBA-15 catalyst showed activity 6.4 times greater than the bulk sulfated zirconia in the cracking reaction.[154]

As discussed in the previous sections, SBA-15 derived catalysts have proved popular candidates for biodiesel synthesis, both via sulfonic acid functionalisation of SBA-15 in order to esterify free fatty acids,[155] or by using the SBA-15 as a support for solid bases such as alkali metals or alkaline earth oxides.[156] However, these templated supports possess long, isolated 5 nm diameter parallel channels which are not conducive to efficient in-pore diffusion and result in poor catalytic turnover.[53] More effort is thus required to tailor catalyst porosity to optimise mass-transport of these bulky and viscous C16-C18 triglycerides or free fatty acids typical of plant oils.

1.6.3 Hierarchical meso-macroporous solids

The incorporation of macropores into mesoporous architectures can minimise diffusion barriers, and potentially enhance the distribution of active sites during catalyst preparation. Simulations suggest that in the Knudsen diffusion regime, where reactants/products are able to enter or exit mesopores but experience attendant diffusion, such bi-modal pore structures can significantly improve active site accessibility.[157]
The first meso-macroporous silica was reported by Yang and co-workers,[158] although it was not tested catalytically at that time. Hierarchical macroporous-mesoporous SBA-15 has been prepared by Dhainaut and co-workers,[23] using a dual templating method of liquid crystal surfactants to form the mesopores, and a polystyrene bead template which is calcined to leave behind macropores. This technique is illustrated below in **Figure 1.10.**

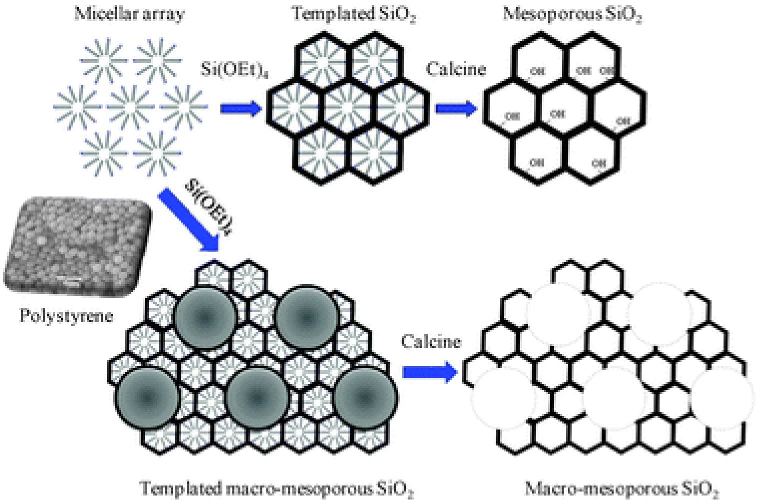

Figure 1.10. Liquid crystal templating route to form mesoporous silica and combined physical templating method using polystyrene microspheres to introduce a macropore network.

When functionalised with sulfonic acid, the meso-macroporous SBA-15 catalyst with the highest macropore density was more than twice as active as the purely mesoporous analogue in the transesterification of the C8 TAG tricaprylin, despite having a lower total surface area and pore volume. This enhancement was attributed to the increased rate of diffusion of the TAG molecules through the macropores into the bulk catalyst, and also due to the increased density of accessible base sites at the edges of the mesopores, after the macropore channels have broken up the mesopore domain size.

There have previously been reports on preparing meso-macroporous alumina with disordered pore arrangements.[159, 160] However, recently, the dual-templating method similar to that used for the preparation of meso-macroporous silica has also led to the development of highly organised tuneable meso-macroporous alumina[161]. Choi and co-workers[162] prepared a macro-mesoporous Pt on alumina catalyst and found it improved the activity of hydrogen oxidation compared to the mesoporous Pt/alumina due to enhanced hydrogen gas diffusion and active site accessibility. Pt supported on macro-mesoporous alumina has also been tested for CO oxidation. The ordered hierarchical structure allows uniform platinum dispersion and rapid CO diffusion allowing the catalyst to outperform commercial Pt/γ-alumina catalysts.[163]

3D ordered macroporous titania containing secondary periodicity at the mesoporous scale can be prepared via hexagonal close packing of polystyrene (PS) colloid crystals combined with the use of a soft mesopore directing agent, P123.[164] These materials exhibit macropores of 170 or 200 nm and 3 nm mesopores. The activity towards methyl blue decomposition was greater than that of a purely mesoporous film, due to the smaller mesopore domain size and improved accessibility of TiO_2 surfaces. This hierarchically structured material exhibits ordered, hexagonally packed spherical macropores, and is around 7 times more active than titania possessing a disordered macroporous network in methyl blue degradation under visible light.

Zeolite (ZSM-5) crystals have been grown on the surface of a 3D trimodal glass scaffold, using an evaporation induced self assembly method.[165] Pluronic P123 and methyl cellulose were used as mesopore and macropore directing agents respectively, generating giant ordered macropores of 300–500 μm, disordered macropores of 10-100 μm and ordered 4–5 nm mesopores with *P6mm* symmetry. The glass–ZSM-5 composite shows 7-fold enhanced activity in the cracking of *n*-hexane than commercial ZSM-5 and slightly enhanced propylene selectivity. Promotion is attributed to the interconnecting pore network, in particular the shorter product contact time associated with improved diffusion through the composite, suppressing secondary reactions.[166]

1.6.4 Incorporation of macropores into hydrotalcites

It has been shown that incorporating macropores into a catalyst can greatly enhance the mass transport abilities of the material, allowing longer chained bulkier molecules to travel quickly through the material to reach the more accessible catalyst active sites. Géraud and co-workers[167, 168] engineered a macroporous Mg-Al hydrotalcite catalyst, via physical templating around a sacrificial polystyrene bead template,[169] as illustrated in **Figure 1.11**.

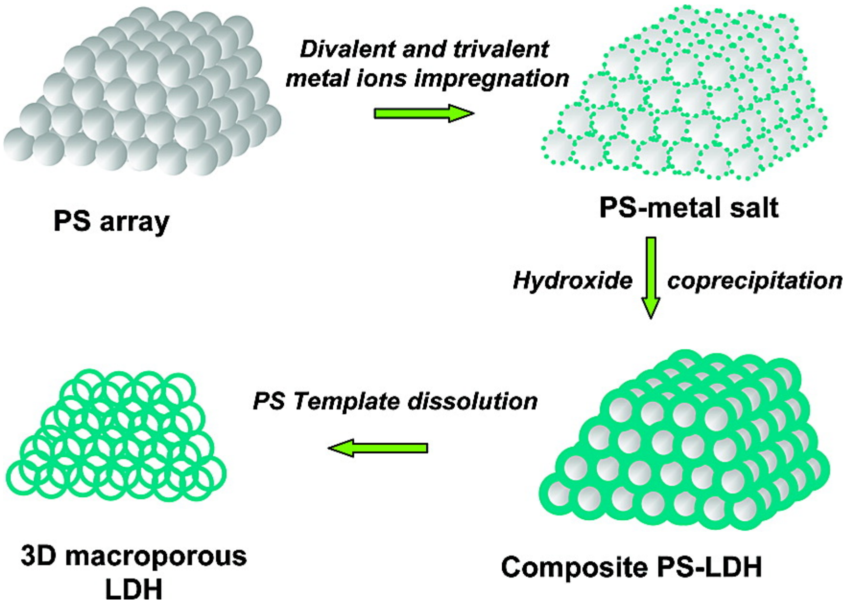

Figure 1.11. Schematic illustrating Géraud's protocol for preparing macroporous hydrotalcites.[168]

This material was prepared with polystyrene beads of such diameter to give 650 nm macropores, along with internal mesoporosity arising from the voids between neighbouring layers. Decatungstate anions, $W_{10}O_{32}$, were introduced into the interlayer space, and the material tested in 2,6-dimethylphenol degradation. The tungstated macroporous material was found to be significantly more active than its conventional counterpart (without macropores), with conversion increasing from around 10 % to around 90 %.[168]

1.7 Thesis Aims

There is a great incentive to move from using liquid base catalysts in industrial biodiesel synthesis to heterogeneous solid base catalysts, for the reasons mentioned earlier in the introduction, including ease of separation of catalyst from the biodiesel product and the opportunity to synthesise biodiesel using a continuous process. Any enhancement to the activity of these solid base catalysts, through increasing their basicity or removing diffusion limitations by tuning the pore architectures, would help to improve their viability for use industrially in the synthesis of biodiesel.

The overall aims of this thesis are to:

a) Tailor the structure of hydrotalcites in an attempt to remove the mass transfer limitations hampering their activity in the transesterification reaction, due to slow diffusion of the large bulky triglycerides through the microporous bulk to reach the active sites. This will be attempted by preparing novel materials, through the incorporation of macropores or the preparation of a thin layer of hydrotalcite on a support.

b) Compare the physicochemical properties of nanostructured hydrotalcites with those of conventional hydrotalcites in order to identify structure-function relations and establish any interdependence of catalyst basicity upon architecture or synthetic protocol.

c) Determine the nature of the active species within Cs doped MgO and thus obtain further insight into the activity enhancement associated with the alkali dopant.

d) Benchmark the nanostructured solid base catalysts in the transesterification of model triglycerides spanning C4-C18 alkyl chains, and a real (olive) oil feedstock, in order to quantify any activity enhancements relative to their conventional counterparts, and thus determine their viability as catalysts for commercial biodiesel synthesis.

1.8 References

1. N. Armaroli and V. Balzani, *Angewandte Chemie-International Edition*, 2007, **46**, 52-66.
2. BP, www.bp.com/statisticalreview, Accessed April 2013.
3. X. Y. Yan, O. R. Inderwildi and D. A. King, *Energy & Environmental Science*, 2010, **3**, 190-197.
4. R. Luque, L. Herrero-Davila, J. M. Campelo, J. H. Clark, J. M. Hidalgo, D. Luna, J. M. Marinas and A. A. Romero, *Energy & Environmental Science*, 2008, **1**, 542-564.
5. UK Department for Transport, Biofuels - risks and opportunities www.dft.gov.uk, Accessed April 2013.
6. G. Knothe, *Topics in Catalysis*, 2010, **53**, 714-720.
7. R. Luque, J. C. Lovett, B. Datta, J. Clancy, J. M. Campelo and A. A. Romero, *Energy & Environmental Science*, 2010, **3**, 1706-1721.
8. www.ebb-eu.org/stats.php#, European Biodiesel Board.
9. U. Constantino, F. Marmottini, M. Nocchetti and R. Vivani, *European Journal of Inorganic Chemistry*, 1998, 1439-1446.
10. K. Narasimharao, A. Lee and K. Wilson, *Journal of Biobased Materials and Bioenergy*, 2007, **1**, 19-30.
11. M. J. Climent, A. Corma, S. Iborra, K. Epping and A. Velty, *Journal of Catalysis*, 2004, **225**, 316-326.
12. M. R. Othman, Z. Helwani, Martunus and W. J. N. Fernando, *Applied Organometallic Chemistry*, 2009, **23**, 335-346.
13. Y. Liu, E. Lotero, J. G. Goodwin and X. Mo, *Applied Catalysis A: General*, 2007, **33**, 138-148.
14. J. Geuens, J. M. Kremsner, B. A. Nebel, S. Schober, R. A. Dommisse, M. Mittelbach, S. Tavernier, C. O. Kappe and B. U. W. Maes, *Energy & Fuels*, 2007, **22**, 643-645.
15. Hu, Du, Z. Tang and Min, *Industrial & Engineering Chemistry Research*, 2004, **43**, 7928-7931.
16. G. Knothe, *Fuel Processing Technology*, 2005, **86**, 1059-1070.
17. S. K. Hoekman, A. Broch, C. Robbins, E. Ceniceros and M. Natarajan, *Renewable and Sustainable Energy Reviews*, 2012, **16**, 143-169.
18. W. M. Antunes, C. D. Veloso and C. A. Henriques, *Catalysis Today*, 2008, 548-554.
19. A. Radich, Energy Information Administration, 2004, p. http://www.eia.doe.gov/oiaf/analysispaper/biodiesel/.
20. J. Van Gerpen, *Fuel Processing Technology*, 2005, **86**, 1097-1107.
21. *Sustainable biofuels: prospects and challenges*, The Royal Society, London, 2008.
22. W. M. J. Achten, L. Verchot, Y. J. Franken, E. Mathijs, V. P. Singh, R. Aerts and B. Muys, *Biomass & Bioenergy*, 2008, **32**, 1063-1084.
23. J. Dhainaut, J. P. Dacquin, A. F. Lee and K. Wilson, *Green Chemistry*, 2010, **12**, 296-303.
24. www.jatrophacurcasplantations.com, Accessed May 2013.
25. www.biogreentech.com, Accessed May 2013.
26. R. Sarin, M. Sharma, S. Sinharay and R. K. Malhotra, *Fuel*, 2007, **86**, 1365-1371.

27. W. M. J. Achten, E. Mathijs, L. Verchot, V. P. Singh, R. Aerts and B. Muys, *Biofuels Bioproducts & Biorefining-Biofpr*, 2007, **1**, 283-291.
28. S. Pinzi, I. L. Garcia, F. J. Lopez-Gimenez, M. D. Luque de Castro, G. Dorado and M. P. Dorado, *Energy & Fuels*, 2009, **23**, 2325-2341.
29. S. Leduc, K. Natarajan, E. Dotzauer, I. McCallum and M. Obersteiner, *Applied Energy*, 2009, **86**, S125-S131.
30. J. Van Gerpen, Animal fats for biodiesel production, http://www.extension.org/pages/30256/animal-fats-for-biodiesel-production#.UiRmyIxwaUk, Accessed Sep 2013.
31. J. Janaun and N. Ellis, *Renewable and Sustainable Energy Reviews*, 2010, **14**, 1312-1320.
32. A. K. Greene, P. L. Dawson, D. Nixon, J. R. Atkins and P. G.G., Safety of animal fats for biodiesel production: a critical review of literature virtual.vtt.fi/virtual/amf/pdf/annex30_vol3.pdf, Accessed 6/9/2013.
33. V. B. Borugadda and V. V. Goud, *Renewable & Sustainable Energy Reviews*, 2012, **16**, 4763-4784.
34. D. Y. C. Leung, X. Wu and M. K. H. Leung, *Applied Energy*, 2010, **87**, 1083-1095.
35. T. M. Mata, A. A. Martins and N. S. Caetano, *Renewable & Sustainable Energy Reviews*, 2010, **14**, 217.
36. R. Luque, *Energy & Environmental Science*, 2010, **3**, 254-257.
37. P. J. l. B. Williams and L. M. L. Laurens, *Energy & Environmental Science*, 2010, **3**, 554-590.
38. K. M. Weyer, D. R. Bush, A. Darzins and B. D. Willson, *Bioenergy Research*, 2010, **3**, 204-213.
39. S. C. James and V. Boriah, *J. Comput. Biol.*, 2010, **17**, 895-906.
40. E. A. Ehimen, Z. F. Sun and C. G. Carrington, *Fuel*, 2010, **89**, 677-684.
41. algae-energy.co.uk, Accessed May 2013.
42. G. Vicente, M. Martinez and J. Aracil, *Bioresource Technology*, 2004, **92**, 297-305.
43. M. S. Graboski and R. L. McCormick, *Progress in Energy and Combustion Science*, 1998, **24**, 125-164.
44. K. Narasimharao, D. R. Brown, A. F. Lee, A. D. Newman, P. F. Siril, S. J. Tavener and K. Wilson, *Journal of Catalysis*, 2007, **248**, 226-234.
45. L. Pesaresi, D. R. Brown, A. F. Lee, J. M. Montero, H. Williams and K. Wilson, *Applied Catalysis a-General*, 2009, **360**, 50-58.
46. E. Lotero, Y. J. Liu, D. E. Lopez, K. Suwannakarn, D. A. Bruce and J. G. Goodwin, *Industrial & Engineering Chemistry Research*, 2005, **44**, 5353-5363.
47. J. A. Melero, J. Iglesias and G. Morales, *Green Chemistry,* 2009, **11**, 1285-1308.
48. D. G. Cantrell, L. J. Gillie, A. F. Lee and K. Wilson, *Applied Catalysis A: General*, 2005, **287**, 183-190.
49. K. Wilson, C. Hardacre, A. F. Lee, J. M. Montero and L. Shellard, *Green Chemistry*, 2008, **10**, 654-659.
50. J. M. Montero, P. Gai, K. Wilson and A. F. Lee, *Green Chemistry*, 2009, **11**, 265-268.
51. Y. Xi and R. J. Davis, *Journal of Catalysis*, 2008, **254**, 190-197.
52. M. J. Kim, S. M. Park, D. R. Chang and G. Seo, *Fuel Processing Technology*, 2010, **91**, 618-624.
53. K. Wilson and A. F. Lee, *Catalysis Science & Technology*, 2012, **2**, 884-897.

54. K. Suwannakarn, E. Lotero, J. G. Goodwin Jr and C. Lu, *Journal of Catalysis*, 2008, **255**, 279-286.
55. T. A. Peters, N. E. Benes, A. Holmen and J. T. F. Keurentjes, *Applied Catalysis A: General*, 2006, **297**, 182-188.
56. A. A. Kiss, A. C. Dimian and G. Rothenberg, *Advanced Synthesis & Catalysis*, 2006, **348**, 75-81.
57. I. K. Mbaraka, D. R. Radu, V. S. Y. Lin and B. H. Shanks, *Journal of Catalysis*, 2003, **219**, 329-336.
58. N. Katada, T. Hatanaka, M. Ota, K. Yamada, K. Okumura and M. Niwa, *Applied Catalysis a-General*, 2009, **363**, 164-168.
59. L. L. Xu, Y. H. Wang, X. Yang, X. D. Yu, Y. H. Guo and J. H. Clark, *Green Chemistry*, 2008, **10**, 746-755.
60. Q. Shu, B. Yang, H. Yuan, S. Qing and G. Zhu, *Catalysis Communications*, 2007, **8**, 2159-2165.
61. O. Babajide, N. Musyoka, L. Petrik and F. Ameer, *Catalysis Today*, 2012, **190**, 54-60.
62. G. R. Peterson and W. P. Scarrah, *J Am Oil Chem Soc*, 1984, **61**, 1593-1597.
63. D. E. López, J. G. Goodwin Jr, D. A. Bruce and E. Lotero, *Applied Catalysis A: General*, 2005, **295**, 97-105.
64. D. E. Lopez, J. G. Goodwin, Jr. and D. A. Bruce, *Journal of Catalysis*, 2007, **245**, 381-391.
65. I. K. Mbaraka and B. H. Shanks, *Journal of Catalysis*, 2005, **229**, 365-373.
66. J. Jitputti, B. Kitiyanan, P. Rangsunvigit, K. Bunyakiat, L. Attanatho and P. Jenvanitpanjakul, *Chemical Engineering Journal*, 2006, **116**, 61-66.
67. S. Sachdeva, J. Turner, J. Horan and A. Herring, in *Fuel Cells and Hydrogen Storage*, eds. A. Bocarsly and D. M. P. Mingos, Springer Berlin Heidelberg, 2011, vol. 141, ch. 45, pp. 115-168.
68. T. Okuhara, N. Mizuno and M. Misono, in *Advances in Catalysis*, eds. W. O. H. D.D. Eley and G. Bruce, Academic Press, 1996, vol. Volume 41, pp. 113-252.
69. T. Okuhara, T. Nishimura, H. Watanabe and M. Misono, *Journal of Molecular Catalysis*, 1992, **74**, 247-256.
70. T. Okuhara, T. Arai, T. Ichiki, K. Y. Lee and M. Misono, *Journal of Molecular Catalysis*, 1989, **55**, 293-301.
71. J. J. Woodford, J.-P. Dacquin, K. Wilson and A. F. Lee, *Energy & Environmental Science*, 2012, **5**, 6145-6150.
72. R. S. Watkins, A. F. Lee and K. Wilson, *Green Chemistry*, 2004, **6**, 335-340.
73. M. Kouzu, T. Kasuno, M. Tajika, S. Yamanaka and J. Hidaka, *Applied Catalysis a-General*, 2008, **334**, 357-365.
74. T. F. Dossin, M.-F. Reyniers, R. J. Berger and G. B. Marin, *Applied Catalysis B: Environmental*, 2006, **67**, 136-148.
75. M. C. G. Albuquerque, I. Jimenez-Urbistondo, J. Santamaria-Gonzalez, J. M. Merida-Robles, R. Moreno-Tost, E. Rodriguez-Castellon, A. Jimenez-Lopez, D. C. S. Azevedo, C. L. Cavalcante, Jr. and P. Maireles-Torres, *Applied Catalysis a-General*, 2008, **334**, 35-43.
76. F. Cavani, F. Trifiro and A. Vaccari, *Catalysis Today*, 1991, **11**, 173-291.
77. V. R. L. Constantino and T. J. Pinnavaia, *Inorganic Chemistry*, 1995, **34**, 883-892.
78. S. Miyata and A. Okada, *Clay Clay Min.*, 1977, **25**, 14-18.
79. O. Marino and G. Mascolo, *Thermochim. Acta*, 1982, **55**, 377-383.
80. W. T. Reichle, *Journal of Catalysis*, 1985, **94**, 547-557.

81. A. Vaccari, *Catalysis Today*, 1998, **41**, 53-71.
82. L. Lv, P. Sun, Z. Gu, H. Du, X. Pang, X. Tao, R. Xu and L. Xu, *Journal of Hazardous Materials*, 2009, **161**, 1444-1449.
83. D. P. Debecker, E. M. Gaigneaux and G. Busca, *Chem.-Eur. J.*, 2009, **15**, 3920-3935.
84. W. Xie, H. Peng and L. Chen, *Journal of Molecular Catalysis A: Chemical,* 2006, **246**, 24-32.
85. V. Dávila, E. Lima, S. Bulbulian and P. Bosch, *Microporous and Mesoporous Materials*, 2008, **107**, 240-246.
86. A. Corma, S. B. A. Hamid, S. Iborra and A. Velty, *Journal of Catalysis*, 2005, **234**, 340-347.
87. K. K. Rao, M. Gravelle, J. S. Valente and F. Figueras, *Journal of Catalysis*, 1998, **173**, 115-121.
88. B. M. Choudary, M. Lakshmi Kantam, C. R. Venkat Reddy, K. Koteswara Rao and F. Figueras, *Journal of Molecular Catalysis A: Chemical*, 1999, **146**, 279-284.
89. Y. Z. Xi and R. J. Davis, *Journal of Catalysis*, 2009, **268**, 307-317.
90. V. K. Diez, C. R. Apesteguia and J. I. Di Cosimo, *Journal of Catalysis*, 2003, **215**, 220-233.
91. H. E. Cross and D. R. Brown, *Catalysis Communications*, 2010, **12**, 243-245.
92. M. Di Serio, R. Tesser, L. Casale, A. D'Angelo, M. Trifuoggi and E. Santacesaria, *Topics in Catalysis*, 2010, **53**, 811-819.
93. V. E. Henrich and P. A. Cox, *The Surface Science of Metal Oxides*, Cambridge University Press, Cambridge, UK, 1994.
94. G. Pacchioni, *Solid State Sciences*, 2000, **2**, 161-179.
95. P. W. Tasker, *Journal of Physics C-Solid State Physics*, 1979, **12**, 4977-4984.
96. D. O. Scanlon, A. Walsh, B. J. Morgan, M. Nolan, J. Fearon and G. W. Watson, *Journal of Physical Chemistry C*, 2007, **111**, 7971-7979.
97. K. Zhu, J. Hu, C. Kuebel and R. Richards, *Angewandte Chemie-International Edition*, 2006, **45**, 7277-7281.
98. M. Verziu, B. Cojocaru, J. Hu, R. Richards, C. Ciuculescu, P. Filip and V. I. Parvulescu, *Green Chemistry*, 2008, **10**, 373-381.
99. M. C. G. Albuquerque, D. C. S. Azevedo, C. L. Cavalcante Jr, J. Santamaría-González, J. M. Mérida-Robles, R. Moreno-Tost, E. Rodríguez-Castellón, A. Jiménez-López and P. Maireles-Torres, *Journal of Molecular Catalysis A: Chemical*, 2009, **300**, 19-24.
100. S. Gryglewicz, *Bioresource Technology*, 1999, **70**, 249-253.
101. M. López Granados, D. Martín Alonso, A. C. Alba-Rubio, R. Mariscal, M. Ojeda and P. Brettes, *Energy & Fuels*, 2009, **23**, 2259-2263.
102. P.-L. Boey, G. P. Maniam and S. A. Hamid, *Chemical Engineering Journal*, 2011, **168**, 15-22.
103. M. Verziu, S. M. Coman, R. Richards and V. I. Parvulescu, *Catalysis Today*, 2011, **167**, 64-70.
104. T. Berger, J. Schuh, M. Sterrer, O. Diwald and E. Knoezinger, *Journal of Catalysis*, 2007, **247**, 61-67.
105. T. Ito, J. Wang, C. H. Lin and J. H. Lunsford, *Journal of the American Chemical Society*, 1985, **107**, 5062-5068.
106. J. S. J. Hargreaves, G. J. Hutchings, R. W. Joyner and C. J. Kiely, *Journal of Catalysis*, 1992, **135**, 576-595.
107. H. Matsuhashi, M. Oikawa and K. Arata, *Langmuir*, 2000, **16**, 8201-8205.

108. E. Finazzi, C. Di Valentin, G. Pacchioni, M. Chiesa, E. Giamello, H. Gao, J. Lian, T. Risse and H.-J. Freund, *Chemistry – A European Journal*, 2008, **14**, 4404-4414.
109. J. M. Montero, K. Wilson and A. F. Lee, *Topics in Catalysis*, 2010, **53**, 737-745.
110. B. R. Cuenya, *Thin Solid Films*, 2010, **518**, 3127-3150.
111. C. M. A. Parlett, D. W. Bruce, N. S. Hondow, A. F. Lee and K. Wilson, *ACS Catalysis*, 2011, **1**, 636-640.
112. J. M. Campelo, A. F. Lee, R. Luque, D. Luna, J. M. Marinas and A. A. Romero, *Chemistry – A European Journal*, 2008, **14**, 5988-5995.
113. N. F. Zheng and G. D. Stucky, *Journal of the American Chemical Society*, 2006, **128**, 14278-14280.
114. M. Zabeti, W. M. A. Wan Daud and M. K. Aroua, *Fuel Processing Technology*, 2009, **90**, 770-777.
115. I. Chorkendorff and J. W. Niemantsverdriet, *Concepts of Modern Catalysis and Kinetics*, Wiley-VCH, Germany, 2003.
116. H. A. Pearce and N. Sheppard, *Surface Science*, 1976, **59**, 205-217.
117. F. Kapteijn, A. D. Vanlangeveld, J. A. Moulijn, A. Andreini, M. A. Vuurman, A. M. Turek, J. M. Jehng and I. E. Wachs, *Journal of Catalysis*, 1994, **150**, 94-104.
118. H. Pines and W. O. Haag, *Journal of the American Chemical Society*, 1960, **82**, 2471-2483.
119. T. Yamaguchi, *Catalysis Today*, 1994, **20**, 199-217.
120. J. Barbier, Jr., L. Oliviero, B. Renard and D. Duprez, *Topics in Catalysis*, 2005, **33**, 77-86.
121. R. Burch and A. R. Flambard, *Journal of Catalysis*, 1982, **78**, 389-405.
122. A. Galarneau, H. Cambon, F. Di Renzo and F. Fajula, *Langmuir*, 2001, **17**, 8328-8335.
123. V. Polshettiwar and R. S. Varma, *Green Chemistry*, 2010, **12**, 743-754.
124. C. Samart, C. Chaiya and P. Reubroycharoen, *Energy Conversion and Management*, 2010, **51**, 1428-1431.
125. I. Lukić, J. Krstić, D. Jovanović and D. Skala, *Bioresource Technology*, 2009, **100**, 4690-4696.
126. D.-W. Lee, Y.-M. Park and K.-Y. Lee, *Catal Surv Asia*, 2009, **13**, 63-77.
127. N. Boz, M. Kara, O. Sunal, E. Alptekin and N. Degirmenbasi, *Turkish Journal of Chemistry*, 2009, **33**, 433-442.
128. H.-J. Kim, B.-S. Kang, M.-J. Kim, Y. M. Park, D.-K. Kim, J.-S. Lee and K.-Y. Lee, *Catalysis Today*, 2004, **93–95**, 315-320.
129. W. Xie and H. Li, *Journal of Molecular Catalysis A: Chemical*, 2006, **255**, 1-9.
130. A. P. Vyas, N. Subrahmanyam and P. A. Patel, *Fuel*, 2009, **88**, 625-628.
131. D. M. Alonso, R. Mariscal, R. Moreno-Tost, M. D. Z. Poves and M. L. Granados, *Catalysis Communications*, 2007, **8**, 2074-2080.
132. S. Benjapornkulaphong, C. Ngamcharussrivichai and K. Bunyakiat, *Chemical Engineering Journal*, 2009, **145**, 468-474.
133. E. S. Umdu, M. Tuncer and E. Seker, *Bioresource Technology*, 2009, **100**, 2828-2831.
134. K. S. W. Sing, D. H. Everett, R. A. W. Haul, L. Moscou, R. A. Pierotti, J. Rouquerol and T. Siemieniewska, *Pure and Applied Chemistry*, 1985, **57**, 603-619.
135. J. Weitkamp, *Solid State Ionics*, 2000, **131**, 175-188.

136. http://www.personal.utulsa.edu/~geoffrey-price/zeolite/index.html, Accessed April, 2013.
137. W. Vermeiren and J. P. Gilson, *Topics in Catalysis*, 2009, **52**, 1131-1161.
138. X. T. Wei and P. G. Smirniotis, *Microporous and Mesoporous Materials*, 2006, **89**, 170-178.
139. A. Carrero, G. Vicente, R. Rodriguez, M. Linares and G. L. del Peso, *Catalysis Today*, 2011, **167**, 148-153.
140. L. L. Su, L. Liu, J. Q. Zhuang, H. X. Wang, Y. G. Li, W. J. Shen, Y. D. Xu and X. H. Bao, *Catal. Lett.*, 2003, **91**, 155-167.
141. J. S. Beck, J. C. Vartuli, W. J. Roth, M. E. Leonowicz, C. T. Kresge, K. D. Schmitt, C. T. W. Chu, D. H. Olson, E. W. Sheppard, S. B. McCullen, J. B. Higgins and J. L. Schlenker, *Journal of the American Chemical Society*, 1992, **114**, 10834-10843.
142. J. S. Beck, C. T. W. Chu, I. D. Johnson, C. T. Kresge, M. E. Leonowicz, W. J. Roth and J. W. Vartuli, *WO Patent 91/11390*, 1991.
143. C. T. Kresge and W. J. Roth, *Chemical Society Reviews*, 2013, **42**, 3663-3670.
144. A. Taguchi and F. Schüth, *Microporous and Mesoporous Materials*, 2005, **77**, 1-45.
145. D. Y. Zhao, J. L. Feng, Q. S. Huo, N. Melosh, G. H. Fredrickson, B. F. Chmelka and G. D. Stucky, *Science*, 1998, **279**, 548-552.
146. D. Y. Zhao, Q. S. Huo, J. L. Feng, B. F. Chmelka and G. D. Stucky, *Journal of the American Chemical Society*, 1998, **120**, 6024-6036.
147. T. W. Kim, F. Kleitz, B. Paul and R. Ryoo, *Journal of the American Chemical Society*, 2005, **127**, 7601-7610.
148. F. Kleitz, S. H. Choi and R. Ryoo, *Chemical Communications*, 2003, 2136-2137.
149. L. Guczi, A. Beck and Z. Paszti, *Catalysis Today*, 2012, **181**, 26-32.
150. H. Dropsch and M. Baerns, *Applied Catalysis a-General*, 1997, **158**, 163-183.
151. S. J. Tauster, *Accounts of Chemical Research*, 1987, **20**, 389-394.
152. C. Pirez, J.-M. Caderon, J.-P. Dacquin, A. F. Lee and K. Wilson, *Acs Catalysis*, 2012, **2**, 1607-1614.
153. F. A. Twaiq, A. R. Mohamed and S. Bhatia, *Microporous and Mesoporous Materials*, 2003, **64**, 95-107.
154. S. Garg, K. Soni, G. M. Kumaran, R. Bal, K. Gora-Marek, J. K. Gupta, L. D. Sharma and G. M. Dhar, *Catalysis Today*, 2009, **141**, 125-129.
155. J. A. Melero, L. F. Bautista, G. Morales, J. Iglesias and D. Briones, *Energy & Fuels*, 2008, **23**, 539-547.
156. E. Li and V. Rudolph, *Energy & Fuels*, 2007, **22**, 145-149.
157. S. Gheorghiu and M. O. Coppens, *Aiche Journal*, 2004, **50**, 812-820.
158. P. Yang, T. Deng, D. Zhao, P. Feng, D. Pine, B. F. Chmelka, G. M. Whitesides and G. D. Stucky, *Science*, 1998, **282**, 2244-2246.
159. J. L. Blin, A. Leonard, Z. Y. Yuan, L. Gigot, A. Vantomme, A. K. Cheetham and B. L. Su, *Angewandte Chemie-International Edition*, 2003, **42**, 2872-2875.
160. W. H. Deng and B. H. Shanks, *Chemistry of Materials*, 2005, **17**, 3092-3100.
161. J. P. Dacquin, J. Dhainaut, D. Duprez, S. Royer, A. F. Lee and K. Wilson, *Journal of the American Chemical Society*, 2009, **131**, 12896-12897.
162. Y.-M. Choi, Y.-I. Lee, S. Kim, N. Myung and Y.-H. Choa, *Electron. Mater. Lett.*, 2012, **8**, 225-230.
163. S.-W. Bian, Y.-L. Zhang, H.-L. Li, Y. Yu, Y.-L. Song and W.-G. Song, *Microporous and Mesoporous Materials*, 2010, **131**, 289-293.

164. J. Du, X. Lai, N. Yang, J. Zhai, D. Kisailus, F. Su, D. Wang and L. Jiang, *Acs Nano*, 2011, **5**, 590-596.

165. F. Ocampo, J. A. Cunha, M. R. de Lima Santos, J. P. Tessonnier, M. M. Pereira and B. Louis, *Applied Catalysis a-General*, 2010, **390**, 102-109.

166. F. Ocampo, H. S. Yun, M. M. Pereira, J. P. Tessonnier and B. Louis, *Crystal Growth & Design*, 2009, **9**, 3721-3729.

167. E. Geraud, V. Prevot, J. Ghanbaja and F. Leroux, *Chemistry of Materials*, 2005, **18**, 238-240.

168. E. Geraud, S. Rafqah, M. Sarakha, C. Forano, V. Prevot and F. Leroux, *Chemistry of Materials*, 2008, **20**, 1116-1125.

169. S. Vaudreuil, M. Bousmina, S. Kaliaguine and L. Bonneviot, *Advanced Materials*, 2001, **13**, 1310-1312.

Chapter 2

Experimental

2.1 Catalyst preparation

2.1.1 Conventional hydrotalcite synthesis

Conventional hydrotalcites were co-precipitated using the alkali-free route published by Cantrell and co-workers.[1] Magnesium nitrate hexahydrate aqueous solution (x cm^3 1.5M $Mg(NO_3)_2{\cdot}6H_2O$) and aluminium nitrate nonahydrate aqueous solution (y cm^3, 1.5 M $Al(NO_3)_3{\cdot}9H_2O$) were mixed together so that $x + y = 50$ cm^3. The Mg:Al ratio was altered so that in 4 different preparations $x: y$ = 1:1, 2:1, 3:1 and 4:1. The mixed nitrate solution was transferred to a dropping funnel above a 3 necked 500 mL round bottomed flask containing distilled water (25 cm^3), held at 65 ºC with stirring. Ammonium carbonate aqueous solution (2 M, 50 cm^3) was added to a second dropping funnel. The nitrate and carbonate precursor solutions were added dropwise to the flask. whilst monitoring the pH of the solution using a Jenway 3305 pH meter, and maintaining it between pH 7.6-8 by the dropwise addition of ammonium hydroxide solution (35 % NH_3). After 70 minutes the precursor addition was completed and the mixture was aged at 65 ºC with stirring for 3 hours, with pH held constant at 7.6-8. The white precipitate which formed was filtered, washed several times in deionised water and dried overnight at 80 ºC. The powder was calcined at 450 ºC for 15 hours under 20 mL min^{-1} O_2, (ramp rate 1 ºC min^{-1}). The material was cooled and rehydrated under flowing wet nitrogen passed through a bubbler at 100 mL min^{-1}, for 48 hours, before being stored in a desiccator.

2.1.1.1 Brucite synthesis

A control sample of brucite was synthesised using the same method as described above for the conventional hydrotalcite synthesis, without the addition of an aluminium precursor. The co-precipitation was carried out using 50 cm^3 of magnesium nitrate rather than a mixed metal nitrate solution. All other conditions remained the same.

2.1.2 Polystyrene bead synthesis

Polystyrene spheres were synthesised using the emulsion polymerisation method of Vaudreuil and co-workers.[2] Potassium persulfate (0.16 g) was dissolved in distilled water (12 cm^3) at 70 ˚C. In a separate 500 cm^3 three-necked round bottomed flask distilled water (377 cm^3) was purged under N_2 (10 mL min^{-1}) at 70 °C. Styrene (50 cm^3) and divinylbenzene (9.5 cm^3) were each washed three times with sodium hydroxide solution (0.1 M, 1:1 vol/vol) followed by three washings with distilled water (1:1 vol/vol) to remove the polymerisation inhibitors. The washed organic phases were added to the purged water phase followed by the potassium persulfate solution. The mixture was left to stir under N_2 (10 mL min^{-1}) for 15 h, filtered and washed three times with distilled water (100 cm^3) and then three times with ethanol (100 cm^3) before being dried at 70 ºC. The average polystyrene bead diameter measured via SEM was found to be 350 nm.

2.1.3 Macroporous hydrotalcite synthesis

Magnesium nitrate hexahydrate solution in 1:1 water: ethanol (x cm^3, 1.5 M) and aluminium nitrate nonahydrate solution in 1:1 water: ethanol (y cm^3, 1.5 M) were mixed together so that $x + y = 50$ cm^3. The Mg:Al ratio was altered so that in 4 different preparations $x: y$ = 1:1, 2:1, 3:1 and 4:1. The mixed nitrate solution was transferred to a dropping funnel above a 3 necked 500 mL round bottomed flask containing polystyrene beads (6 g), suspended in 1:1 water: ethanol solution (25 cm^3) with stirring, at 65 ºC. A second dropping funnel, containing ammonium carbonate aqueous solution (2 M, 50 cm^3) was attached to the round-bottomed flask. The nitrate and carbonate precursor solutions were added dropwise to the flask, whilst monitoring the pH of the solution using a Jenway 3305 pH meter, and maintaining it between pH 7.6-8 via the dropwise addition of ammonium hydroxide solution (35 % NH_3). After 70 min the precursor addition was complete, and the mixture was aged at 65 ºC with stirring for 3 h, with pH held constant at 7.6-8. The white precipitate which formed was then filtered, washed several times in deionised water and dried overnight at 80 ºC. The powder was calcined at 450 ºC for 15 h under 20 mL min^{-1} oxygen, (ramp rate 1 ºC min^{-1}).

The material was cooled under flowing wet nitrogen (passed through a bubbler) at 100 mL min^{-1} for 48 h, before being stored in a desiccator.

2.1.4 Preparation of an ordered macroHT

Close packed arrays of polystyrene beads were first prepared. Polystyrene beads (3 g) were placed in a 1:1 solution of water: ethanol (180 cm^3) and magnetically stirred at 350 RPM for 8 hours in order to form a colloidal suspension. This suspension was split into 6 centrifuge tubes (each containing 30 cm^3) which were centrifuged for 16 hours at 1200 RPM, followed by 10,000 RPM for 6 h. The excess liquid was then pipetted from the centrifuge tubes and the bead arrays allowed to dry overnight in a vacuum oven.

The close packed polystyrene bead crystallites (0.6 g) were placed into a glass sample tube. Magnesium nitrate hexahydrate (3.077 g, 0.012 mol) and aluminium nitrate nonahydrate (1.125 g, 0.003 mol) were dissolved in 10 mL 1:1 water: ethanol solution. This mixed metal nitrate solution was added dropwise (4 mL) to the polystyrene beads until the beads were soaked through with a slight excess of solution. After 24 h aging at room temperature, the beads were dried overnight in an oven at 50 ºC to remove excess water and ethanol.

Ammonium carbonate (1.922 g, 0.02 mol) was dissolved in 12.5 mL 2:1 water: ethanol solution. 4mL ammonia was added to increase the pH. After stirring, 4 mL of this mixed solution was added dropwise to the dried beads. After allowing to soak in for an hour, a further mL of carbonate solution was added. After a further 24 h aging at room temperature, the beads were dried overnight in an oven at 50 ºC to remove excess water and ethanol. The material was calcined at 450 ºC for 15 h under 20 mL min^{-1} oxygen, (ramp rate 1 ºC min^{-1}). The material was cooled under flowing wet nitrogen (passed through a bubbler) at 100 mL min^{-1} for 48 h, before being stored in a desiccator.

2.1.5 HT on alumina synthesis

Commercial γ-alumina (Degussa, 5 g) was dried for 1 h at 80 ºC. To this, magnesium methoxide solution (8-10 wt% in methanol, 21.8 cm^3) was added, enough to just form a homogeneous paste on mixing. After 15 min stirring, the mixture was dried under vacuum at 80 ºC for 1 h to remove excess methanol. This gave a 10 wt% Mg sample. In order to graft higher weight percentages of magnesium onto alumina, successive magnesium methoxide graftings were carried out onto the alumina samples, adding 10 wt% Mg each time. As the pore volume of the alumina shrank, the excess solvent required removal on the rotary evaporator before drying in the vacuum oven.

The 10 wt% Mg, 20 wt% Mg, 40 wt% Mg and 50 wt% Mg samples (500 mg) were calcined at 450 ºC for 15 h under 20 mL min^{-1} O_2 (ramp rate 1 ºC min^{-1}). After cooling to room temperature under N_2 (20 mL min^{-1}), the powders were added to a 100 mL round bottomed pressure vessel with distilled water (50 cm^3 for every 300 mg of grafted alumina powder) and heated to 125 ºC with stirring for 21 h on a Radleys hotplate. After cooling the flasks to room temperature, the HT on alumina samples were filtered, washed with deionised water and dried in a vacuum oven overnight at 80 ºC, before being stored in a desiccator.

2.1.6 SBA-15 synthesis

Pure silica SBA-15 was synthesised using the method of Zhao and co-workers.[3] The structure directing agent, Pluronic® P123 (10 g) was dissolved in water (75.5 cm^3) and hydrochloric acid (2 M, 291.5 cm^3), with stirring, at 35 °C. Tetramethoxysilane (15.5 cm^3) was added and left for 20 h with agitation. The resulting gel was hydrothermally treated under sealed conditions for 24 h at 100 °C without agitation. The solid was filtered, washed with water (1000 cm^3) and dried at room temperature before calcination at 500 °C for 6 h in air (ramp rate 1 °C min^{-1}).

2.1.7 Macro-mesoporous SBA-15(MMSBA-15) synthesis

The meso-macroporous SBA-15 silica support was prepared using the method published by Dhainaut and co-workers.[4] Pluronic® P123 (10 g) was dissolved in water (75 cm^3) and hydrochloric acid (2 M, 290 cm^3), with stirring, at 35 °C. Polystyrene beads (45 g) were added to the solution and left to stir for 1 h .

Tetramethoxysilane (15.0 cm^3) was then added and left for 20 h with agitation. The resulting gel was aged under sealed conditions for 24 h at 100 °C without agitation. The solid was filtered, washed with water (1000 cm^3) and dried at room temperature before calcination at 550 °C for 6 h in air (ramp rate 0.5 °C min^{-1}).

2.1.8 Grafting an alumina surface onto SBA-15 (Al-SBA-15) or MMSBA-15 (Al-MMSBA-15)

A mesoporous silica core alumina surface SBA-15 (Al-SBA-15 or Al-MMSBA-15) was assembled using the method of Landau and co-workers,[5] with the exception that SBA-15 was used instead of MCM-41. Consecutive grafting cycles were carried out using an identical protocol each time, making adjustments to the quantities to maintain the initial ratios. Aluminium-tri-*sec*-butoxide (14.5 g) was dissolved in anhydrous toluene (100 cm^3) at 85 °C with stirring. Triethylamine (2.1 cm^3) was added to the solution followed by dried SBA-15 or MMSBA-15 (1 g). After 6 h stirring at 85 °C the solution was filtered under vacuum (~0.1 bar) to recover the solid, which was washed three times in toluene (100 cm^3). The alumina surface was hydrolysed in ethanol (318 cm^3) containing water (1.6 cm^3) for 24 h at 25 °C with stirring. The solid product was recovered by filtration under vacuum (~0.1 bar) and washed with ethanol (300 cm^3) before drying at 80 ºC in a vacuum oven overnight. A three step calcination sequence was then used: the material was first heated to 250 °C for 1 h, then 400 °C for 1 h and finally 500 °C for 4 h (constant ramp rate 1 °C min^{-1}).

2.1.9 Hydrotalcite preparation on SBA-15 (HT-SBA-15) or MMSBA-15 (HT-MMSBA-15)

Magnesium methoxide solution (8-10 wt% in methanol) was added to Al-SBA-15 or Al-MMSBA-15 (400 mg, dried for 1 h at 80 ºC), at the minimum quantity to just form a homogeneous paste on mixing. After stirring for 15 minutes, the mixture was dried under vacuum at 80 ºC for 1 hour to remove excess methanol.

In order to graft enough Mg to form the same surface Mg:Al atomic ratio as for the 50 wt% HT on alumina sample (5.78:1), this grafting step was repeated successive times until the correct volume of magnesium methoxide had been added (10.8 cm^3 for the MMSBA-15 and 20.7 cm^3 for the higher surface area SBA-15).

The resultant grafted material was calcined at 450 ºC for 15 h under 20 mL min^{-1} O_2 (ramp rate 1 ºC min^{-1}). After cooling to room temperature under N_2 (20 mL min^{-1}), the powder was added to a 100 ºC round bottomed pressure vessel with distilled water (50 cm^3 for every 300 mg of powder) and heated to 125 ºC with stirring for 21 h on a Radleys hotplate. After cooling the flasks to room temperature, the resultant HT-SBA-15 or HT-MMSBA-15 sample was filtered, washed with deionised water and dried in a vacuum oven overnight at 80 ºC, before being stored in a desiccator.

2.1.10 Preparation of NanoMgO-500

For this study a benchmark commercial NanoMgO material was used (99.6% NanoActive Magnesium Oxide Plus, Nanoscale corporation). The commercial production of this material involves a sol-gel method, developed by Utamapanya and co-workers.[6, 7] Briefly, a 10 wt% solution of magnesium methoxide in methanol is prepared by dissolving magnesium ribbon in methanol under nitrogen. The methoxide solution is hydrolysed overnight by the drop-wise addition of deionised water in the presence of toluene. The resulting sol is transferred to an autoclave and pressurised to 100 psi (6.89 bar) of nitrogen. Slow heating to 265 ºC leads to the creation of a supercritical atmosphere and after a 10 min equilibration time the autoclave is vented. The resulting white powder is dried in an oven to remove residual solvent. The dried powder is then heat treated under vacuum to create an oxide material with a particle size less than 4 nm.

The commercial nanoMgO was annealed under 10 mL min^{-1} He at a 5 ºC min^{-1} ramp rate to 500 ºC, held for 5 h, and then cooled and stored in a desiccator prior to use.

2.1.11 Cs-MgO synthesis

Magnesium methoxide (8-10 wt% in methanol) was added to toluene at a 1:5 mass ratio. To this, caesium hydroxide ($CsOH \cdot H_2O$, 96% Alfa Aesar) in methanol was added drop wise with stirring at room temperature, at a concentration to achieve 20 wt% Cs doping of magnesium oxide. Deionised water (0.45 mL for every 10 mL magnesium methoxide used) was then added drop wise, and the solution stirred overnight to ensure complete hydrolysis of the magnesium methoxide solution. The resulting hydroxide gel was treated in a steel autoclave with a 200 mL glass insert. The system was flushed with N_2 gas and pressurised to 6.89 bar before being heated to 265 ºC at 1 ºC min^{-1}, equilibrated at this temperature for 10 min, and subsequently slowly vented at temperature (caution must be taken to avoid super-heated methanol vapour) before cooling to room temperature. The resulting Cs-MgO sample was then dried in air at 120 ºC for 2 ho and stored in a desiccator. The Cs-MgO was annealed under 10 mL min^{-1} He at 5 ºC min^{-1} to 500 ºC, held for 5 h, and then cooled and stored in a desiccator prior to use.

2.2 Catalyst characterisation

2.2.1 Powder X-ray diffraction

X-ray diffraction (XRD) patterns were recorded on a Panalytical X'pertPro diffractometer fitted with an X'celerator detector, using a Cu K_α (1.54 Å) source with a nickel filter, calibrated against an Si standard. Low angle patterns were recorded over a range of $2\theta = 0.3\text{-}8°$ (step size 0.01°, scan speed 0.014° s^{-1}) and wide angle patterns over a range of $2\theta = 5\text{-}80°$ (step size 0.02°, scan speed 0.020° s^{-1}).

Cu K_α (1.54 Å, 8.04 keV) X-ray photons, generated via the demotion of a high energy shell electron to a lower vacancy (in a copper anode), are fired at a homogeneous powder sample. In a randomly organised homogeneous sample, there will be enough material correctly orientated to allow constructive interference from crystal planes or ordered pore walls.[8] This arises from elastic scattering of the photons which if in-phase, as shown in **Figure 2.1**, results in constructive interference, i.e. they reinforce rather than cancel out.

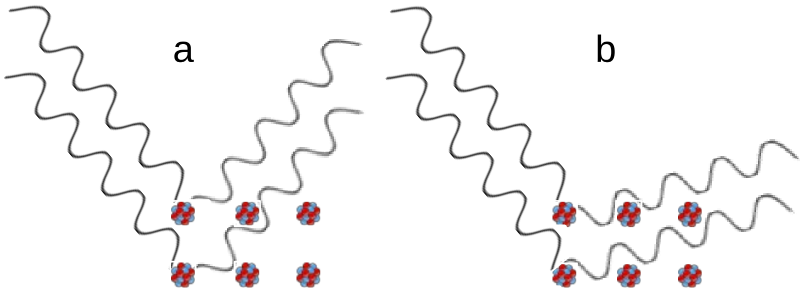

Figure 2.1. Simplified illustration showing a) constructive and b) deconstructive interference of X-ray photons.

For constructive interference to occur then Bragg's Law must apply (**Equation 2.1.)**. For set refraction angles, the distance between scatterers must be equal to an integer multiplied by the X-ray wavelength. **Figure 2.2** illustrates Bragg's X-Ray diffraction.

$$2dsin\theta = n\lambda$$ **Equation 2.1**

n = order of interference (integer) λ = incident wavelength, d = lattice spacing and θ = diffraction angle

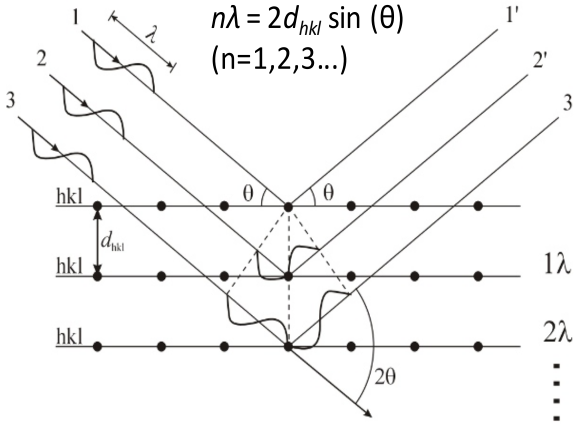

Figure 2.2 – Schematic illustrating Bragg's X-Ray and the relationship between lattice spacing and constructive interference.[9]

Around 3 % of the ingoing X-ray photons will be elastically scattered and diffracted by the crystal planes. The other 97 % leave the crystal as transmitted radiation. The angle of the X-rays is altered and as a 2θ value is reached where constructive interference can occur for the crystal phase being examined, the diffracted X-rays are recorded by the detector. This gives rise to characteristic diffraction patterns unique to individual materials.[8, 10] Diffraction peaks only occur if long range order is present (crystalline materials or ordered porosity), with a minimum detectable crystallite size of ~2 nm.[11]

Peak width increases with decreasing particle size,[10] due to incomplete cancelling of scattered X-rays close to the peak maxima. This arises because the refraction from the next lattice plane, when just off the maxima, is only slightly out of phase and cancels weakly. In large crystals the combination of multiple refractions overcome this, whereas the limited number of lattice planes in small crystals diminishes this effect.[8] The peak width can therefore be utilised for particle size determination by the Scherrer Equation (**Equation 2.2**).[12]

$$PS_{av} = \frac{k\lambda}{\left(\sqrt{(B^2 - S^2)COS\theta}\right)}$$

Equation 2.2 – Scherrer equation

PS_{ave} = Particle size (Å); B = FWHM of diffraction peak; S = 0.15 (systematic broadening caused by diffractometer); k = 0.9 (constant)

2.2.2 Nitrogen porosimetry

N_2 porosimetry was undertaken on a Quantachrome Nova 1200 porosimeter using NovaWin v2.2 analysis software. Micropore analysis was carried out using an Autosorb porosimeter, at lower relative pressures. Samples were degassed at 120 °C for 2 h prior to N_2 adsorption. Adsorption/desorption isotherms were recorded at -196 °C. BET surface areas were calculated over the relative pressure range 0.01-0.3 where a linear relationship was observed. Pore diameters and volumes were calculated applying either the HK method (micropores) or BJH method (mesopores) to the desorption isotherm for relative pressures <0.02 and >0.35 respectively.

Physisorption occurs when enough energy is lost during an inelastic gas collision from an adsorbate to an adsorbent to forbid spontaneous desorption, yet no more energy is lost via chemical bond formation. N_2 physisorption only occurs at temperatures below the N_2 boiling point, due to nitrogen's weak enthalpy of adsorption.[13] This permits multilayer adsorption, as the enthalpy of vaporisation (condensation) from adsorbate- adsorbate interactions is close in value to the enthalpy of adsorption. Adsorbate attractions to both the surface, and each other in multilayer adsorption, arises due to Van der Waals forces (dipole to dipole attractions).[13, 14]

Isotherms are generated by the static volumetric technique,[15] N_2 is incrementally dosed and the amount adsorbed (under dynamic equilibrium with rate of adsorption = rate of desorption) at a given pressure and constant temperature recorded. The isotherm type divulges information regarding the adsorbents. There are six classifications of isotherm, depicted in **Figure 2.3**.[16]

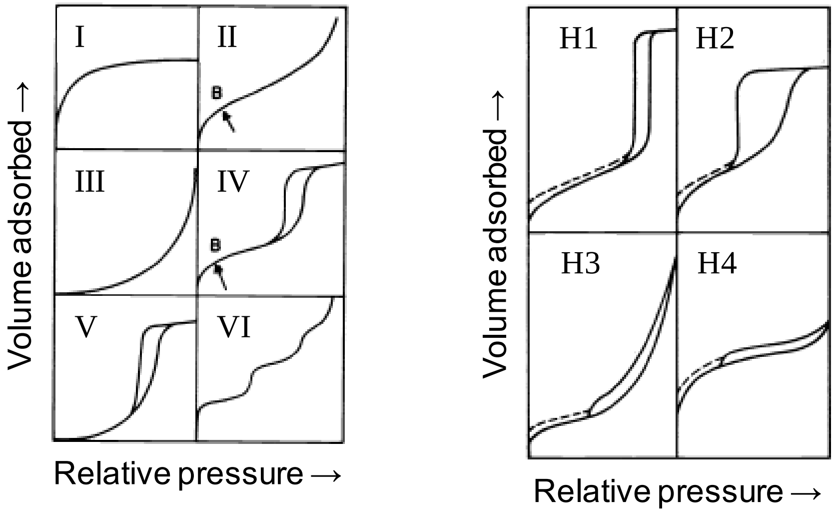

Figure 2.3 – Common adsorption isotherms and hysteresis types.[17]

Type I represents microporous materials where a strong interaction between adsorbate and adsorbent occurs from their close proximity within micropores; type II is typical for either nonporous or macroporous materials; the unusual type III occurs when adsorbate interactions are greater than those with the surface; hysteresis observed in types IV and V is indicative of mesoporous supports; and type VI indicates consecutive adsorbate layer formation due to uniform surface.

Hysteresis, witnessed in isotherm types IV and V, presents as four types, as shown in **Figure 2.3**. It occurs due to differences in condensation (adsorption) and evaporation (desorption) within mesopores.[15] Adsorption occurs from the pore wall inwards. The close proximity between adsorbate and pore wall enhances the attractive interaction, leading to capillary condensation, and therefore there is a much sharper increase in the volume of gas adsorbed compared to non-porous materials. Desorption occurs from the liquid surface at pore openings, where there is a strong interaction,[15] lowering the pressure that gas evaporation occurs relative to the condensation process. Hysteresis shape reveals further information; type H1 is witnessed for uniform pore sizes, whereas H2 represents non-uniformity ink bottle pore shapes. In the case of non-uniform pores, adsorption (condensation) will occur at the narrowest part of the pore and not fill the wider cross section until the vapour pressure has increased sufficiently. On desorption however, no evaporation will occur until the vapour pressure relating to evaporation from the widest cross-section of the pore has been reached, giving this much wider hysteresis loop.[18] Slit shaped pores produce H3 and H4.[16]

Total surface areas were calculated by the BET equation (**Equation 2.3**).[19] It is a development of the Langmuir theory to accommodate multilayer formation via an additional parameter, C. This accounts for differences between mono and multilayer interactions, with a low value indicating a stronger interaction between adsorbate species than adsorbate-adsorbent and vice versa for high values.[16] Surface areas are determined from the monolayer volume assuming N_2 molecules close pack and each occupies 0.162 nm^2 (**Equation 2.4**).[13, 15, 16]

$$\frac{P}{V_a(P_0-P)} = \frac{1}{V_m C} + \frac{C-1}{V_m C}\left(\frac{P}{P_0}\right)$$ **Equation 2.3** – BET (linear)

$$V_m = \frac{1}{(Gradient+Intercept)}$$

$$C = \left(\frac{Gradient}{Intercept}\right) + 1$$

$$sa = \frac{V_m \sigma N_a}{mv}$$ **Equation 2.4**

P = pressure; P_0 = saturation pressure; V_a = volume adsorbed; V_m = monolayer volume; C = multilayer adsorption parameter; sa = surface area; σ = N_2 area (0.162 nm^2); N_a = Avogadro number; m = sample mass; v = gas molar volume

Microporosity was assessed using the HK method.[20] This method assumes that all pores of a certain size will fill at a certain relative pressure, and therefore involves a direct mathematical relationship between relative pressure and pore size. It is valid up to pore diameters of 2 nm.

The BJH method allowed mesopore diameters to be deduced. This applies the Kelvin equation (**Equation 2.5**),[15] which relates the curvature of the meniscus of the condensed N_2 in the pores to pore radius, and predicts the pressure at which the adsorbate will spontaneously evaporate for a given pore diameter. Calculations at each pressure change allow pore size distribution to be determined.

$$ln\left(\frac{P}{P_0}\right) = -\left(\frac{2\gamma \upsilon cos\theta}{RTr_m}\right)$$ **Equation 2.5** – Kelvin equation

P/P_0 = relative pressure of vapor in equilibrium with condensed gas meniscus; γ = liquid surface tension; υ = condensed adsorbate molar volume; cosθ = adsorbate surface contact angle (0 for N_2 thus cosθ = 1); R = gas constant; T = temperature; r_m = mean radius of condensed gas meniscus

2.2.3 Thermal gravimetric analysis

Thermal gravimetric analysis (TGA) was performed on a Stanton Redcroft STA-780 thermal analyser fitted with a temperature programmer, DC amplifier and balance control. Samples (10-20 mg) were placed into an alumina crucible on a balance, next to a reference alumina crucible containing around 15 mg of pre-treated and inert γ-alumina. Samples were heated to 700 ºC at 10 ºC min^{-1} under a flow of 20 mL min^{-1} He gas. The mass of the sample was monitored with increasing temperature and differential thermal analysis (DTA) was performed using PicoLog recording software on a linked computer.

TGA monitors the change in mass of a sample when heated. This technique can identify the loss of water of crystallisation, adsorbed surface species or decomposition of bulk phases via gas production. DTA can provide extra information about any exothermic or endothermic processes occurring within the sample which may not incur a mass loss, for example a change in crystalline structure. Differences between the temperature of the sample and that of the inert reference material are measured during heating.

2.2.4 Electron microscopy

2.2.4.1 Scanning electron microscopy

Scanning electron microscopy (SEM) images were recorded on a Carl Zeiss Evo-40 SEM operating at 10 kV. Samples were mounted on aluminium stubs using adhesive carbon tape and gold splutter coated to reduce charging. An electron beam, generated via a gun at the top of the microscope, is focused through a series of electromagnetic lenses onto the sample. These electrons hit the sample and lose energy through interactions occurring in multiple ways, generating high energy backscattering electrons, secondary electrons through inelastic scattering and X-ray radiation. In secondary electron imaging (SEI) mode, SEM images are formed by detection of these secondary electrons that result from the displacement of a k orbital (1s) electron.[21] The low energy, ~50 eV, of the secondary electrons means that their escape is impeded and therefore the technique is surface sensitive. Scanning coils within the microscope allow the electron beam to raster over a sample. Image contrast is generated from the morphology of the sample; surfaces at right angles to the beam are brightest and as surfaces tilt towards being parallel to the beam increasingly darker areas are observed. This allows the production of a 3-D image of the sample surface.

2.2.4.2 Energy dispersive X-ray analysis

Samples were analysed using Oxford INCA energy EDX analysis software linked to the SEM with a 30 mm two light element capable atmospheric twin window (ATW) detector. EDX measures the X-ray radiation produced as the electron beam is fired at the sample. The electron beam excites ground state electrons in atoms of the sample, which are then ejected from the atom. As an electron from a higher energy shell moves to fill the hole left by the ejected electron, the difference in energy between the higher energy shell and lower energy shell is released as an X-ray. Measurement of these X-rays provides information about the atomic structure of the sample, as the energy of the X-rays are characteristic of the element from which they were emitted.[22]

The X-ray penetration depth is about 10 μm.[23] Therefore, EDX is a bulk technique when compared to the 1-3 nm penetration depth through XPS analysis. The atomic ratios calculated via EDX analysis in this study are considered bulk ratios, with those calculated from XPS surface ratios.

2.2.4.3 Transmission electron microscopy

High resolution TEM images were recorded on a Philips EM208 TEM operating at 80 kV with a tungsten filament. Samples were prepared by dispersion in methanol and drop-casting onto a copper grid coated with a holey carbon support film (Agar Scientific Ltd). Images were analysed using ImageJ 1.41.

For TEM, the electron beam is transmitted through an ultrathin sample. It is the interaction (or lack of) of the electron beam with the sample which generates the image.[21] All images are 2-D representations of the sample. Variations in thickness, atomic mass and density all contribute to the degree of interaction (diffraction) between beam and sample. The wavelength of electrons (~12.3 pm at 10 kV decreasing to 2.5 pm at 200 kV) is significantly shorter than both visible and x-ray radiation, so microscope resolution can be enhanced to an atomic level under high resolution TEM conditions.[21]

2.2.5 CO_2 temperature programmed desorption

CO_2 pulse chemisorption experiments, followed by temperature programmed desorption (TPD) of the CO_2 saturated samples were carried out on a Quantachrome ChemBet3000 system, coupled to an MKS Minilab Mass spectrometer.

The catalyst sample being tested (~ 50 mg) was placed into a quartz chemisorption cell plugged with quartz wool and attached to the ChemBet. A furnace was raised around the cell with a thermocouple inside the quartz U-shaped cell parallel with the sample. The set up is illustrated in **Figure 2.4**.

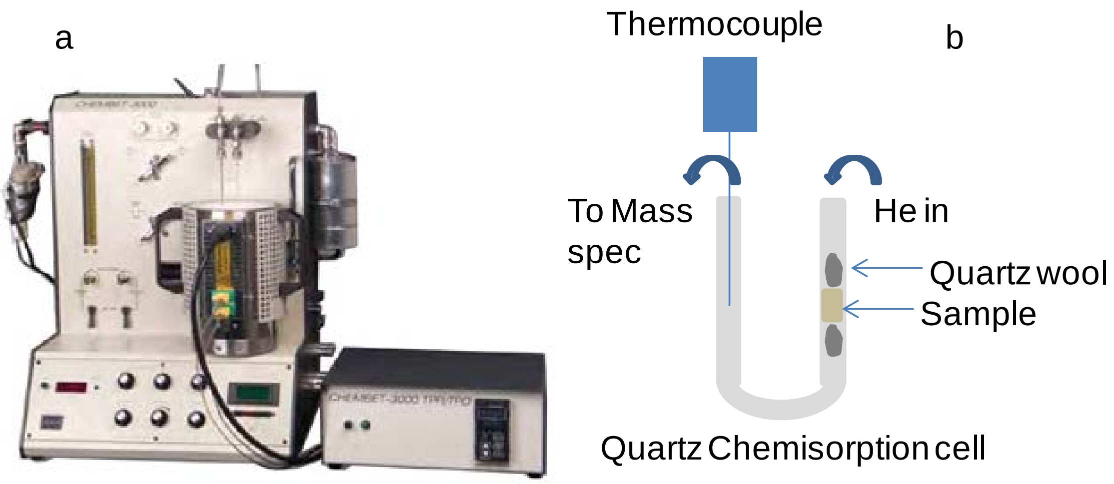

Figure 2.4. a) The ChemBet 3000 system and b) a schematic of the chemisorption cell set up.

The sample was outgassed at 120 ºC for 2 h under He (20 mL min^{-}). The sample was then cooled to 40 ºC. The experiments were carried out at 40 ºC to avoid fluctuations in room temperature affecting the results.

CO_2 gas was pulsed through the cell and over the sample in 50 μL doses. The amount of CO_2 reaching the ChemBet detector was recorded on an attached computer. Once 3 peaks of the same height and count had been recorded by the detector the sample was saturated, as all of the CO_2 was travelling through the system and no more was adsorbing to the sample. The sample was then heated to 450 ºC at 10 ºC min^{-1} under a flow of He to desorb the CO_2. The gas flow was ionised on entering the mass spectrometer. The m/z = 44 signal was followed from the mass spectrometer detector, corresponding to the $CO_2^{+\cdot}$ molecular ion being desorbed from the sample. The mass spec signal was calibrated by heating a known amount of $CaCO_3$ up to 800 ºC in a quartz sample tube on the ChemBet and recording the signal on the MS. The peak area corresponded to a known amount of CO_2 and therefore by measuring the mass spec. peak areas of unknown samples, the amount of CO_2 desorbing can be determined.

CO_2 is known as a Lewis acid probe molecule. It is assumed that one CO_2 molecule adsorbs to one base site and therefore the number of CO_2 molecules desorbed from the surface during a TPD experiment gives the number of base sites per mass of sample analysed. The CO_2 can adsorb as an acidic molecule to basic sites of hydrotalcites in several ways, as monodentate, bidentate and bicarbonate anions, detected through IR studies.[24] **Figure 2.5** illustrates these different CO_2 species.

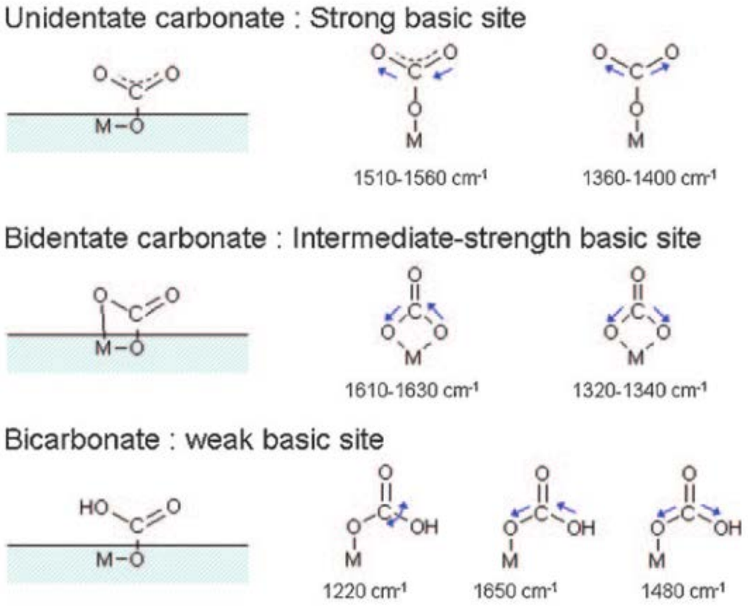

Figure 2.5. Adsorbed CO_2 species on a basic solid, and the associated IR signals, taken from Debecker and co-workers.[25]

The monodentate carbonate anion adsorbs to low coordinate oxygen atoms and therefore accounts for strong basic sites.[26, 27] The bidentate anion forms at intermediate strength acid-base pairs, such as Mg^{2+}-O^{2-}.[27] Bicarbonate anions form at weakly basic surface hydroxyl groups in Mg rich hydrotalcites.[28]

2.2.6 X-ray photoelectron spectroscopy

XPS was performed on a Kratos Axis HSi X-ray photoelectron spectrometer fitted with a charge neutraliser and magnetic focusing lens employing Al K_α monochromated radiation (1486.6 eV). Spectral fitting was performed in CasaXPS version 2.3.14. Binding energies were charge corrected to adventitious C 1s at 284.6 eV. Errors were estimated by varying a Shirley background across reasonable limits.

XPS gives information on elemental composition, oxidation state and local elemental environment of the sample. X-rays routinely employed are Mg Kα (1253.6 eV) and Al Kα (1486.6 eV) which due to their low energy, relative to XAS, are classed as soft X-rays.[29] The incident X-ray source excites a core electron, which is emitted as a photoelectron, if adequate energy is supplied. [14, 29] A schematic representation of this photoelectron emission can be seen in **Figure 2.6**.[10, 30]

XPS is intrinsically surface sensitive, due to the short distance that a photoelectron can escape from (1-3 nm), its escape depth. The low escape depth is due to interactions between the ejected photoelectron and electrons of other atoms imparting short electron mean free path values over the electron energy range of 0-1000 eV.[30]

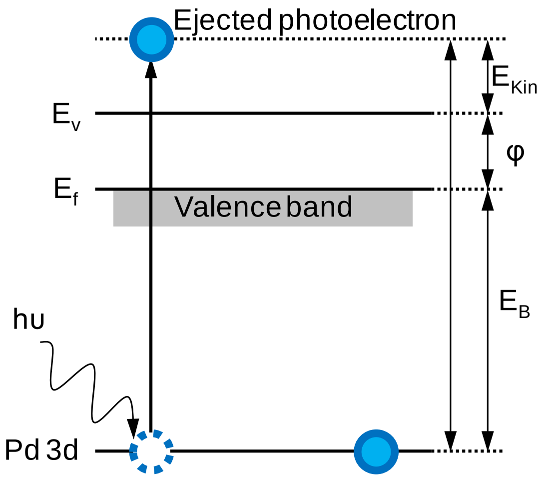

Figure 2.6. – Schematic depiction of photoionisation (E_{kin} = Photoelectron kinetic energy; hν = photon energy (Planck's constant multiplied by frequency); E_b = electron binding energy; φ = work function; E_f = Fermi level; E_v = vacuum level)

The ejected photoelectron possesses a discrete kinetic energy, which is characteristic of the element and its environment. Quantification of this, and the intensity of photoelectrons at said energy, produces an XPS spectrum. Typically spectra are plotted as a function of the binding energy which is deduced from the following relationship (**Equation 2.6**).

$$E_{kin} = hv - E_b - \varphi_{\mathrm{sp}}$$

Equation 2.6

E_{kin} = Photoelectron kinetic energy; hν = photon energy; E_b = electron binding energy; φ_{sp} = spectrometer work function

Work function relates to the energy required to eject an electron at the Fermi level into the vacuum, i.e. the ionisation potential.[10] For conducting samples, an electrical connection between the sample and spectrometer aligns their Fermi levels. For insulating samples, e.g. silica, charge referencing is required.[10] This is achieved by systematically shifting binding energies by a common value, so that a known peak is aligned at its correct value. This accounts for uniform shifts in binding energies, to higher values, due to an increasing positive charge at the analyte surface. Charge neutralisers can help to compensate for this.

Oxidation state and the local elemental environment influence subtle shifts in photoelectron binding energy of an element.[10, 30] As the oxidation state of an atom increases, the binding energy increases, due to the greater attractive force of the nucleus felt by fewer electrons. The binding energy of an atom also increases as the electronegativity of adjacent atoms increases. Generally the outermost filled electron shell is probed as it experiences the greatest effect of these changes and therefore gives the greatest resolution.

Electrons ejected from orbitals which boast angular momentum ($l > 0$, i.e. p, d and f orbitals) are affected by spin coupling between orbital angular momentum (l) and electron spin magnetic fields (m_s), with the sum of the two giving total angular momentum (j). This interaction is either favourable or not, as m_s is either anti-clockwise (+½) or clockwise (-½) and thus two values for j exist. This spin coupling results in peak doublets (spin orbital splitting),[10] with predetermined ratios equal to $2j + 1$. For 2p orbitals $l = 1$ and thus $j = 3/2$ and 1/2. The area ratio of the two spin orbit peaks will be 2:1, corresponding to 4 electrons in the $2p_{3/2}$ orbital and 2 electrons in the $2p_{1/2}$ orbital. Favourable coupling increases binding energy and occurs when forces oppose, $j = 1/2$.

An example of this spin orbital splitting can be observed when fitting the Si 2p peak in pure silica, as shown in **Figure 2.7.** The number of components fitted to an XPS spectrum depends on the number of environments that the element being analysed is found in within the sample. For example if magnesium is found as both MgO and within an MgAl hydrotalcite crystal structure in the same sample, the Mg 2s peak will have 2 different components with differing binding energies, peak areas and FWHMs. For the Si 2p peak in **Figure 2.7**, there is one silicon environment in pure silica, which has been fitted as two components due to spin orbit splitting, therefore both component peaks have the same FWHM. The peak at lower binding energy has an area twice that of the higher binding energy component.

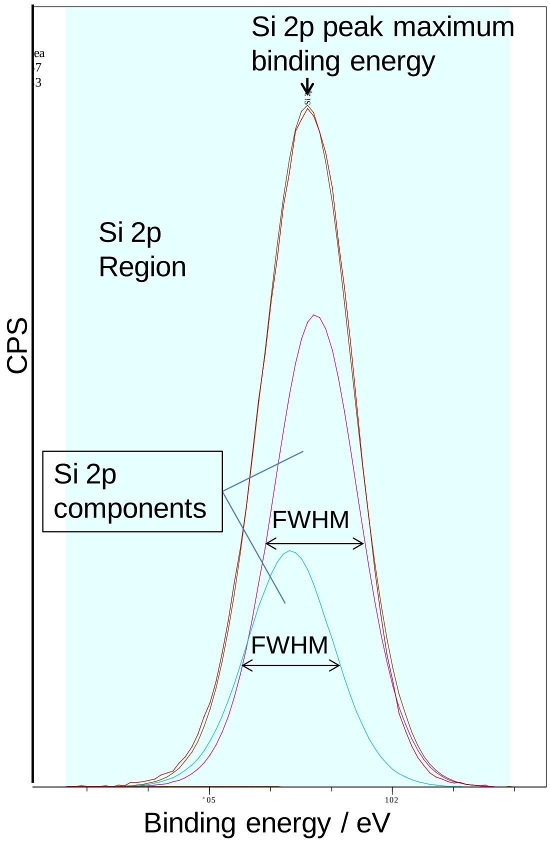

Figure 2.7. Example XPS spectrum of the Si 2p region for pure silica, showing the two components due to spin orbital splitting.

2.2.7 X-ray absorption spectroscopy – X-ray absorption near edge structure and extended x-ray absorption fine structure

XAS measurements were performed at beamline B18 of the Diamond Light Source using a Si(111) monochromator and Pt coated mirrors so as to avoid interference from absorption by Cr coated mirrors over the Cs region. Measurements were undertaken in air at the Cs L_{III}-edge using a Vortex fluorescence detector, with samples diluted in cellulose to achieve a ~ 20 wt% Cs loading and then pressed into pellets. XANES and EXAFS spectra were normalised, background subtracted, and fitted, using the Athena (version 0.9.1) and Artemis (version 0.9.1) components of the IFEFFIT (version 1.2.11d) software suite respectively. Structural parameters for the fits were obtained from data for model compounds obtained from the Inorganic Crystal Structure Database[31] for Cs2O (27919-ICSD), CsOH (15274-ICSD), Cs2CO3 (14156-

ICSD) and Cs2Mg(CO3)2(H2O)4 (87949-ICSD). Local Cs coordination environments were used in FEFF to generate model χ(k) and radial distribution functions for comparison with the Cs-MgO experimental data.

In a similar manner to XPS, XAS also involves the generation of photoelectrons but instead of evaluating these directly the technique assesses their influence on the absorption of subsequent X-ray photons. Simply, the technique is an X-ray photon in, X-ray photon out measurement, which eliminates the need for ultra-high vacuum systems, permitting characterisation of materials under atmospheric conditions and more attractively the option of in-situ/operando investigations.[32] Typically X-ray photon energies are tuned from ~300 eV below to ~1000 eV above the absorption edge, this being the minimum energy at which an electron can be ejected from the atomic orbital of interest. Electrons from a shell close to the nucleus are generally targeted, which results in increasingly energetically demanding transformations. After a photoelectron is discharged, the atom is excited by virtue of the unfilled electron orbital and affects subsequent X-ray photon absorption. This excited state can be partially stabilised by fluorescence, ‘electron hole’ shifting or alternatively through absorption of scattered photoelectrons, including backscattering of the original. The scattering of photoelectrons by their neighbouring atoms induces a multitude of effects, both constructive or deconstructive in regards to subsequent photon absorption.[10] Spectra attained comprise bulk information regarding both electronic and local geometric information, even where sample periodicity is absent.[29] **Figure 2.8** gives an example of a typical XAS spectrum for caesium, showing the Cs L_{III} absorption edge at 5012.0 eV.

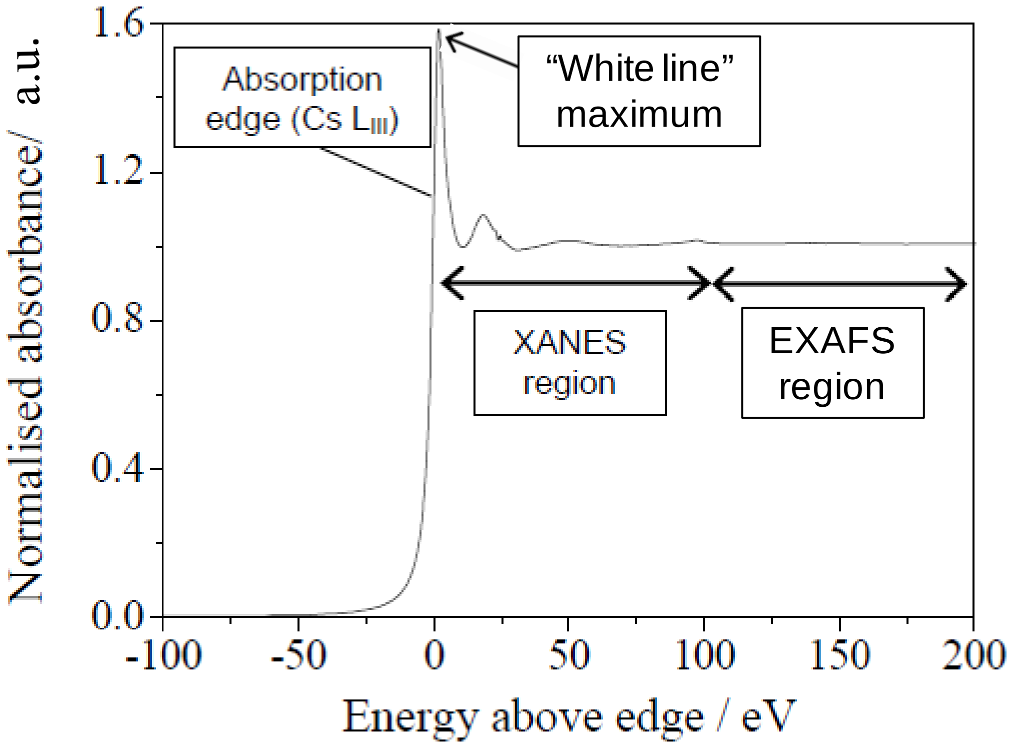

Figure 2.8. An example of an XAS spectrum for the Cs L_{III} edge.

Electronic transitions of p electrons into the d and f orbitals are known as white lines, which are only observed in heavier elements with partially filled d and f orbitals, such as the Cs L_{III} edge. The intensity of a white line is proportional to the number of unfilled d or f states.[33]

The first 100 eV or so after the absorption edge is the X-ray Absorption Near Edge Structure (XANES) region, which divulges oxidation state information.[10, 30] It arises from the promotion of core energy electrons to unoccupied higher energy orbitals above the Fermi level.[34] There are also interactions between low energy ejected photoelectrons and valence electrons.[35]

The EXAFS region follows and continues for ~1000 eV or as far as oscillations are observable. Photoelectrons here possess higher kinetic energy, on the grounds of the increasing incident X-ray energy, which allow them to propagate further. Single and multiple scattering of the photoelectrons by the surrounding atoms result and allow local geometry to be scrutinised.

2.3 Transesterification reactions

2.3.1 C4-C18 TAG and olive oil transesterification

Transesterification reactions were performed using a Radleys Starfish parallel reactor at 60 ºC. 10 mmol of triglyceride was added to a 50 mL round bottomed flask fitted with a condenser, along with methanol (12.5 mL) and 0.0025 mol dihexyl ether (0.59 cm^3, Aldrich 97%) as an internal standard. 18.5 wt% butanol (35 wt% for C18 and olive oil) was added to aid the solubility of the triglyceride. The reaction mixture was magnetically stirred at 600 RPM in air. A t=0 sample (0.15 cm^3) was removed before catalyst addition and analysed to ensure GC reproducibility. 50 mg of catalyst was added to each flask at the start of the reaction. 0.15 cm^3 aliquots were periodically syringed from the reaction mixture, filtered and added to 1.6 cm^3 DCM in a GC vial. For triolein and olive oil reactions, the aliquots were diluted in 25 cm^3 DCM after filtering before being added to the GC vial. Samples were removed hourly for 6 hours, with more frequent sampling over the first 60 minutes of reaction in order to accurately calculate initial rates. A 24 hour sample was also taken. The TAG conversion and FAME formation were followed by analysis of the aliquots using a Varian 450 GC fitted with a flame ionisation detector (FID) and an 8400 autosampler. C4-C12 TAGs and associated products were analysed using a Zebron Inferno ZB-5HT capillary column (15 m × 0.32 mm i.d. and 0.1 μm film thickness). Triolein and olive oil transesterification reactions were analysed via on-column injection on a CP-simdist wide-bore column (10 m × 0.53 mm i.d. and 0.1 μm film thickness) with temperature programmed injector. Initial rates were calculated from the linear portion of the conversion profile over the first 60 minutes of the reaction. Turn over frequencies (TOFs) were determined by normalising these initial rates to base site density.

2.3.2 High pressure olive oil transesterification

The high pressure olive oil transesterification was performed using a Radleys starfish parallel reactor at 90 ºC. 10 mmol of olive oil (9.72 mL) was added to an ACE® glass pressure flask, along with methanol (12.5 mL) and 0.0025 mol dihexyl ether (0.59 cm^3, Aldrich 97%) as an internal standard. 25 wt% butanol was added to aid the solubility of the olive oil. The reaction mixture was magnetically stirred at 600 RPM in air. A t=0 sample (0.15 cm^3) was removed before catalyst addition and analysed to ensure GC reproducibility. 250 mg Cs-MgO was added to the flask at the start of the reaction. 0.15 cm^3 aliquots were periodically syringed from the reaction mixture, filtered, diluted with 25cm^3 DCM and added to a GC vial. Samples were only removed after 3 hours and 24 hours, to avoid depressurising the system too frequently. The TAG conversion and FAME formation were followed by analysis of the aliquots using a Varian 450 GC fitted with a flame ionisation detector (FID) and an 8400 autosampler via on-column injection on a CP-simdist wide-bore column (10 m × 0.53 mm i.d. and 0.1 μm film thickness) with temperature programmed injector.

2.3.2 Homogeneous catalyst comparative test

A tributyrin transesterification was carried out in the same way as described above, however 1mL of a 6 mM $Mg(OMe)_2$ methanolic solution was added as a catalyst. This amount was calculated to give the same number of methoxy anions as base sites in 50 mg of macroHT in order to compare the homogeneous and heterogeneously catalysed reactions directly.

2.3.3 Recycling tests

In order to test catalyst reusability, a tributyrin transesterification was scaled up so that enough catalyst could be recovered to carry out further reactions. 20 mmol tributyrin (5.88 cm^3) was added to a 100 cm^3 round-bottomed flask, along with methanol (25 cm^3) and 0.005 mol dihexyl ether (1.18 cm^3). 100 mg of catalyst was added to the flask. The transesterification reaction was carried out as described in section 2.3.1, and after 24 hours of reaction the catalyst was filtered under vacuum, washed in methanol, and dried overnight in a vacuum oven at 40 ºC. 50 mg of the recovered catalyst was then re-tested in a tributyrin transesterification to determine how much of the original activity had been retained.

The recovered convHT and macroHT catalysts were shown to be inactive as catalysts in the transesterification reaction and so were re-activated by calcining at 450 ºC for 15 hours under 20 mL min^{-1} O_2, (ramp rate 1 ºC min^{-1}), and cooling under flowing wet nitrogen for 48 hours. The reactivated catalysts were then tested again in a further tributyrin transesterification reaction.

2.4 List of chemicals used

Aluminium nitrate nonahydrate	Sigma-Aldrich, ACS reagent ≥ 98%
Aluminium tri-sec butoxide	Sigma-Aldrich, 97% (Aldrich)
Ammonium carbonate	Sigma-Aldrich, ACS reagent ≥ 30% NH_3 basis
Ammonium hydroxide solution	Sigma-Aldrich, ACS reagent, 28.0-30.0% NH_3
Caesium hydroxide	Alfa Aesar, 96%
Dichloromethane	Fisher Scientific, unstabilised ≥ 99.8% HPLC
Dihexyl ether	Sigma-Aldrich, 97% (Aldrich)
Divinylbenzene	Sigma-Aldrich, technical grade 80% (Aldrich)
Ethanol	Sigma-Aldrich, ≥ 99.5%, absolute
Gamma alumina	Degussa, 85-115 m^2 g^{-1}
Glyceryl tributyrate (Tributyrin)	Sigma-Aldrich, ≥ 99% (Sigma)
Glyceryl trioctanoate (Tricaprylin)	Sigma-Aldrich, ≥ 99% (Sigma)
Glyceryl trioleate (Triolein)	Sigma-Aldrich, ≥ 99% (Sigma)
Hydrochloric acid	Sigma-Aldrich, ACS reagent, 37%
Magnesium methoxide solution	Sigma-Aldrich, 6-10 wt% in methanol
Magnesium nitrate hexahydrate	Sigma-Aldrich, ACS reagent, 99%
Methanol	Fisher scientific, ≥ 99.9% HPLC
NanoMgO	NanoScale Corporation, 99.6% NanoActive Magnesium Oxide Plus

Olive oil	Sainsbury's, Bertolli extra virgin
Pluronic® P123	Sigma-Aldrich, Average M_n ~ 5800
Potassium persulfate	Sigma-Aldrich, ACS reagent ≥ 99.0%
Sodium hydroxide pellets	Fisher Scientific, Bioreagents
Styrene	Sigma-Aldrich, *ReagentPlus*® ≥99%
Tetramethoxysilane	Sigma-Aldrich, 98% (Aldrich)
Toluene	Fisher Scientific, 99.8+ % CertiFied HPLC
Toluene (anhydrous)	Acros Organics, Extra Dry over molecular sieve, ≥ 99.8%
Triethylamine	Sigma-Aldrich, ≥99%
Trilaurin	Acros Organics, 98%

2.5 References

1. D. G. Cantrell, L. J. Gillie, A. F. Lee and K. Wilson, *Applied Catalysis A: General*, 2005, **287**, 183-190.
2. S. Vaudreuil, M. Bousmina, S. Kaliaguine and L. Bonneviot, *Advanced Materials*, 2001, **13**, 1310-1312.
3. D. Y. Zhao, Q. S. Huo, J. L. Feng, B. F. Chmelka and G. D. Stucky, *J. Am. Chem. Soc.*, 1998, **120**, 6024-6036.
4. J. Dhainaut, J. P. Dacquin, A. F. Lee and K. Wilson, *Green Chemistry*, 2010, **12**, 296-303.
5. M. V. Landau, E. Dafa, M. L. Kaliya, T. Sen and M. Herskowitz, *Microporous and Mesoporous Materials*, 2001, **49**, 65-81.
6. S. Utamapanya, K. J. Klabunde and J. R. Schlup, *Chemistry of Materials*, 1991, **3**, 175-181.
7. www.nanoscalecorp.com/content.php/chemicals/resources/, Accessed April 2013.
8. C. Hammond, *Basics of Crystallography and Diffraction*, Oxford University Press, New York, 2001.
9. Katholieke Universiteit Leuven Nuclear solid state group, 2010, **X-ray diffraction – Bruker D8 Discover**, [online] Available at: <http://fys.kuleuven.be/iks/nvsf/experimental-facilities/x-ray-diffraction-2013-bruker-d2018-discover> [Accessed March 2012].
10. J. W. Niemantsverdriet, *Spectroscopy in Catalvsis: An introduction*, Wiley-VCH, Darmstadt, 2007.
11. N. Pernicone, *Cattech*, 2003, **7**, 196-204.
12. P. Scherrer, *Gottinger Nachrichten*, 1918, **2**, 98.
13. R. P. H. Gasser, *An introduction to chemisorption and catalysis by metals*, Oxford University Press, New York, 1985.
14. G. A. Somorjai and Y. Li, *Introduction to surface chemistry and catalysis*, John Wiley & Sons Inc, Hoboken, 2010.

15. P. A. Webb and C. Orr, *Analytical Methods in Fine Particle Technology*, Micromeritics, Norcross, 1997.
16. F. Rouquerol, J. Rouquerol and K. S. W. Sing, *Adsorption by powders & porous solids: principles, methodology and applications*, Academic Press, Bodmin, 1999.
17. D. H. Everett, R. A. W. Haul, L. Moscou, R. A. Pierotti, J. Rouquerol and T. Siemieniewska, *Pure Appl. Chem*, 1985, **57**, 603.
18. J. W. McBain, *J. Am. Chem. Soc.*, 1935, **57**, 699-700.
19. S. Brunauer, P. H. Emmett and E. Teller, *J. Am. Chem. Soc.*, 1938, **60**, 309-319.
20. G. Horvath and K. Kawazoe, *J. Chem. Eng. Jpn.*, 1983, **16**, 470-475.
21. T. G. Rochow and P. A. Tucker, *Introduction to microscopy by means of light, electrons, X rays, or acoustics*, Springer, New York, 1994.
22. J. Goldstein, *Scanning electron microscopy and X-ray microanalysis*, Springer, 2003.
23. B. C. R., E. C. A. and W. S., *Encyclopedia of Materials Characterization: Surfaces, Interfaces, Thin Films*, Gulf professional publishing, 1992.
24. J. I. Di Cosimo, V. K. Diez, M. Xu, E. Iglesia and C. R. Apesteguia, *Journal of Catalysis*, 1998, **178**, 499-510.
25. D. P. Debecker, E. M. Gaigneaux and G. Busca, *Chem.-Eur. J.*, 2009, **15**, 3920-3935.
26. S. Abello, F. Medina, D. Tichit, J. Perez-Ramirez, X. Rodriguez, J. E. Sueiras, P. Salagre and Y. Cesteros, *Applied Catalysis A: General*, 2005, **281**, 191-198.
27. V. K. Diez, C. R. Apesteguia and J. I. Di Cosimo, *Journal of Catalysis*, 2003, **215**, 220-233.
28. R. Philipp and K. Fujimoto, *Journal of Physical Chemistry*, 1992, **96**, 9035-9038.
29. R. Richards, ed., *Surface and Nanomolecular Catalysis*, CRC Press, Boca Ranton, 2006.
30. I. Chorkendorff and J. W. Niemantsverdriet, *Concepts of modern catalysis and kinetics*, Wiley-VCH, Mörlenbach, 2003.
31. Inorganic Crystal Structure Database, FIZ Karlsruhe GmbH 1998 - 2013. http://www.fiz-karlsruhe.com/icsd.htm.
32. M. A. Newton and W. van Beek, *Chemical Society Reviews*, 2010, **39**, 4845-4863.
33. G. Meitzner, G. H. Via, F. W. Lytle and J. H. Sinfelt, *Journal of Physical Chemistry*, 1992, **96**, 4960-4964.
34. J. C. Fuggle and J. E. Inglesfield, *Topic in Applied Physics, Voulme 69, Unoccupied Electronic States. Fundamentals for XANES, EELS, IPS and BIS*, Springer-Verlag, New York, USA, 1992.
35. V. H. and K. D.C., *Handbook of heterogeneous catalysis, volume 2,* Wiley-VCH, Weinheim, Germany, 1997.

Chapter 3

Conventional versus macroporous hydrotalcites

3.1 Introduction

Hydrotalcites, with the general formula $[M(II)_{1-x}M(III)_{x}(OH)_2]^{x+}(A^{n-}_{x/n})\cdot mH_2O$, belong to a class of anionic clays known as layered double hydroxides.[1,2] Hydrotalcites comprise positively charged, brucite-like layers, wherein substitution of M^{2+} by M^{3+} ions has occurred. Charge balancing anions, commonly carbonate, are located in the interlayer space, although the intercalation of various organic anions have been reported.[3,4] Different di- and tri-valent cations can be used in their synthesis e.g. Zn^{2+}/Al^{3+}, and x, the trivalent cation degree of substitution, can take values in the range $0.2 \leq x \leq 0.33$.[5] This study focuses on MgAl hydrotalcites. The general structure of a hydrotalcite is shown in **Figure 3.1**.

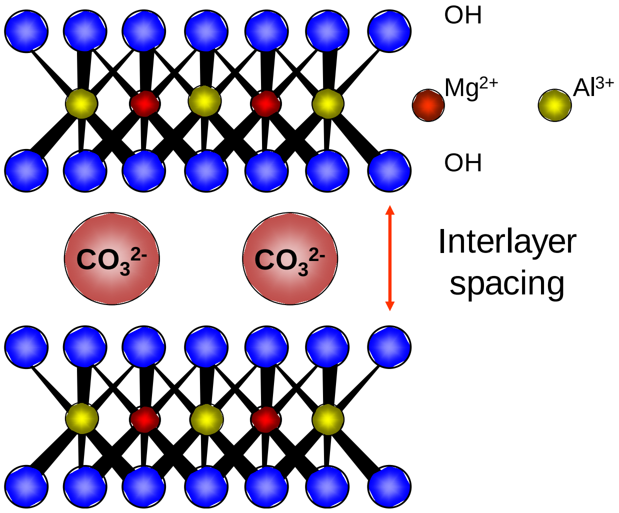

Figure 3.1. Layered double hydroxide structure of a MgAl hydrotalcite.[6]

Calcination of hydrotalcites leads to loss of the interlayer carbonate anions and formation of a mixed metal oxide material.[7] However, when exposed to water, the layered double hydroxide structure can re-form through rehydration, a process known as "the memory effect",[8] with hydroxide anions replacing carbonate in the interlayer space. Such rehydrated hydrotalcites have been reported as active solid base catalysts in the transesterification of triglycerides,[9-12] widely employed for biodiesel synthesis.

The rehydration step is critical for the formation of Brønsted base sites within the hydrotalcite catalyst. Commonly, a vapour phase rehydration procedure is used, although this is a time consuming process. Liquid phase rehydration, by which the hydrotalcite is placed in deionised water at high temperature and pressure, has also been reported in the literature.[13]

Real oil feedstocks used in biodiesel synthesis contain long-chained, bulky triacyl glycerides (TAGs).[14,15] The use of microporous hydrotalcites to catalyse their transesterification is therefore likely to be slow and rate-limited by diffusion through the micropores to the active (basic) sites. Géraud and co-workers first reported the preparation of macroporous hydrotalcites via co-precipitation around sedimented polystyrene beads used as a sacrificial template.[16] However, no literature exists reporting on the catalytic application of these macroporous hydrotalcites, which may be well-suited for triglyceride transesterification.

Géraud's method of hydrotalcite synthesis requires the use of alkali. This is not ideal as incomplete removal of the alkali during the preparation may lead to leaching from the catalyst, allowing the alkali to react with free fatty acids in the biodiesel feedstock to produce unwanted soap by-product, creating separation problems.[17] Previously, Cantrell and co-workers[6] developed an alkali-free route to prepare hydrotalcites, and so for this research their method was adapted to incorporate a sacrificial polystyrene bead template and thus prepare alkali-free macroporous hydrotalcites. However, the protocol involves stirring, and not a sedimentation step for the beads to allow the formation of an ordered macroporous structure, as in Géraud's method. Therefore as a follow on later in the chapter, the preparation of an ordered macroHT via alkali-free co-precipitation around a sedimented polystyrene bead crystal was also examined.

The main aim of this chapter was to prepare a series of conventional and macroporous hydrotalcites with varying Mg:Al ratios using an alkali-free co-precipitation synthesis, to compare their physicochemical properties and any relationship between hierarchical pore structure and basicity. After characterisation, the aim was to test the materials in the transesterification of varying chain length triglycerides from a model C4 triglyceride up to olive oil, a real biodiesel feedstock, to examine the effect of the incorporation of macropores on the hydrotalcite activity. It was hypothesised that the incorporation of macropores into the hydrotalcite framework would facilitate diffusion of the long-chained bulky triglycerides found in real oils to the active sites of the hydrotalcites, therefore increasing the rate of FAME production.

3.2 Results and discussion

A series of both conventional and macroporous hydrotalcites with nominal Mg:Al ratios varying from 1:1 to 4:1 were prepared as described in Chapter 2. Briefly, the alkali-free co-precipitation method of Cantrell and co-workers[6] was used to prepare the conventional hydrotalcites. This method was adapted to incorporate sacrificial polystyrene bead templating as reported by Géraud and co-workers[18] in order to prepare alkali-free macroporous hydrotalcites. Both sets of materials were calcined and rehydrated in the vapour phase before further analysis. Characterisation was carried out on the full series of both conventional and macroporous hydrotalcites. However, direct comparisons between the two different types of hydrotalcites were carried out between the highest Mg:Al ratio (2:1), and therefore most active, hydrotalcites from both series, referred to as the convHT and macroHT samples. The hydrotalcites were then tested as catalysts in the transesterification of varying chain length triglycerides (TAGs) to form FAME.

3.2.1 Characterisation of conventional and macroporous hydrotalcites

After bulk elemental analysis was performed to determine actual Mg:Al ratios, the structure of the materials was confirmed using powder X-ray diffraction (XRD), N_2 porosimetry and electron microscopy. TGA, XPS and CO_2 TPD analysis were also carried out to determine more about the chemical environment of the hydrotalcites.

3.2.1.1 EDX

EDX analysis was carried out on the full series of conventional and macroporous hydrotalcites. The actual Mg:Al ratios compared to the nominal values can be seen in **Table 3.1**.

Table 3.1. Bulk Mg:Al ratios as determined by EDX analysis, for the conventional and macroporous hydrotalcite series.

	Actual Mg:Al ratio determined by EDX analysis	
Nominal Mg:Al ratio	Conventional hydrotalcites	Macroporous hydrotalcites
1:1	0.41:1 +/- 0.07	0.38:1 +/- 0.06
2:1	0.82:1 +/- 0.03	0.83:1 +/- 0.03
3:1	0.92:1 +/- 0.06	1.28:1 +/- 0.06
4:1	1.95:1+/- 0.10	2.02:1 +/- 0.10

The bulk ratios achieved are much lower than the nominal ratios, however they are comparable between both series of materials, suggesting that any subsequent reactivity differences must originate from structure/morphology effects and not their intrinsic composition. The low pH used during the synthesis may account for the lower Mg incorporation, as the higher the pH, the more soluble $Mg(OH)_2$ is compared to $Al(OH)_{3.}$[19] There is loss of some of the magnesium added into the reaction, suggesting the possible formation of excess brucite.[20] This may be formed as very small crystallites, or in an amorphous phase, as it cannot be easily detected in the XRD.

3.2.1.2 XRD

Powder XRD patterns for the full series of conventional and macroporous hydrotalcites can be seen in **Figure 3.2** and **Figure 3.3** respectively. The diffraction patterns reveal a main crystal phase for all materials with common sets of reflections at 11.6°, 23.4°, 35°, 39.2º, 47.1°, 61.1° and 62°, characteristic of MgAl hydrotalcites.[1,21] The peak at 31º is assigned to $Mg_5(CO_3)_4(OH)_2{\cdot}4H_2O$,[22] which accounts for some of the excess magnesium not incorporated into the hydrotalcite. The intensity of this peak compared to the hydrotalcite peaks decreases with increasing Mg:Al ratio, therefore there is a larger degree of hydrotalcite crystallisation with increasing Mg:Al ratio.

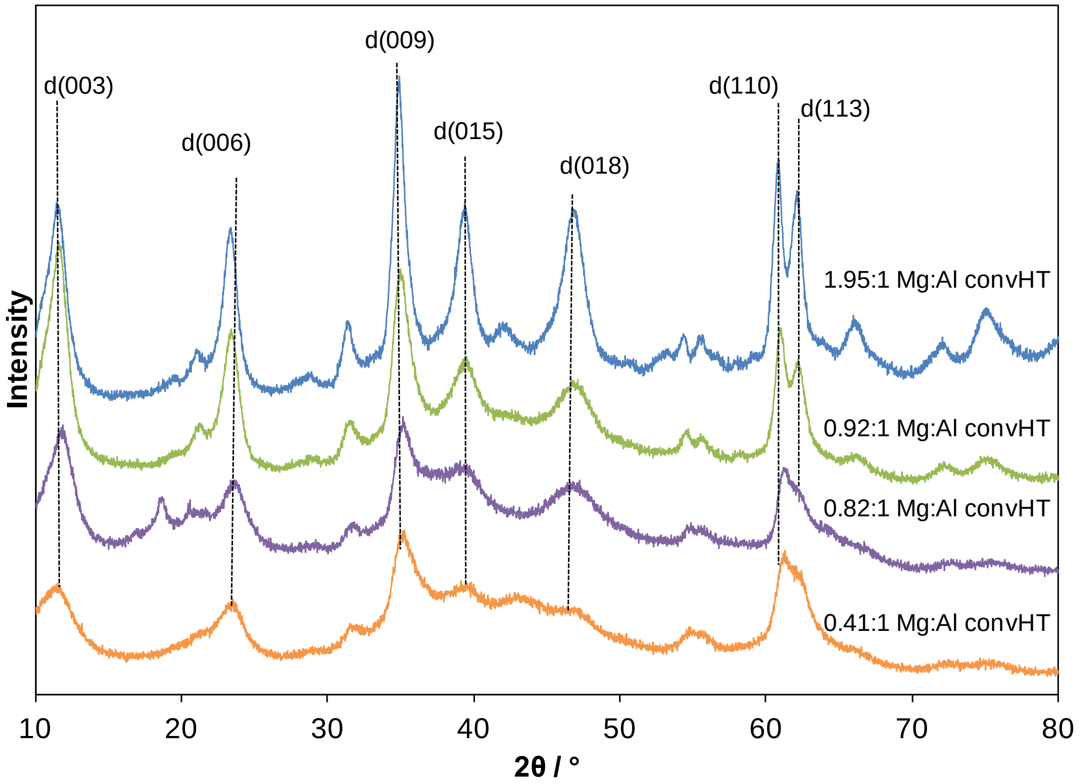

Figure 3.2. Powder XRD patterns for the full series of conventional hydrotalcites.

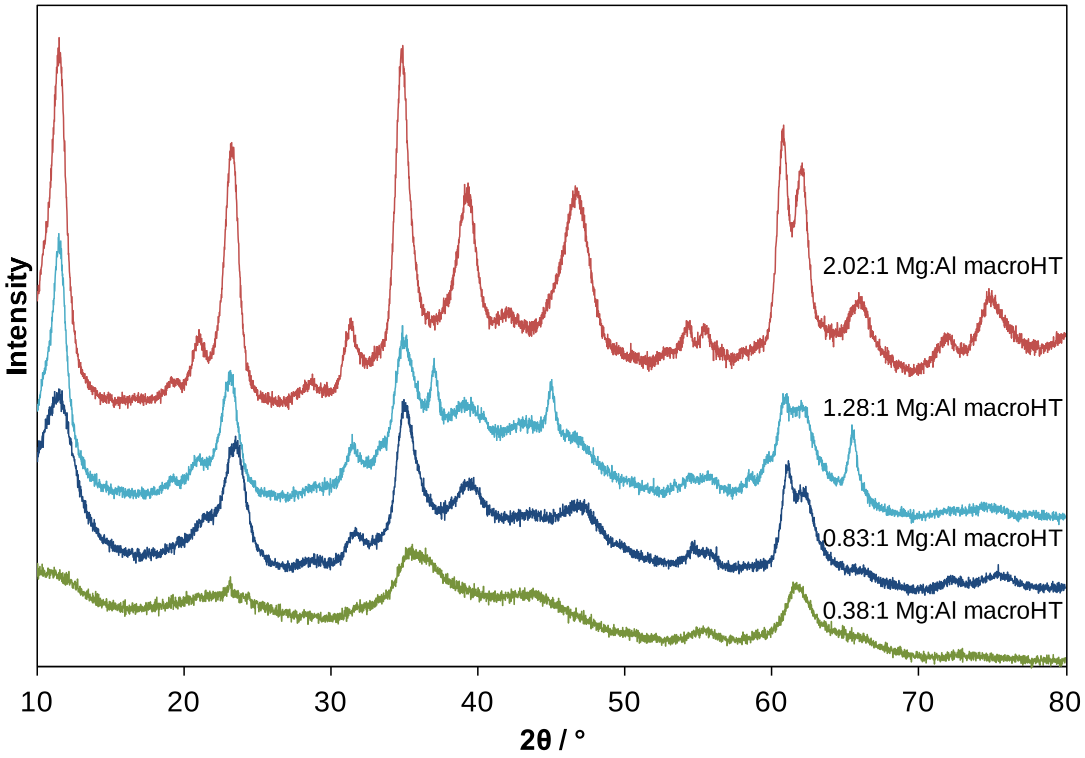

Figure 3.3. Powder XRD patterns for the full series of macroporous hydrotalcites.

This increasing degree of rehydration to form a hydrotalcite crystalline structure with increasing Mg:Al ratio can be observed by examining the XRD patterns, as the intensity of the hydrotalcite peaks increase and become more well-defined. Thermodynamic studies have shown that as Mg:Al ratio increases, the Gibbs free energy of hydration for the mixed oxides decreases.[23] The rehydration reaction therefore becomes thermodynamically more favourable at higher Mg:Al ratios and occurs faster, forming a more crystalline hydrotalcite structure.

Volume-averaged crystallite sizes were determined from line broadening using the Scherrer equation[24] and can be seen below in **Table 3.2**. The crystallite sizes are all very small indicating that there are extended porous architectures formed via the agglomeration or fusion of these nanocrystalline platelets. As the Mg:Al ratio decreases, line broadening occurs suggesting smaller crystallites and a less ordered structure. It has been shown in literature via multinuclear NMR spectroscopy[25] that a hydrotalcite with an Mg:Al ratio of 2:1 has an ordered honeycomb structure where each Mg centre is surrounded by 3 Mg and 3 Al octahedra, and each Al centre surrounded by 6 Mg octahedra.[26] This is the most ordered form of hydrotalcite, and Mg:Al ratios closer to this have higher ordering.

Table 3.2. Crystallite sizes and interlayer spacings for the conventional and macroporous hydrotalcites as determined from the powder XRD patterns.

Catalyst	Volume average crystallite size / nm	Interlayer spacing, *d* / nm
0.41:1 Mg:Al convHT	1.6 +/- 0.13	0.76 +/- 0.01
0.82:1 Mg:Al convHT	2.2 +/- 0.18	0.75 +/- 0.01
0.92:1 Mg:Al convHT	5.1 +/- 0.41	0.76 +/- 0.01
1.95:1 Mg:Al convHT	6.2 +/- 0.50	0.77 +/- 0.01
0.38:1 Mg:Al macroHT	0.9 +/- 0.07	0.79 +/- 0.01
0.83:1 Mg:Al macroHT	2.4 +/- 0.19	0.77 +/- 0.01
1.28:1 Mg:Al macroHT	4.7 +/- 0.38	0.77 +/- 0.01
2.02:1 Mg:Al macroHT	6.2 +/- 0.50	0.77 +/- 0.01

For a hydrotalcite model with 3R stacking of the brucite layers, the lattice parameter, *c*, corresponds to three times the interlayer spacing, *d*, between two consecutive layers.[27] *c*=3d(003),[27] and so from measuring the peak position of the d(003) reflection from the powder XRD patterns, and converting from degrees into nanometres, the interlayer spacings for each hydrotalcite can be determined. These values are reported in **Table 3.2**. The values are almost identical across all of the materials, and correspond to the intercalation of a hydroxide anion.[28]

The lattice parameter, *a*, for each hydrotalcite was calculated using the d(110) peak position, where $a = 2d_{110}$,[1] and the results plotted below in **Figure 3.4.** Lattice parameter increases with increasing Mg:Al ratio, due to the fact that the Mg^{2+} cation is larger than the Al^{3+} cation. Vegard's law states that at a constant temperature, a linear relationship exists between a crystal lattice parameter of an alloy and the concentration of the constituent elements.[29] For hydrotalcites, Vegard's law has been shown to be valid for Mg:Al ratios of up to 2:1.[30] The plot in **Figure 3.4** shows that this linear relationship is valid for both the conventional and macroporous hydrotalcite series synthesised. This plot could therefore be used to estimate the Mg:Al ratio of new hydrotalcite materials synthesised.

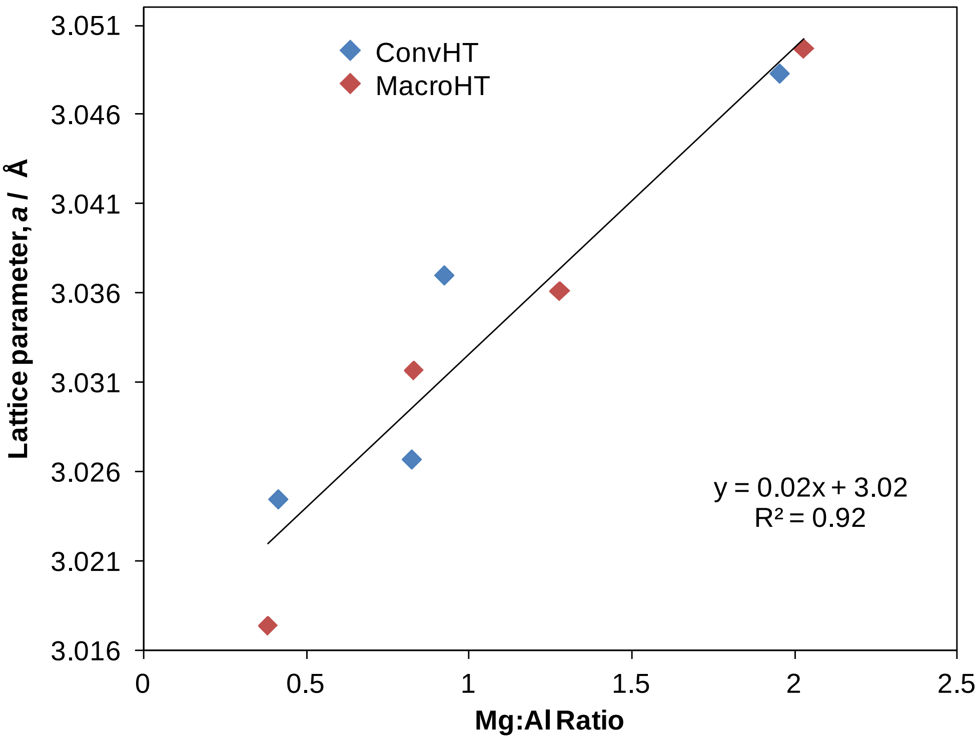

Figure 3.4. Plot of lattice parameters versus EDX Mg:Al ratio for hydrotalcites.

3.2.1.3 N_2 porosimetry

N_2 adsorption-desorption isotherms for both of the hydrotalcite series can be seen in **Figure 3.5** and **Figure 3.6**. The isotherms have been offset for clarity. **Table 3.3** reports the BET surface areas and total mesopore volumes as determined using the BJH method.[31]

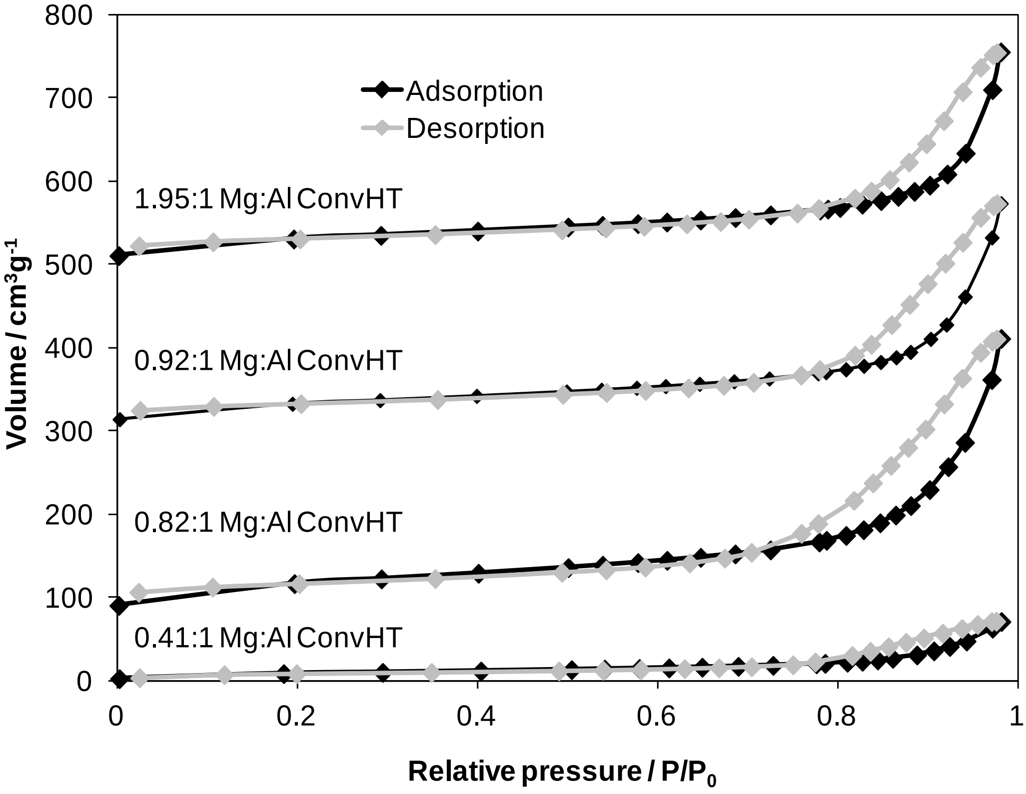

Figure 3.5. N_2 porosimetry isotherms for the series of conventional hydrotalcites.

Both the conventional and macroporous hydrotalcites possess type II H3 isotherms consistent with microporous crystallites with interplatelet mesoporous voids.[32] In general, excluding the 0.83:1 Mg:Al ratio sample, the macroporous hydrotalcites exhibit less hysteresis than the conventional hydrotalcites. This may suggest that the pores are more accessible for the macroporous hydrotalcites as hysteresis is indicative of bottle neck shaped pores with restricted access.[33]

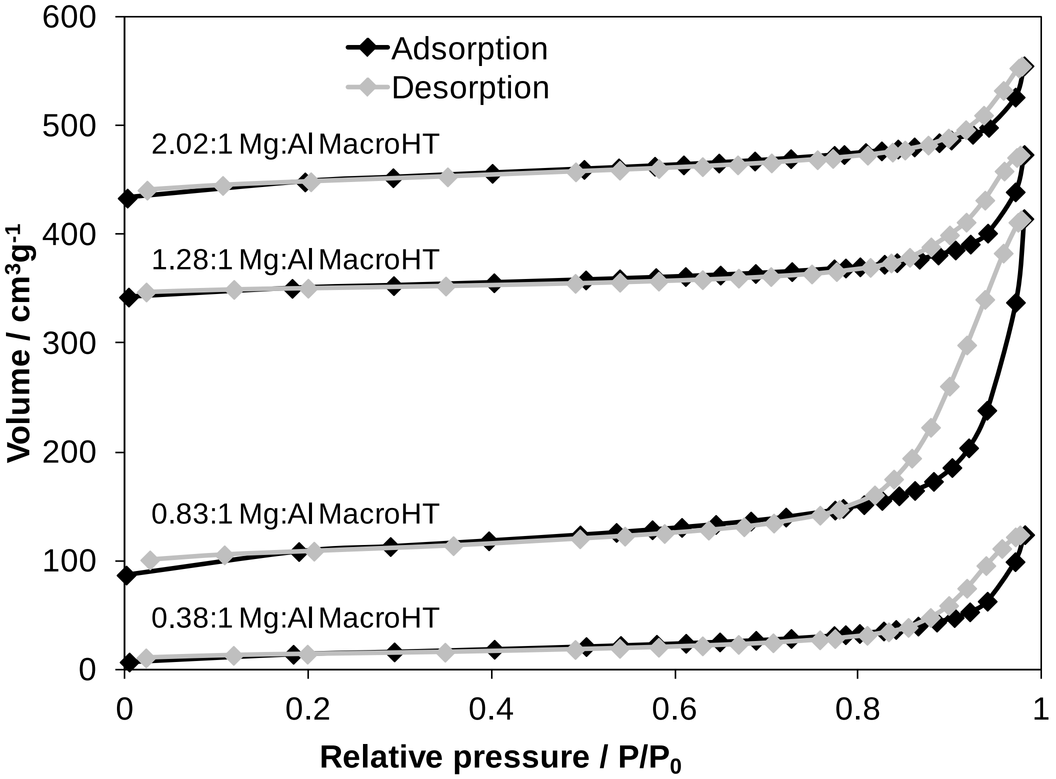

Figure 3.6. N_2 porosimetry isotherms for the series of macroporous hydrotalcites.

Table 3.3. Surface areas, total pore volumes and average pore diameters for conventional and macroporous hydrotalcites as determined by N_2 porosimetry.

	BET surface area / m^{2}g^{-1}	BJH total pore volume / cm^{3}g^{-1}	BJH average pore diameter / nm
0.41:1 Mg:Al convHT	49.4 +/- 4.9	0.16 +/- 0.01	11.99 +/- 0.75
0.82:1 Mg:Al convHT	148.1 +/- 14.8	0.52 +/- 0.04	9.22 +/- 0.72
0.92:1 Mg:Al convHT	116.3 +/- 11.6	0.41 +/- 0.03	13.98 +/- 1.03
1.95:1 Mg:Al convHT	48 +/- 4.8	0.21 +/- 0.01	3.44 +/- 0.39
0.38:1 Mg:Al macroHT	50.6 +/- 5.0	0.19 +/- 0.01	18.90 +/- 2.00
0.83:1 Mg:Al macroHT	118.6 +/- 11.9	0.52 +/- 0.04	16.08 +/- 1.45
1.28:1 Mg:Al macroHT	57.9 +/- 5.79	0.21 +/- 0.01	15.99 +/- 1.52
2.03:1 Mg:Al macroHT	62 +/- 6.2	0.18 +/- 0.01	3.43 +/- 0.39

With higher Al content, more charge balancing carbonate anions can be found in the interlayer space, and therefore on calcination a more open, porous structure is formed.[34]

This accounts for the decrease in surface area and total pore volume for Mg:Al ratios above 0.8:1. One possible hypothesis for the particularly low surface area observed in the 0.4:1 Mg:Al ratio samples is a greater aggregation of the very small crystallites seen in these materials, due to their particularly low ordering and crystallinity. The average pore diameter decreases in general with increasing Mg:Al ratio, meaning that as the hydrotalcite structure becomes more ordered, the larger crystallites can pack more closely together with fewer voids and there are smaller spaces between crystallites.

Micropore analysis was carried out over the highest Mg loading convHT and macroHT samples. The N_2 adsorption-desorption isotherms for these two materials taken with a base relative pressure of 1.3×10^{-6} can be seen in **Figure 3.7**, along with the micropore size distributions shown in **Figure 3.8**. **Table 3.4** reports on the micropore volumes and diameters, calculated using the HK method.[35]

Table 3.4. Micropore analysis data for convHT and macroHT

Catalyst	Micropore volume (HK) / $cm^3\ g^{-1}$	Total pore volume (BJH) / $cm^3\ g^{-1}$	Fractional micropore volume / %	Average micropore diameter / nm
ConvHT	0.0185 +/- 0.003	0.060 +/- 0.004	30	0.492 +/- 0.003
MacroHT	0.0271 +/- 0.003	0.091 +/- 0.006	30	0.838 +/- 0.003

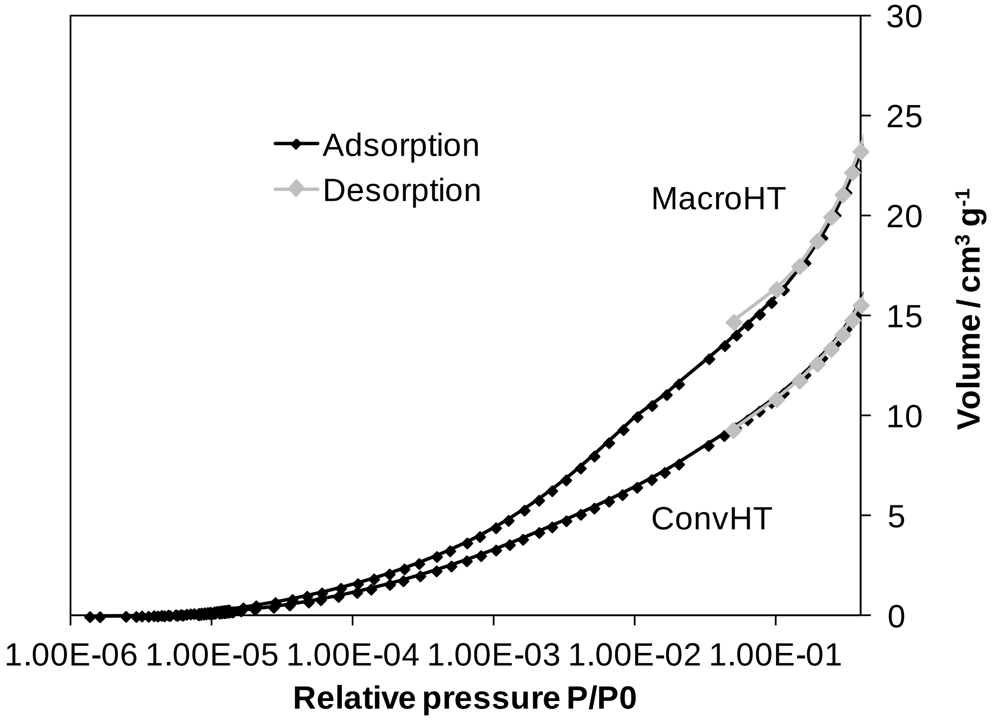

Figure 3.7. N_2 adsorption-desorption isotherm taken over the micropore region for convHT and macroHT.

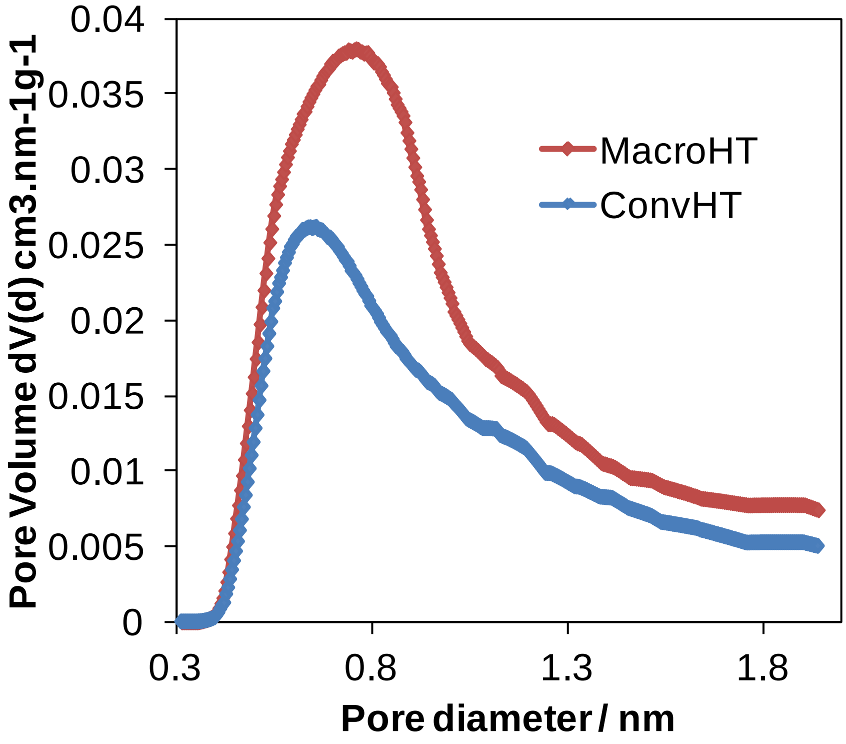

Figure 3.8. HK pore size distributions for convHT and macroHT.

The macroHT material shows increased total and micropore volumes compared to the convHT, a larger mean micropore diameter and a higher BET surface area. This increase in microporosity is attributed to a higher initial dispersion of hydroxycarbonate nanocrystallites in the macroHT during precipitation around the polystyrene bead perimeter. Rehydration of the thin mixed metal oxide shell formed after calcination of the polystyrene beads into crystalline hydrotalcite is easier than for the bulk convHT, producing thin layers of crystalline hydrotalcite, with more distorted platelet edge sites where the interlayer space becomes more accessible and therefore there is a higher degree of microporosity. The convHT precipitates in large 3D agglomerates with less distorted edge sites, open interlayer spaces and therefore decreased microporosity. **Figure 3.9** represents this schematically. This hypothesis is supported by electron microscopy (**section 3.2.1.5**).

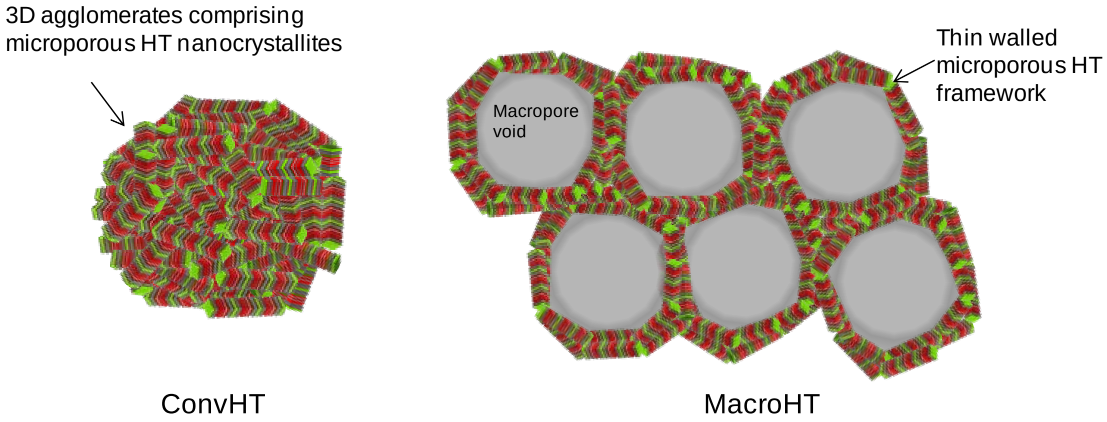

Figure 3.9. Cartoon illustrating possible role of macropores in regulating recrystallisation of microporous HT in convHT versus macroHT catalysts.

3.2.1.4 TGA

TGA profiles for convHT and macroHT can be seen below in **Figure 3.10**.

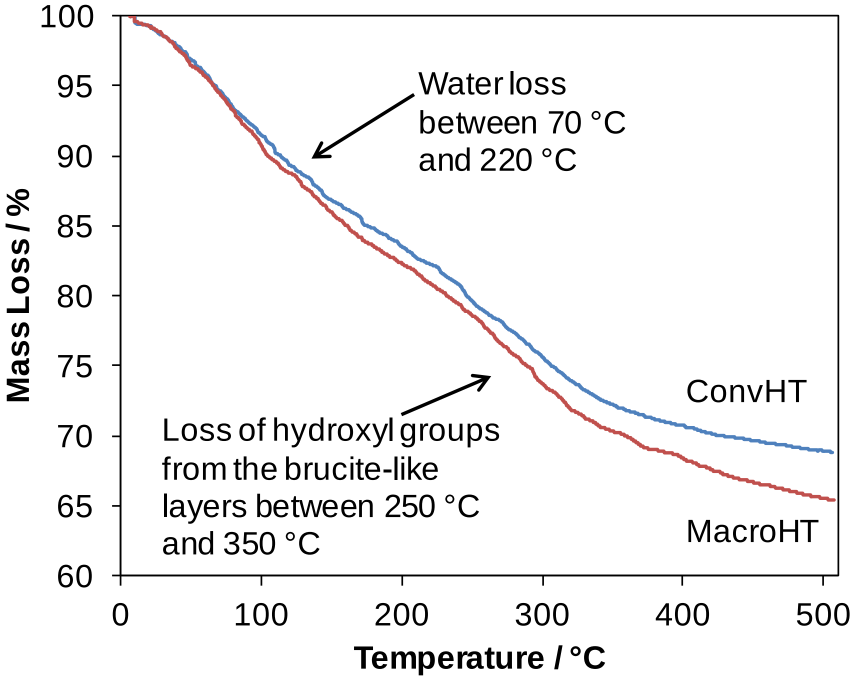

Figure 3.10. TGA profile showing mass loss over temperature for the 2:1 Mg:Al ratio convHT and macroHT samples.

There are two main weight loss regions associated with rehydrated hydrotalcites containing hydroxide as the interlayer anion. The first weight loss, between about 70 ºC and 220 ºC is attributed to the loss of water molecules adsorbed to the hydrotalcite surface, as well as interlayer water.[36] The weight loss at higher temperatures is attributed to the loss of hydroxide anions from within the brucite-like layers.[37] Both hydrotalcites display these characteristic weight losses.

Based on the general formula for hydrotalcites of $[M(II)_{1-x}M(III)_x(OH)_2]^{\chi+}(A^{n-}_{\chi/n})\cdot mH_2O$, the molecular formula for the convHT sample can be derived as $[Mg_{0.66}Al_{0.34}(OH)_2]\ (OH)_{0.34}\cdot 0.47\ H_2O$, where $m = 0.81\text{-}x$.[38] The macroHT has the molecular formula $[Mg_{0.67}Al_{0.33}(OH)_2]\ (OH)_{0.33}\cdot 0.48\ H_2O$. Using these formulae the theoretical weight loss for each of the two regions can be calculated, and these values, along with the experimental weight losses measured from the TGA profiles, can be seen below in **Table 3.5**.

Table 3.5. Theoretical and experimental TGA weight losses for the 2:1 Mg:Al convHT and macroHT samples.

	ConvHT	MacroHT
Theoretical weight loss due to interlayer water / %	11.5	11.8
Experimental weight loss due to interlayer water / %	12.4 +/- 0.1	13.6 +/- 0.1
Theoretical weight loss due to interlayer hydroxide anions / %	28.9	28.6
Experimental weight loss due to interlayer hydroxide anions / %	7.38 +/- 0.1	8.2 +/- 0.1

The experimental values for water loss are in good agreement with the theoretical values, indicating that the material consists of a layered double hydroxide structure with water molecules in-between the layers. The experimental weight loss for the hydroxide anions of the hydrotalcite structure is much lower than the theoretical structure would predict, suggesting that the material contains a phase other than that of just pure hydrotalcite. There may be areas of MgO and alumina trapped within the hydrotalcite crystalline structure, therefore not affecting the water content, but causing there to be a smaller percentage of hydroxide as interlayer anions and bound in the brucite-like layers than expected.

The macroHT sample loses a slightly larger overall weight percentage up to 500 ºC. This suggests that the macroporous hydrotalcite contains more hydrotalcite crystalline phase than the conventional hydrotalcite, most likely due to easier rehydration of the thin crystalline walls of the macroHT.

3.2.1.5 Electron microscopy

SEM images were obtained for both the conventional and macroporous hydrotalcites. Example images can be seen in **Figure 3.11**, along with a TEM image for macroHT.

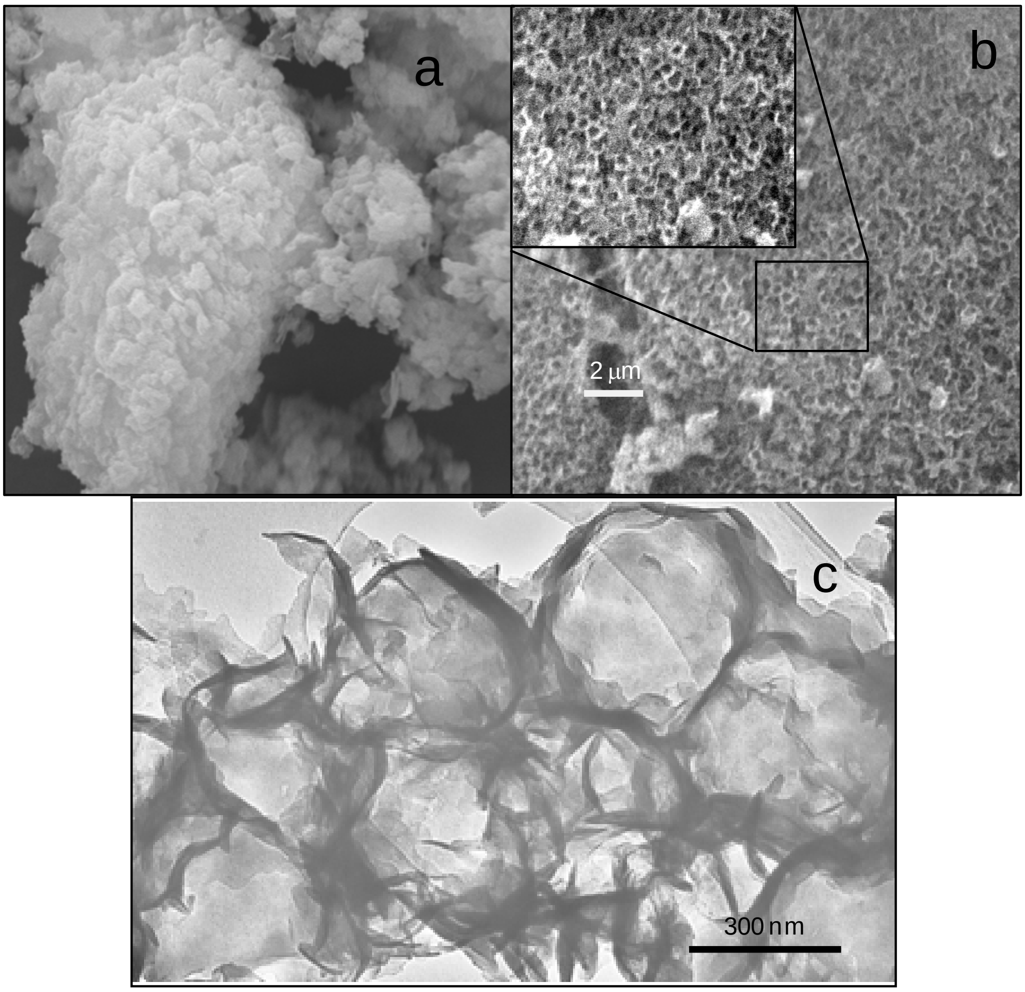

Figure 3.11. SEM images of a) a conventional hydrotalcite and (b) a macroporous hydrotalcite, and (c) TEM image of a macroporous hydrotalcite.

The images reveal a sand-rose structure characteristic of conventional hydrotalcites present in both materials.[39] However, the conventional hydrotalcite is made up of large, (around 200 nm to 1 µm) compact particles (**Fig. 3.11.a**), whereas the macroHT sample has a thin-walled (around 20 nm) honeycomb architecture (**Fig. 3.11.b**). The morphology of the macroHT sample arises from uniformly distributed macropores, with a mean diameter of 310 nm. This is slightly lower than the 350 nm diameter of the polystyrene beads used in the synthesis, most likely due to shrinkage of the beads before calcination. The TEM image of the macroHT (**Fig. 3.11.c**) reveals that the macropores are not highly ordered throughout the structure, reflecting the stirring protocol used during the synthesis.

3.2.1.6 XPS

XPS analysis was carried out on the series of conventional and macroporous hydrotalcites. The Mg 2s, Al 2p and O 1s regions were all examined and the raw data and fittings for these peaks can be seen in **Figures 3.12-3.15**.

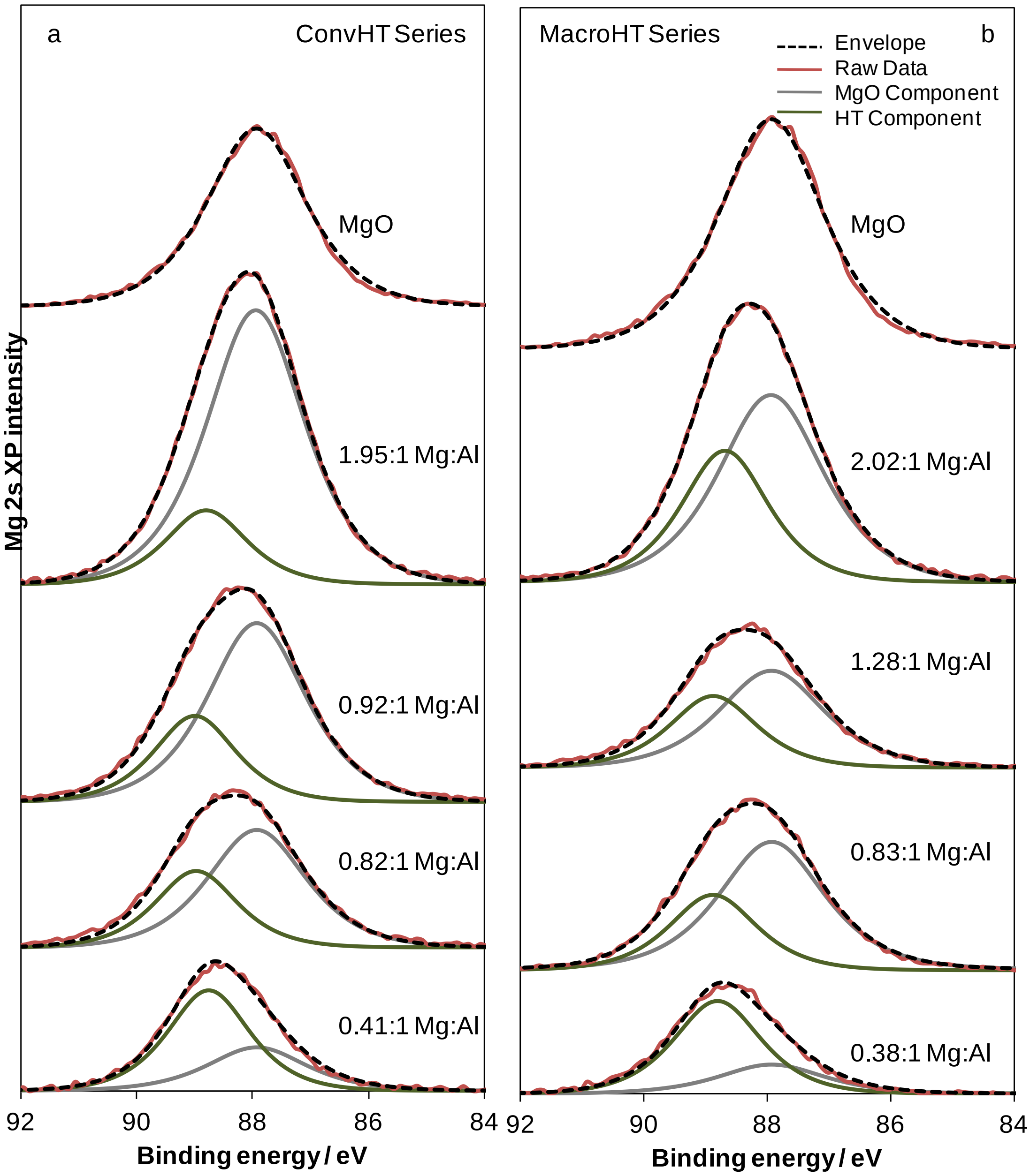

Figure 3.12. XP spectra showing the Mg 2s chemical environments for a) the series of conventional hydrotalcites and b) the series of macroporous hydrotalcites.

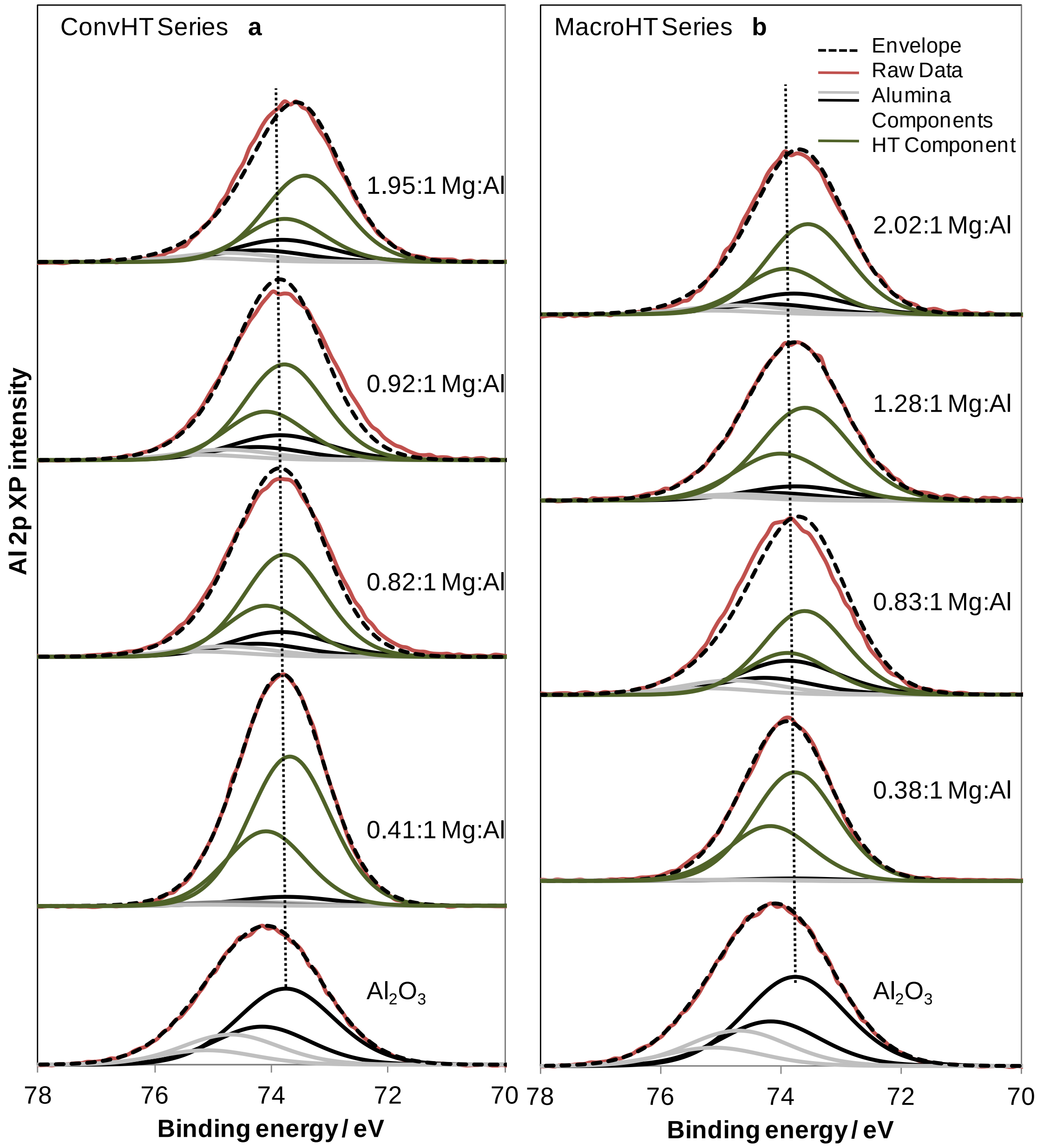

Figure 3.13. XP spectra showing the Al 2p chemical environments for a) the series of conventional hydrotalcites and b) the series of macroporous hydrotalcites. The vertical dotted line represents the binding energy of the major alumina component, indicating a shift to lower binding energy for the Al 2p peak maxima with increasing Mg content.

On examination of the Mg 2s spectra, two components have been fitted, an MgO component fitted using a standard, and a higher binding energy single hydrotalcite phase. A similar fitting can be seen in the Al 2p spectra, there is a main chemical environment at a binding energy of 72.5 eV, as of that reported for an alumina surface[40] which consists of two components, along with a single hydrotalcite phase. The spectra show that MgO and alumina is present in all of the samples, along with the single hydrotalcite phase.

Table 3.6 and **Table 3.7** show the surface Mg:Al ratios determined by XPS analysis for each material, compared to the bulk Mg:Al ratios determined by EDX analysis. The surface hydrotalcite Mg:Al ratio has also been calculated using the ratio of the hydrotalcite components of both the Mg 2s and Al 2p peaks. **Figure 3.14** shows plots of these surface ratios over the bulk for both hydrotalcite series.

Table 3.6. Bulk and surface Mg:Al atomic ratios for the conventional hydrotalcite series.

Bulk Mg:Al ratio determined by EDX analysis	Surface Mg:Al ratio determined by XPS analysis	Surface hydrotalcite Mg:Al ratio determined by XPS analysis
0.41:1 +/- 0.001	0.29:1 +/- 0.008	0.23:1 +/- 0.006
0.82:1 +/- 0.001	0.55:1 +/- 0.02	0.37:1 +/- 0.01
0.92:1 +/- 0.002	0.72:1 +/- 0.02	0.41:1 +/- 0.01
1.95:1+/- 0.003	1.14:1 +/- 0.03	0.42:1 +/- 0.01

Table 3.7. Bulk and surface Mg:Al atomic ratios for the macroporous hydrotalcite series.

Bulk Mg:Al ratio determined by EDX analysis	Surface Mg:Al ratio determined by XPS analysis	Surface hydrotalcite Mg:Al ratio determined by XPS analysis
0.38:1	0.41:1 +/- 0.01	0.12:1 +/- 0.003
0.83:1	0.53:1 +/- 0.01	0.44:1 +/- 0.01
1.28:1	1.01:1 +/- 0.03	0.59:1 +/- 0.02
2.02:1	1.30:1 +/- 0.04	0.89:1 +/- 0.02

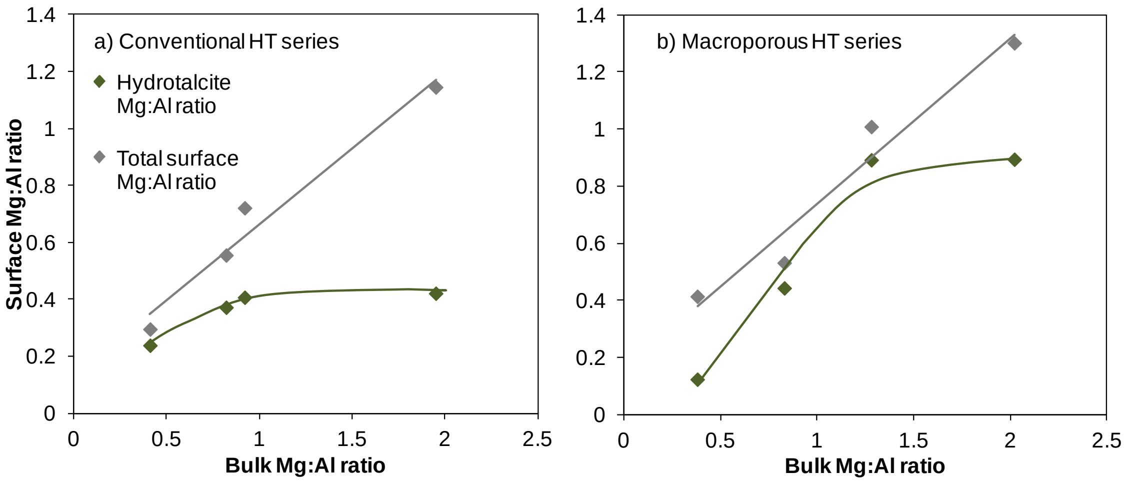

Figure 3.14. Plots showing total surface Mg:Al ratio and surface hydrotalcite Mg:Al ratio over bulk Mg:Al ratio for the conventional and macroporous hydrotalcite series.

The total surface Mg:Al ratio is found to be lower than the bulk, although both increase linearly with a similar gradient. The surface hydrotalcite Mg:Al ratio does increase with increasing bulk Mg:Al ratio, as more Mg is added during the hydrotalcite preparation, however it does not rise as rapidly as the total surface Mg:Al ratio, and plateaus off before the maximum amount of Mg has been added. Therefore as more Mg is added during the synthesis, a greater proportion of the extra Mg forms MgO in the final material rather than hydrotalcite. Forcing Mg into the hydrotalcite is difficult, particularly at the low pH reaction conditions, and so as more Mg is added, a larger amount is found as MgO.

The XRD diffraction patterns reveal that there is no crystalline phase for MgO in the materials, and therefore this MgO most likely exists as well dispersed small crystallites throughout the bulk, possibly trapped within the hydrotalcite.

On comparison between the conventional and macroporous hydrotalcite series, it can be observed that the macroporous Mg:Al hydrotalcite surface ratio reaches a higher value before levelling off than for the conventional hydrotalcite series. The highest loading macroHT has an Mg:Al ratio two thirds that of the total surface Mg:Al ratio, compared to one third for the highest loading conventional hydrotalcite. This increase is assigned to the greater ease of hydrotalcite crystallisation around the polystyrene bead supports, along with greater dispersion of the nanocrystallites in thin walls, allowing more Mg to enter the hydrotalcite structure at the more crystalline surface than for convHT.

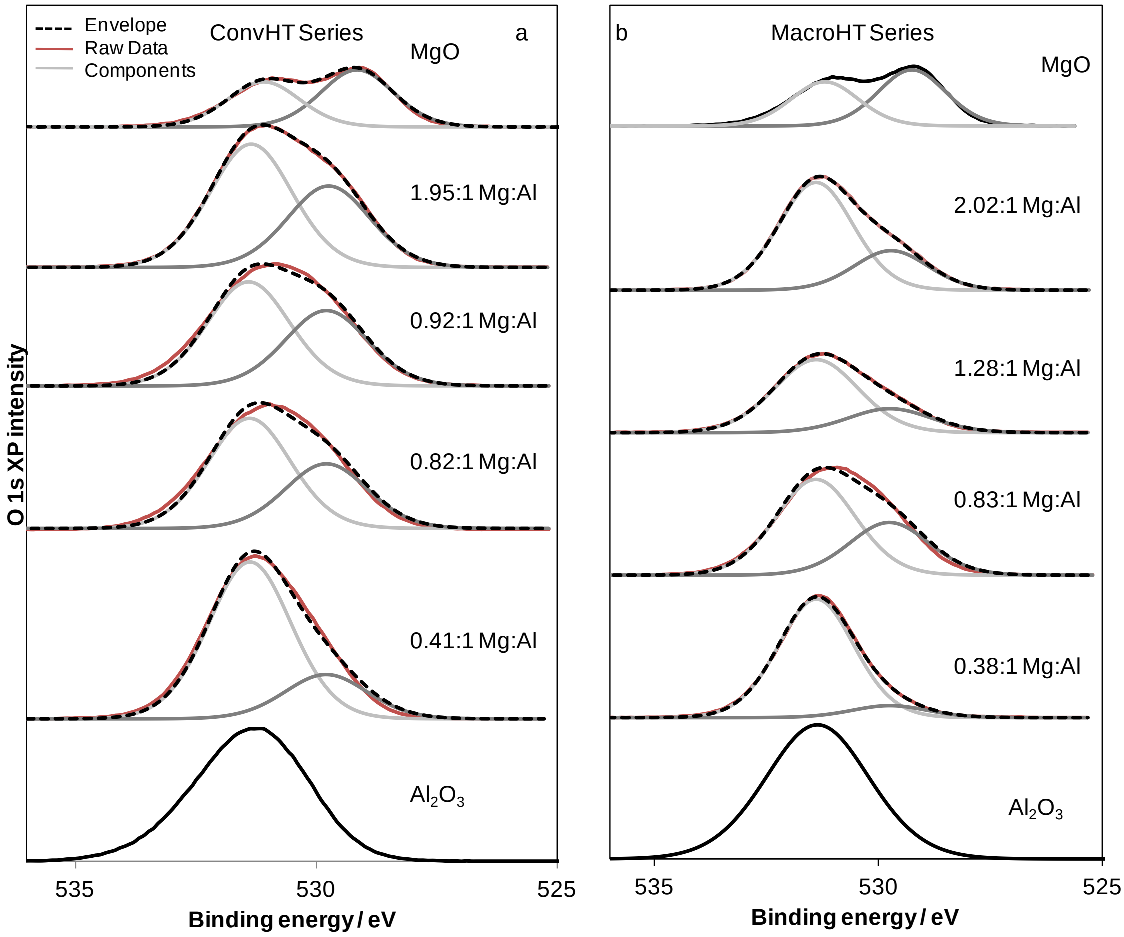

Figure 3.15. XP spectra showing the O 1s chemical environments for a) the series of conventional hydrotalcites and b) the series of macroporous hydrotalcites.

The Al_2O_3 O 1s peak only shows one chemical environment, at binding energy, 531 eV. This is assigned to a surface hydroxyl environment.[41] However, on increasing the Mg:Al ratio the O1s peaks for hydrotalcites become broader and more comparable to the O1s peak of MgO. Fitting shows there to be two chemical environments, the second at binding energy 529.5 eV being assigned to the more basic Mg-O^{2-} environment.[42] This peak intensity increases with increasing Mg:Al ratio, indicating that the proportion of MgO increases as we move to higher bulk Mg:Al ratios across the series, reinforcing the trends seen in the Mg 2s and Al 2p spectra.

3.2.1.7 CO_2 TPD

CO_2 pulse chemisorption was carried out on the hydrotalcite materials as described in Chapter 2. Briefly, known volumes of CO_2 were dosed over an out-gassed sample of hydrotalcite, until the sample was saturated. CO_2 is an acid probe molecule and it is assumed that each molecule of CO_2 adsorbs onto one base site of the hydrotalcites, forming a bicarbonate species with the hydroxide anions or surface hydroxyl groups.[34] To accurately measure these CO_2 molecules, after saturation of the surface, the hydrotalcite is heated up to 500 °C and the CO_2 that desorbs measured using a mass spectrometer, to give a base site density.

The CO_2 TPD profiles for both the conventional and macroporous hydrotalcites can be seen below in **Figure 3.16** and **Figure 3.17**. The TPD profile for nanoMgO calcined at 500 °C has been superimposed onto **Figure 3.16** as a comparison.[43] The base site densities for all materials are presented in **Table 3.8**. The different strength hydrotalcite base sites have been labelled on **Figure 3.17**.

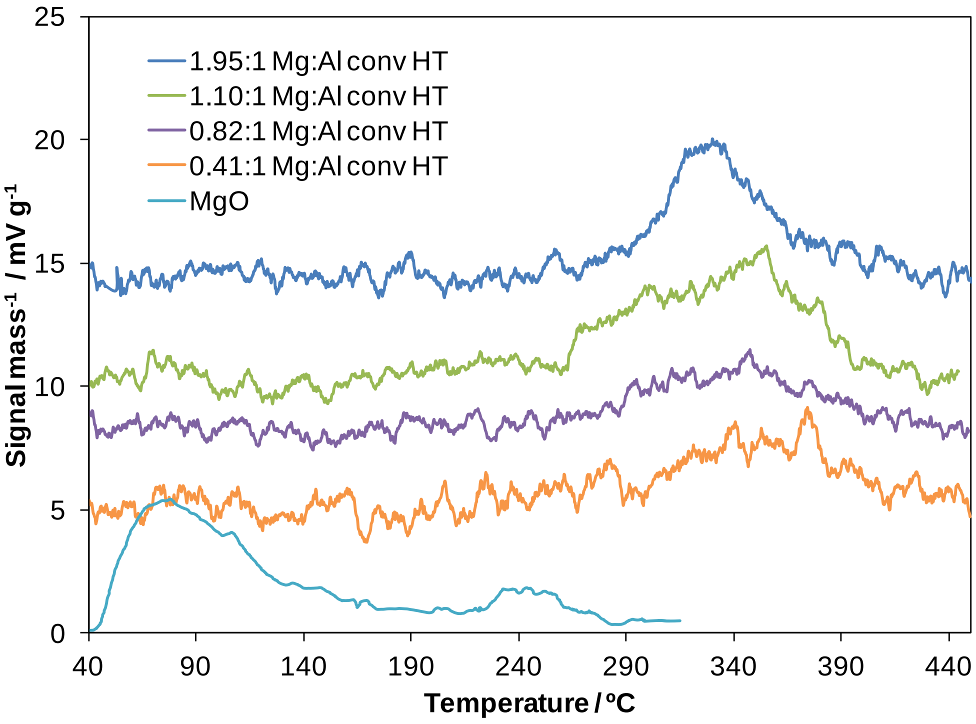

Figure 3.16. CO_2 TPD profiles for the conventional hydrotalcite series along with nanoMgO calcined at 300 °C for comparison, offset for clarity.

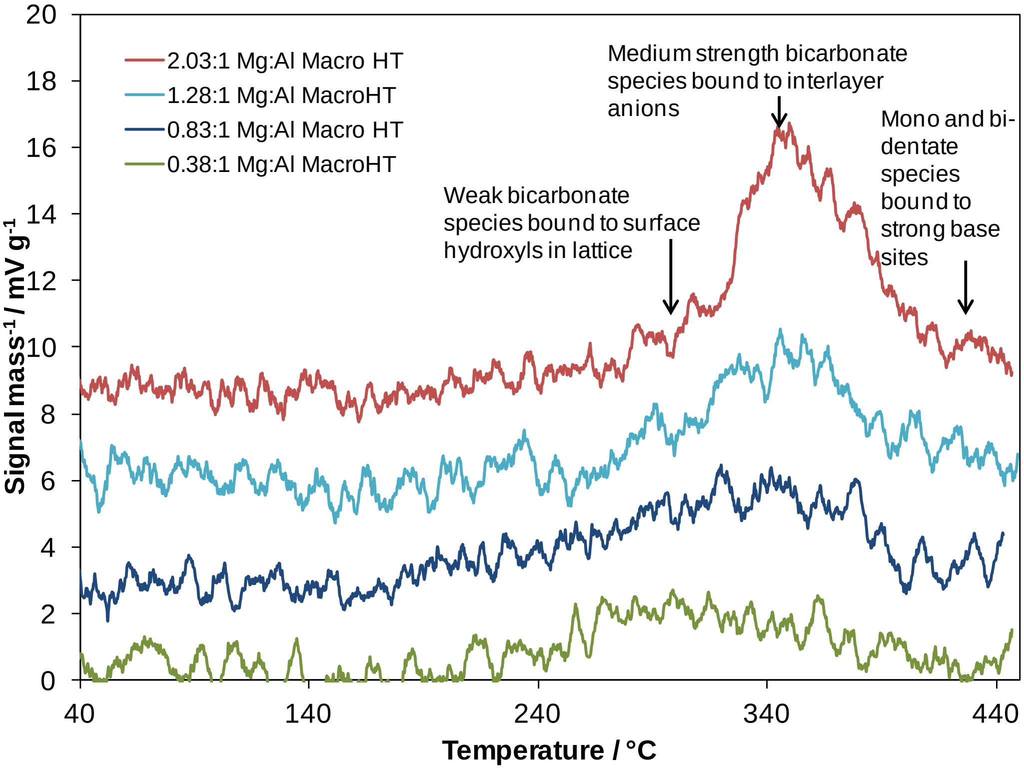

Figure 3.17. CO_2 TPD profiles for the macroporous hydrotalcite series, offset for clarity.

Table 3.8. Number of base sites and CO_2 desorption temperatures for conventional and macroporous hydrotalcites as determined by CO_2 TPD analysis.

Hydrotalcite	Number of base sites / g^{-1}	Desorption peak max temp. / ºC
0.41:1 conventional	3.38×10^{19}	330.2 +/- 0.2
0.82:1 conventional	5.35×10^{19}	336.7 +/- 0.2
0.92:1 conventional	7.60×10^{19}	340.9 +/- 0.2
1.95:1 conventional	8.55×10^{19}	349.8 +/- 0.2
0.38:1 macroporous	3.72×10^{19}	298.5 +/- 0.2
0.83:1 macroporous	4.61×10^{19}	341.8 +/- 0.2
1.28:1 macroporous	4.90×10^{19}	345.5 +/- 0.2
2.03:1 macroporous	7.68×10^{19}	349.7 +/- 0.2

The profiles all show one broad peak for CO_2 desorption. The number of base sites increases with increasing Mg:Al ratio for both series, along with the CO_2 desorption temperature, indicating an increase in the strength of the basic sites with increasing Mg content. Rehydrated hydrotalcites contain Brønsted base sites due to the interlayer hydroxide anions.[44] These Brønsted base sites have been shown to be very active for the transesterification reaction.[45] There will also be weakly Brønsted basic surface hydroxyl groups in the brucite-like layers. CO_2 molecules will adsorb to both of these sites as a bicarbonate species.[46] The large, broad desorption peak is attributed to the combination of these weak and medium strength bicarbonate species.[47]

As the Mg:Al ratio increases, the degree of hydrotalcite crystallinity increases, as observed in the XRD patterns. Therefore, there will be a greater amount of layered double hydroxide material, and more interlayer hydroxide anions. The charge density of the layers will also decrease, meaning the hydroxide interlayer anions will be attracted to the layers less strongly and will become more strongly basic themselves, explaining the observed increase in CO_2 desorption peak max. temperature with increasing Mg:Al ratio. Abello and co-workers[47] observe the CO_2 desorption peak maximum in their rehydrated hydrotalcites at the slightly higher temperature of 400 ºC, but that is when examining a more basic hydrotalcite with a much higher Mg:Al ratio of 3.5:1.

Abello and co-workers[47] also observe a small shoulder on the CO_2 desorption peak at the higher temperature of 550 ºC, which they assign to monodentate carbonate species bound to low-coordination oxygen anions and bidentate carbonate species forming on Mg^{2+}-O^{2-} pairs.[48] This small shoulder can just about be observed at the tail of the highest Mg:Al ratio TPD profiles, but these base sites contribute very slightly to the overall base site density.

The TPD profile for nanoMgO shows desorption peaks at much lower temperatures than for the conventional and macroporous hydrotalcites, with no overlapping area, showing that the MgO present in the materials is not involved in the catalysis and is inert, most likely trapped within the aggregated hydrotalcite crystallites.

The strength and base site density between conventional and macroporous hydrotalcite is comparable, suggesting that there is no difference in the nature of the active base sites, or the overall total amount of crystalline hydrotalcite present between the two series of materials.

3.2.2 Transesterification of triglycerides

When characterising conventional versus macroporous hydrotalcites, the Mg:Al ratio and chemical environments have been shown to be very similar. It is the larger scale structuring of these materials which differs, and therefore it is these differences which should provide an interesting effect when studying their activity in the transesterification of triglycerides, along with the effect of altering Mg:Al ratio.

The hydrotalcites were tested in the transesterification of varying chain length triglycerides, from a model C4 chain length, through to a C18 chain length, as well as olive oil, a real oil feedstock.

3.2.2.1 Tributyrin transesterification (C4 chain TAG)

Tributyrin is a C4 chain triglyceride. **Figure 3.18** shows the structure of this molecule and the reaction being tested. It is used as a model triglyceride for the transesterification reaction as the chain length is much shorter than any real oil which would be used to synthesise biodiesel, however it is much more soluble in methanol and therefore easier to work with.

The full series of both conventional and macroporous hydrotalcites were tested in the transesterification of tributyrin with methanol as a solvent at 60 ºC. Butanol was also used as a co-solvent to keep conditions constant between chain lengths, although it was not required in this instance as tributyrin is soluble in methanol.

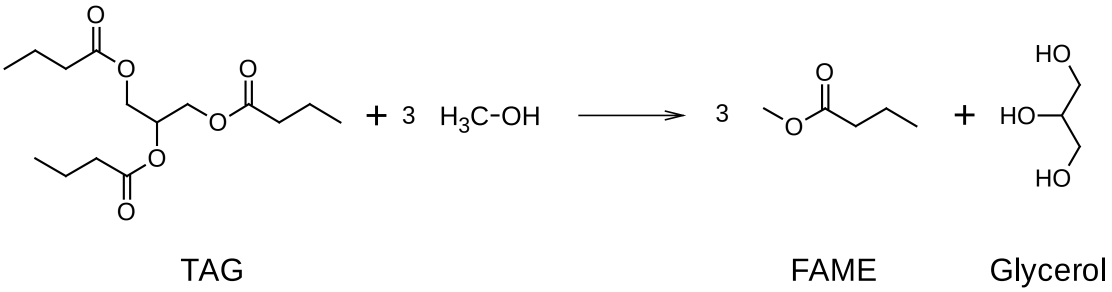

Figure 3.18. Reaction scheme showing the tributyrin transesterification.

3.2.2.1.a Conventional hydrotalcite series

The reaction profiles, along with product and intermediate formation profiles for the conventional hydrotalcite series can be seen in **Figures 3.19** to **3.22**. The reaction data is presented in **Table 3.9**.

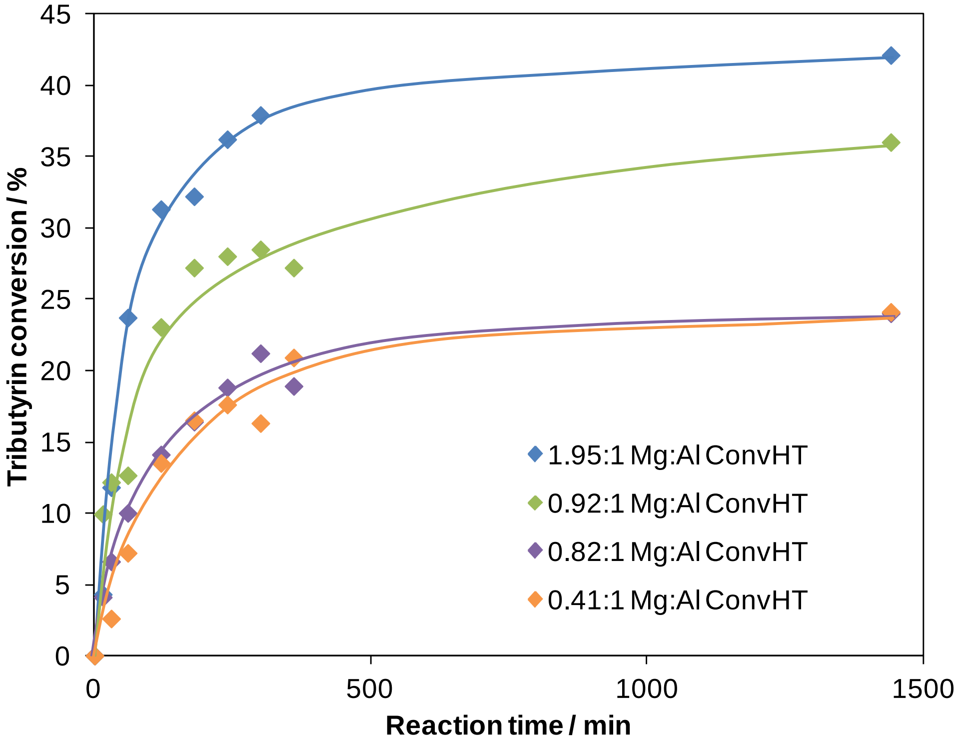

Figure 3.19. Reaction profiles showing tributyrin transesterification over time for the series of conventional hydrotalcites.

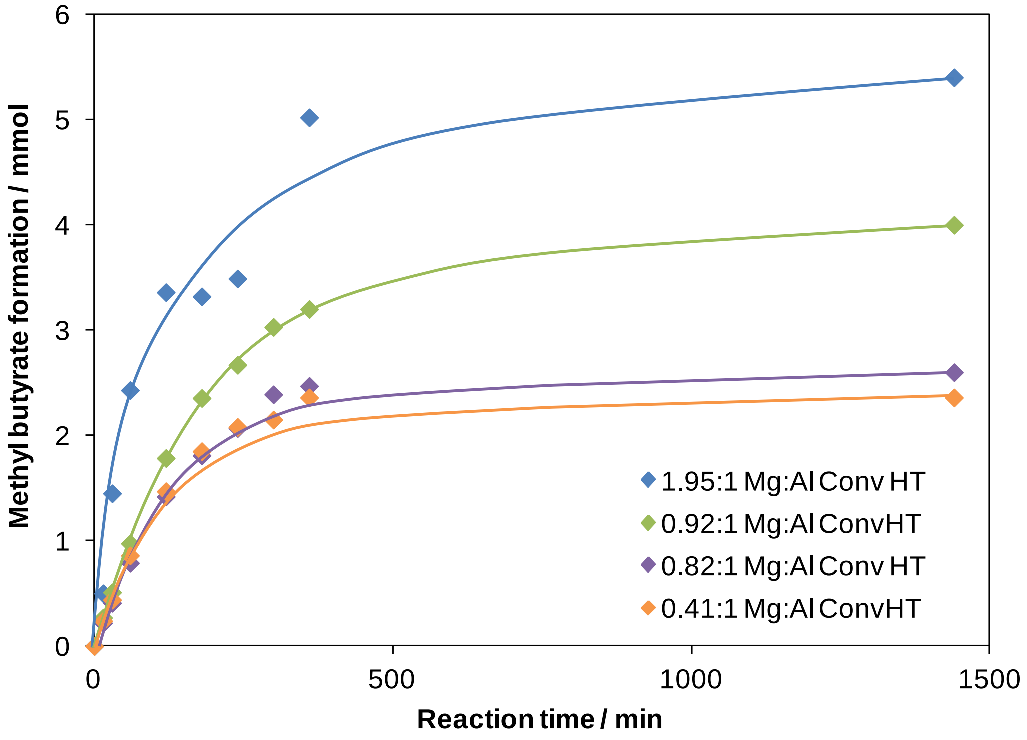

Figure 3.20. Methyl butyrate (MB) formation over time for the conventional hydrotalcite series during the transesterification of tributyrin.

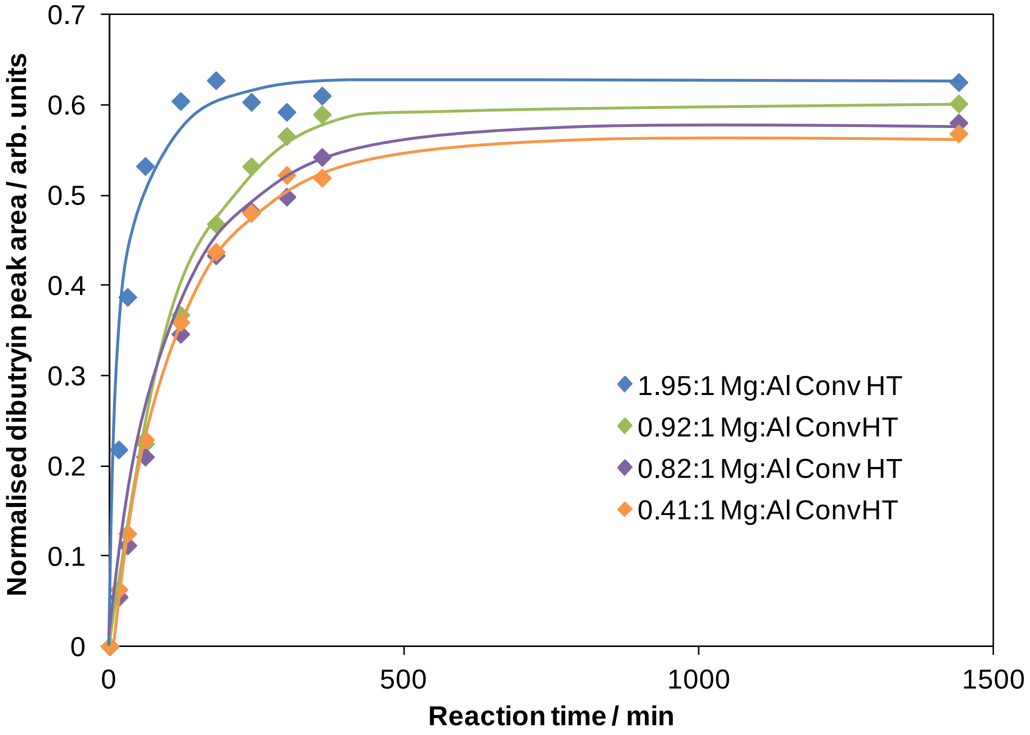

Figure 3.21. Intermediate dibutyrin formation over time for the conventional hydrotalcite series during the transesterification of tributyrin.

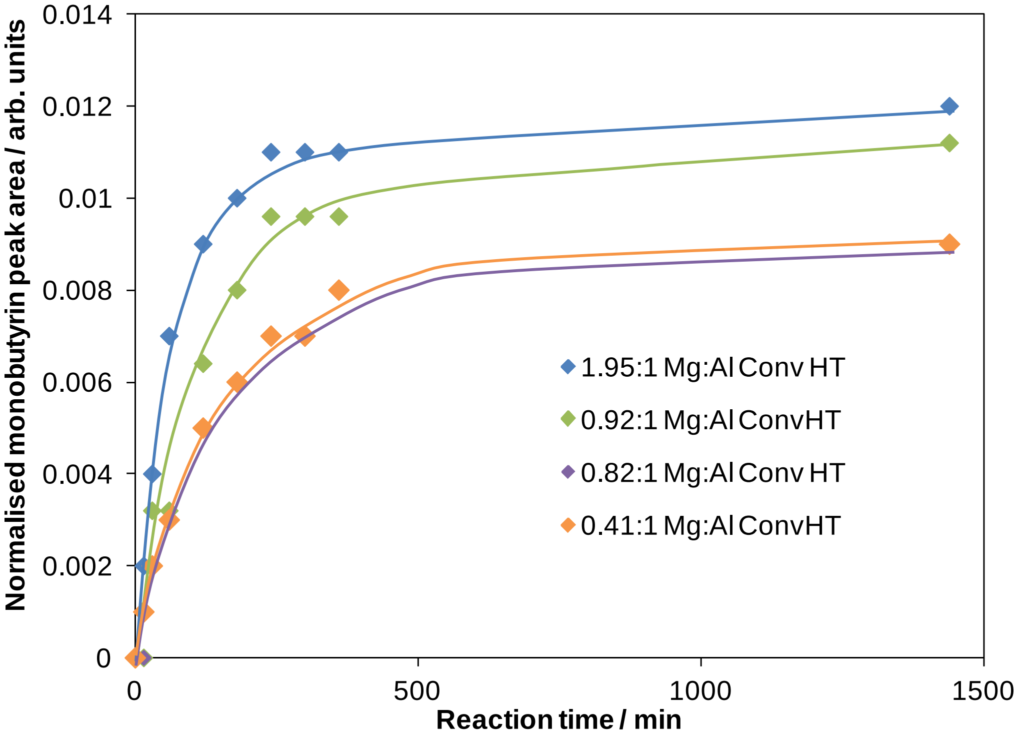

Figure 3.22. Intermediate monobutyrin formation over time for the series of conventional hydrotalcites during the transesterification of tributyrin.

The profiles all show two reaction regimes, linear TAG conversion during the first 50-200 minutes of reaction, followed by slower TAG conversion to reach a plateau after approximately 500 minutes. This plateau is assigned to de-activation of the hydrotalcites, most likely due to a side hydrolysis reaction of the methyl butyrate product over the catalysts, forming butyric anions which then replace the hydroxide anions in the interlayer space and expand the interlayer distance.[49]

Table 3.9. Reaction data for the series of conventional hydrotalcites as catalysts in the transesterification of tributyrin.

Mg:Al ratio	Initial rate / mmol g^{-1} min^{-1}	TOF / min^{-1}	TAG conversion after 24 h / %	MB selectivity after 24 h / %
0.41:1	0.12 +/- 0.02	2.28	22.4 +/- 1.5	32 +/- 1.5
0.82:1	0.22 +/- 0.03	2.38	23.5 +/- 1.5	37 +/- 1.5
0.92:1	0.34 +/- 0.02	2.67	34.0 +/- 1.5	40 +/- 1.5
1.95:1	0.78 +/- 0.01	5.49	42.1 +/- 1.5	43 +/- 1.5

The initial rate increases with increasing Mg:Al ratio, which would be anticipated due to the increase in number of base sites. However, there is also an increase in TOF values, the number of triglyceride molecules converted per base site per minute, across the series. Therefore the strength of the base sites increases with increasing Mg:Al ratio, as observed with the increasing CO_2 desorption temperatures seen in section 3.2.1.7. This supports the idea that the hydroxide anions and surface Mg-OH bonds show increased basicity with increasing Mg:Al ratio, due to the decrease in the charge density of the hydrotalcite layers.

There is also an enhanced selectivity towards the FAME product with increasing Mg:Al ratio. As the TOF increases, successive transesterifications from TAG to the intermediates DAG and MAG through to FAME will occur more quickly, so more complete transesterifications to the FAME product will occur, increasing the selectivity to this product.

3.2.2.1.b Macroporous hydrotalcite series

The full series of macroporous hydrotalcites were tested in the transesterification of tributyrin. The triglyceride conversion profiles, intermediate and product formation profiles can be seen in **Figures 3.23-3.26**. The reaction data is presented in **Table 3.10**.

Table 3.10. Reaction data for the series of macroporous hydrotalcites as catalysts in the transesterification of tributyrin.

Mg:Al ratio	Initial rate / mmol g^{-1} min^{-1}	TOF / min^{-1}	TAG conversion after 24 h / %	FAME selectivity after 24 h / %
0.38:1	0.19 +/- 0.02	3.01	20.0 +/- 1.5	32 +/- 1.5
0.83:1	0.28 +/- 0.01	3.67	22.6 +/- 1.5	35 +/- 1.5
1.28:1	0.33 +/- 0.06	4.01	25.1 +/- 1.5	30 +/- 1.5
2.03:1	2.18 +/- 0.02	17.06	65.0 +/- 1.5	43.4 +/- 1.5

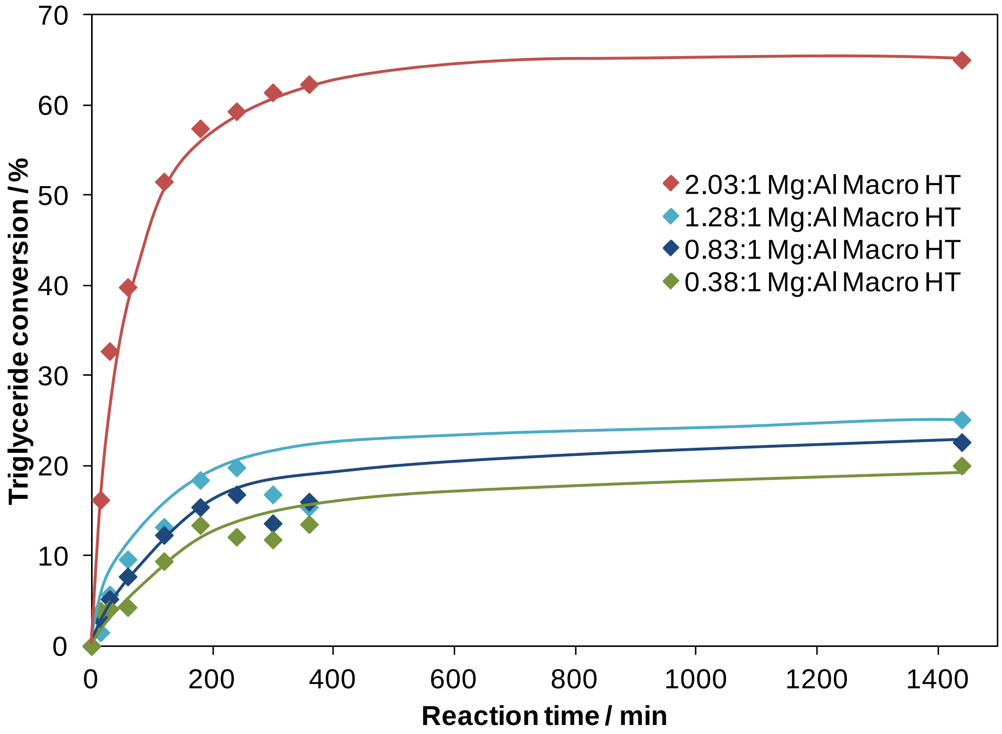

Figure 3.23. Reaction profiles showing tributyrin transesterification over time for the series of macroporous hydrotalcites.

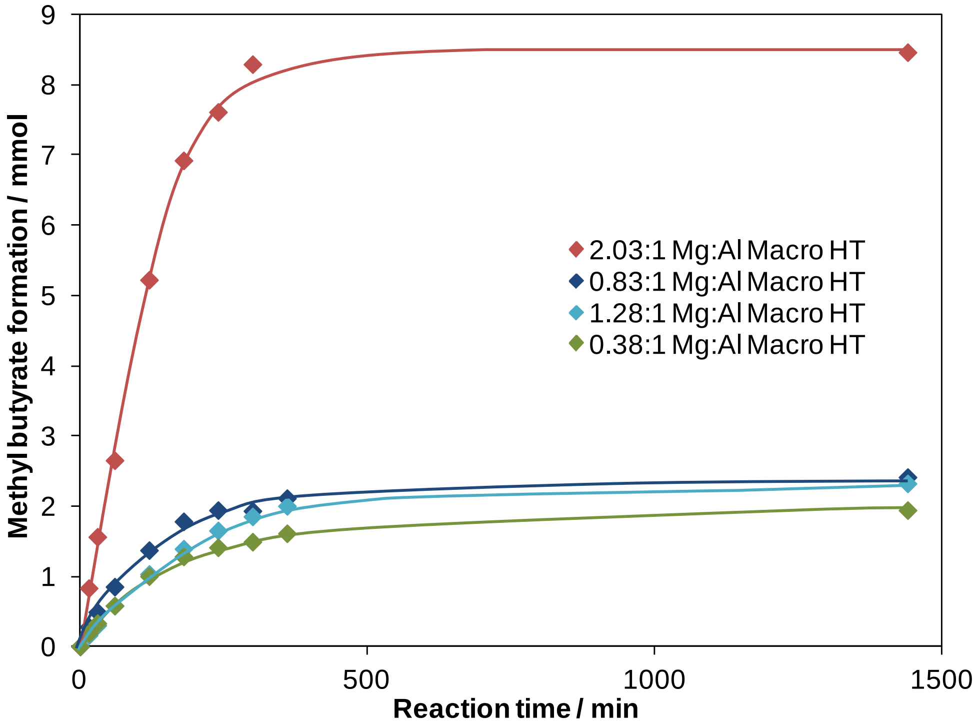

Figure 3.24. Methyl butyrate formation over time for the macroporous hydrotalcite series during the transesterification of tributyrin.

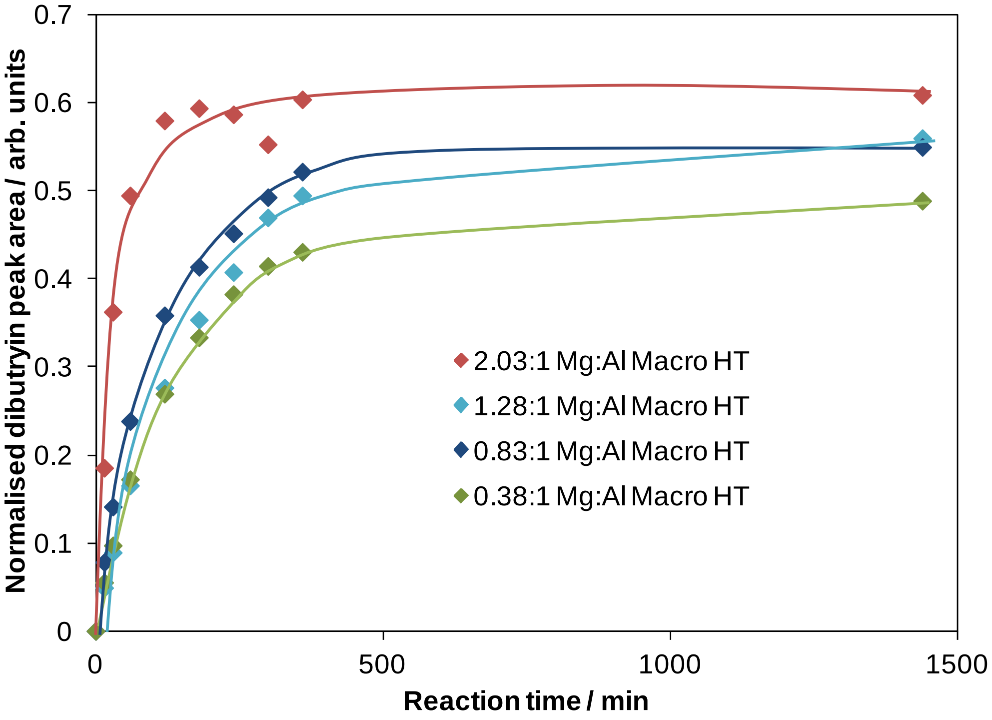

Figure 3.25. Intermediate dibutyrin formation over time for the macroporous hydrotalcite series during the transesterification of tributyrin.

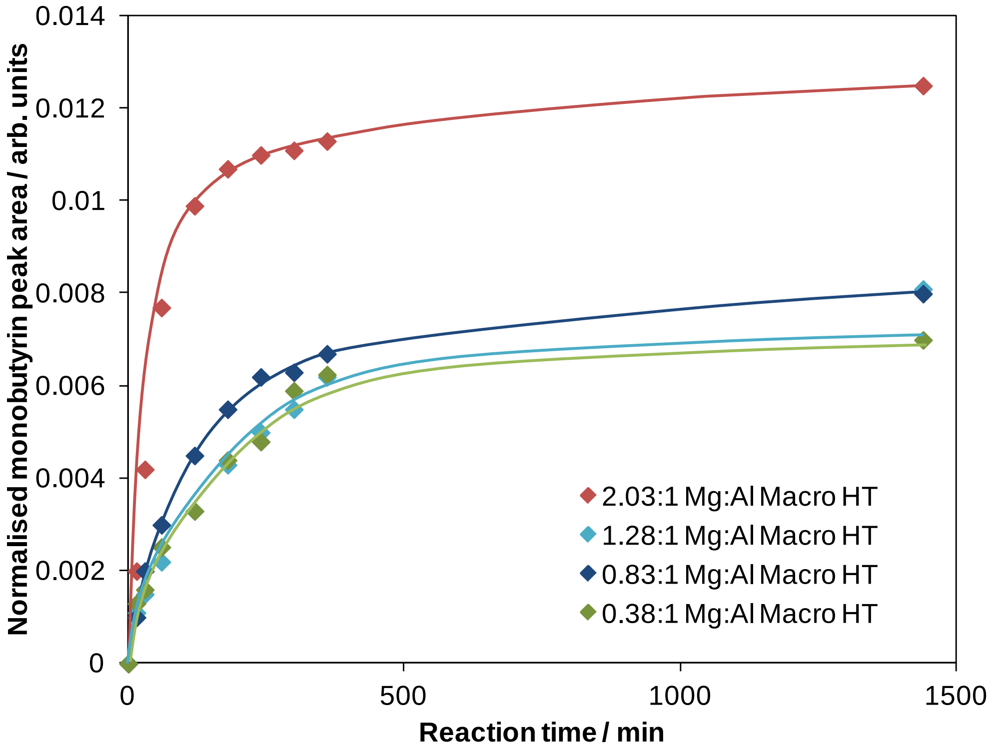

Figure 3.26. Intermediate monobutyrin formation over time for the series of macroporous hydrotalcites during the transesterification of tributyrin.

Again, a similar trend is seen on increasing Mg:Al ratio as for the conventional hydrotalcite series. There is an increase in initial rate due to the increase in total base sites, plus the increase in TOF due to the increase in base site strength, as discussed previously. The 2:1 Mg:Al macroHT vastly outperforms the rest of the catalyst series due to its greater crystallinity and more ordered structure, as well as greater base site strength.

3.2.2.1.c Comparison of convHT versus macroHT

The highest Mg loading samples convHT and macroHT were directly compared to examine the differences between conventional and macroporous hydrotalcites during the transesterification of tributyrin. **Figure 3.27** shows a comparison of the tributyrin conversion profiles, and methyl butyrate formation profiles. The reaction data is reported in **Table 3.11**.

Table 3.11. Reaction data for convHT and macroHT during the C4 transesterification reaction.

Catalyst	Initial rate / mmol g^{-1} min^{-1}	TOF / min^{-1}	TAG conversion after 24 h / %	FAME selectivity after 24 h / %
ConvHT	0.78 +/- 0.01	5.49	42.1 +/- 1.5	43 +/- 1.5
MacroHT	2.18 +/- 0.02	17.06	65.0 +/- 1.5	43 +/- 1.5

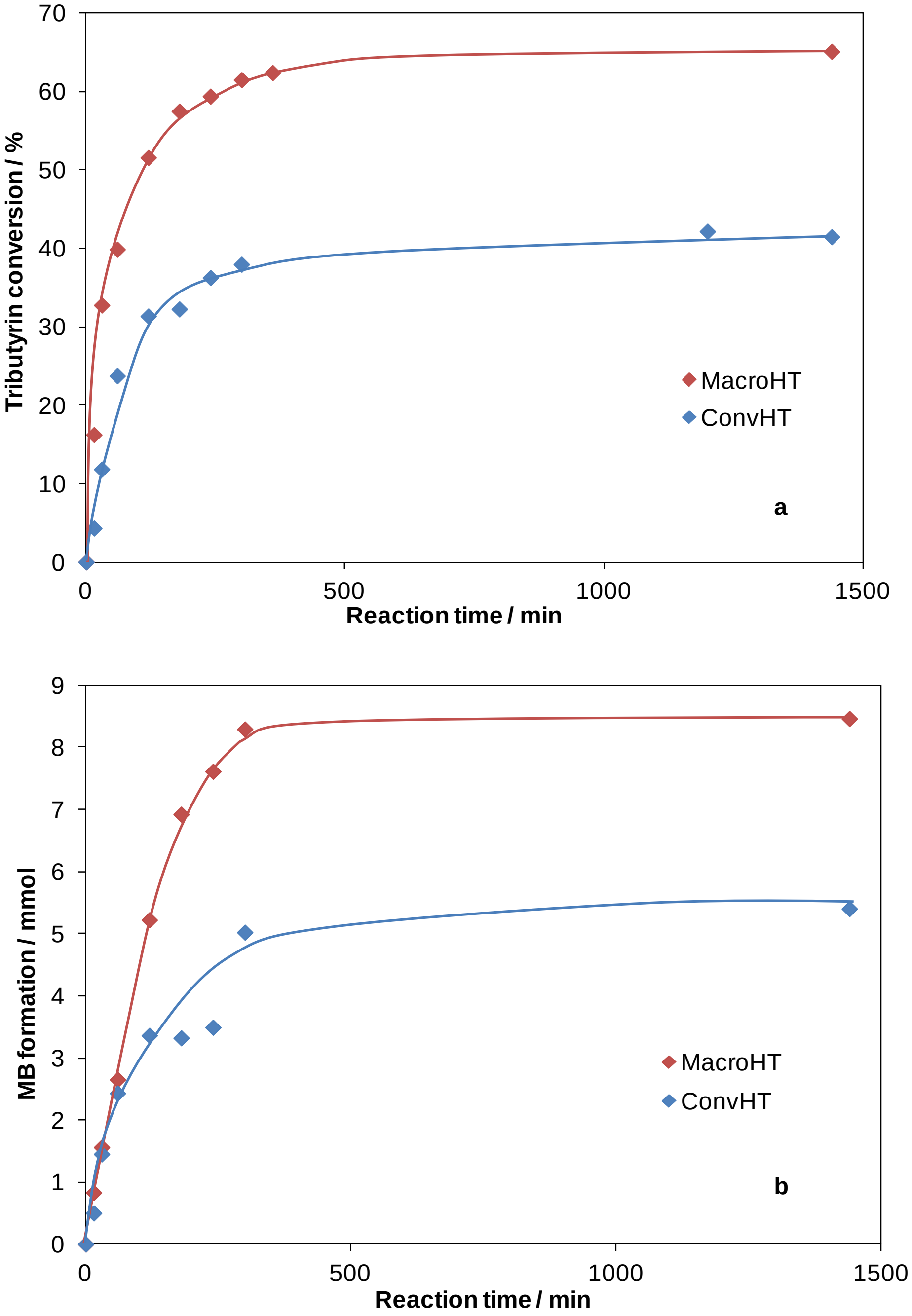

Figure 3.27. ConvHT versus macroHT for a) tributyrin conversion and b) methyl butyrate formation during the transesterification of tributyrin.

The macroHT outperforms the convHT, with a 3 fold enhancement in TOF. The macropores of the macroHT remove any diffusion limitations for the TAGs moving through the bulk catalyst to reach the active sites, as well as providing greater accessibility to the base sites found at the hydrotalcite crystallite edges. Although the C4 TAG is not very bulky, there will still be slow diffusion through the mesoporous voids in the bulk conventional hydrotalcite material to reach the base sites of the microporous crystallites. Therefore, TOF enhancement is obtained by the introduction of macropores to the hydrotalcite structure.

3.2.2.1.d Homogeneous catalyst comparative test

There are many well reported reasons why switching to heterogeneous catalysts over homogeneous catalysts is preferable, such as ease of separation of the catalyst from the biodiesel product, as well as catalyst reusability.[50,51] However, the activity of the homogeneous catalyst magnesium methoxide was compared to the convHT and macroHT catalysts in the transesterification of tributyrin as a control test.

A number of molecules of magnesium methoxide solution in methanol equivalent to the number of macroHT base sites was added in place of heterogeneous hydrotalcite in the tributyrin transesterification, and the triglyceride conversion plotted, as can be seen below in **Figure 3.28.**

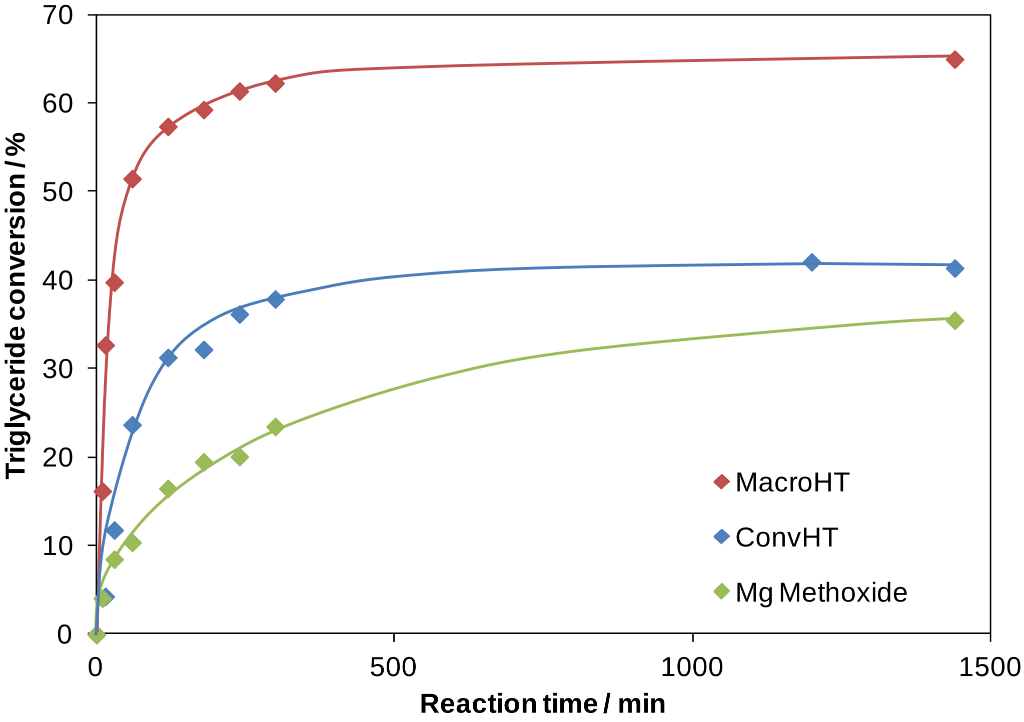

Figure 3.28. Tributyrin transesterification profiles comparing the homogeneous $Mg(OCH_3)_2$ catalyst to the most active 2:1 Mg:Al convHT and macroHT.

The initial rate for the transesterification with $Mg(OMe)_2$ as the catalyst is 0.4 mmol g^{-1} min^{-1}, twice as slow as the convHT initial rate, and giving a TOF value about half that of the convHT. This result shows that on gaining the benefits mentioned previously in the use of heterogeneous catalysts, the activity is also enhanced when using hydrotalcites compared to their homogenous counterparts. The difference in the results between these catalysts demonstrates that the hydrotalcites show true heterogeneous activity, with negligible Mg leaching, as can be observed through XPS analysis of the spent catalysts in section 3.2.3.2.

3.2.2.2 Tricaprylin transesterification (C8 chain TAG)

The tricaprylin transesterification reaction scheme is illustrated in **Figure 3.29**. This triglyceride has a C8 chain and so is bulkier and more viscous than the C4 triglyceride. The effect of this extra chain length was investigated by testing both series of materials in the transesterification of tricaprylin at 60 ºC using methanol as a solvent. Butanol was again added as a co-solvent to keep conditions constant throughout, although tricaprylin is soluble in methanol.

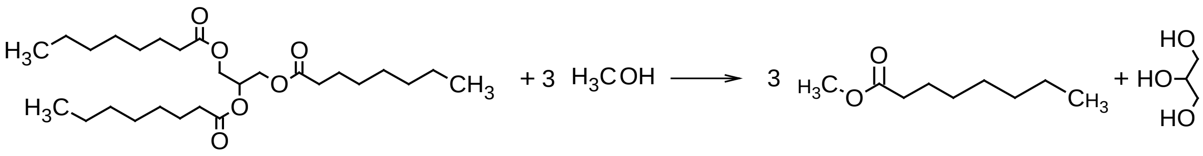

Figure 3.29. The tricaprylin transesterification reaction.

3.2.2.2.a Conventional hydrotalcite series

The tricaprylin conversion, methyl caprylate and intermediate formation profiles for the full series of conventional hydrotalcites can be seen in **Figures 3.30-3.33**. The reaction data is reported in **Table 3.12**.

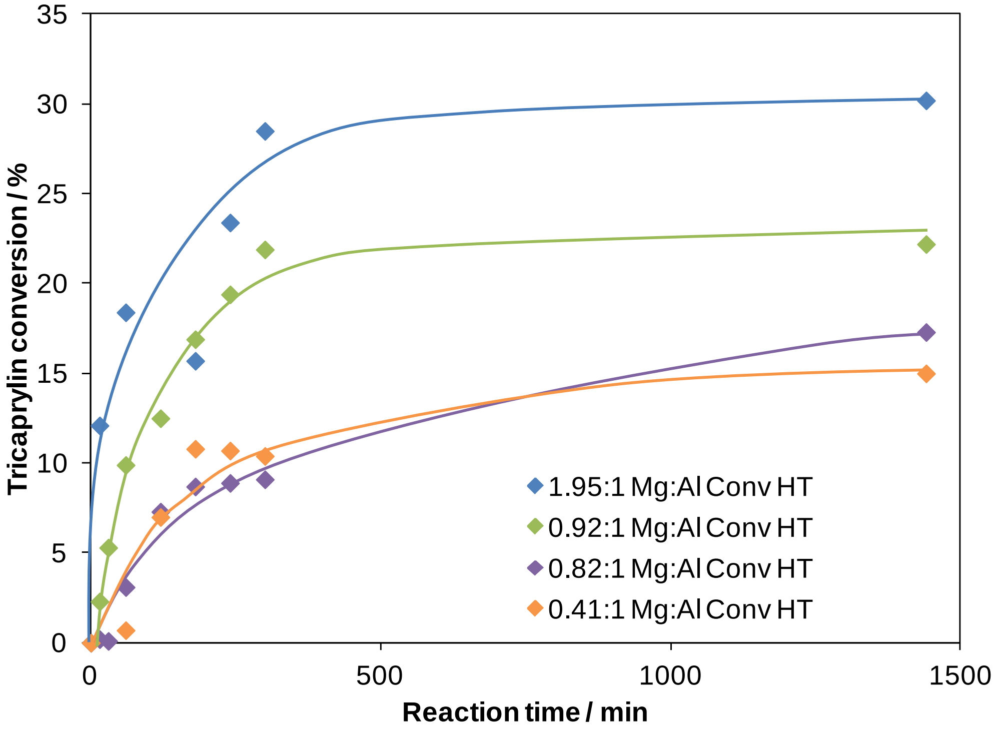

Figure 3.30. Reaction profiles showing tricaprylin transesterification over time for the series of conventional hydrotalcites.

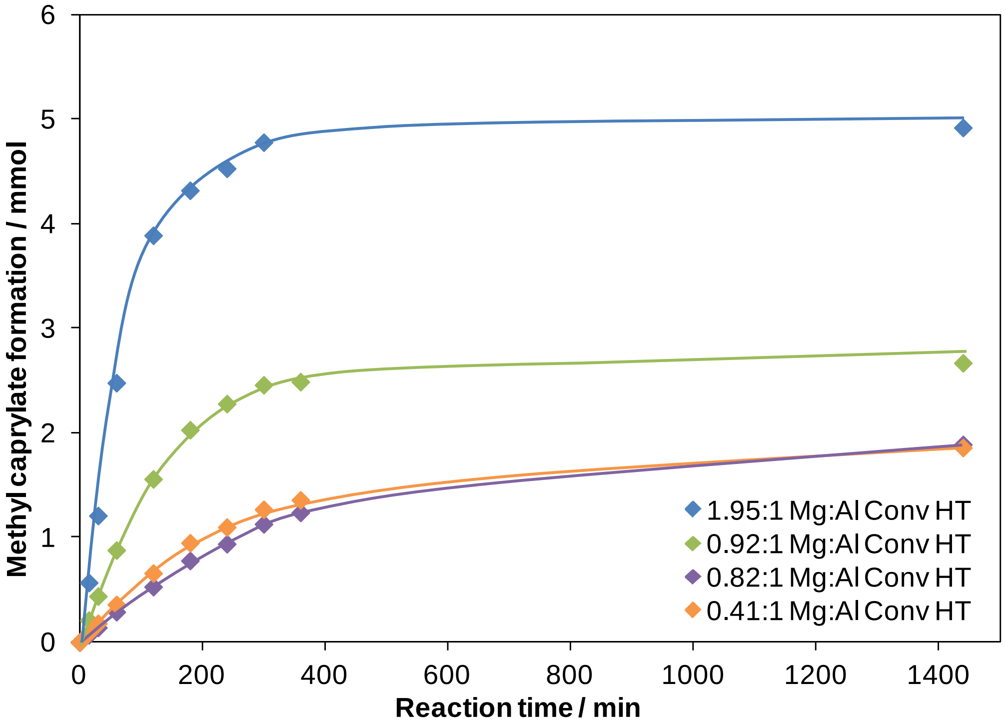

Figure 3.31. Methyl caprylate (MC) formation over time for the conventional hydrotalcite series during the transesterification of tricaprylin.

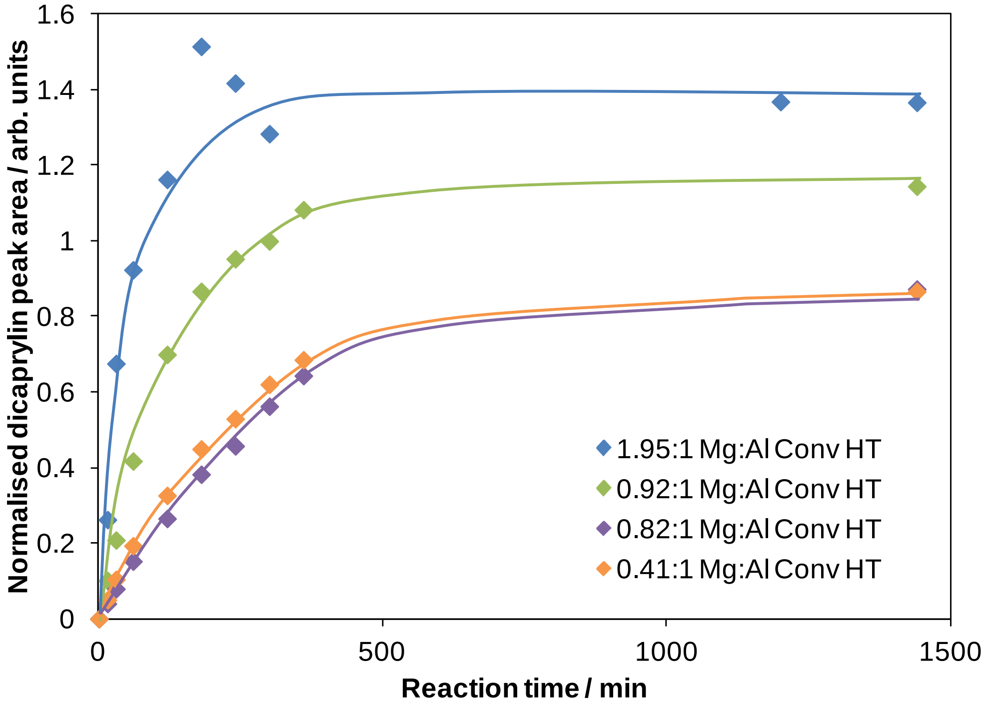

Figure 3.32. Intermediate dicaprylin formation over time for the conventional hydrotalcite series during the transesterification of tricaprylin.

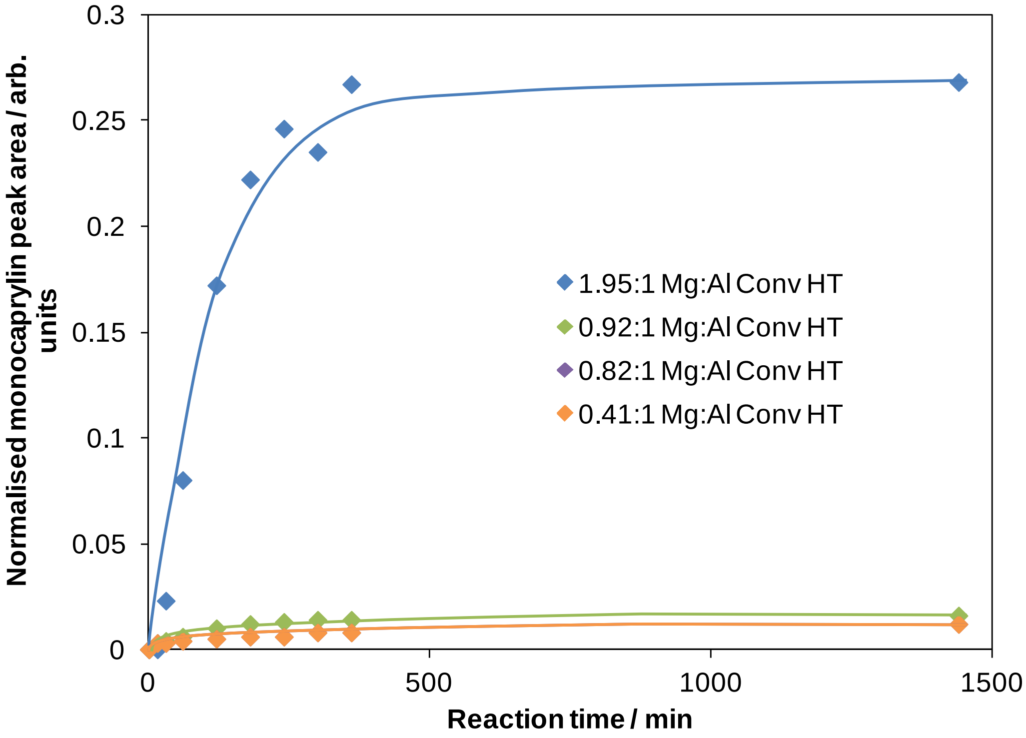

Figure 3.33. Intermediate monocaprylin formation over time for the series of conventional hydrotalcites during the transesterification of tricaprylin.

Table 3.12. Reaction data for the series of conventional hydrotalcites as catalysts in the transesterification of tricaprylin.

Mg:Al ratio	Initial rate / mmol g^{-1} min^{-1}	TOF/ min^{-1}	TAG conversion after 24 h / %	MC selectivity after 24 h / %
0.41:1	0.06 +/- 0.02	0.89	15.3 +/- 1.5	40.6 +/- 1.5
0.82:1	0.08 +/- 0.01	0.92	17.3 +/- 1.5	36.4 +/- 1.5
0.92:1	0.24 +/- 0.02	1.86	21.8 +/- 1.5	40.9 +/- 1.5
1.95:1	0.42 +/- 0.13	2.98	30.2 +/- 1.5	54.3 +/- 1.5

Again, the trend of increasing initial rate and TOF values with increasing Mg:Al ratio can be seen across the series. However, in this case the initial rate values are, on average, twice as slow as those for the C4 transesterification, due to slower diffusion of the bulkier TAG molecules through the bulk to the hydrotalcite active sites.

3.2.2.2.b Macroporous hydrotalcite series

The tricaprylin conversion, methyl caprylate and intermediate formation profiles for the full series of macroporous hydrotalcites can be seen in **Figures 3.34-3.37**. The reaction data is reported in **Table 3.13**.

Table 3.13. Reaction data for the series of macroporous hydrotalcites as catalysts in the transesterification of tricaprylin.

Mg:Al ratio	Initial rate / mmol g^{-1} min^{-1}	TOF / min^{-1}	TAG conversion after 24 h / %	MC selectivity after 24 h / %
0.38:1	0.10 +/- 0.004	1.62	19.5 +/- 1.5	34.8 +/- 1.5
0.83:1	0.13 +/- 0.01	1.73	21 +/- 1.5	35.5 +/- 1.5
1.28:1	0.23 +/- 0.02	2.78	29.5 +/- 1.5	55.4 +/- 1.5
2.03:1	1.33 +/- 0.09	10.43	50.7 +/- 1.5	55.7 +/- 1.5

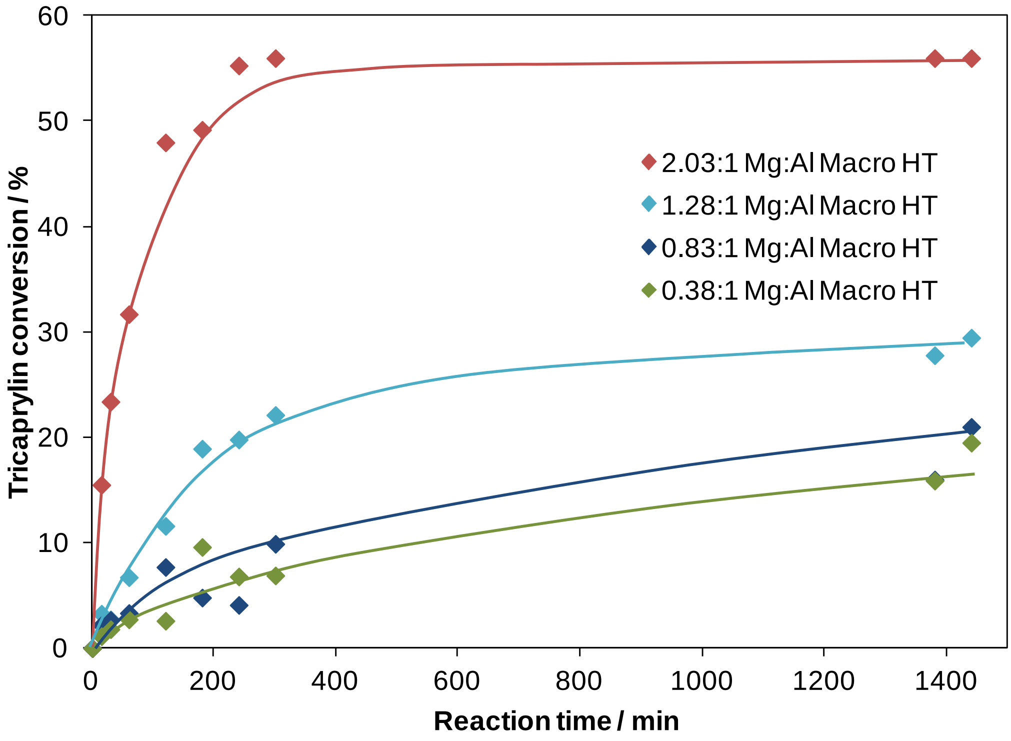

Figure 3.34. Reaction profiles showing tricaprylin transesterification over time for the series of macroporous hydrotalcites.

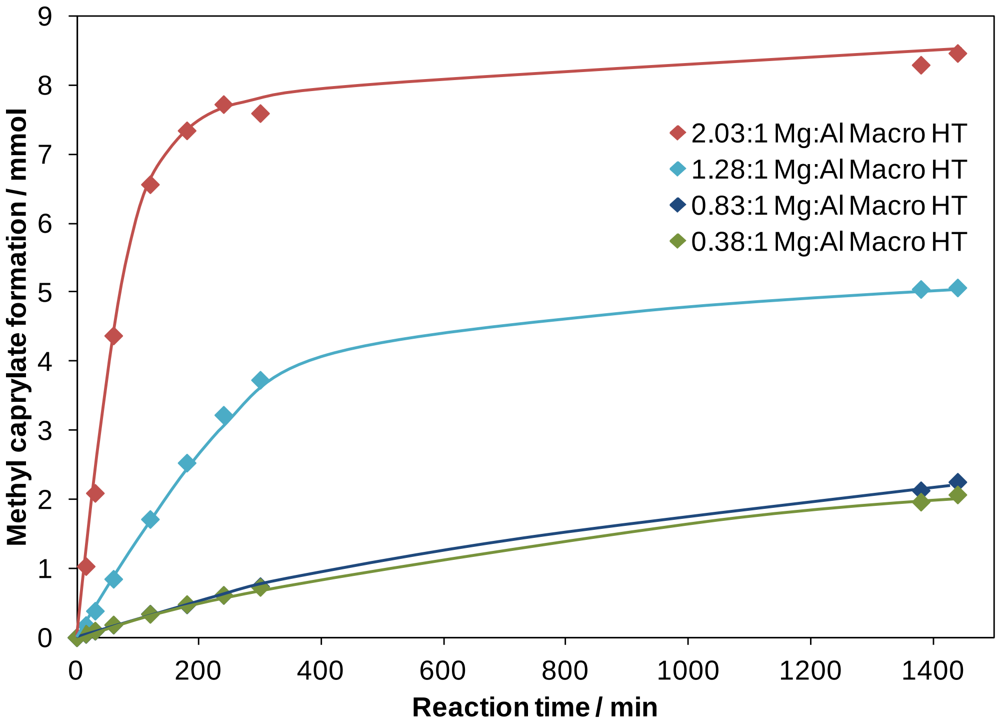

Figure 3.35. Methyl caprylate formation over time for the macroporous hydrotalcite series during the transesterification of tricaprylin.

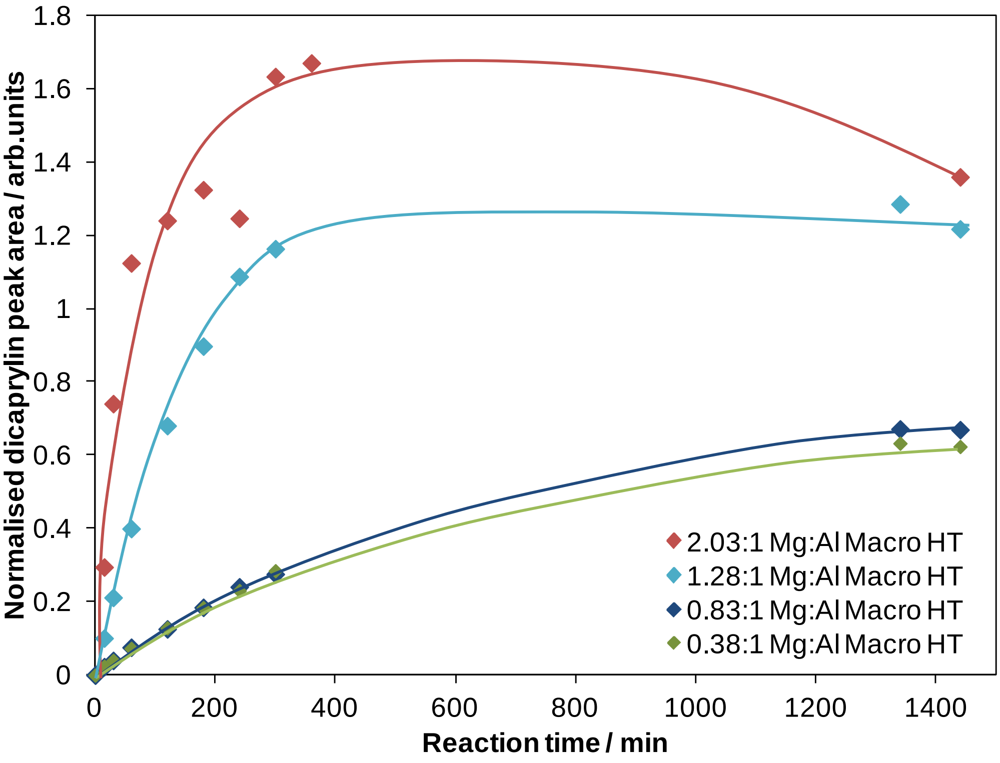

Figure 3.36. Intermediate dicaprylin formation over time for the macroporous hydrotalcite series during the transesterification of tricaprylin.

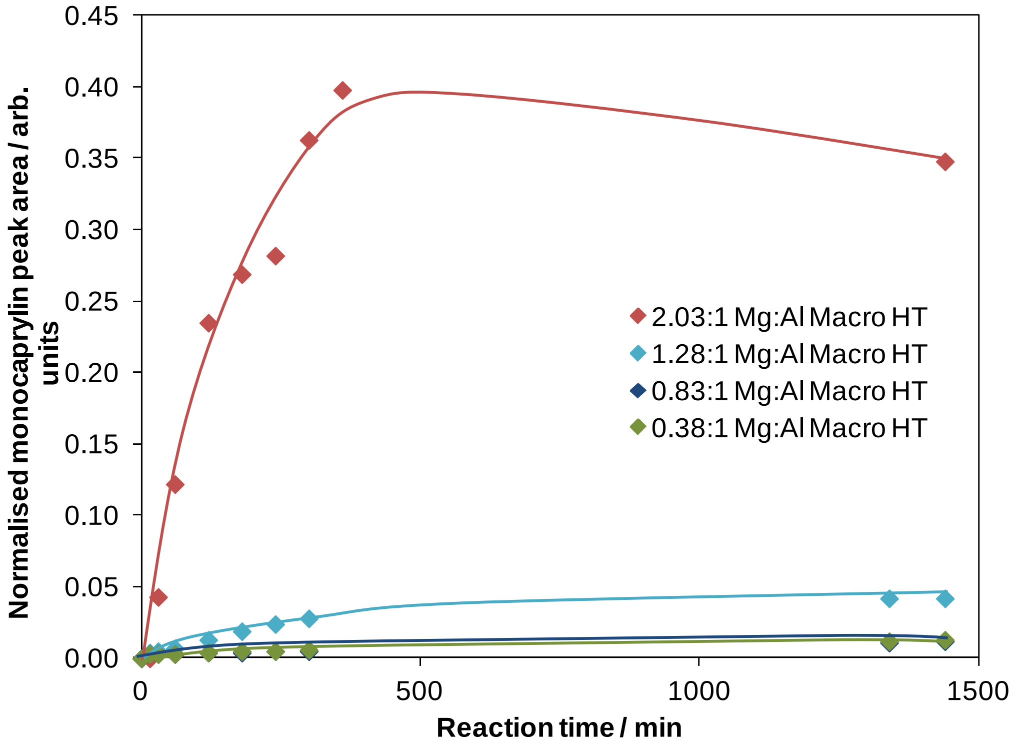

Figure 3.37. Intermediate monocaprylin formation over time for the series of macroporous hydrotalcites during the transesterification of tricaprylin.

The selectivity of the macroHT sample is high enough that before 24 hours of reaction has been completed the amount of the intermediates dicaprylin and monocaprylin reach a peak and start to decrease, as these intermediates themselves are converted to the methyl caprylate FAME product. This is not observed in any of the other, slower reaction profiles.

As seen for the conventional hydrotalcite series, the initial rate values have decreased on moving from the C4 TAG to the C8 TAG due to the slower movement and decreased solubility in methanol of the bulkier molecule and therefore slower rate of reaction.
The previously discussed trend of increasing initial rates and TOF values with increasing Mg:Al ratios is still observed for the macroporous series during this reaction.

3.2.2.2.c Comparison of convHT versus macroHT

The reaction and product formation profiles comparing convHT and macroHT for the C8 transesterification reaction can be seen in **Figure 3.38**. The reaction data is reported in **Table 3.14**.

Table 3.14. Reaction data for stoichiometric convHT versus macroHT in the transesterification of tricaprylin.

Catalyst	Initial rate / mmol g^{-1} min^{-1}	TOF / min^{-1}	TAG conversion after 24 h / %	FAME selectivity after 24 h / %
ConvHT	0.42 +/- 0.13	2.98	30.2 +/- 1.5	54.3 +/- 1.5
MacroHT	1.33 +/- 0.09	10.43	50.7 +/- 1.5	55.7 +/- 1.5

On moving to a bulkier, C8 chain length triglyceride, there is a greater benefit of incorporating macropores into the hydrotalcite structure to aid diffusion of the bulky TAG molecules to the hydrotalcite active sites, with a 3.5 times TOF enhancement when the macroHT is tested in the C8 transesterification compared to the convHT, slightly higher than for the C4 reaction. The enhancement in TOF comes without loss of FAME selectivity and with improved conversion.

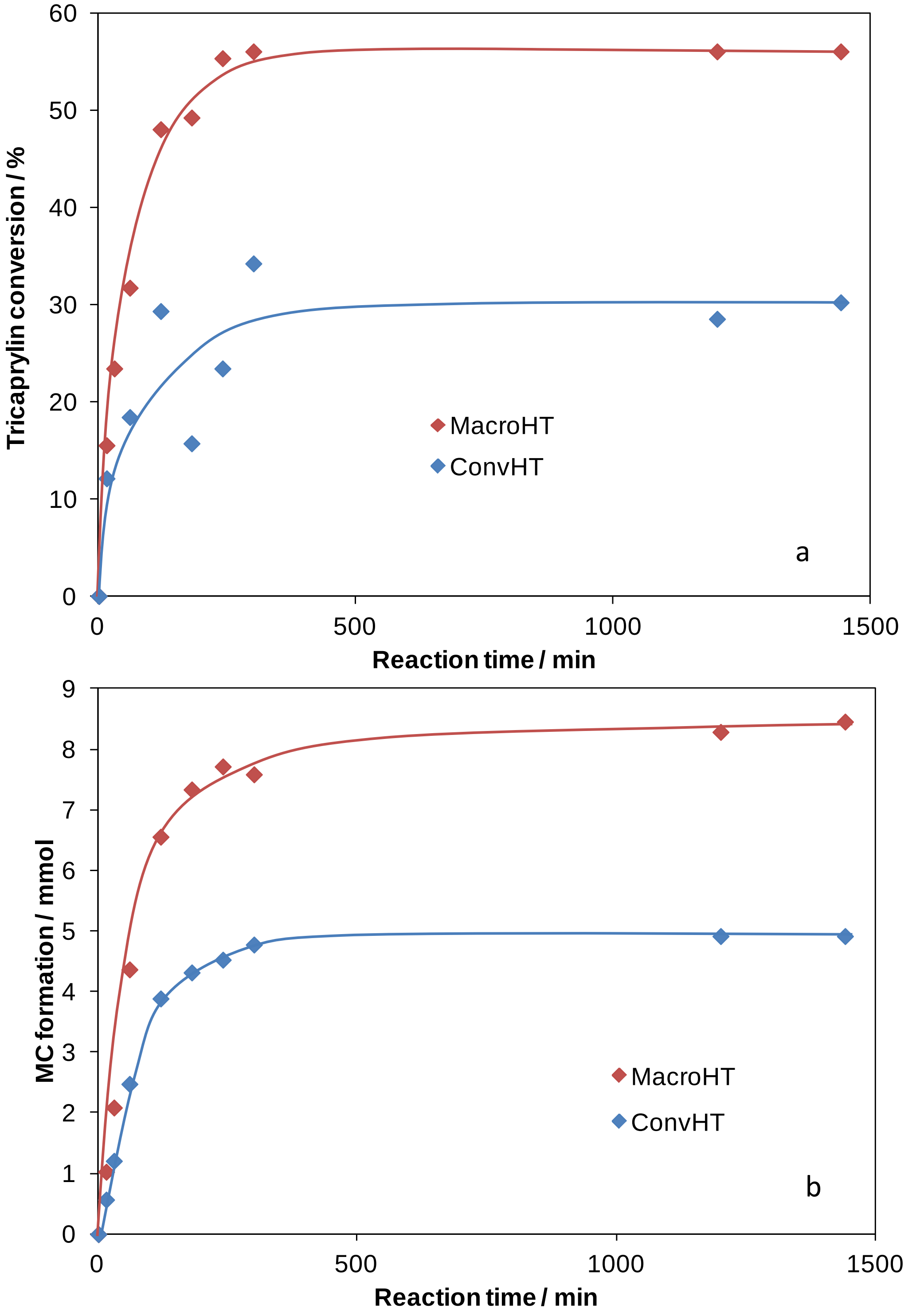

Figure 3.38. ConvHT versus macroHT for a) tricaprylin conversion and b) methyl caprylate formation during the transesterification of tricaprylin.

3.2.2.3 Trilaurin transesterification (C12 chain TAG)

The relationship between increasing Mg:Al ratio and increasing catalytic activity across both series of materials has now been established. The lower Mg:Al ratio hydrotalcites in both series show poor conversions and slow initial rates due to their lack of basic sites and low crystallinity. Therefore, for the longer chained triglycerides, the reactions were carried out testing just the 2:1 Mg:Al ratio convHT and macroHT samples and comparing these two materials, as for these two catalysts enough conversion occurs to allow accurate initial rate values to be determined. It is at these longer chain lengths where the comparison between conventional and macroporous hydrotalcite should become most interesting.

Trilaurin is a C12 chain length triglyceride. The carbon chains are saturated, making them very immobile and therefore at room temperature trilaurin exists in solid form. The longer chained alcohol, butanol, is required as a co-solvent in this reaction to solubilise the trilaurin in methanol. **Figure 3.39** shows the structure of trilaurin.

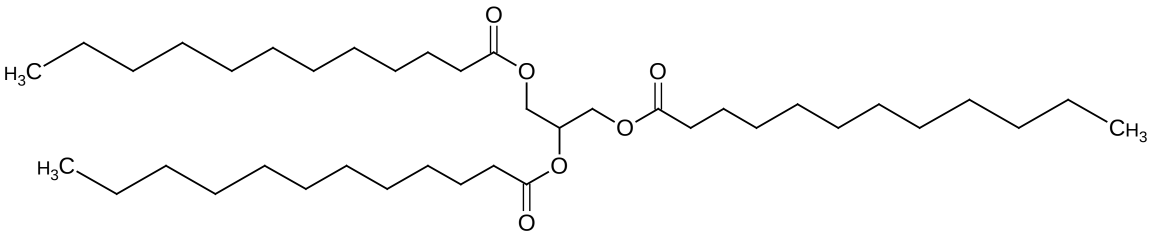

Figure 3.39. The C12 chain length triglyceride, trilaurin.

The reaction profiles, along with intermediate and product formation profiles for the trilaurin transesterification reaction testing convHT and macroHT can be seen in **Figures 3.40-3.43**. The reaction data is reported in **Table 3.15**.

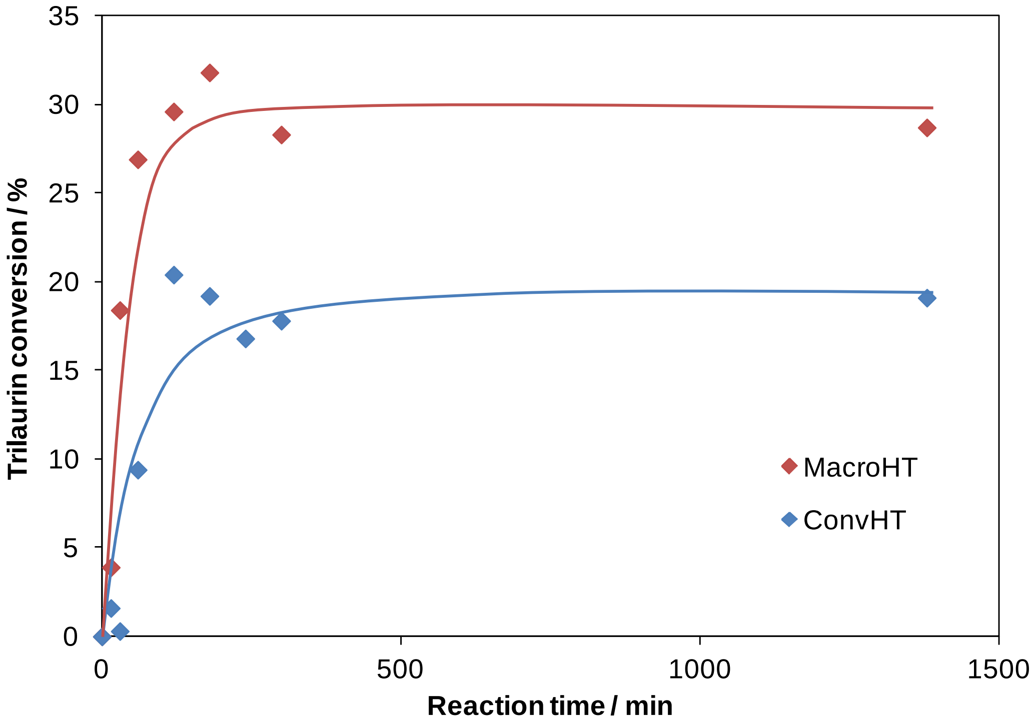

Figure 3.40. Reaction profiles showing trilaurin transesterification over time for convHT and macroHT.

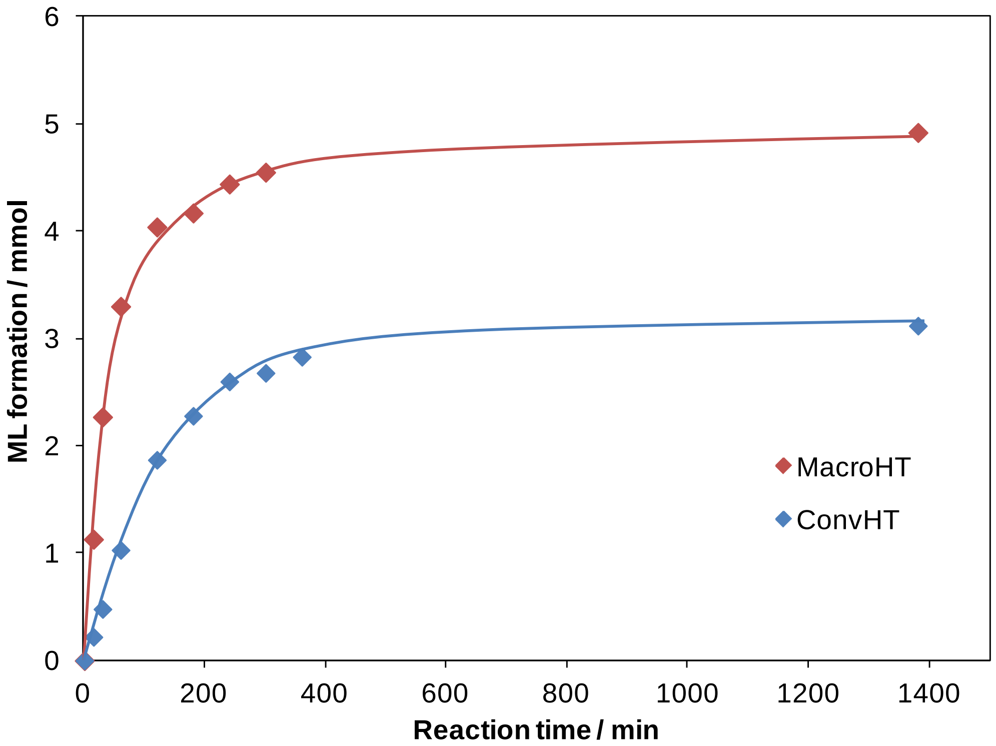

Figure 3.41. Methyl laurate formation over time for convHT and macroHT during the transesterification of trilaurin.

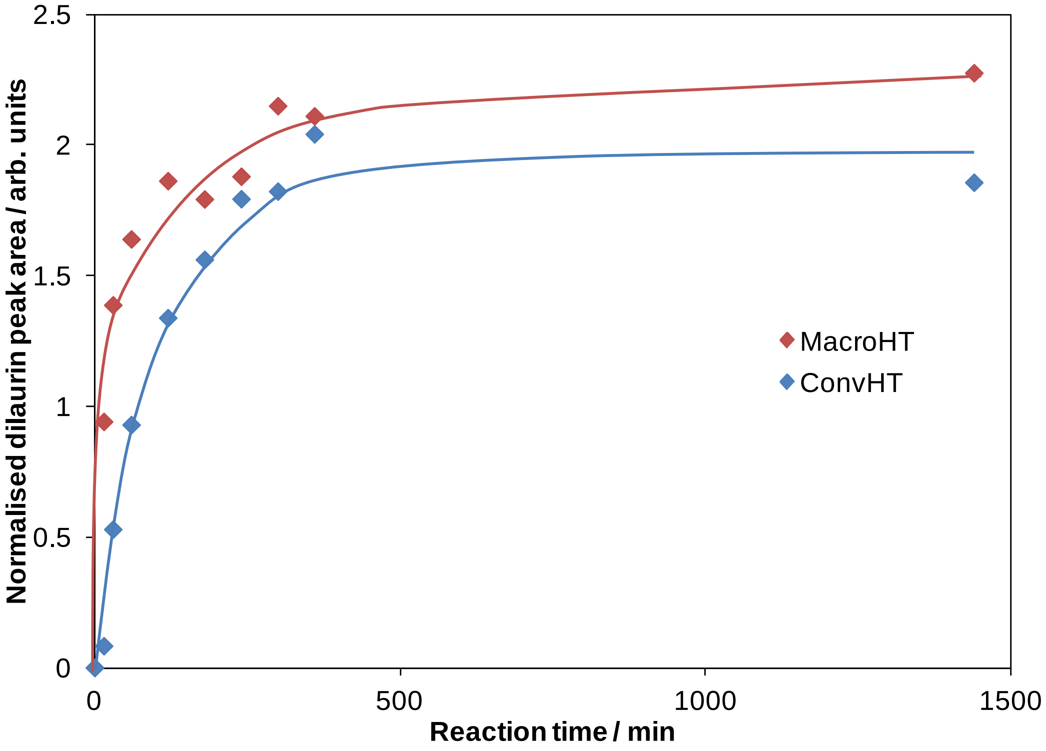

Figure 3.42. Intermediate dilaurin formation over time for convHT and macroHT during the transesterification of trilaurin

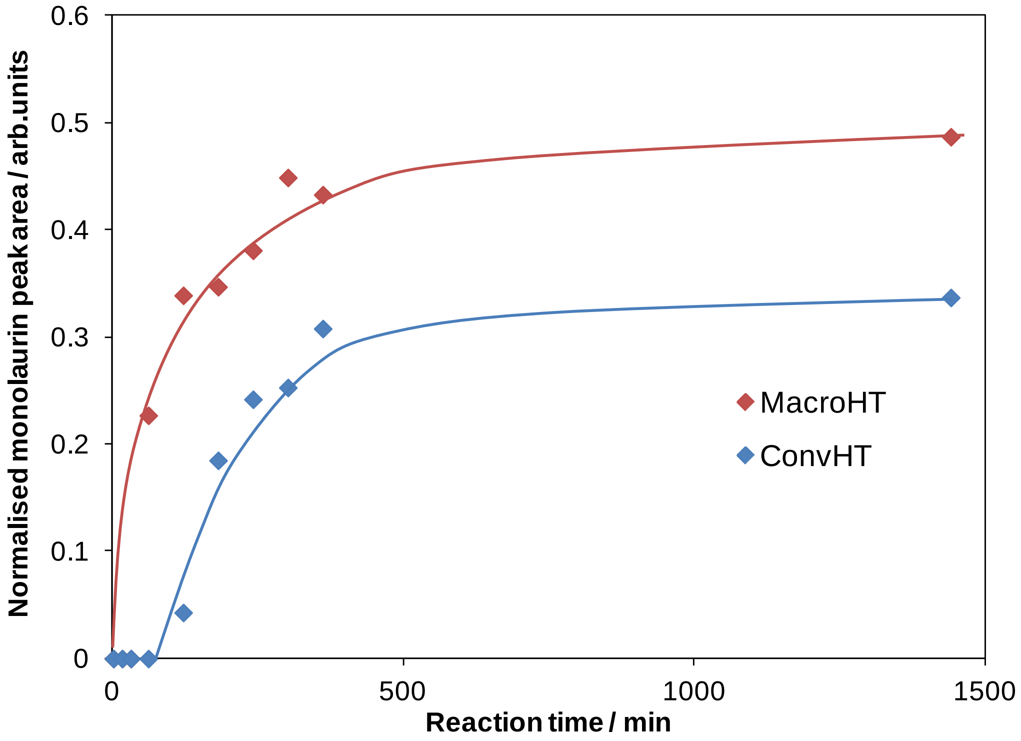

Figure 3.43. Intermediate monolaurin formation over time for convHT and macroHT during the transesterification of trilaurin.

Table 3.15. Reaction data for convHT versus macroHT in the transesterification of trilaurin.

Catalyst	Initial rate / mmol g^{-1} min^{-1}	TOF / min^{-1}	TAG conversion after 24 h / %	FAME selectivity after 24 h / %
ConvHT	0.26 +/- 0.05	1.83	19.1 +/- 1.5	54.5 +/- 1.5
MacroHT	0.94 +/- 0.07	7.37	28.7 +/- 1.5	57.2 +/- 1.5

On moving to this bulky, sterically hindered triglyceride, the macroHT shows a superior catalytic activity compared to the convHT, with a fourfold enhancement in TOF, greater than that seen during the C4 and C8 transesterifications. The overall rates and conversions are lower for both materials than seen for the shorter chain triglycerides, as the trilaurin is less soluble in methanol and moves more slowly, even without diffusion limitations within the catalyst.

3.2.2.4 Triolein transesterification (C18 chain TAG)

The convHT and macroHT samples were tested in the transesterification of glyceryl trioleate, a C18 chain length unsaturated triglyceride, the structure of which can be seen in **Figure 3.44**.

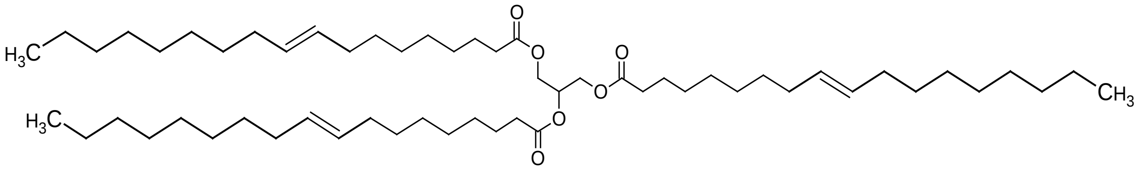

Figure 3.44. Structure of glyceryl trioleate.

The reaction profile and product formation profile for the C18 transesterification reaction can be seen in **Figure 3.45** and **Figure 3.46**. The reaction data is reported in **Table 3.16**.

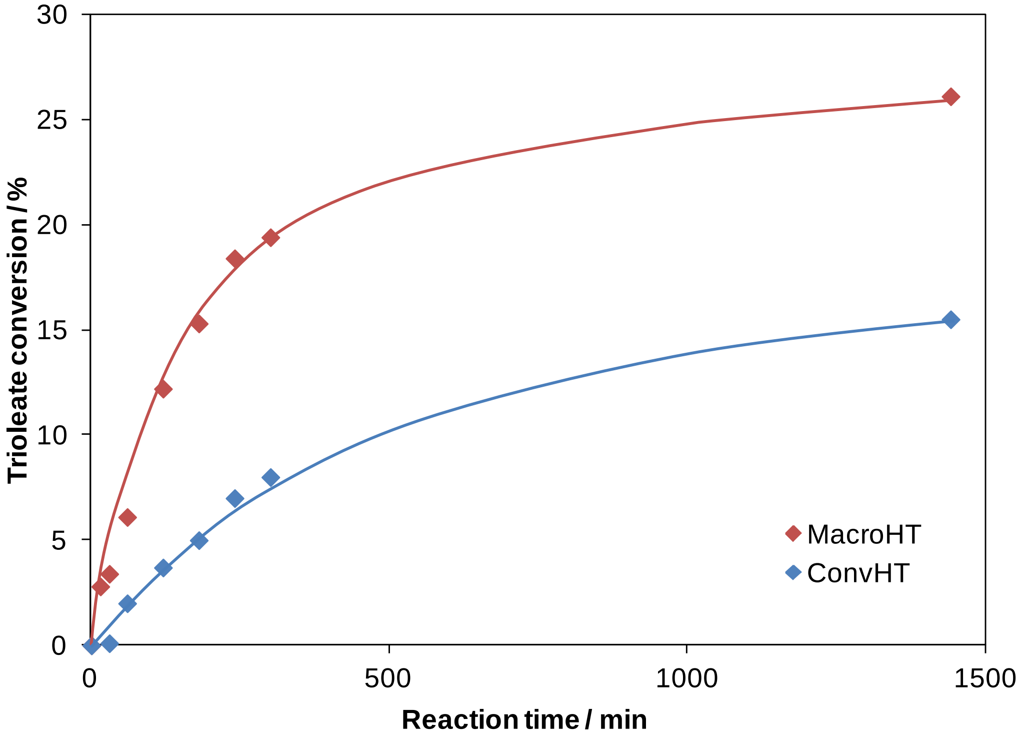

Figure 3.45. Reaction profiles showing triolein transesterification over time for convHT and macroHT.

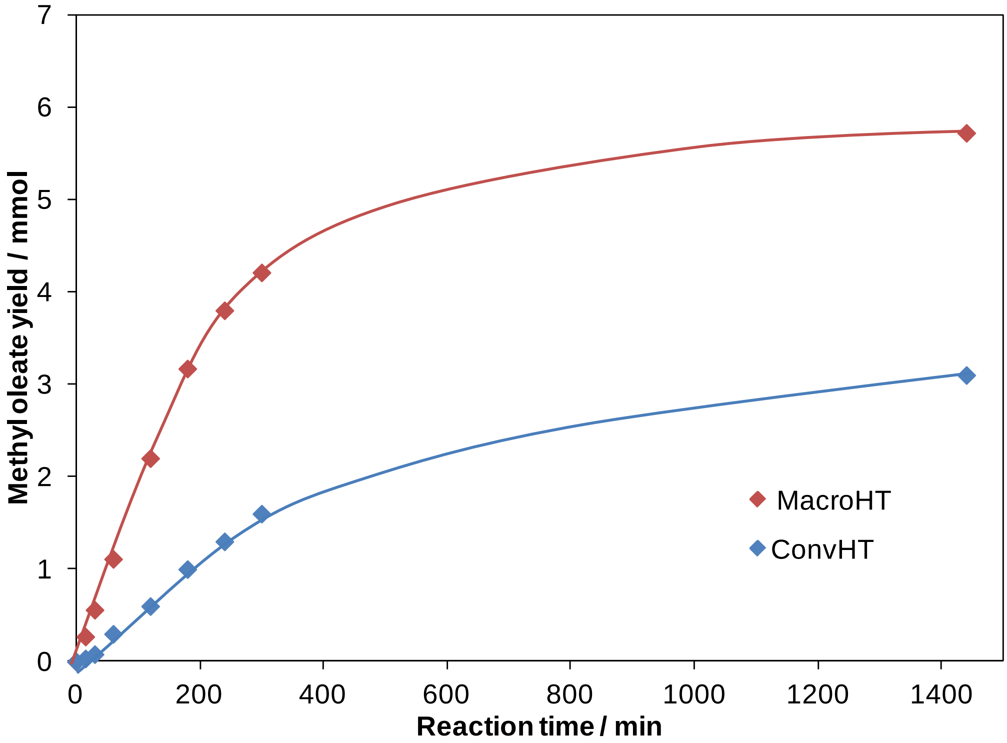

Figure 3.46. Methyl oleate formation over time for convHT and macroHT during the transesterification of triolein.

Table 3.16. Reaction data for convHT versus macroHT in the transesterification of triolein.

Catalyst	Initial rate / mmol g^{-1} min^{-1}	TOF / min^{-1}	TAG conversion after 24 h / %	FAME selectivity after 24 h / %
ConvHT	0.026 +/- 0.01	0.18	15.5 +/- 1.5	66.7 +/- 1.5
MacroHT	0.22 +/- 0.006	1.73	26.1 +/- 1.5	73.1 +/- 1.5

On moving to this, the bulkiest and most sterically hindered triglyceride, the macroHT shows a far superior catalytic activity than the convHT, with a greater than 9 fold enhancement in TOF. The benefit of the macropores is even greater with increased triglyceride chain length.

3.2.2.5 Olive oil transesterification

The convHT and macroHT samples were tested in the transesterification of olive oil, a real oil feedstock that can be used in the production of biodiesel.[52] There were two main peaks in the GC trace relating to triglycerides. The first peak was assigned to glyceryl trioleate, as the trace matched up with the triglyceride tested in the previous section, and this is the most prevalent constituent of olive oil. The second peak was assigned to the oleic-oleic-palmitic triglyceride (OOP), as this is reported to be the second major constituent of olive oil.[53] The structure of this triglyceride can be seen in **Figure 3.47**. The reaction profiles for conversion of both triglycerides can be seen in **Figure 3.48** and **Figure 3.49**. The formation of methyl oleate was also plotted and is shown in **Figure 3.50**. The reaction data is reported in **Table 3.17**.

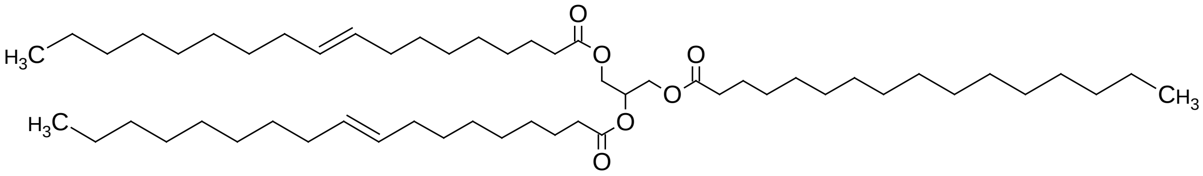

Figure 3.47. Structure of the triglyceride with oleic-oleic-palmitic (OOP) fatty acid components.

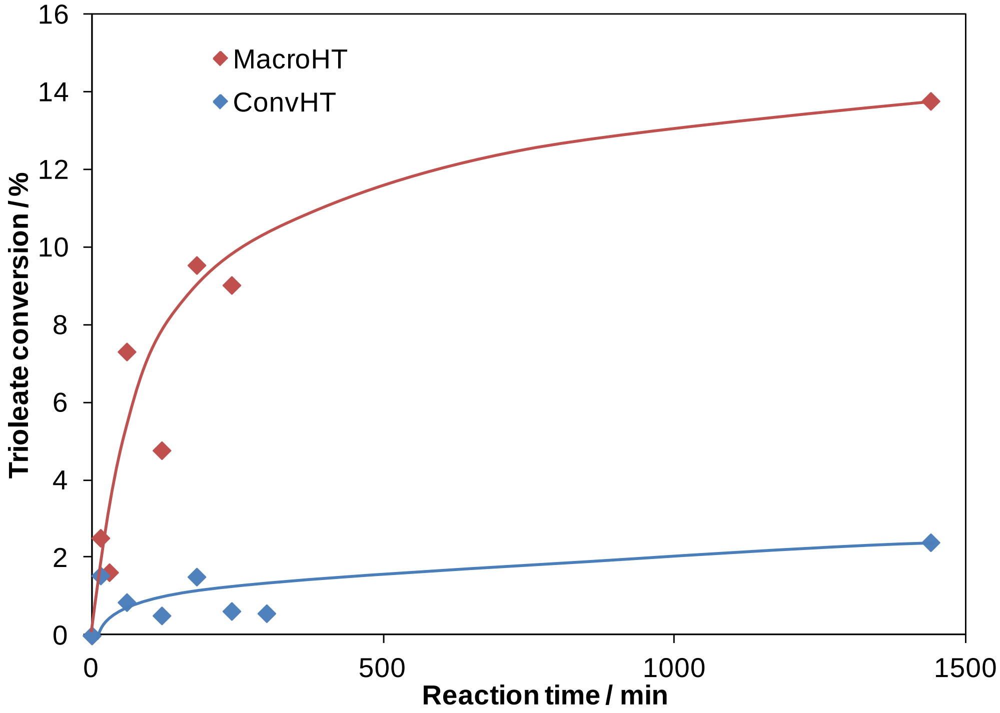

Figure 3.48. Reaction profiles showing triolein transesterification over time for convHT and macroHT during the transesterification of olive oil.

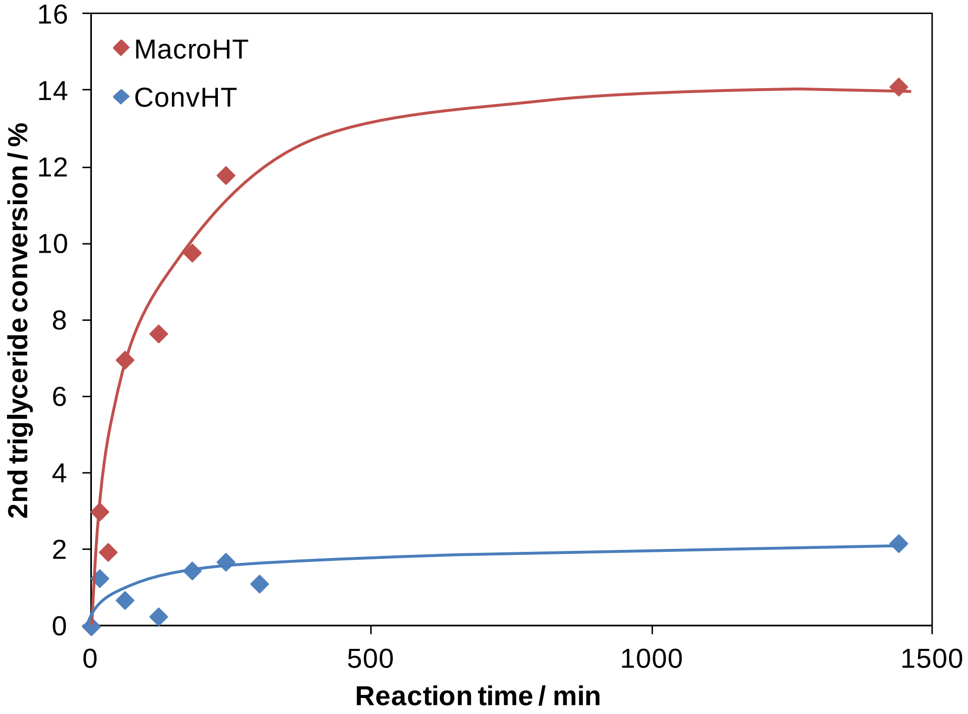

Figure 3.49. Profiles showing conversion of the OOP triglyceride for convHT and macroHT during the transesterification of olive oil.

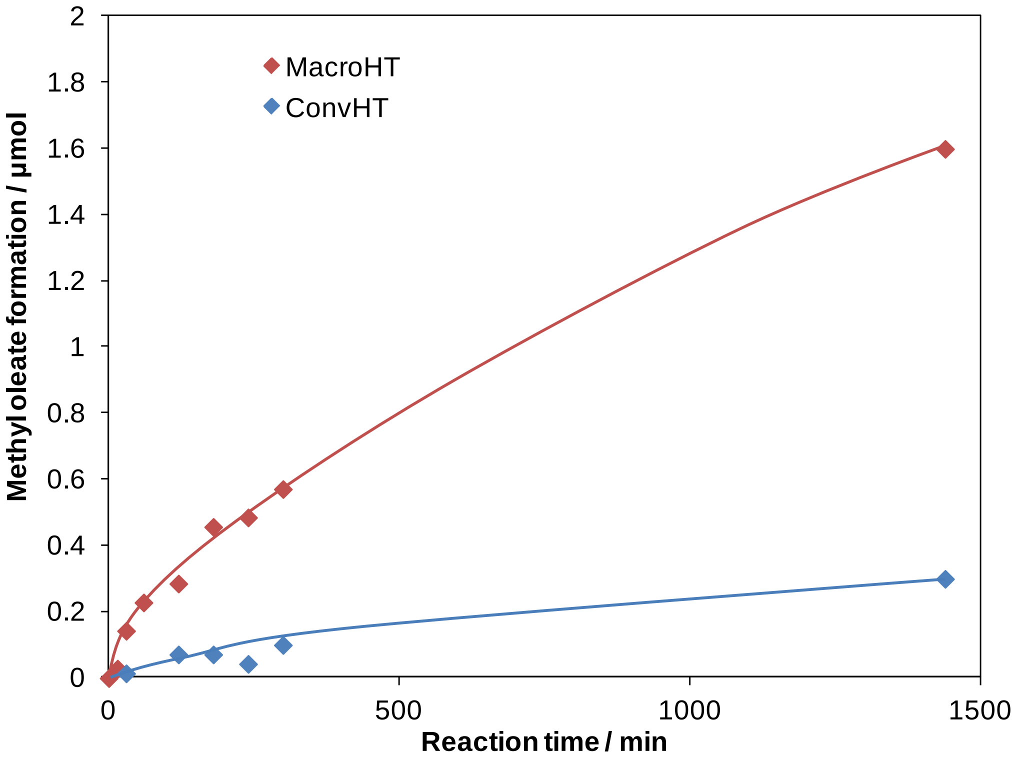

Figure 3.50. Methyl oleate formation over time for convHT and macroHT during the transesterification of olive oil.

Table 3.17. Reaction data for convHT versus macroHT in the transesterification of olive oil.

	ConvHT	MacroHT
Triolein conversion initial rate / mmol g^{-1} min^{-1}	0.012 +/- 0.0008	0.1 +/- 0.01
OOP triglyceride initial rate / mmol g^{-1} min^{-1}	0.01 +/- 0.0006	0.11 +/- 0.01
Overall initial rate / mmol g^{-1} min^{-1}	0.022 +/- 0.0014	0.222 +/- 0.02
TOF / min^{-1}	0.15	1.74
Triolein conversion after 24 h / %	2.4 +/- 1.5	13.8 +/- 1.5
OOP triglyceride conversion after 24 h / %	2.2 +/- 1.5	14.1 +/- 1.5

In the case of both catalysts, the initial rate is virtually identical for conversion of the two triglycerides. From observation of the two very similar structures this is to be expected, as although the palmitic acid component of the OOP triglyceride has a C16 chain length, it is saturated and therefore there will be little difference in the steric hindrance of the two triglycerides.

It has been proposed that the deactivation of hydrotalcites occurs via reaction of fatty acids, formed after ester hydrolysis, with the hydrotalcite base sites; generating, for example, butyric anions which then replace the hydroxide anions in the interlayer space.[49].This base site poisoning may occur more quickly during the transesterification of olive oil, due to the presence of free fatty acids in the oil feedstock. Therefore, the ability of the triglycerides within the oil to diffuse quickly through the macropores to reach a greater number of base sites will minimise the effect of the poisoning on the initial rates and result in a greater enhancement compared to the conventional hydrotalcite. This effect is observed in the results, as although the TOF values are very similar to those observed in the glyceryl trioleate transesterification, the macroHT TOF is now 11.6 times faster than that of the conventional hydrotalcite.

3.2.2.6 Comparison of TOF values for convHT and macroHT

Figure 3.51 shows the TOF enhancement via macroHT compared to convHT catalysts in the transesterification of TAGs, as well as olive oil, in methanol.

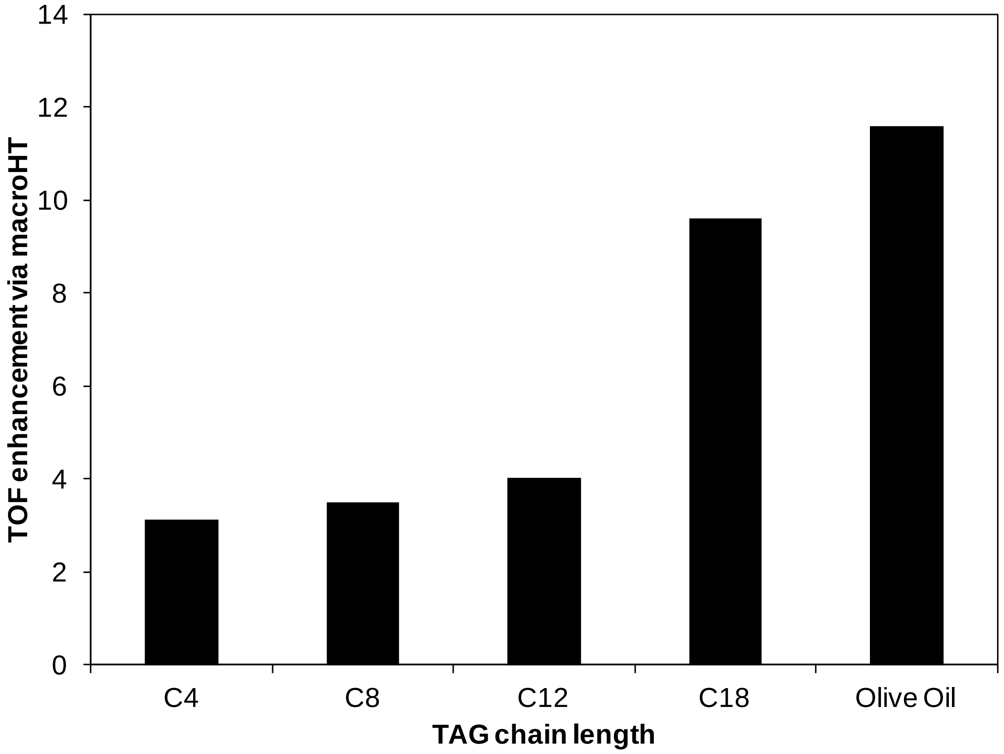

Figure 3.51. Ratio of macroHT: convHT TOF values in the transesterification of varying chain length triglycerides; showing increasing TOF enhancement via macroHT with increasing TAG chain length.

With increasing triglyceride size/bulk, there is a dramatic improvement in the macroHT performance over its conventional counterpart. This superior catalytic activity is attributed to a combination of direct and indirect effects associated with the macropores. In terms of a direct effect, macropores allow enhanced triglyceride mass-transport from the bulk reactant medium through macropore "super-highways" to hydrotalcite nanocrystallites. This rate enhancement increases as the chain length of the triglyceride increases. Therefore macropores provide significant benefits for the transesterification of long chain triglycerides that dominate real oil feedstocks, such as the olive oil example shown above. The Mg:Al ratio and basicity of the convHT and macroHT samples are comparable, and the exceptional rate enhancements only emerge upon changing the reactant size, and so there is no evidence to suggest different types of base site between the two materials. Therefore, the indirect effect of the macropores is as described earlier in the characterisation section; that macropores influence the catalyst preparation and eventual hydrotalcite architecture, by promoting the formation of a thin-walled mixed-metal oxide framework during calcination, and therefore increasing the micropore surface area in the rehydrated hydrotalcite and increasing the accessibility of the interlayer hydroxide anions once the TAG molecules have been more easily transported through the bulk to the hydrotalcite nanocrystallites.

Hierarchical macroporous-mesoporous solid acid architectures have been shown to promote tricaprylin and trioleate transesterification compared to their mesoporous analogue,[54] but the macroHT material reported here represents the first demonstration that such ideas can be extended to macroporous-microporous solid base catalysts.

An area that remains experimentally challenging is the determination of the relative accessibility of base sites of the convHT and macroHT to the different chain length triglycerides, as direct measurement of intrapore molecular diffusion coefficients is extremely difficult. The visualisation of meso versus macropore diffusion will remain an obstacle without further improvement in the spatial resolution of magnetic resonance imaging. Molecular dynamics simulation[55] and Monte-Carlo modelling[56] are offering a short term solution to quantifying mass transport versus reaction kinetics in the catalysis of viscous bio-oil mixtures, and are aiding the design of future porous solid acids and bases.

3.2.2.7 Triglyceride conversion versus FAME selectivity

FAME selectivity versus triglyceride conversion was plotted for all hydrotalcite catalysed reactions to examine whether or not a global pattern could be observed. The plot can be seen in **Figure 3.52.**

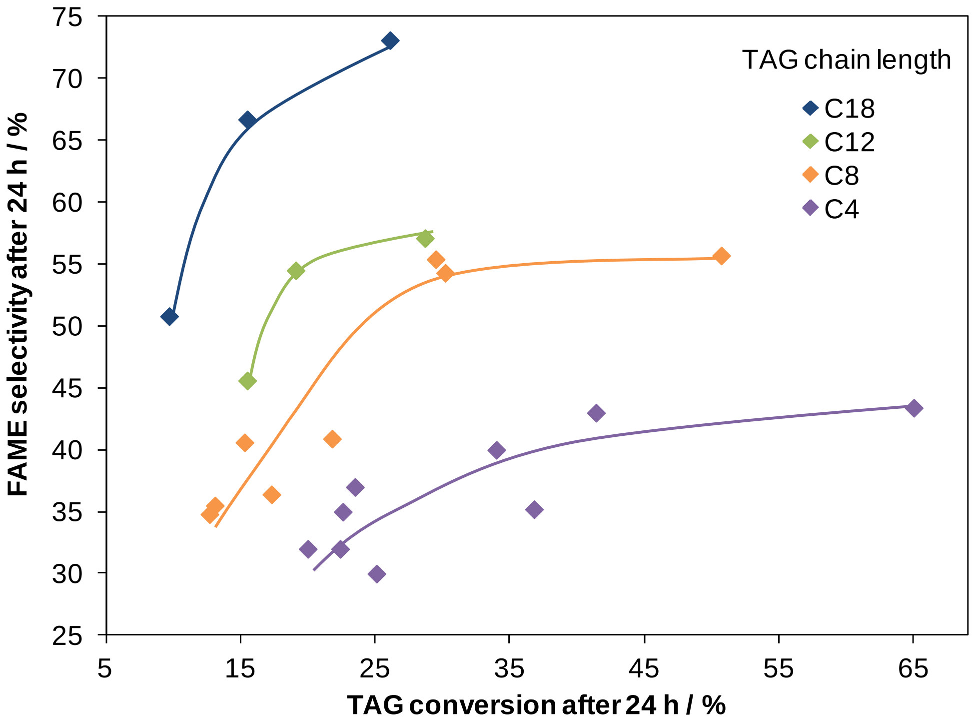

Figure 3.52. Plot showing FAME selectivity versus triglyceride conversion for all hydrotalcite catalysed reactions.

For each individual triglyceride, there is a global increase in selectivity with increase in percentage triglyceride conversion. This is what would be expected as the catalysts which give greater overall conversions also show faster initial rates, and so more TAG is converted to DAG and MAG more quickly, over 24 hours then these intermediates have more time to be converted all the way to FAME. The materials which give higher conversion also have a greater number of base sites, allowing more molecules to be converted over 24 hours, leading to a greater amount of FAME being produced. The lines of best fit start to level off above about 40 % conversion. At this stage, glycerol may be starting to block some of the active sites as the plots of conversion over time also tail off.

Interestingly, on moving to longer chained, bulkier TAGS, although overall conversions decrease, the selectivity to FAME increases. The DAG and MAG molecules will be less bulky than the TAG, so will move faster and react more quickly, as well as diffusing through the conventional hydrotalcites more quickly. This effect will become more noticeable on increasing TAG bulk. Therefore, as TAG chain length increases, for each TAG molecule converted a greater proportion of complete conversion to FAME occurs.

3.2.3 Reusability of convHT and macroHT catalysts

3.2.3.1 Recycling tests

The reusability of a catalyst is an important factor when determining how commercially viable or industrially useful it may be. To test the reusability of the convHT and macroHT samples a scaled up tributyrin transesterification was carried out under the same reaction conditions as in previous tests. After 24 hours, the catalysts were removed from the reaction mixture, washed with methanol and dried overnight in a vacuum oven at 40 ºC. The catalysts were then returned to a fresh reaction to observe how much activity had been retained. The reaction profiles for both the fresh and recycled catalysts can be seen in **Figure 3.53**.

On re-use after recovery from the initial reaction, neither the convHT nor macroHT show any activity in the transesterification of tributyrin. Deactivation of the hydrotalcite catalysts is assigned to a side hydrolysis reaction of the methyl butyrate over the hydrotalcites, forming butyric anions which replace the hydroxide anions in the interlayer space and expand the interlayer distance.[49] This would explain why the reaction profiles all plateau off after about 500 minutes, as all of the accessible hydroxide anions have been replaced by butyric anions.

It may be possible to increase the reusability of the catalysts by introducing a double washing, with both methanol and an apolar solvent, to remove any apolar compounds retained in the catalyst.

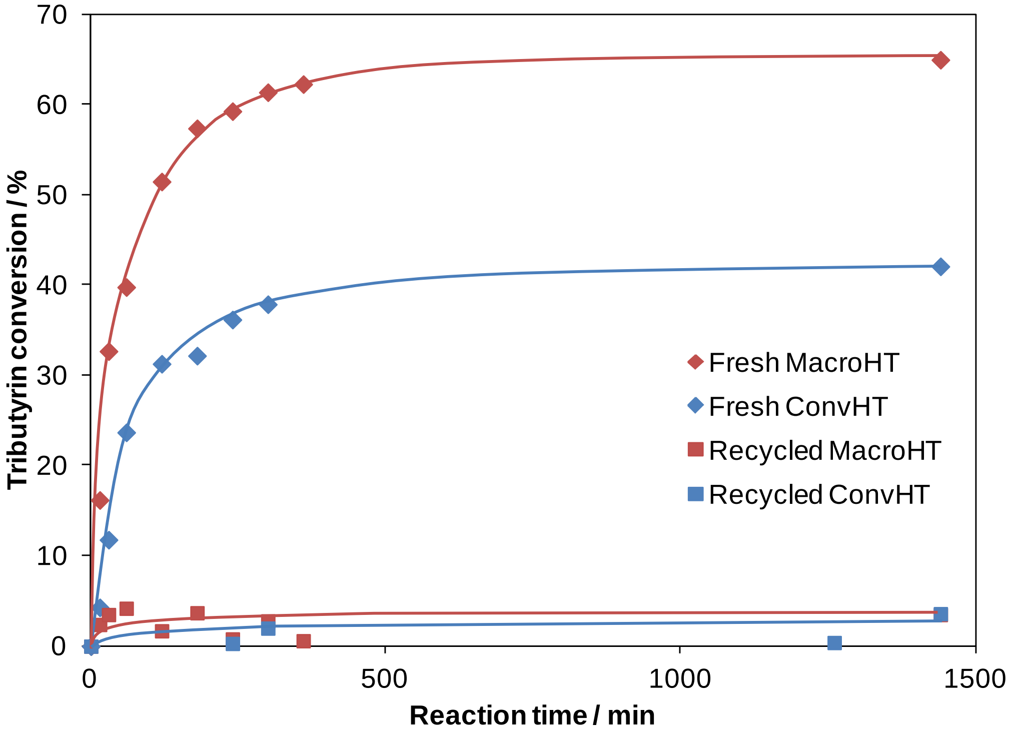

Figure 3.53. Reaction profiles showing triglyceride conversion for both fresh and recycled convHT and macroHT in the transesterification of tributyrin.

3.2.3.2 XPS analysis of spent catalysts

XPS analysis was carried out on the catalysts recovered after 24 hours of tributyrin transesterification, but before any reactivation. The C 1s chemical environments can be seen in **Figure 3.54** and **Figure 3.55**. The XPS data obtained compared to the fresh materials can be observed in **Table 3.18**.

Table 3.18. Surface Mg:Al ratios for spent versus fresh convHT and macroHT.

Sample	**Mg:Al Ratio**	**Carbonate / atomic %**	**Organic carbon component / atomic %**
ConvHT Fresh	1.93	5.37	0
ConvHT Spent	1.74	16.38	15.14
MacroHT Fresh	2.12	5.21	0
Macro HT Spent	2.24	5.19	5.13

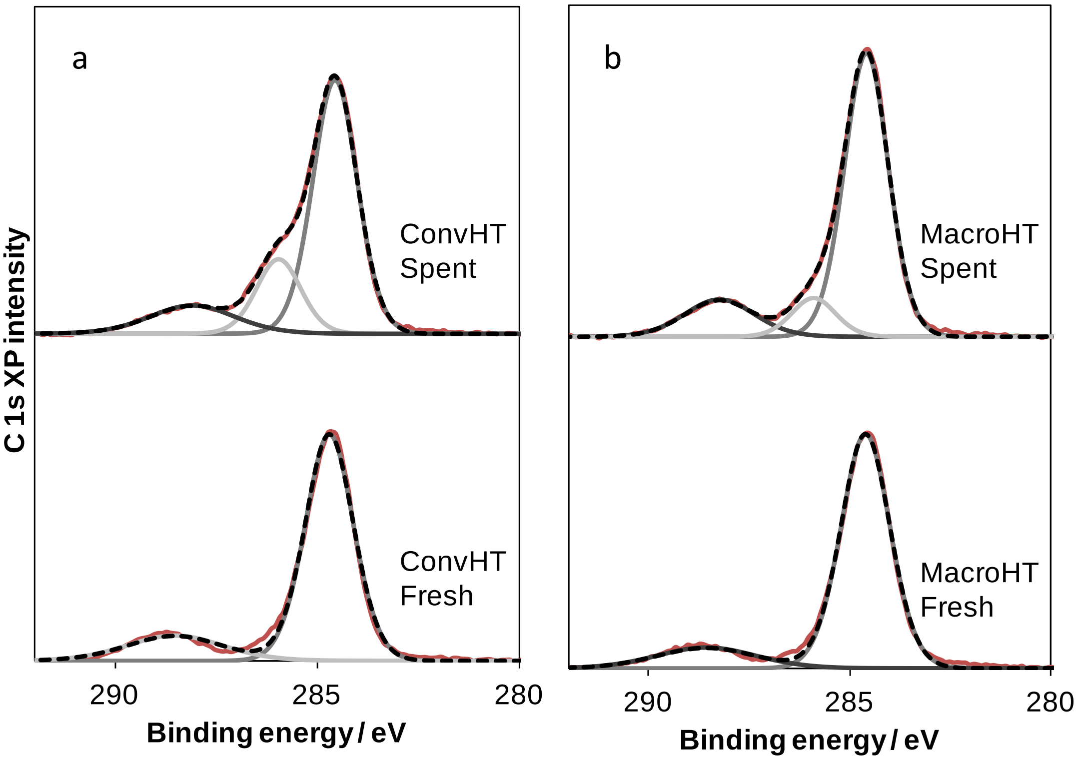

Figure 3.54. XP spectra showing the C 1s chemical environments for a) fresh and spent convHT and b) fresh and spent macroHT.

XPS analysis of the C 1s regions for both convHT and macroHT samples show the appearance of a new carbon species after recovery from the transesterification reaction at binding energy 285.5 eV. This is assigned to the presence of organic material bound to the active sites.[57] There is a smaller overall atomic percentage of organic content bound to the macroHT after reaction, however the introduction of 5.13 at% organic carbon is still enough to cause total deactivation, as seen for the convHT, due to butyric acid binding to all of the available active sites. The extra spent carbon content seen for convHT will be most likely due to the bulky TAG molecules, intermediates and glycerol diffusing slowly through the material and becoming trapped within the micropores due to the lack of macropore super highways.

The Mg:Al ratios are similar for both the fresh and spent hydrotalcites, so there is no significant metal leaching during the reaction.

3.2.3.3 Catalyst tests on the recycled-reactivated hydrotalcite samples

The recovered materials were re-calcined and the rehydration procedure repeated in an attempt to reactivate the convHT and macroHT samples. The reactivated and recycled catalyst reaction profiles compared to fresh can be seen below in **Figure 3.55**. **Table 3.19** reports on the reaction data for the recycled-reactivated convHT and macroHT samples compared to the fresh materials.

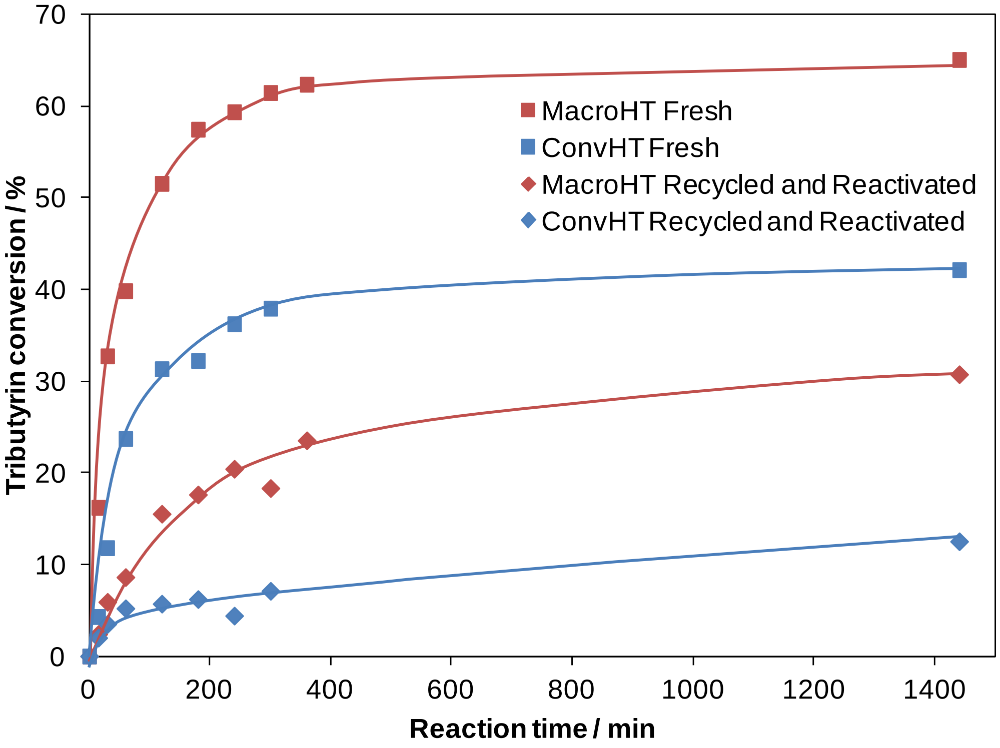

Figure 3.55. Triglyceride conversion for fresh versus recycled-reactivated convHT and macroHT during the transesterification of tributyrin.

Table 3.19. Reaction data for recycled-reactivated convHT and macroHT samples compared to fresh in the tributyrin transesterification reaction.

	Initial rate / mmol g^{-1} min^{-1}	Tributyrin conversion after 24 h / %
ConvHT fresh	0.78 +/- 0.01	42.1 +/- 1.5
ConvHT recycled-reactivated	0.18 +/- 0.05	15.4 +/- 1.5
MacroHT fresh	2.18 +/- 0.02	65.0 +/- 1.5
MacroHT recycled-reactivated	0.35 +/- 0.02	30.7 +/- 1.5

The macroHT sample has converted about 50 % of the tributyrin it did when fresh, whereas the convHT has converted about 37 %. The initial rate has dropped by a factor of about 6 for the macroHT, compared to about 4.5 for the convHT.

On calcination of the de-activated hydrotalcites, any organic material poisoning the base sites such as butyric anions should be burnt out and the mixed metal oxides reformed. Rehydration should then re-occur when the mixed oxides are subjected to water vapour. XPS analysis on the spent-reactivated catalysts would allow insight into whether or not this does occur. With no characterisation on the re-activated materials it is difficult to know exactly why the full activity has not been restored. However, on repeated calcinations and rehydration, the formation of the hydrotalcite crystalline structure becomes more difficult, due to segregation of Al.[13] The rehydration of the thin-walled macroHT should be easier than for the large crystallites of the convHT as water will not need to penetrate as far into the mixed oxide. Therefore, although neither hydrotalcite may be fully rehydrated with 100 % of the base sites as of the fresh material, the reactivated convHT may consist of more mixed oxide material and less base site density than the reactivated macroHT, as well as possessing a less-ordered, crystalline structure. Further characterisation on spent and re-activated convHT and macroHT samples would need to be carried out in order to prove or disprove this theory.

3.2.4 Preparation of an ordered macroHT

In the alkali-free method of preparing a macroHT material, the conventional hydrotalcite synthesis was adapted to incorporate polystyrene templating as reported by Géraud and co-workers.[58] . However, the preparation still involved the normal stirring protocol employed during the synthesis of conventional hydrotalcites. This led to a non-ordered distribution of macropores throughout the hydrotalcite, as described in section 3.2.1.5. An attempt was therefore made to carry out the alkali-free co-precipitation synthesis around sedimented polystyrene beads with no stirring, in an aim to prepare an ordered macroHT material, without the addition of alkali during the synthesis.

3.2.4.1 Characterisation

3.2.4.1.a EDX

EDX analysis was initially carried out in order to determine the Mg:Al ratio of the ordered macroHT. The bulk Mg:Al ratio was found to be 2.51:1, slightly higher than for the convHT and macroHT samples but still lower than the nominal ratio used during the preparation, as found for the convHT and macroHT samples.

3.2.4.1.b XRD

XRD analysis was carried out on the ordered macroHT sample. The profile, compared to that of the macroHT can be seen in **Figure 3.57**.

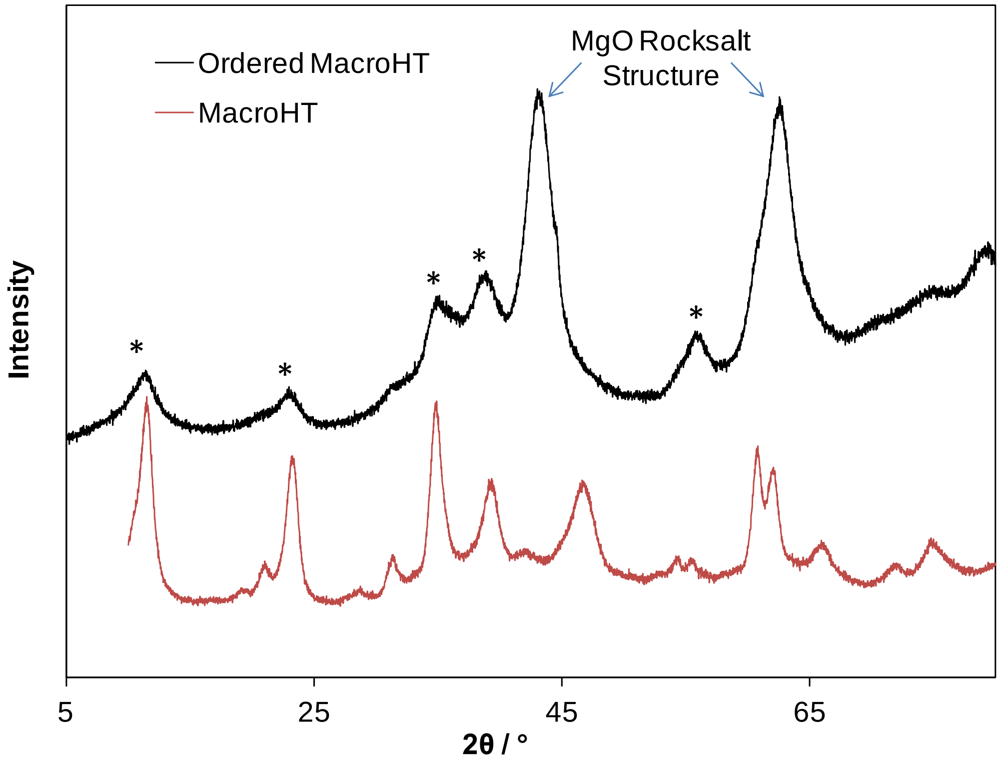

Figure 3.57. XRD patterns for macroHT and ordered macroHT samples. The asterix, *, denotes the peaks relating to the hydrotalcite crystal structure.

There is a hydrotalcite crystal phase present as peaks can be seen at 11.6°, 23.4°, 35° and 39.2°. However, the peaks at 42° and 62°, marked with an asterix, are assigned to an

MgO phase with rocksalt structure.[59] Some Al may also be present within the MgO lattice.[13]

The adapted preparation involves adding mixed metal nitrates to the polystyrene beads and allowing them to soak in. Carbonate and ammonia solution is then added and allowed to soak through the PS crystallite in order to precipitate the hydrotalcite. Due to the lack of stirring, there may be areas of metal nitrates which do not come into contact with carbonate. These small areas of mixed metal nitrate will form the MgO rocksalt structure with alumina dispersed through the lattice on calcination, and will not form a hydrotalcite structure via the memory effect under vapour phase rehydration conditions.

The volume averaged crystallite size calculated via the Scherrer equation for the hydrotalcite crystal phase was found to be 1.22 +/- 0.10 nm. These crystallites are much smaller than for the macroHT and convHT, suggesting a less ordered structure. For hydrotalcites with Mg:Al ratios higher than the stoichiometric ratio of 2:1, the structure becomes less ordered again, and so smaller crystallites will form.[25] The interlayer spacing was found to be 0.78 nm, corresponding to the presence of hydroxide anions in the interlayer space of the hydrotalcite crystal. The d(110) peak for the ordered macroHT hydrotalcite crystalline phase is hidden behind the mixed metal oxide peak and so it is not possible to calculate a lattice parameter for this material.

3.2.4.1.c N_2 porosimetry

N_2 porosimetry was carried out on the ordered macroHT. The adsorption-desorption isotherm, compared to that of the macroHT sample, can be seen in **Figure 3.58**.

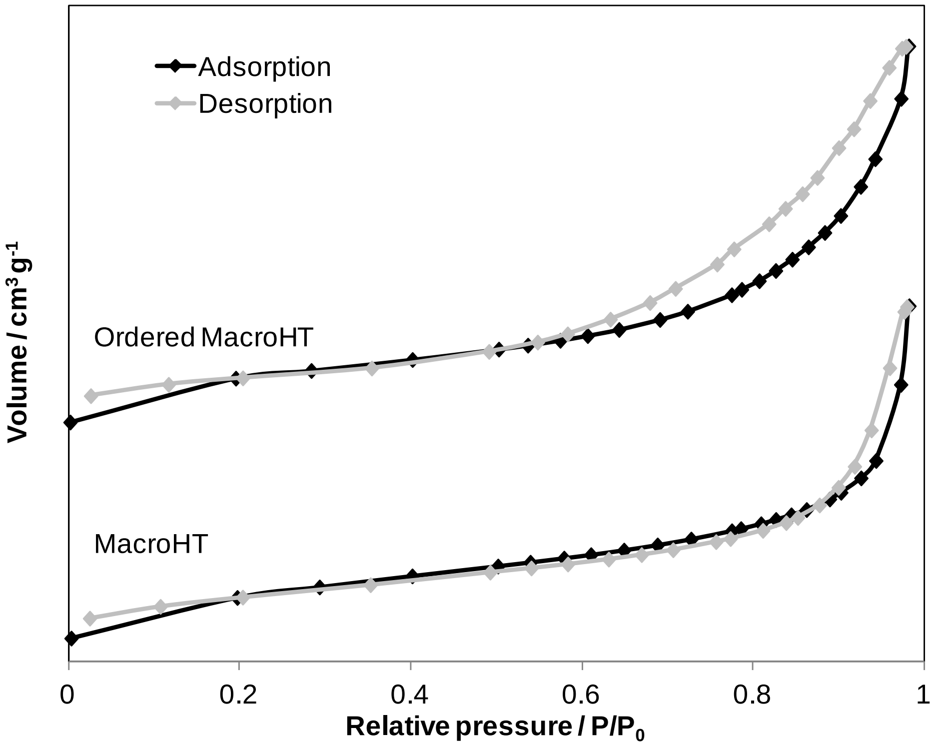

Figure 3.58. N_2 porosimetry isotherms for ordered macroHT and macroHT.

The surface area of the ordered macroHT is 83 +/- 8.3 m^2g^{-1} , compared to 62 +/- 6.2 m^2g^{-1} and 48 +/- 4.8 m^2g^{-1} for the macroHT and convHT respectively. This again suggests the formation of thin walls around the PS bead template, the higher macropore density in the ordered macroHT leading to the higher surface area.

3.2.4.1.d TGA

The TGA profiles for the macroHT and ordered macroHT samples can be seen below in **Figure 3.59**. The characteristic weight losses discussed previously for hydrotalcites (section 3.2.1.4) are observed for the ordered macroHT. By 500 ºC, the ordered macroHT has lost a smaller percentage of its weight than the macroHT sample. This effect can be assigned to the presence of MgO rock-salt structure as this phase is stable up to 1000 ºC, at which point a spinel structure is formed.[60]

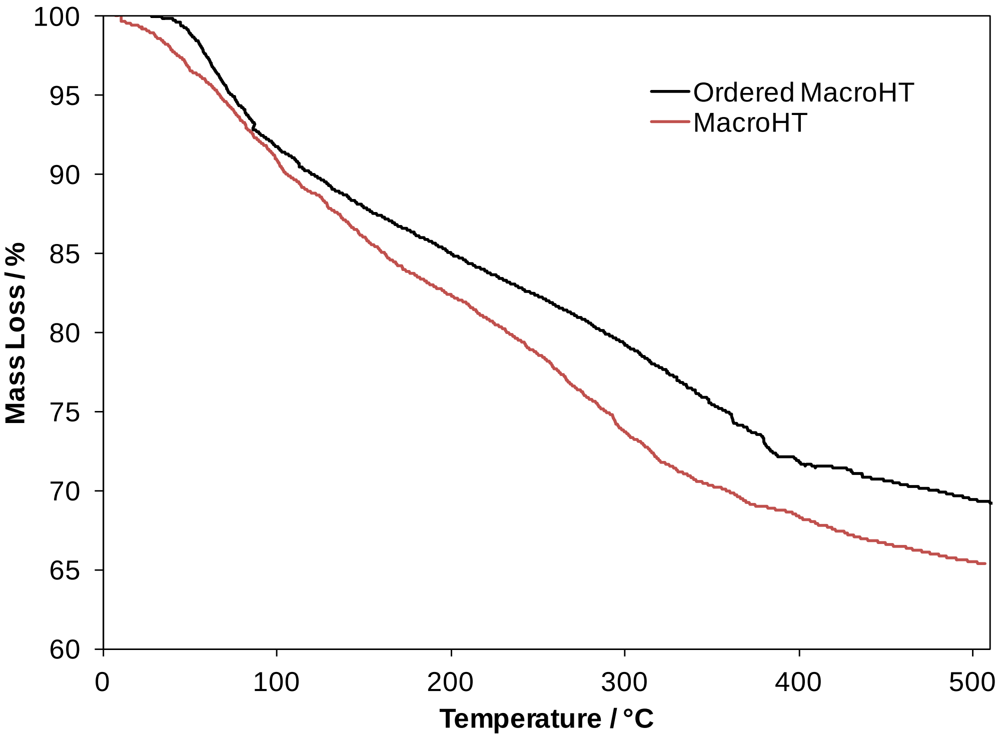

Figure 3.59. TGA profiles for macroHT and ordered macroHT.

3.2.4.1.e SEM

An example SEM image for the ordered macroHT can be seen in **Figure 3.60**.

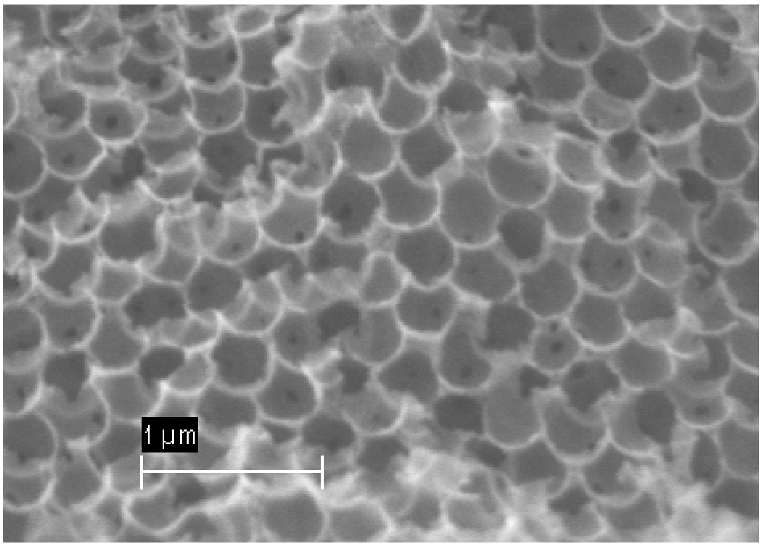

Figure 3.60. SEM image showing structure of ordered macroHT.

A honeycomb arrangement of PS beads can be observed, formed due to the sedimentation of the polystyrene beads before the hydrotalcite preparation commenced, during which time the PS beads would have formed the most space-saving arrangement. This SEM study shows that the ordered macroHT does have a different macropore arrangement to that of the macroHT sample.

3.2.4.1.f XPS

XPS analysis was carried out on the ordered macroHT. The chemical environments for Mg 2s, Al 2p, O 1s and C 1s compared to those for the convHT and macroHT samples can be seen in **Figure 3.61** and **Figure 3.62.**

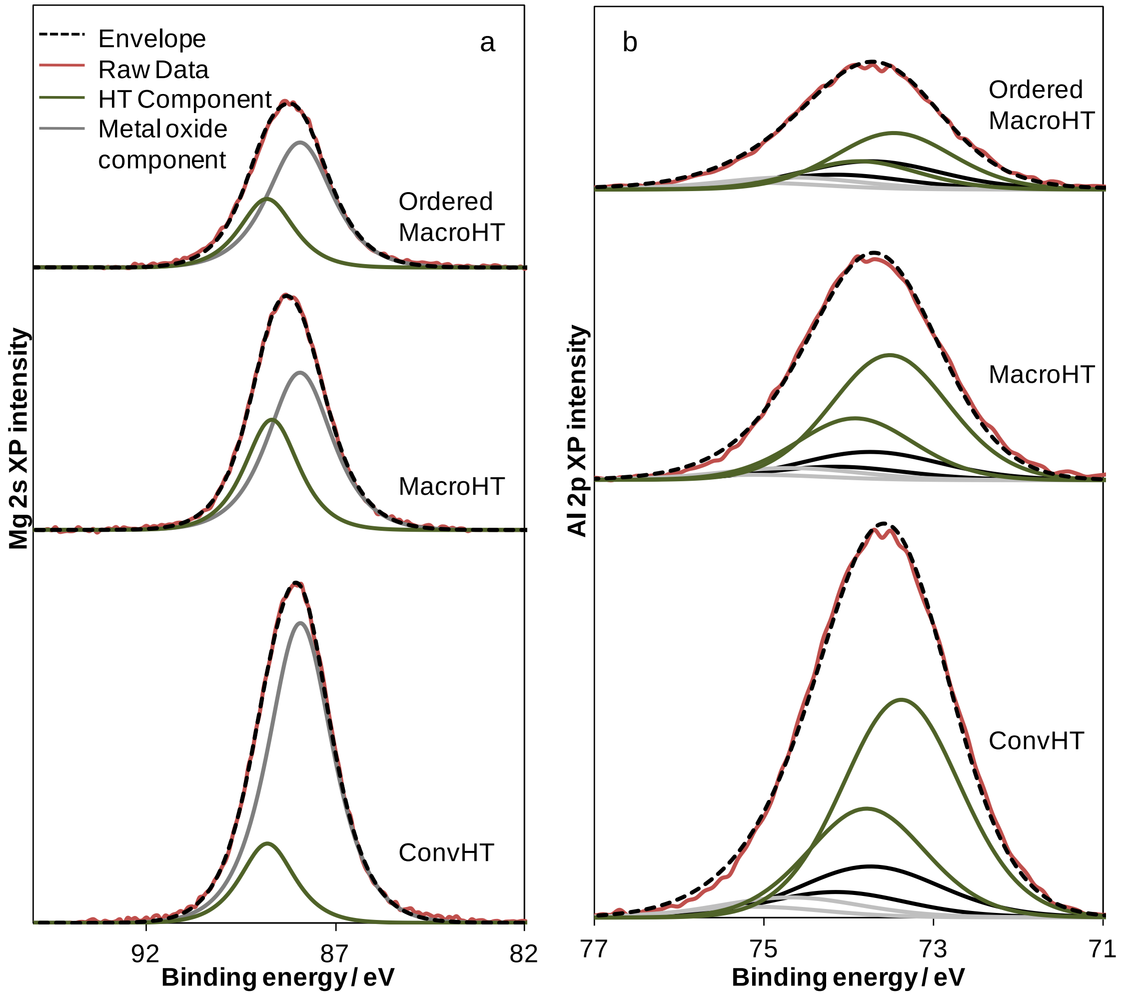

Figure 3.61. XP spectra showing a) the Mg 2s and b) the Al 2p chemical environments for convHT, macroHT and ordered macroHT.

The ordered macroHT contains an MgO component and an alumina component, along with a single hydrotalcite phase, as for convHT and macroHT. **Table 3.20** reports the total surface Mg:Al ratio and hydrotalcite surface Mg:Al ratio for the ordered macroHT, compared to the macroHT and convHT samples.

Table 3.20. Comparison of bulk and surface Mg:Al ratios for convHT, macroHT and ordered macroHT.

	Bulk Mg:Al ratio	Total surface Mg:Al ratio	Surface hydrotalcite Mg:Al ratio
ConvHT	1.95:1	1.14:1	0.42:1
MacroHT	2.02:1	1.30:1	0.89:1
Ordered macroHT	2.51:1	1.67:1	1.50:1

The results show that although the total surface Mg:Al ratio is about two thirds that of the bulk Mg:Al ratio in all cases, the surface hydrotalcite Mg:Al ratio is proportionally much higher than for the macroHT. Therefore, during the synthesis more Mg has been able to incorporate into the surface hydrotalcite structure

As discussed previously, during the preparation the mixed metal nitrates have time to soak into the polystyrene bead crystallite before co-precipitation. Therefore the metal nitrates will be thoroughly mixed and well dispersed over the polystyrene beads. These thin layers can form hydrotalcites on carbonate addition with the greater dispersion allowing easier incorporation of magnesium into the hydrotalcite structure at the surface.

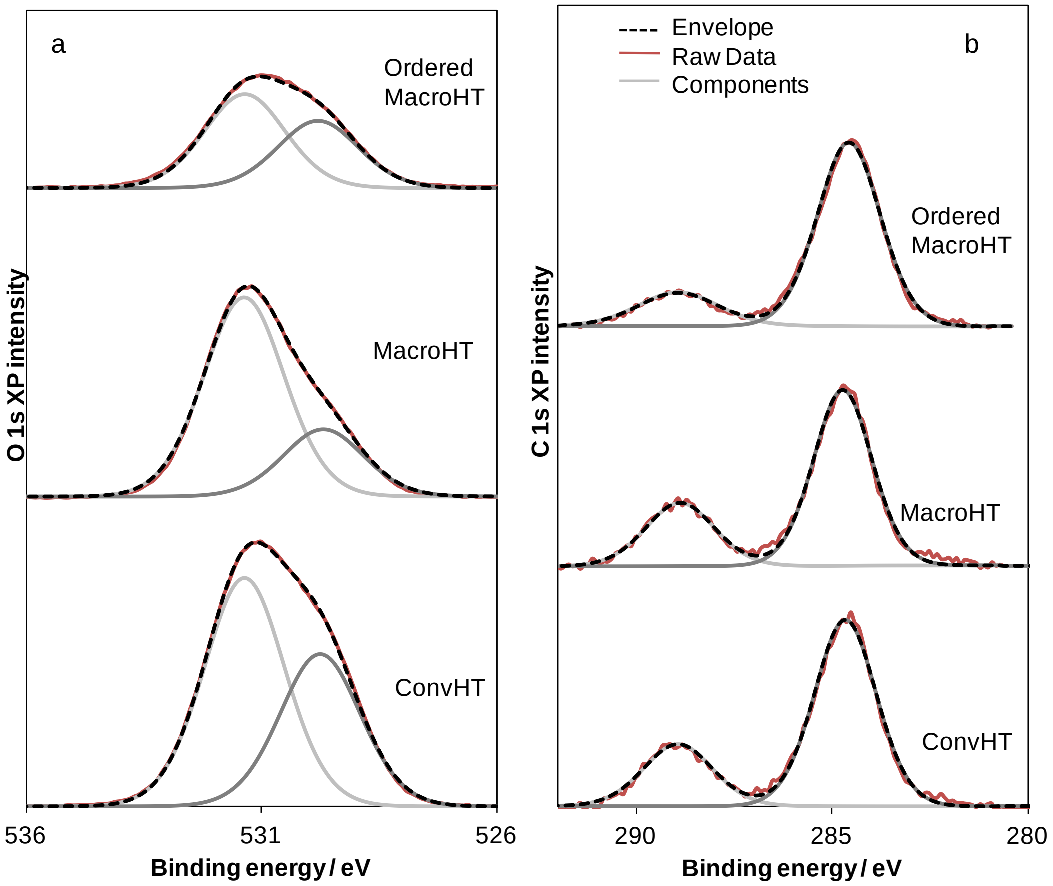

Figure 3.62. XP spectra showing a) the O 1s chemical environments and b) the C1s chemical environments for convHT, macroHT and ordered macroHT.

The ordered macroHT O1s region also shows two components, as for the convHT and macroHT. The higher binding energy component due to hydroxide anions and the lower binding energy component due to the more basic Mg-O^{2-} environment. The greater proportion of surface Mg-O^{2-} for the ordered macroHT compared to the macroHT is attributed to the crystalline MgO observed in the XRD spectrum.

3.2.4.1.g CO_2 TPD

CO_2 TPD analysis was performed on the ordered macroHT sample in order to determine the base site density. The TPD profile for the ordered macroHT can be seen in **Figure 3.63**. The base site densities for convHT, macroHT and ordered macroHT are reported in **Table 3.21**.

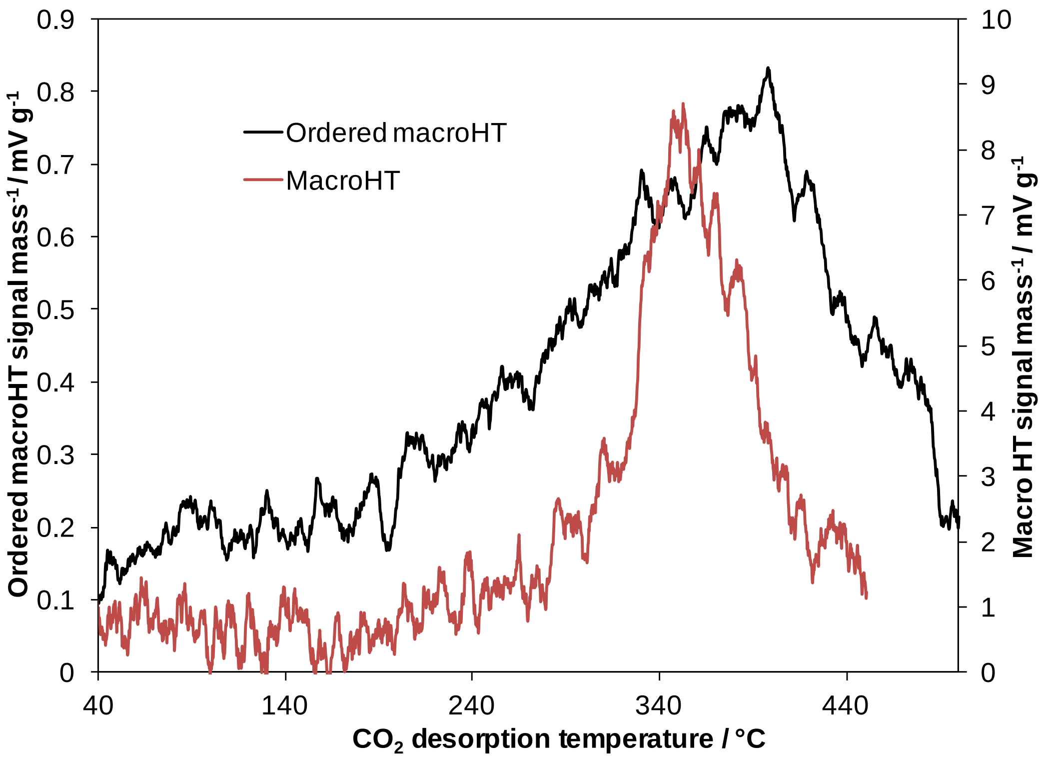

Figure 3.63. CO_2 TPD profile for ordered macroHT compared to the macroHT.

Table 3.21. Base site densities for convHT, macroHT and ordered macroHT as determined by CO_2 TPD analysis.

	Base site density / g^{-1}
ConvHT	8.55×10^{19}
MacroHT	7.68×10^{19}
Ordered MacroHT	3.10×10^{19}

The ordered macroHT has a broader CO_2 desorption peak. There is a larger proportion of the peak found as a shoulder at high temperature between about 440 ºC and 450 ºC. As discussed in section 3.2.1.7, this region is due to carbonate bound in mono or bidentate species to Mg-O^{2-} pairs or unsaturated oxygen. Through XPS it has been observed that there is more Mg at the hydrotalcite surface for the ordered macroHT than for the macroHT, which may account for a larger proportion of the base sites being found at this higher temperature. It may also be due to surface base sites found on the crystalline MgO present in the ordered macroHT material.

The base site density is much lower than for the macroHT, due to the presence of areas of crystalline MgO. An example profile for MgO can be seen in **Figure 3.16** and the base sites are mainly found at 80 ºC, with a few at 240 ºC. The MgO present may account for a few of the base sites in the ordered macroHT at around 240 ºC. The MgO rocksalt structure consists of (111) facets with 2 alternating planes of Mg^{2+} cations and O^{2-} anions.[61] These Mg^{2+}-O^{2-} Lewis base pairs are only found at the surface of the MgO and so a lot of the material will be un-reactive, hence the low base site density.

The peak desorption temperature is at 398 ºC, higher than for the convHT and macroHT samples, and comparable to the literature value of Abello and co-workers[47]. This is most likely due to the higher Mg:Al ratio found within the hydrotalcite lattice.

3.2.4.2 Transesterification of triglycerides

The ordered macroHT sample was tested in the transesterification of triglycerides and the results compared to those of the convHT and macroHT samples, to determine whether ordering of the macropores causes any further enhancement to catalytic activity.

3.2.4.2.a C4 TAG transesterification

The tributyrin conversion profile and methyl butyrate formation profiles for the ordered macroHT compared to the convHT and macroHT samples can be seen in **Figure 3.64** and **Figure 3.65**. The reaction data is reported in **Table 3.22**.

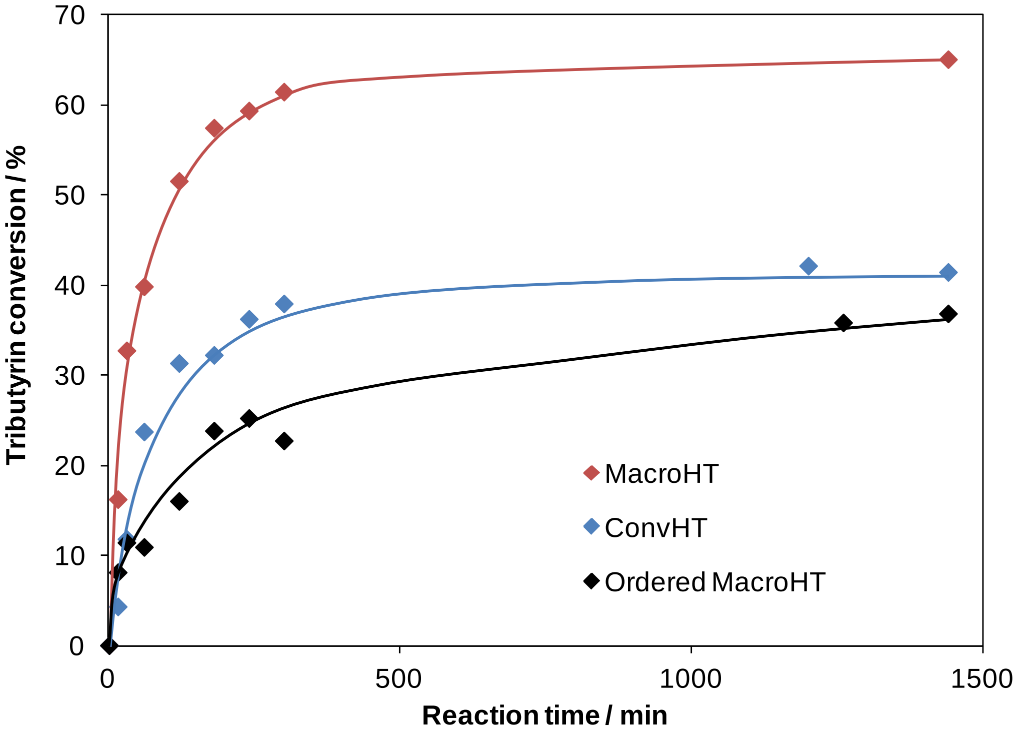

Figure 3.64. Reaction profiles showing tributyrin transesterification over time for convHT, macroHT and ordered macroHT.

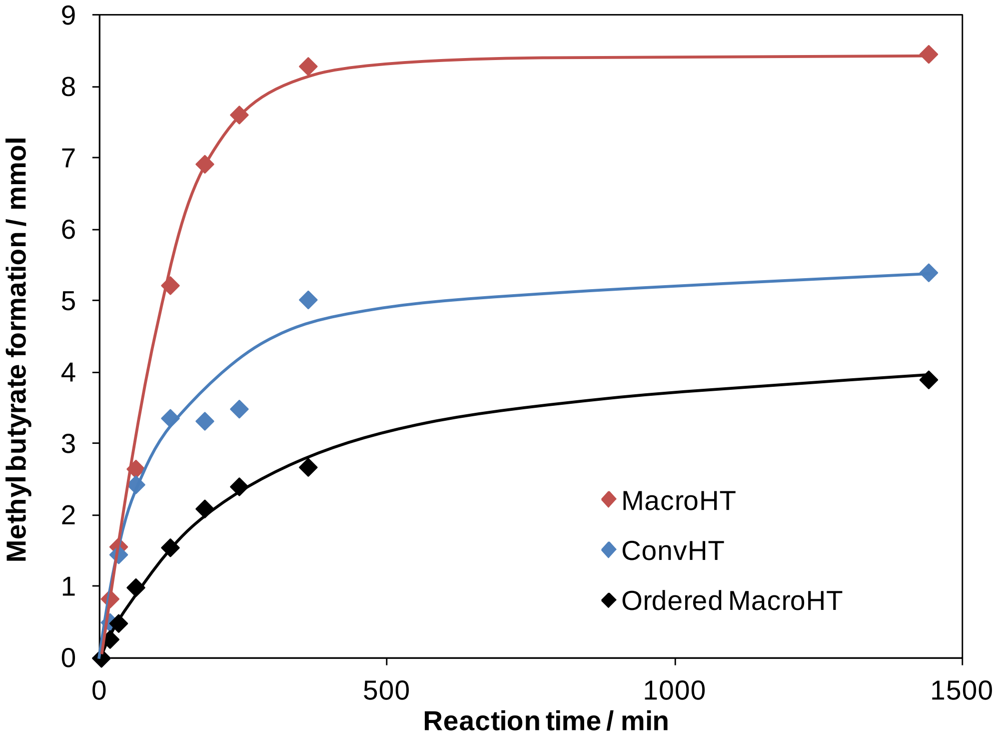

Figure 3.65. Methyl butyrate formation over time for convHT, macroHT and ordered macroHT during the transesterification of tributyrin.

Table 3.22. Reaction data for convHT, macroHT and ordered macroHT for C4 transesterification.

	Initial rate / mmol g^{-1} min^{-1}	TOF / min^{-1}	TAG conversion after 24 h / %	FAME selectivity after 24 h / %
ConvHT	0.78 +/- 0.01	5.49	42.1 +/- 1.5	43 +/- 1.5
MacroHT	2.18 +/- 0.02	17.06	65.0 +/- 1.5	43 +/- 1.5
Ordered MacroHT	0.82 +/- 0.06	16.01	36.8 +/- 1.5	35 +/- 1.5

On first examination, the initial rate and overall conversion is lower for the ordered macroHT. However, due to the lower base site density its TOF value is actually very similar to that of the macroHT. Therefore there appears to be no TOF enhancement on carrying out transesterification via an ordered macroHT, compared to the standard macroHT. The FAME selectivity is lower due to the slower rate of conversion meaning there are fewer full conversions from TAG through MAG and DAG to FAME.

3.2.4.2.b C12 TAG transesterification

The trilaurin conversion profiles, and methyl laurate formation profiles for the ordered macroHT compared to convHT and macroHT can be seen in **Figure 3.66** and **Figure 3.67**. The reaction data is reported in **Table 3.23**.

Table 3.23. C12 transesterification reaction data for convHT, macroHT and ordered macroHT.

	Initial rate / mmol g^{-1} min^{-1}	TOF / min^{-1}	TAG conversion after 24 h / %	FAME selectivity after 24 h / %
ConvHT	0.26 +/- 0.05	1.83	19.1 +/- 1.5	54.5 +/- 1.5
MacroHT	0.94 +/- 0.07	7.37	28.7 +/- 1.5	57.2 +/- 1.5
Ordered macroHT	0.45 +/- 0.07	8.66	15.5 +/- 1.5	45.6 +/- 1.5

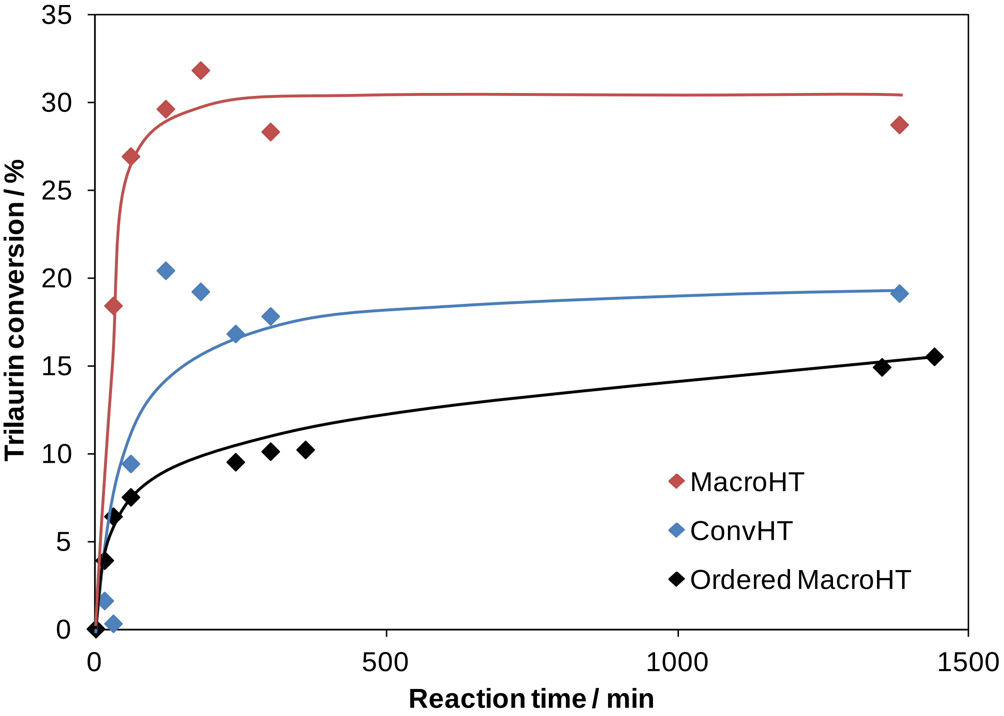

Figure 3.66. Reaction profiles showing trilaurin transesterification over time for convHT, macroHT and ordered macroHT.

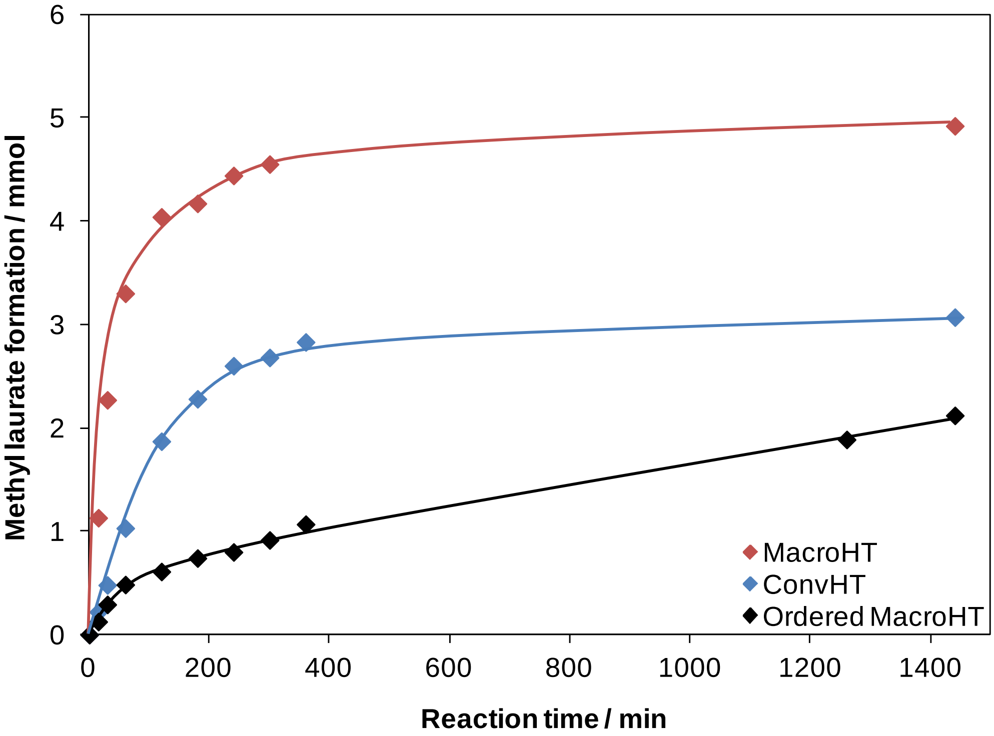

Figure 3.67. Methyl laurate formation over time for convHT, macroHT and ordered macroHT during the transesterification of trilaurin.

Again, although the initial rate and conversions are lower the TOF value is very similar to that of the macroHT.

3.2.4.2.c C18 TAG transesterification

The triolein conversion profiles, and methyl oleate formation profiles for the ordered macroHT compared to convHT and macroHT can be seen in **Figure 3.68** and **Figure 3.69**. The reaction data is reported in **Table 3.24**.

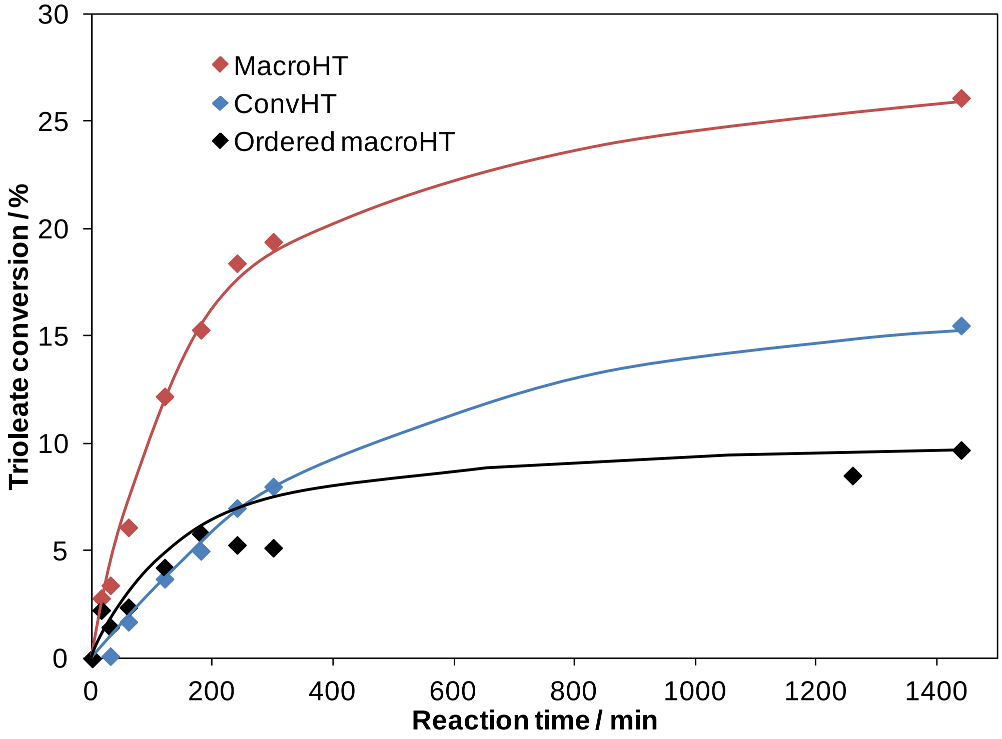

Figure 3.68. Reaction profiles showing triolein transesterification over time for convHT, macroHT and ordered macroHT.

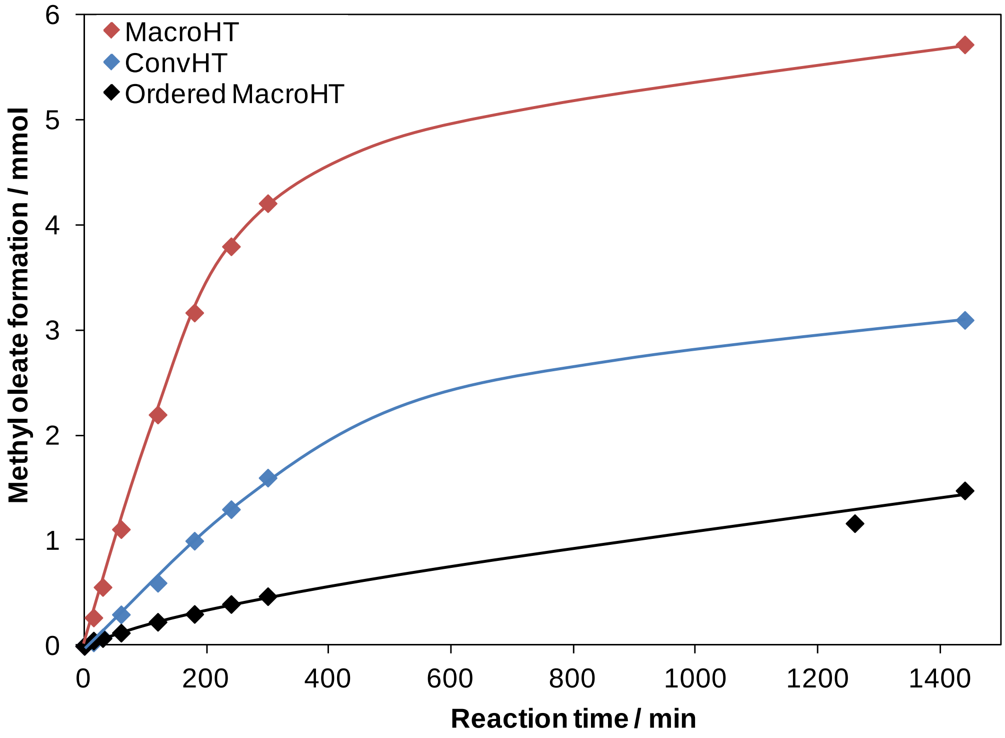

Figure 3.69. Methyl oleate formation over time for convHT, macroHT and ordered macroHT during the transesterification of triolein.

Table 3.24. C18 transesterification reaction data for convHT, macroHT and ordered macroHT.

	Initial rate / mmol g^{-1} min^{-1}	TOF / min^{-1}	TAG conversion after 24 h / %	FAME selectivity after 24 h / %
ConvHT	0.026 +/- 0.01	0.18	15.5 +/- 1.5	66.7 +/- 1.5
MacroHT	0.22 +/- 0.006	1.73	26.1 +/- 1.5	73.1 +/- 1.5
Ordered macroHT	0.094 +/- 0.01	1.83	9.7 +/- 1.5	50.8 +/- 1.5

Again, the ordered macroHT shows a TOF value very similar to that of the macroHT. On moving from C4 to C18 TAG chain length, the ordered macroHT shows the same trends of decreasing TAG conversion and increasing FAME selectivity, as seen for all previous hydrotalcites.

3.2.4.2.d Comparison of TOF values for macroHT and ordered macroHT

Figure 3.70 shows the TOF enhancements for macroHT and ordered macroHT compared to the convHT during the transesterification of C4-C18 triglycerides.

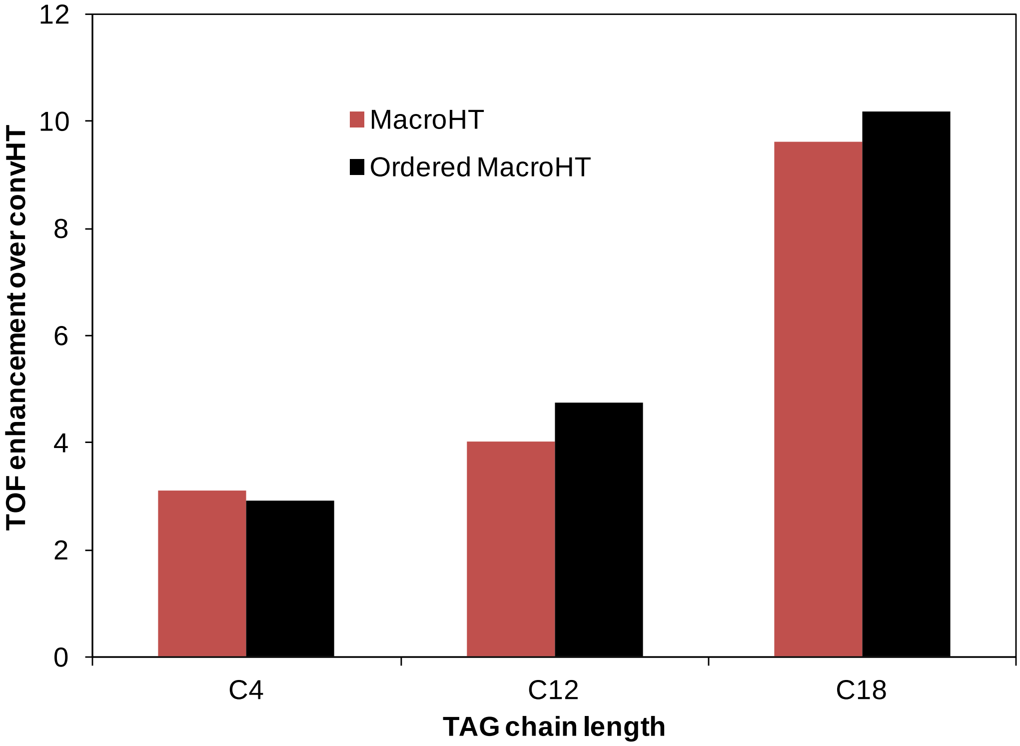

Figure 3.70. TOF enhancement for macroHT and ordered macroHT versus convHT.

Any genuine enhancement seen via ordered macroHT compared to macroHT for the C12 and C18 TAG is not very large. Therefore this enhancement is assigned to intrinsic differences in the basicity and structure of the hydrotalcite, rather than the ordering of the macropores. The Mg:Al ratio is slightly higher for the ordered macroHT, giving increased basicity within the hydrotalcite structure, as shown by CO_2 TPD. There is also an increase in BET surface area.

As the enhancement does not increase with increasing triglyceride chain length, it is not assigned to an increased mass transport rate of the TAG molecules to the active catalyst sites, and therefore it is the incorporation of macropores which have the beneficial effect on transesterification of TAGs, not the ordering of them. The macroHT has the added benefit of more complete rehydration due to the ability to stir the starting materials through the synthesis to ensure full hydrotalcite co-precipitation, and therefore increased base site density and enhanced FAME selectivity.

3.3 Conclusions

A series of conventional and macroporous hydrotalcites were prepared using an alkali-free co-precipitation route, with polystyrene bead templating used to incorporate the macropores, followed by calcination and rehydration.

On increasing the Mg:Al ratio across both series, the basicity increased, due to the formation of more crystalline hydrotalcites meaning the presence of more interlayer hydroxide anions, as well as greater electron density in the layers leading to more basic hydroxyl groups.

On comparison of the conventional and macroporous hydrotalcites, the Mg:Al ratio, hydrotalcite crystalline phase and basicity were found to be comparable. However, incorporation of PS beads during the HT synthesis lead to the genesis of a thin-walled macroHT compared to the large aggregated crystallites found for the convHT. This affect was attributed to a greater dispersity of hydroxycarbonate nanocrystallites around the polystyrene beads during co-precipitation. This led to a greater microporosity and surface area for the macroHT, and therefore a larger number of easily accessible edge site hydroxide interlayer anion base sites within the hydrotalcite crystallites at the macroporous surface.

The direct effect of the incorporation of macropores into the hydrotalcite structure was shown to be enhanced diffusion of the large, bulky triglycerides found in biodiesel feedstocks through the macropore "super highways" to the active sites of the hydrotalcite, leading to a dramatic enhancement in TOF compared to the conventional hydrotalcite which increased with increasing TAG chain length and bulk.
Ordering of the macropores within the hydrotalcite structure was not shown to give any further TOF enhancement on increasing TAG chain length than that already observed for the macroHT.

These results are the first demonstration of the promotion of bulky TAG conversion via the use of macroporous-microporous hydrotalcites as solid-base catalysts.

3.4 References

(1) Cavani, F.; Trifiro, F.; Vaccari, A. *Catalysis Today* **1991**, *11*, 173-291.

(2) Climent, M. J.; Corma, A.; Iborra, S.; Epping, K.; Velty, A. *Journal of Catalysis* **2004**, *225*, 316-326.

(3) Roelofs, J.; van Bokhoven, J. A.; van Dillen, A. J.; Geus, J. W.; de Jong, K. P. *Chemistry-a European Journal* **2002**, *8*, 5571-5579.

(4) Constantino, V. R. L.; Pinnavaia, T. J. *Inorganic Chemistry* **1995**, *34*, 883-892.

(5) Valente, J. S.; Lima, E.; Toledo-Antonio, J. A.; Cortes-Jacome, M. A.; Lartundo-Rojas, L.; Montiel, R.; Prince, J. *Journal of Physical Chemistry C* **2010**, *114*, 2089-2099.

(6) Cantrell, D. G.; Gillie, L. J.; Lee, A. F.; Wilson, K. *Applied Catalysis A: General* **2005**, *287*, 183-190.

(7) Abello, S.; Perez-Ramirez, J. *Microporous and Mesoporous Materials* **2006**, *96*, 102-108.

(8) Dávila, V.; Lima, E.; Bulbulian, S.; Bosch, P. *Microporous and Mesoporous Materials* **2008**, *107*, 240-246.

(9) Kim, M. J.; Park, S. M.; Chang, D. R.; Seo, G. *Fuel Processing Technology* **2010**, *91*, 618-624.

(10) Navajas, A.; Campo, I.; Arzamendi, G.; Hernandez, W. Y.; Bobadilla, L. F.; Centeno, M. A.; Odriozola, J. A.; Gandia, L. M. *Applied Catalysis B-Environmental* **2010**, *100*, 299-309.

(11) Navajas, A.; Arzamendi, G.; Romero-Sarria, F.; Centeno, M. A.; Odriozola, J. A.; Gandía, L. M. *Catalysis Communications* **2012**, *17*, 189-193.

(12) Corma, A.; Hamid, S. B. A.; Iborra, S.; Velty, A. *Journal of Catalysis* **2005**, *234*, 340-347.

(13) Hibino, T.; Tsunashima, A. *Chemistry of Materials* **1998**, *10*, 4055-4061.

(14) Di Serio, M.; Ledda, M.; Cozzolino, M.; Minutillo, G.; Tesser, R.; Santacesaria, E. *Industrial & Engineering Chemistry Research* **2006**, *45*, 3009-3014.

(15) Pinzi, S.; Garcia, I. L.; Lopez-Gimenez, F. J.; de Castro, M. D. L.; Dorado, G.; Dorado, M. P. *Energy & Fuels* **2009**, *23*, 2325-2341.

(16) Geraud, E.; Rafqah, S.; Sarakha, M.; Forano, C.; Prevot, V.; Leroux, F. *Chemistry of Materials* **2008**, *20*, 1116-1125.

(17) Ma, F. R.; Hanna, M. A. *Bioresource Technology* **1999**, *70*, 1-15.

(18) Geraud, E.; Prevot, V.; Leroux, F. *Journal of Physics and Chemistry of Solids* **2006**, *67*, 903-908.

(19) Constantino, U.; Marmottini, F.; Nocchetti, M.; Vivani, R. *European Journal of Inorganic Chemistry* **1998**, 1439-1446.

(20) Lopez, T.; Bosch, P.; Ramos, E.; Gomez, R.; Novaro, O.; Acosta, D.; Figueras, F. *Langmuir* **1996**, *12*, 189-192.

(21) Chibwe, K.; Jones, W. *Journal of the Chemical Society - Chemical Communications* **1989**, 926.

(22) *JCPDS X-Ray Diffraction Database, International Centre for Diffraction Data* **2001**, *USA*.

(23) Bravo-Suarez, J. J.; Paez-Mozo, E. A.; Oyama, S. T. *Quimica Nova* **2004**, *27*, 601-614.

(24) Scherrer, P. *Nachr. Ges. Wiss. Göttingen* **1918**, *26*, 98-100.

(25) Sideris, P. J.; Nielsen, U. G.; Gan, Z.; Grey, C. P. *Science* **2008**, *321*, 113-117.

(26) Pfeiffer, H.; Martinez-dIcruz, L.; Lima, E.; Flores, J.; Vera, M. A.; Valente, J. S. *Journal of Physical Chemistry C* **2010**, *114*, 8485-8492.

(27) Rives, V. *Materials Chemistry and Physics* **2002**, *75*, 19-25.

(28) Miyata, S. *Clays and Clay Minerals* **1983**, *31*, 305-311.

(29) Denton, A. R.; Ashcroft, N. W. *Physical Review A* **1991**, *43*, 3161-3164.

(30) Brindley, G. W.; Kikkawa, S. *American Mineralogist* **1979**, *64*, 836-843.

(31) Barrett, E. P.; Joyner, L. G.; Halenda, P. P. *Journal of the American Chemical Society* **1951**, *73*, 373-380.

(32) Sing, K. S. W.; Everett, D. H.; Haul, R. A. W.; Moscou, L.; Pierotti, R. A.; Rouquerol, J.; Siemieniewska, T. *Pure and Applied Chemistry* **1985**, *57*, 603-619.

(33) McBain, J. W. *Journal of the American Chemical Society* **1935**, *57*, 699-700.

(34) Di Cosimo, J. I.; Diez, V. K.; Xu, M.; Iglesia, E.; Apesteguia, C. R. *Journal of Catalysis* **1998**, *178*, 499-510.

(35) Horvath, G.; Kawazoe, K. *Journal of Chemical Engineering of Japan* **1983**, *16*, 470-475.

(36) Greenwell, H. C.; Holliman, P. J.; Jones, W.; Velasco, B. V. *Catalysis Today* **2006**, *114*, 397-402.

(37) Abello, S.; Medina, F.; Tichit, D.; Perez-Ramirez, J.; Groen, J. C.; Sueiras, J. E.; Salagre, P.; Cesteros, Y. *Chemistry-a European Journal* **2005**, *11*, 728-739.

(38) Mascolo, G.; Marino, O. *Mineralogical Magazine* **1980**, *43*, 619-621.

(39) Adachi-Pagano, M.; Forano, C.; Besse, J. P. *Journal of Materials Chemistry* **2003**, *13*, 1988-1993.

(40) King, D. E.; Swartz, W. E. *Journal of Chemical Education* **1987**, *64*, 981-983.

(41) Barr, T. L.; Seal, S.; Wozniak, K.; Klinowski, J. *Journal of the Chemical Society-Faraday Transactions* **1997**, *93*, 181-186.

(42) Peng, X. D.; Richards, D. A.; Stair, P. C. *Journal of Catalysis* **1990**, *121*, 99-109.

(43) Montero, J. M.; Wilson, K.; Lee, A. F. *Topics in Catalysis* **2010**, *53*, 737-745.

(44) Debecker, D. P.; Gaigneaux, E. M.; Busca, G. *Chemistry-a European Journal* **2009**, *15*, 3920-3935.

(45) Xi, Y.; Davis, R. J. *Journal of Catalysis* **2008**, *254*, 190-197.

(46) Philipp, R.; Fujimoto, K. *Journal of Physical Chemistry* **1992**, *96*, 9035-9038.

(47) Abello, S.; Medina, F.; Tichit, D.; Perez-Ramirez, J.; Rodriguez, X.; Sueiras, J. E.; Salagre, P.; Cesteros, Y. *Applied Catalysis A: General* **2005**, *281*, 191-198.

(48) Diez, V. K.; Apesteguia, C. R.; Di Cosimo, J. I. *Journal of Catalysis* **2003**, *215*, 220-233.

(49) Xi, Y. Z.; Davis, R. J. *Journal of Catalysis* **2009**, *268*, 307-317.

(50) Brito, A.; Borges, M. E.; GarÃn, M.; HernÃ¡ndez, A. *Energy and Fuels* **2009**, *23*, 2952-2958.

(51) Gomes, J. F.; Puna, J. F.; Bordado, J.; Correia, M. J. N. *Reaction Kinetics and Catalysis Letters* **2008**, *95*, 273-279.

(52) Dorado, M. P.; Ballesteros, E.; Arnal, J. M.; Gomez, J.; Gimenez, F. J. L. *Energy & Fuels* **2003**, *17*, 1560-1565.

(53) Damiani, P.; Burini, G. *Journal of Agricultural and Food Chemistry* **1980**, *28*, 1232-1236.

(54) Dacquin, J. P.; Lee, A. F.; Pirez, C.; Wilson, K. *Chemical Communications* **2012**, *48*, 212-214.

(55) Dacquin, J.-P.; Cross, H. E.; Brown, D. R.; Duren, T.; Williams, J. J.; Lee, A. F.; Wilson, K. *Green Chemistry* **2010**, *12*, 1383-1391.

(56) Kapil, A.; Wilson, K.; Lee, A. F.; Sadhukhan, J. *Industrial & Engineering Chemistry Research* **2011**, *50*, 4818-4830.

(57) Briggs, D.; Beamson, G. *Analytical Chemistry* **1992**, *64*, 1729-1736.

(58) Geraud, E.; Prevot, V.; Ghanbaja, J.; Leroux, F. *Chemistry of Materials* **2006**, *18*, 238-240.

(59) Jianzhou, Z.; Laiyu, L.; Xiangrong, C.; Yu-Lin, B. *Physica B: Condensed Matter* **2007**, *387*, 245-249.

(60) Lopez, T.; Ramos, E.; Bosch, P.; Asomoza, M.; Gomez, R. *Materials Letters* **1997**, *30*, 279-282.

(61) Veldurthi, S.; Shin, C.-H.; Joo, O.-S.; Jung, K.-D. *Microporous and Mesoporous Materials* **2012**, *152*, 31-36.

Chapter 4

Hydrotalcites supported on alumina

4.1 Introduction

Supporting metal nanoparticles, alkali metals or alkaline earth oxides on a high surface area material such as silica or alumina is a widely reported, cost-effective way of generating a catalyst with a large surface area and allowing good dispersion of the metal, or metal oxide, particles.[1-3] MgO has been supported on alumina via Mg salt impregnation,[4] a material active as a solid base catalyst in reactions such as the self-condensation of *n*-butyraldehyde.[5] Supported hydrotalcites have also been prepared in literature. Co-precipitation can be carried out around a gamma-alumina support,[6] in a similar way to the preparation of the macroporous hydrotalcite in **Chapter 3**, in which hydrotalcites are co-precipitated around a polystyrene bead template.[7] This technique is still a bulk hydrotalcite synthesis, with the alumina providing mechanical strength, and not the formation of a thin hydrotalcite layer on an alumina surface. Hydrotalcites have been prepared by adding an M(II) salt solution to alumina at high pH, causing the alumina to partially dissolve and provide the aluminium cations, allowing a hydrotalcite to form at the surface.[8] However this procedure requires concentrated sodium hydroxide solution, and avoiding alkali in the synthesis is desirable to prevent alkali leaching from the catalyst into a reaction mixture. Hydrotalcite thin films have also been prepared using an electrophoretic technique,[9] where a colloidal suspension of commercial hydrotalcite is coated onto an alumina support using an electric field. This is not a hydrotalcite synthesis, but a deposition of pre-synthesised hydrotalcite onto alumina.
Hydrotalcite thin films on alumina have a high adsorption capacity for CO_2 and are therefore reported as CO_2 sorbents in literature.[10, 11] However, there are no reports on the catalytic activity of hydrotalcites supported on alumina for the transesterification of triglycerides to form biodiesel. It is anticipated that the increased surface area of the support should enhance the catalytic activity compared to bulk, conventional hydrotalcites; the thin, open layer of HT on alumina removing diffusion limitations associated with TAG transesterification. Preparing a hydrotalcite on a support could also reduce the cost of using hydrotalcite as a catalyst in a fixed-bed reactor for continuous biodiesel production.

Hydrotalcites are commonly synthesised using a co-precipitation technique[12], however alternative routes have been reported on in literature, for example sol-gel synthesis,[13-15] or urea hydrolysis.[16, 17] Hydrotalcites have also been prepared via hydrothermal synthesis,[18, 19] where MgO and Al_2O_3 are mixed in an aqueous suspension, before being treated in an autoclave at high temperature and pressure for several days in order to form a hydrotalcite with hydroxide intercalating anions. With this technique in mind, it was proposed that if hydrotalcites can be prepared via mixing of MgO and Al_2O_3 at high pressure and temperature in water, then if Mg and Al could be brought into intimate contact on the surface of alumina and then calcined to form a homogeneous mixed metal oxide layer, that on applying a hydrothermal treatment a hydrotalcite layer on top of alumina could be obtained. An impregnation of Mg methoxide onto the alumina surface by mixing at room temperature was the chosen preparative route. **Figure 4.1** illustrates the proposed novel synthesis described.

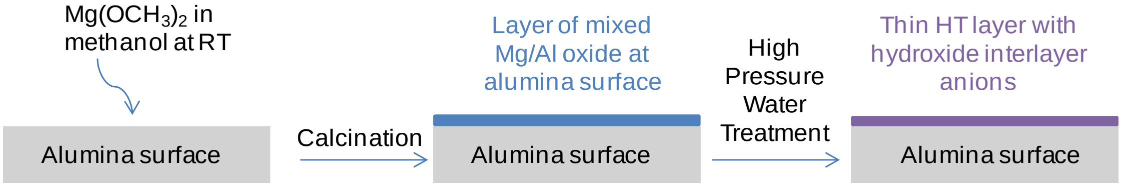

Figure 4.1. Cartoon illustrating novel method of preparing HT on alumina.

Davis and co-workers report on a hydrothermal treatment to reconstruct calcined hydrotalcites by stirring with de-carbonated water in a sealed Teflon vessel at 140 ºC for 24 hours.[20] In this work their hydrothermal treatment was adapted to a slightly lower temperature, in order to minimise the energy requirements to successfully transform mixed oxides into hydrotalcite. This preparative route not only uses less extreme hydrothermal conditions than previously reported for hydrotalcite reconstruction, it also reduces the need for the use of nitrate precursors, as required in the conventional co-precipitation route.[21, 22]. This prevents NO_x, a greenhouse gas[23], being released into the environment during calcination, reducing the environmental impact of the synthesis.

This chapter will investigate the novel preparation of a thin layer of MgAl hydrotalcite on alumina. The weight percentage of magnesium impregnated onto the alumina will be varied in order to examine the difference in structure and reactivity of the materials prepared. After a full characterisation of the series of materials, they will be tested as catalysts in the transesterification of triglycerides to form FAME biodiesel molecules. The aim is that in preparing a supported thin layer of hydrotalcite, a catalyst with improved activity to that of the bulk conventional hydrotalcite can be obtained due to the increased accessibility of the hydrotalcite base sites.

4.2 Results and discussion

Magnesium graftings were carried out on alumina as described in **Chapter 2**. Briefly, magnesium methoxide in methanol was added to alumina at 10 wt % Mg, stirred at room temperature for one hour and the excess solvent removed on a rotary evaporator. To achieve higher Mg weight percentages this grafting was repeated successive times, drying the alumina in a vacuum oven between each grafting. The material was then calcined at 450 ºC to form MgO/Al_2O_3 before carrying out a hydrothermal treatment in water at 125 ºC for 21 h to prepare a layer of hydrotalcite on alumina. The series of HT on alumina materials were characterised and then tested in the transesterification of varying chain length triglycerides, in order to compare their activity to that of conventional hydrotalcite.

4.2.1 Catalyst characterisation

Full characterisation was carried out on the series using EDX, XRD, N_2 porosimetry, TGA, XPS and CO_2 TPD analyses to determine as much as possible about the structural and chemical properties of hydrotalcite on alumina.

4.2.1.1 EDX

EDX analysis was carried out in order to determine the bulk Mg weight percentages compared to the nominal Mg wt% added into the reaction. The results can be seen in **Table 4.1**.

Table 4.1. Mg weight percentages for the HT on alumina series as determined by EDX analysis.

Nominal Mg content / wt%	Actual Mg content / wt%
10	5.1 +/- 0.4
20	9.2 +/- 0.5
40	14.2 +/- 0.7
50	16.7 +/- 0.4

The actual weight percentages are all lower than the nominal values. The nominal weight percent values are calculated for the grafting of Mg onto alumina. However, they do not take into account the addition of hydrogen and oxygen when forming hydrotalcite during the hydrothermal treatment, meaning the actual proportion of Mg will be smaller in the final material. As the Mg weight percent increases, the proportion of hydrotalcite formed increases (as shown in XPS section 4.2.1.6), therefore the difference between the nominal and actual Mg weight percent values increases, as a greater amount of hydroxide anions and water are incorporated into the material.

On moving along the series, the Mg weight percentage does increase, allowing the structural and chemical properties of the materials to be compared and discussed in relation to varying magnesium content. The catalysts will be labelled using their actual weight percent values through the chapter, e.g. 5% Mg is the catalyst which contains 5 weight percent magnesium.

4.2.1.2 XRD

Powder X-ray diffraction patterns for the full series of hydrotalcites on alumina after the calcination and hydrothermal treatment can be seen in **Figure 4.2**. The diffraction patterns show that a hydrotalcite crystalline phase is present as all of the characteristic hydrotalcite peaks can be observed.[24] The peak at around 67º is due to the alumina support.[25] Volume averaged crystallite sizes were determined from line broadening using the Scherrer equation,[26] and are reported in **Table 4.2**. The crystallite sizes are similar across the series and much larger than the 6 nm reported in **Chapter 3** for the convHT. Therefore, the hydrotalcite structure is more crystalline and ordered when formed on the alumina support than for the conventional hydrotalcite. This result is supported by observing the diffraction patterns in **Figure 4.2**; the peaks for the HT on alumina series are much sharper and more intense than for convHT.

The convHT sample being compared was rehydrated using a vapour phase technique at room temperature, rather than the liquid phase hydrothermal treatment in water at 125 ºC, as for the HT on alumina series. As discussed in **Chapter 3**, the rehydration does not occur fully under these weaker vapour phase rehydration conditions as un-reacted areas of mixed oxide remain within the convHT matrix, therefore crystal growth may be limited. Hydrothermal treatment is also reported in literature to enhance the crystallinity of hydrotalcites.[27]

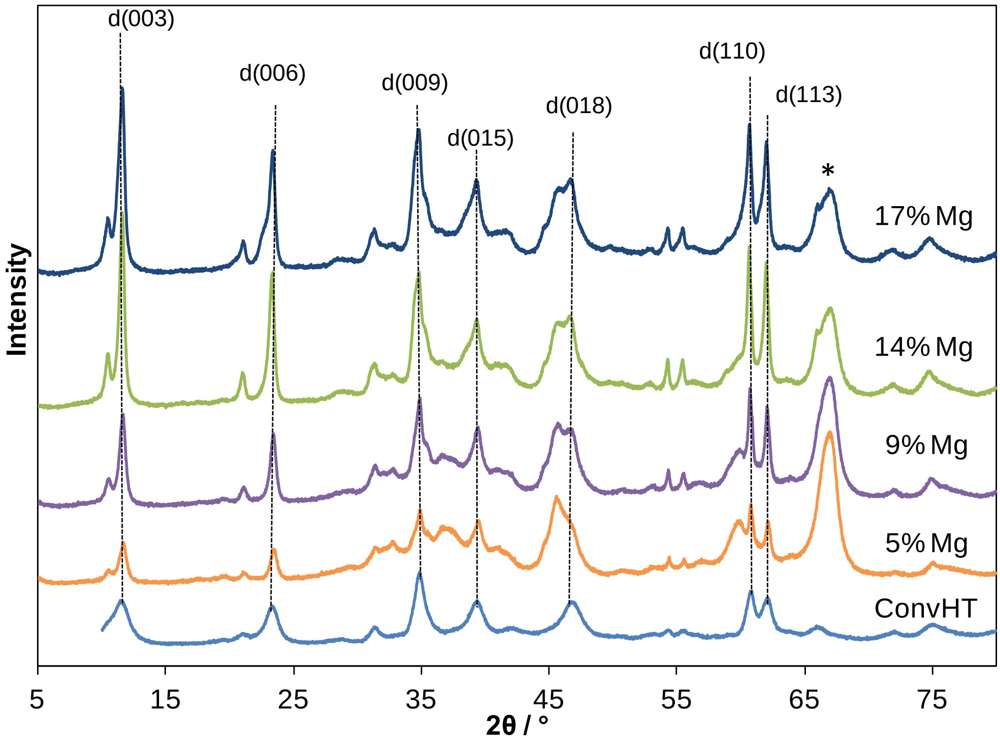

Figure 4.2. XRD profiles for the series of HT on alumina catalysts, offset for clarity, and compared to convHT. The alumina peak is marked with an asterix, *.

Table 4.2. Crystallite sizes, interlayer spacings and lattice parameters for the HT on alumina series as determined via analysis of the XRD powder diffraction patterns.

Catalyst	Volume average crystallite size / nm	Interlayer spacing, *d* / nm	Lattice Parameter, *a* / Å	Mg:Al ratio extrapolated from Fig.4.2.
5 wt% Mg	27 +/- 2.2	0.76 +/- 0.01	3.046	1.79:1
9 wt% Mg	33 +/- 2.6	0.76 +/- 0.01	3.050	1.90:1
14 wt% Mg	36 +/- 2.9	0.76 +/- 0.01	3.052	2.13:1
17 wt% Mg	31 +/- 2.5	0.77 +/- 0.01	3.051	2.08:1

As a comparison, some fresh conventional hydrotalcite was calcined and rehydrated using the hydrothermal treatment in the liquid phase. The XRD profiles for the vapour phase rehydrated convHT (convHT-VPR) and the hydrothermally treated, liquid phase rehydrated convHT (convHT-LPR) are compared in **Figure 4.3**. **Table 4.3** reports on the crystallite sizes of the two materials.

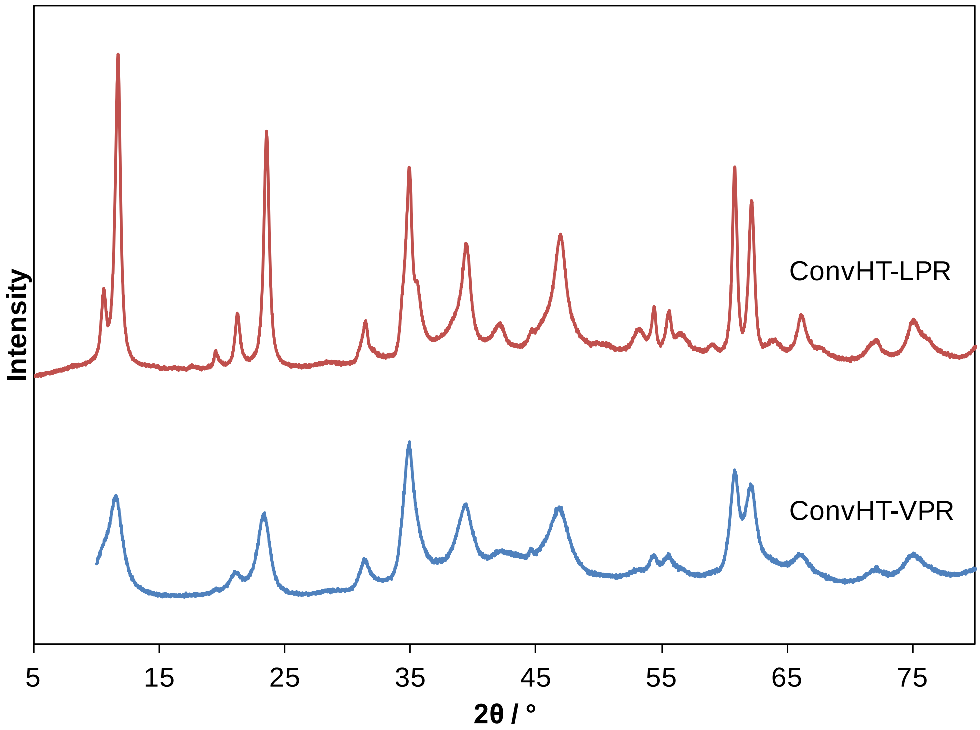

Figure 4.3. XRD profiles comparing convHT rehydrated in the vapour phase (convHT-VPR) with convHT rehydrated hydrothermally in the liquid phase (convHT-LPR)

Table 4.3. Crystallite sizes for convHT-VPR and convHT-LPR as determined via analysis of the XRD powder diffraction patterns.

	Volume average crystallite size / nm
ConvHT-VPR	6.2 +/- 0.50
ConvHT-LPR	35 +/- 2.8

The crystallite size has increased dramatically for the convHT after hydrothermal treatment, to a value equal to those of the HT on alumina series. Therefore, it is the stronger conditions of the hydrothermal treatment allowing the extra crystal growth and greater rehydration seen for the HT on alumina series.

The interlayer spacing, *d*, between two consecutive layers corresponds to three times the lattice parameter *c*.[28] *c* = 3d(003), and so from measuring the peak position of the d(003) reflection from the powder XRD patterns, and converting from degrees into nanometres, the interlayer spacings for each hydrotalcite have been determined and reported in **Table 4.2**. The values are all consistent with that of a hydrotalcite crystalline structure with hydroxide interlayer anions.[29]

The lattice parameter, *a*, was calculated using the d(110) peak position, where $a = 2d_{110}$,[24] reported in **Table 4.2**. The values were then added to the graph constructed in **Chapter 3** showing the Vegard's Law relationship between lattice parameter and Mg:Al ratio, which states that at a constant temperature a linear relationship exists between a crystal lattice parameter of an alloy, and the concentration of the constituent elements.[30] The Mg:Al ratio of the hydrotalcites could then be determined by reading the values from the graph, shown in **Figure 4.4**.

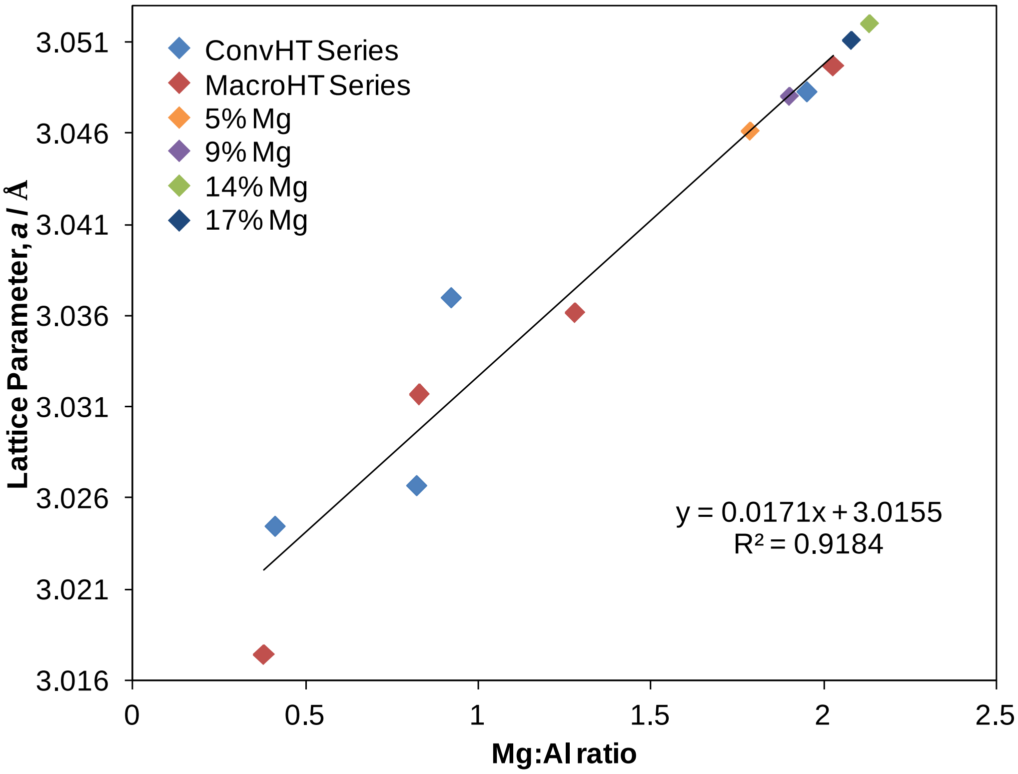

Figure 4.4. Plot of lattice parameter versus Mg:Al ratio for conventional and macroporous hydrotalcites. The lattice parameters of the HT on alumina series have been plotted in order to extrapolate bulk hydrotalcite Mg:Al ratios.

The Mg:Al ratios are reported in **Table 4.2** and all very similar to that of the 1.95:1 Mg:Al convHT. A 2:1 Mg:Al ratio is formed when the hydrotalcite crystal is in its most ordered form, with an ordered honeycomb structure where each Mg centre is surrounded by 3 Mg and 3 Al octahedra, and each Al centre surrounded by 6 Mg octahedra.[31]

This result gives us some insight into hydrotalcite formation on the alumina surface. If at the first Mg grafting one thin layer of hydrotalcite was formed, and with successive Mg graftings the same hydrotalcite layer remained but more Mg incorporated into the lattice, then we would observe an increase in Mg:Al ratio on successive Mg graftings. As this is not the case, it suggests that the hydrotalcite structure is the same for each material, and that with increasing Mg content it is the thickness, or amount, of the hydrotalcite layer which increases, with the composition remaining unchanged and in its most ordered form.

4.2.1.3 N_2 porosimetry

N_2 porosimetry was carried out on the full series of hydrotalcites on alumina. The N_2 adsorption-desorption isotherms can be seen below in **Figure 4.5**. The BJH pore size distributions have been plotted and can be seen in **Figure 4.6**. The BET surface areas, BJH total pore volumes and average pore diameters are reported in **Table 4.4**.

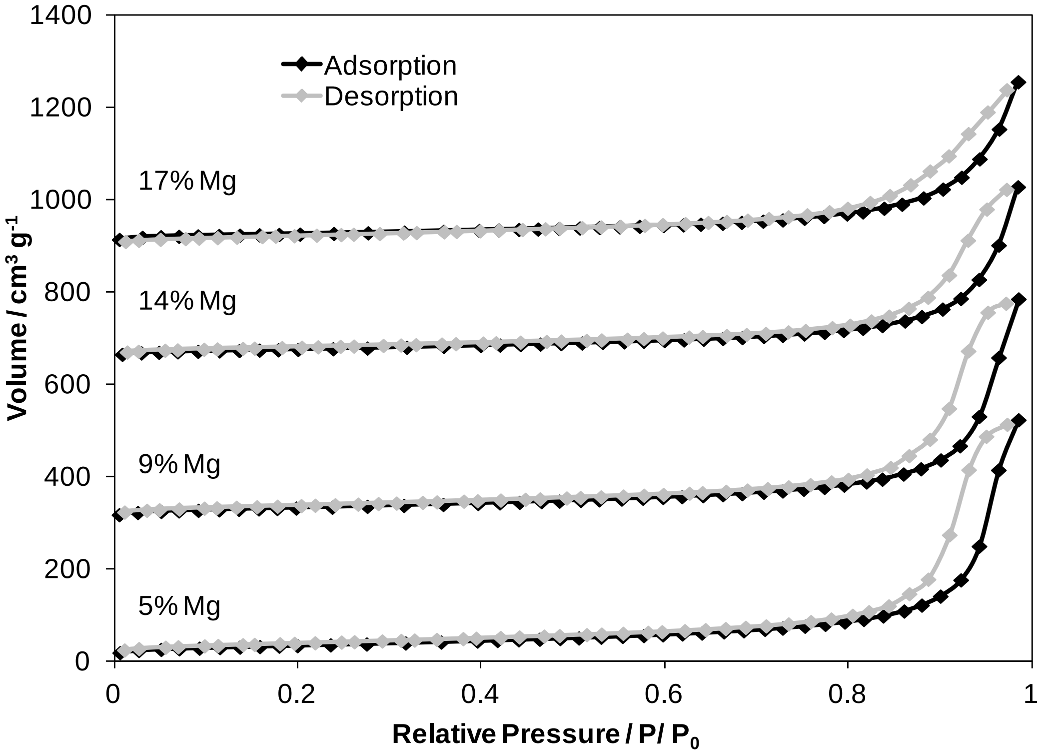

Figure 4.5. N_2 adsorption-desorption isotherms for the HT on alumina series. The isotherms have been offset for clarity.

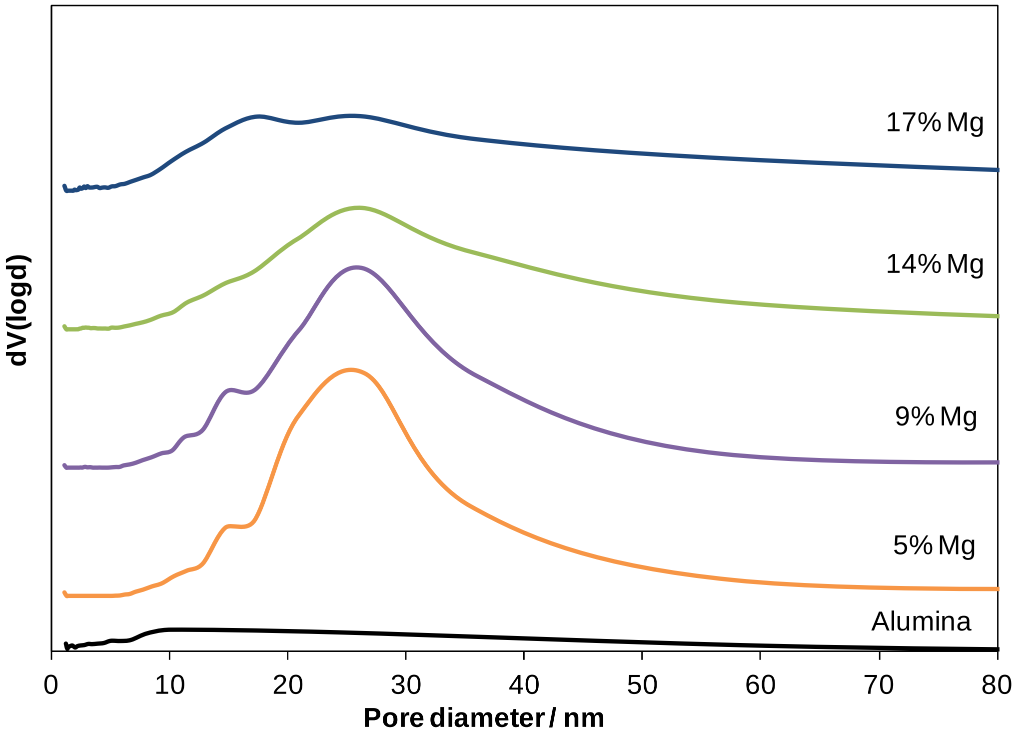

Figure 4.6. BJH pore size distributions for the HT on alumina series. The parent alumina pore size distribution has been shown for comparison.

Table 4.4. Surface area, total pore volumes and average pore diameters for the HT on alumina series as determined by N_2 porosimetry.

Catalyst	BET surface area / m^2 g^{-1}	Total BJH pore volume / cm^3 g^{-1}	Average BJH pore diameter / nm
5 wt% Mg	119 +/- 11.9	0.81 +/- 0.10	20.82 +/- 2.8
9 wt% Mg	113 +/- 11.3	0.75 +/- 0.09	26.33 +/- 4.8
14 wt% Mg	90 +/- 9.0	0.59 +/- 0.07	26.26 +/- 4.6
17 wt% Mg	88 +/- 8.8	0.57 +/- 0.07	17.38 +/- 1.8
Alumina	110 +/- 11.1	0.23 +/- 0.02	1.24 +/- 0.06
ConvHT	48 +/- 4.8	0.21 +/- 0.01	3.44 +/- 0.4

The surface areas are much higher for the HT on alumina series than for the convHT, due to the large surface area of the alumina support (110 m^2/g). At low Mg loadings the surface area is very similar to that of the alumina. However, as the amount of hydrotalcite on the alumina surface increases, the surface area decreases, tending towards that of convHT.

The BJH pore volumes, the distributions of which are plotted in **Figure 4.6**, are all significantly higher than the parent alumina material. As hydrotalcite crystallites form on the alumina surface, porous spaces will be found between them. As the amount of hydrotalcite on the alumina surface increases, the total pore volume will decrease as the crystallite islands spread out across more of the alumina surface.

4.2.1.4 TGA

TGA analysis was carried out for the full series of materials. The samples were heated up to 700 ºC under a flow of He. The profiles can be seen in **Figure 4.7**. The profiles for convHT and the parent alumina have been included as a comparison. **Table 4.5** reports on the weight losses of the two regions.

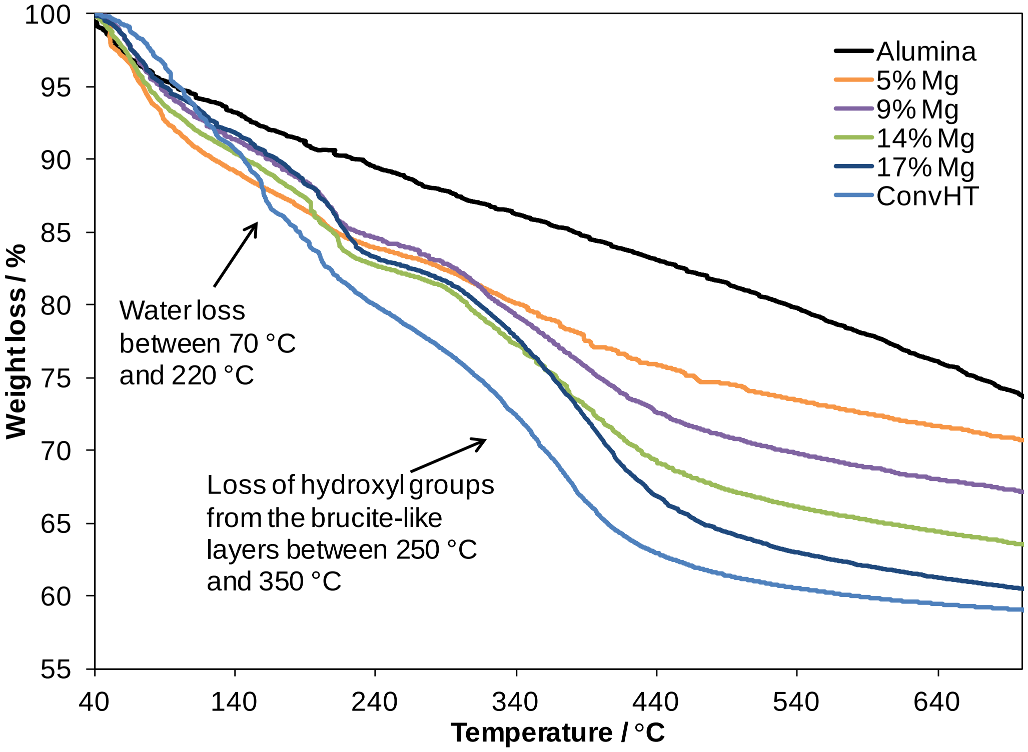

Figure 4.7. TGA profiles for the HT on alumina series as well as for convHT and the parent alumina.

Table 4.5. Weight loss during TGA analysis for the HT on alumina series and convHT.

	Weight loss due to interlayer and surface water / %	Weight loss due to hydroxide anions / %
Alumina	6.3 +/- 0.1	3.17 +/- 0.1
5 % Mg	11.1 +/- 0.1	4.07 +/- 0.1
9 % Mg	11.9 +/- 0.1	5.56 +/- 0.1
14 % Mg	12.7 +/- 0.1	6.01 +/- 0.1
17 % Mg	12.2 +/- 0.1	6.17 +/- 0.1
ConvHT	12.5 +/- 0.1	7.38 +/- 0.1

The hydrotalcite on alumina profiles all display the two characteristic weight loss regions for hydrotalcites. The first weight loss, between about 70 ºC and 220 ºC is attributed to the loss of water molecules adsorbed to the hydrotalcite surface, as well as interlayer water.[32] The weight loss at higher temperatures is attributed to the loss of hydroxide anions from within the brucite-like layers[33].

The percentage weight loss due to hydroxide interlayer anions increases across the HT on alumina series with increasing amount of hydrotalcite, although the values are still lower than that of the convHT, as even accounting for areas of mixed oxide within the convHT structure, there is still a smaller overall percentage of hydrotalcite in the alumina supported materials. The values are all higher than that of the parent alumina, showing that extra hydroxide anions have been incorporated due to the hydrotalcite structure, and it is not just hydroxide anions at the alumina surface contributing.

The percentage weight loss values for interlayer and surface water are all very similar to those of the conventional hydrotalcite. Although there is less hydrotalcite material, this is most likely due to the greater surface area for water to adsorb to, due to the alumina support.

4.2.1.5 CO_2 TPD

CO_2 TPD analysis was carried out on the full series of hydrotalcites on alumina. The profiles can be seen in **Figure 4.8,** along with a scaled down profile for convHT as a comparison. The base site densities calculated from the area of the peaks, along with the peak maximum temperatures, are reported in **Table 4.6.**

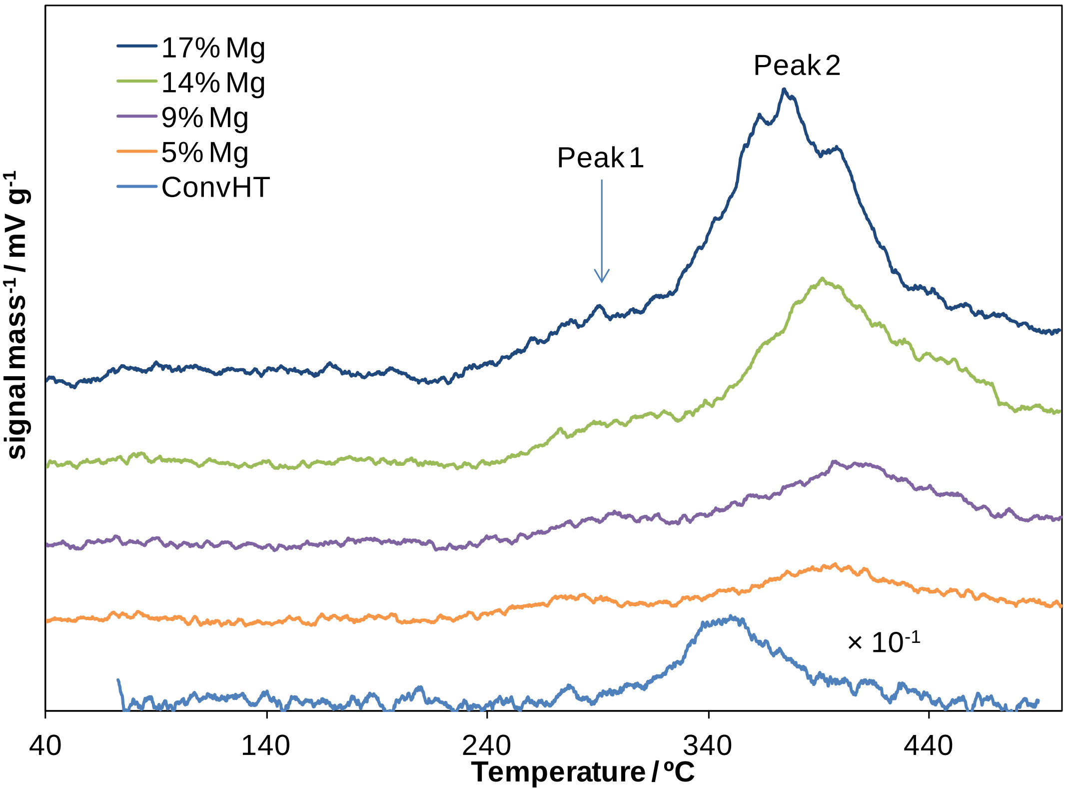

Figure 4.8. CO_2 TPD profiles for the HT on alumina series and convHT.

Table 4.6. Base site densities for the HT on alumina series.

Catalyst	Peak 1 base site density / g^{-1} $\times 10^{18}$	Peak 1 max. temp.[a] / °C	Peak 2 base site density / g^{-1} $\times 10^{18}$	Peak 2 max. temp.[a] / °C	Total base site density / g^{-1} $\times 10^{18}$	Total base site density / m^2	Total base site density / Mg atom
5% Mg	1.03	283.9	3.66	397.6	4.69	3.94×10^{16}	0.0038
9% Mg	1.12	297.1	5.30	397.2	6.43	5.71×10^{16}	0.0029
14% Mg	1.63	314.0	10.88	391.5	12.51	1.39×10^{17}	0.0036
17% Mg	3.77	291.0	18.20	374.6	21.97	2.50×10^{17}	0.0052
ConvHT			85.5	349.8	85.5	1.38×10^{18}	0.077

[a] Experimental error of +/- 0.2 °C

Overall, the base site densities are much lower than that of the bulk conventional hydrotalcite, due to the presence of the alumina support. The total base site density increases across the series with increasing amounts of hydrotalcite. When base site density is normalised to surface area, the same trend is seen, as more Mg is grafted to the alumina surface, the HT material per m^2 increases, and therefore so does base site density. The surface area of the convHT does not contain any support material, and therefore the base site density per m^2 is higher.

Peak 1 is assigned to bicarbonate species bound to the surface hydroxide anions of the brucite-like hydrotalcite layers, which are more weakly basic than the interlayer hydroxide anions.[34] The strength of these base sites remains fairly consistent over the series, due to the similar Mg:Al ratios. This peak is more distinct than seen for the convHT in **Chapter 3** due to the greater surface area of the materials.

Peak 2 is assigned to bicarbonate species bound to the interlayer hydroxide anions.[35] As the hydrotalcite crystallites increase in size and thickness on the surface of the alumina, the number of these hydroxide anions at edge sites, where their electron charge density is being withdrawn less strongly by the positively charged layers, decreases. This theory could account for the decrease in the peak maximum temperature and therefore base strength seen for Peak 2 on increasing the weight percent magnesium, tending towards that of the bulk conventional hydrotalcite.

When comparing the base site density of the materials per Mg atom, the densities for the HT on alumina series are fairly consistent. As more Mg is grafted onto the alumina surface, the greater the number of base sites, and each Mg atom grafted down adds a similar number of base sites from HT material. The convHT value is an order of magnitude higher than for the HT on alumina series. The co-precipitation technique allows infinite mixing of the Mg and Al and therefore it is probable that for each Mg atom in the material, less MgO and more HT is formed giving more base sites per Mg atom. This result shows that co-precipitation is still the best technique to prepare hydrotalcite material.

4.2.1.6 XPS

XPS analysis was carried out on the HT on alumina series. The XP spectra for the Mg 2s and Al 2p chemical environments can be seen in **Figure 4.9.**

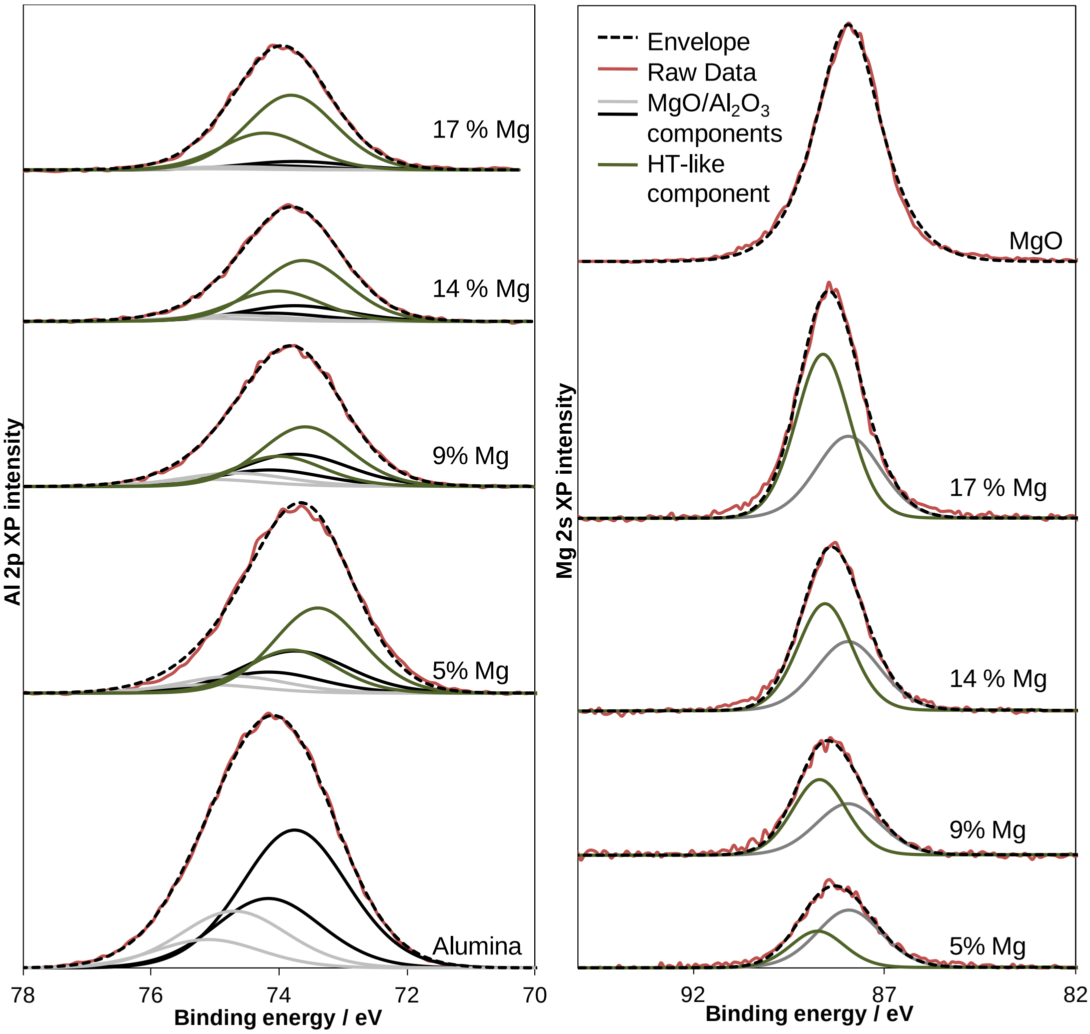

Figure 4.9. XP spectra showing a) the Al 2p and b) the Mg 2s chemical environments for the HT on alumina series.

On examining the Mg 2s XP spectra, two components can be fitted, a peak at a lower binding energy coinciding with that of MgO, and a higher binding energy hydrotalcite component. The proportions of the surface corresponding to these two different types of Mg environment have been plotted in **Figure 4.10**.

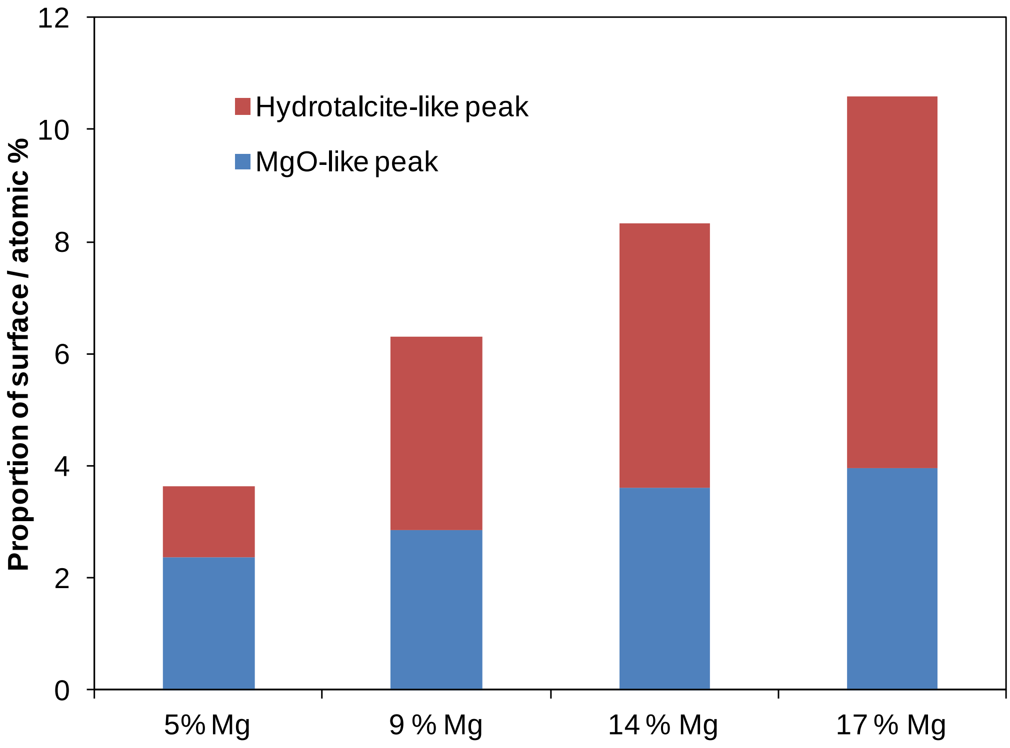

Figure 4.10. Bar chart indicating atomic percentages of surface Mg found as hydrotalcite and MgO in the HT on alumina series XPS spectra.

Both MgO and hydrotalcite are present on the alumina surface. The amount of MgO present remains fairly constant across the series. As more Mg is grafted onto the surface, the amount of hydrotalcite increases. The MgO formed does not appear in the XRD pattern, and so is not crystalline. There may be areas of MgO trapped within the hydrotalcite crystal structure, as discussed in **Chapter 3** for the conventional and macroporous hydrotalcites.

On examination of the Al 2p peaks, both alumina and hydrotalcite components can be fitted. **Figure 4.11** shows the proportion of the surface corresponding to the two types of Al environments for the HT on alumina series.

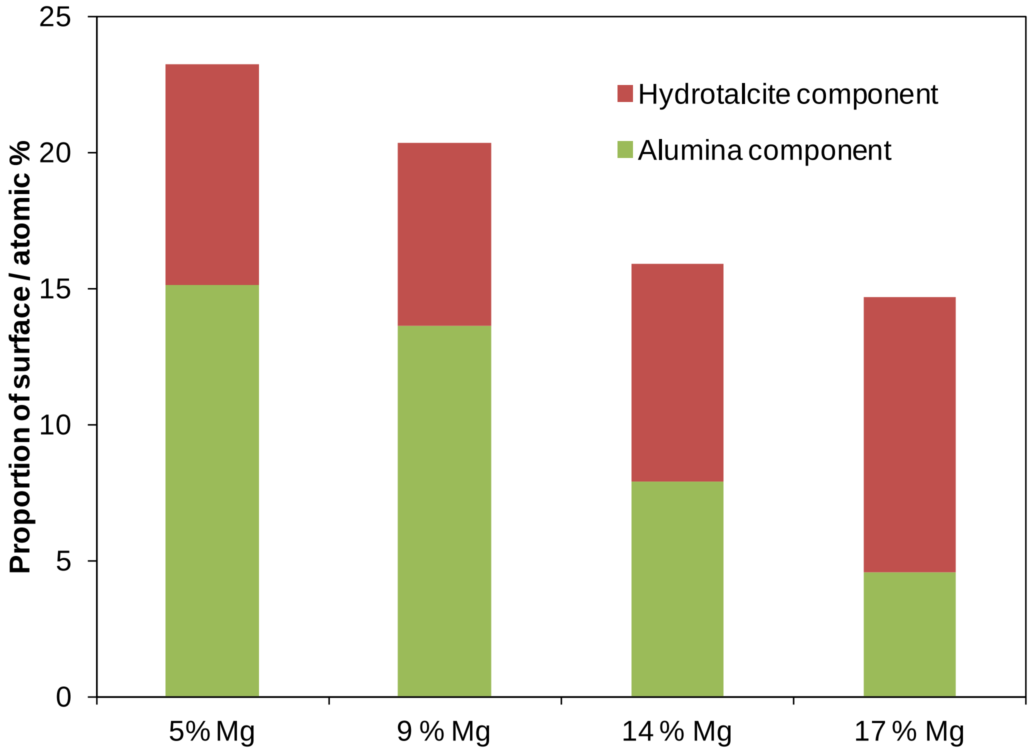

Figure 4.11. Bar chart indicating atomic percentages of surface Al found as hydrotalcite or Al_2O_3 in the HT on alumina series, via analysis of the XPS spectra.

XPS metal to support intensity ratios have been shown to provide important information about dispersion of supported metal particles on oxide surfaces,[36] and whether or not monolayer formation has occurred. In this case the alumina: hydrotalcite ratio can provide this important information. The intensity of the alumina component was plotted over the intensity of the hydrotalcite components, and the resulting graph can be seen in **Figure 4.12.**

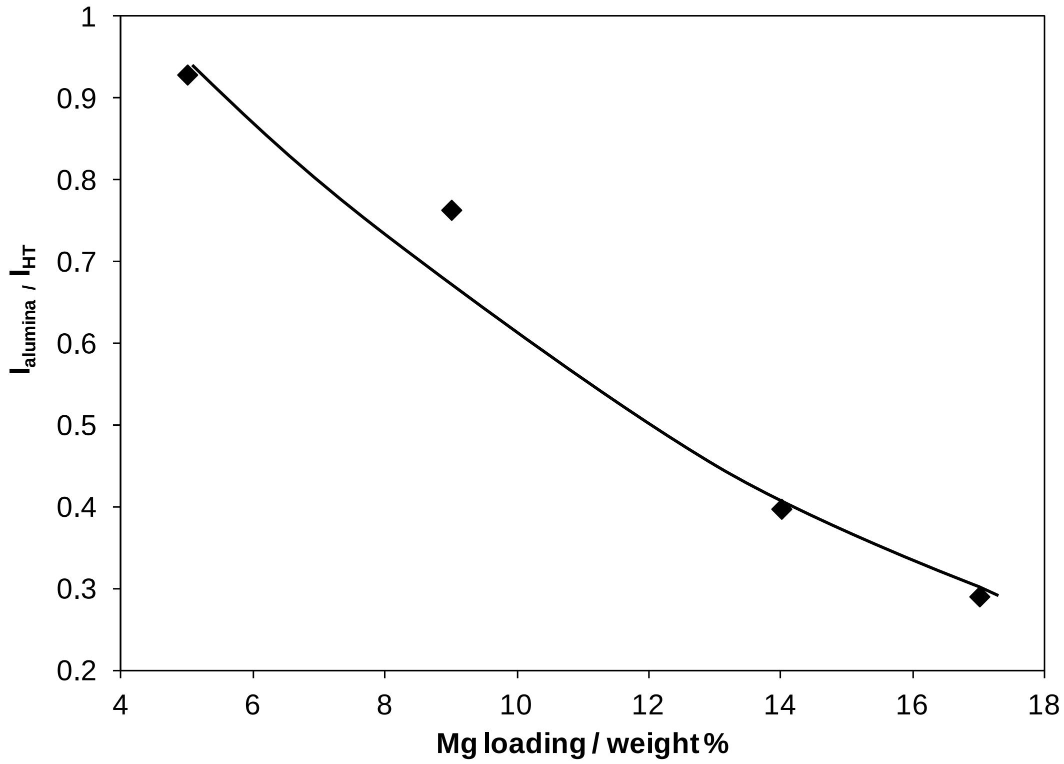

Figure 4.12. Graph showing the ratio of the HT/alumina Al 2p XPS intensities versus Mg loading.

The decrease in alumina intensity provides evidence that a grafting process is occurring. If some alumina had dissolved and formed hydrotalcite crystallites in solution away from the bulk alumina, the decrease in the alumina signal intensity would not be visible, as there would be a large amount of bulk alumina remaining.

However, by observing **Figure 4.12** it can also be determined that monolayer formation has not occurred. If this was the case, then the alumina intensity would drop much more dramatically, reaching zero by a few HT monolayers.

Theoretically, an estimate of the number of monolayers of hydrotalcite that should have formed on the alumina surface can be calculated. The unit cell of a 2:1 Mg:Al hydrotalcite, shown in **Figure 4.13**, has dimensions of 3 × 3 × 22 Å.

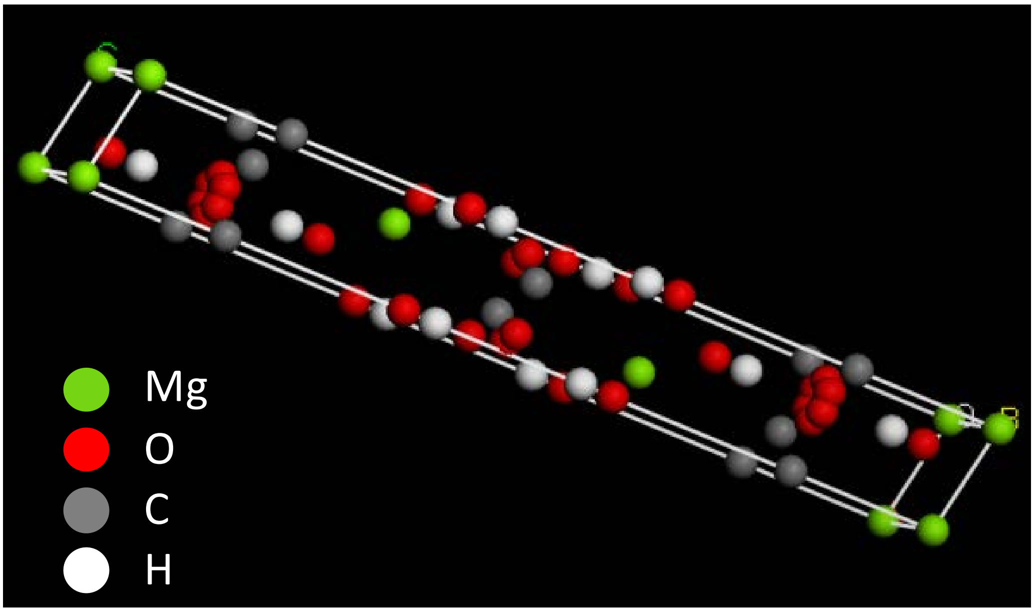

Figure 4.13. Diagram of the unit cell of a 2:1 Mg:Al hydrotalcite, with space group R-3m.[37]

The surface area of 3 × 3 Å contains 1 Mg atom. Therefore to coat 9 $Å^2$ of the alumina surface with one monolayer of 2:1 Mg:Al hydrotalcite when Al is incorporated into the lattice would require 2/3 Mg atom.

Therefore, to coat the 550 m^2 of alumina added in the prep. with 1 monolayer of hydrotalcite requires $((550 \times 10^{20}) / 9) \times 2/3$ Mg atoms. **Table 4.7** tabulates these calculations and shows the theoretical number of monolayers of 2:1 Mg:Al HT on the alumina surface for each Mg wt% material, taking into account the number of Mg atoms added in the synthesis.

Table 4.7. Monolayer calculations for the HT on alumina series.

Bulk Mg wt%	5 %	9 %	14 %	17 %
No. of Mg atoms added in prep.	9.92×10^{21}	1.98×10^{22}	3.97×10^{22}	4.96×10^{22}
Mg:Al ratio of HT formed	1.79	1.9	2.13	2.08
Mg atoms required for 1 monolayer	3.52×10^{21}	3.73×10^{21}	4.19×10^{21}	4.08×10^{21}
Theoretical monolayers	2.82	5.30	9.48	12.13

Therefore enough Mg is added to be in a multilayer formation regime even at the lowest Mg weight percentage, if the hydrotalcite is forming in layers. As this is not the case, a different theory is required for the formation of hydrotalcite on the alumina surface. The hydrotalcite is most likely forming as islands on the alumina surface, with areas of exposed alumina remaining. These HT crystallite islands will grow in height and width with increasing Mg wt%, as the constant composition means that each time more Mg is added, more HT must form, but will not fully coat the alumina surface. This theory of hydrotalcite formation is illustrated in **Figure 4.14**.

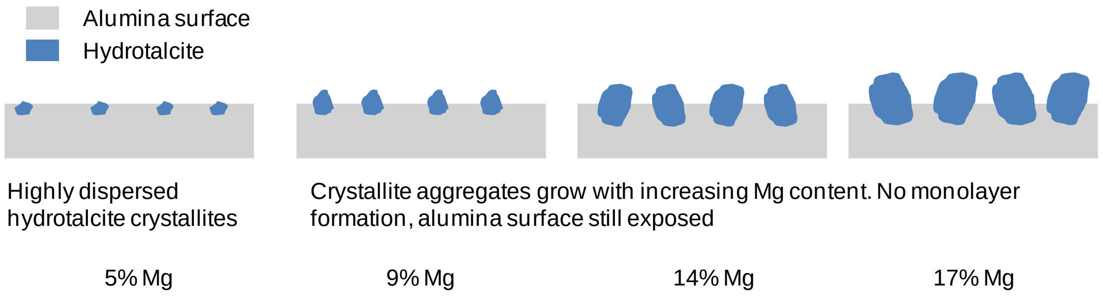

Figure 4.14. Cartoon depicting the proposed theory of formation of HT on the alumina surface.

This theory, and the lack of monolayer formation, can be supported by measuring peak intensity ratios in the XRD spectra of the HT on alumina series and comparing them to those of bulk conventional hydrotalcite, as reported in **Table 4.8**.

Table 4.8. XRD peak intensity ratios for the HT on alumina series and convHT.

Catalyst	d(003):d(006) intensity ratio	d(003):d(110) intensity ratio
5 wt% Mg	1.09	0.68
9 wt% Mg	1.17	0.83
14 wt% Mg	1.34	1.17
17 wt% Mg	1.38	1.19
ConvHT	1.09	0.87

If the hydrotalcite had coated the alumina and was only a few monolayers thick, there would be large differences in the intensity of the XRD peaks when compared to the convHT, depending on the plane direction; planes cutting through the hydrotalcite layer parallel to the alumina surface giving very high intensities, with planes perpendicular to the alumina surface not giving XRD peaks due to the very thin monolayer. Through observation of the XRD profiles in **Figure 4.2**, this does not appear to be the case, and by comparing the ratios in **Table 4.8**, it can be observed that there are no major differences between the bulk convHT and the HT on alumina series. The increase seen on increasing Mg weight percent will be due to the increasing size of the HT "islands".

Figure 4.15 shows the O 1s chemical environments for the HT on alumina series.

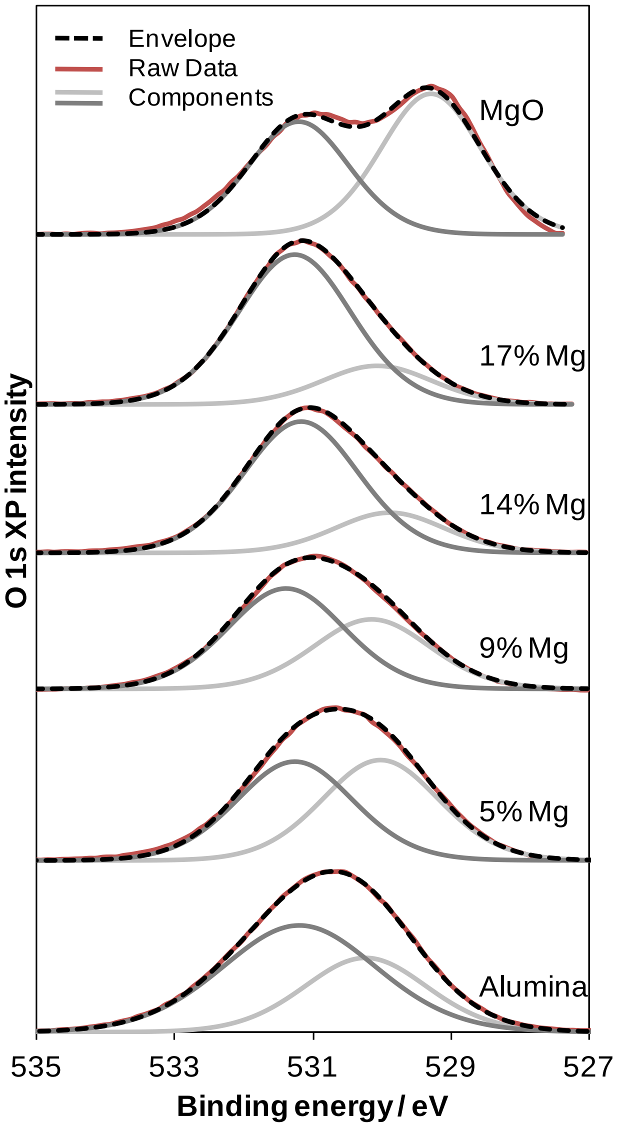

Figure 4.15. XP spectra showing a) the C 1s chemical environments and b) the O 1s chemical environments for the HT on alumina series.

The O1s peak has two components. The lower binding energy component is due to oxides MgO or Al_2O_3. The higher binding energy peak is due to oxygen bound in hydrotalcites or hydroxide bonds. As Mg content increases, the amount of oxygen bound in the hydroxide/hydrotalcite component increases, due to the increasing hydrotalcite content.

4.2.2 Transesterification of triglycerides

The series of hydrotalcites on alumina were tested as catalysts in the transesterification of triglycerides to form FAME, the reaction used to synthesise biodiesel, as described in **Chapter 2**. Briefly, 50 mg of catalyst was added to 10 mmol of triglyceride, using a 30:1 methanol: oil ratio. Butanol was also used as a co-solvent in all reactions to help solubilise the longer chained triglycerides. The reactions were carried out at 60 ºC and aliquots were removed from the reaction at various time intervals and analysed using a GC, in order to plot triglyceride conversion and FAME formation over 24 hours.

The triglyceride chain length was varied to examine the effect of increasing triglyceride bulk on the catalyst activity, from C4 up to C18, tending towards that of a real biodiesel feedstock.

4.2.2.1 Tributyrin transesterification (C4 chain TAG)

The full series of HT on alumina catalysts were tested in the transesterification of tributyrin, a short chained C4 triglyceride. The tributyrin conversion profile, along with the methyl butyrate and intermediate formation profiles can be seen below in **Figures 4.16 - 4.19**. The reaction data is reported in **Table 4.9.**

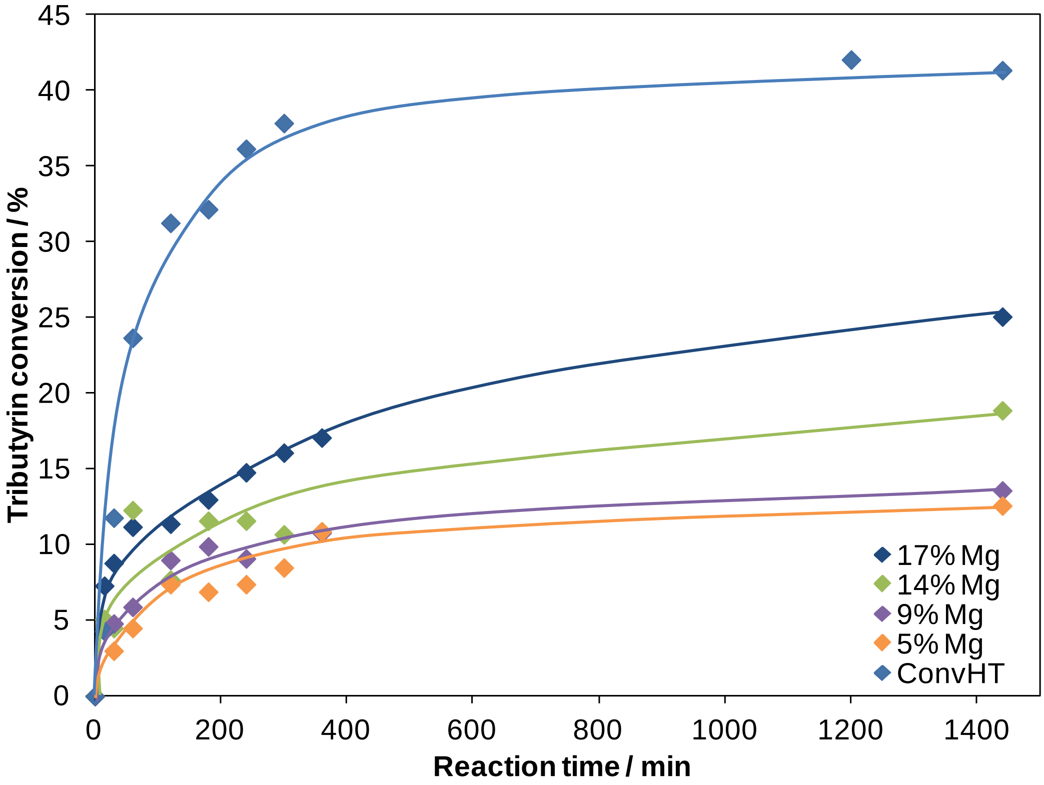

Figure 4.16. Reaction profiles showing tributyrin transesterification over time for the HT on alumina series. The convHT profile has been added for comparison.

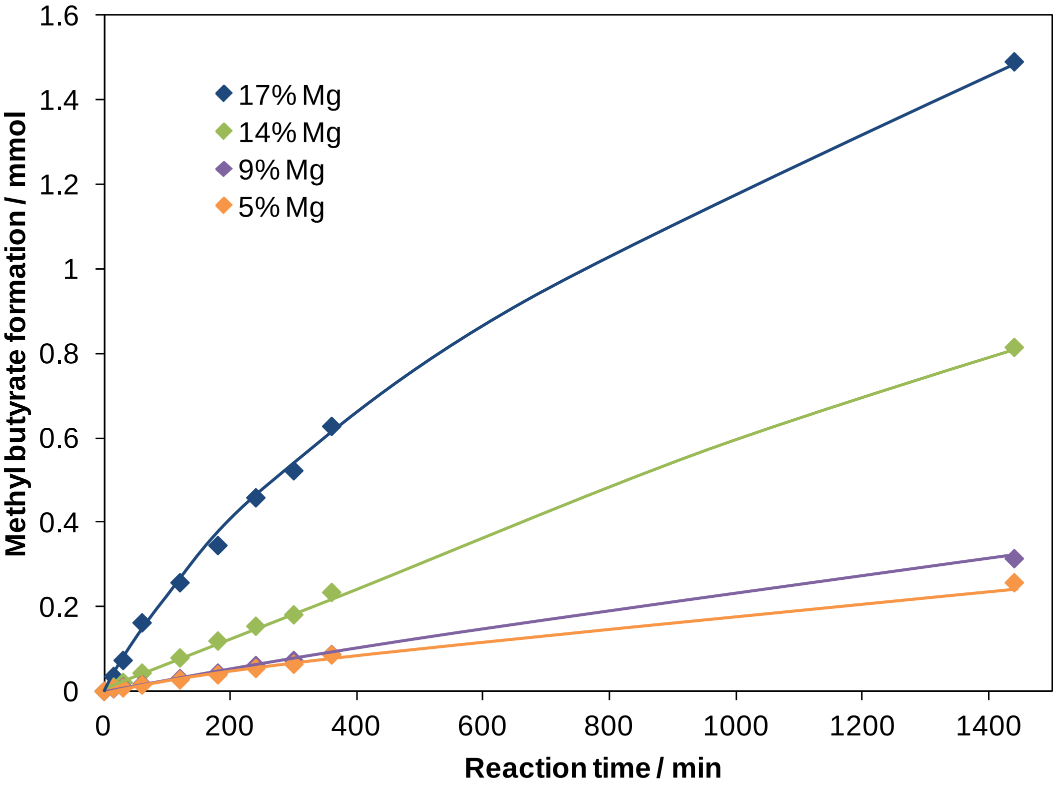

Figure 4.17. Methyl butyrate formation over time for the HT on alumina series during the transesterification of tributyrin.

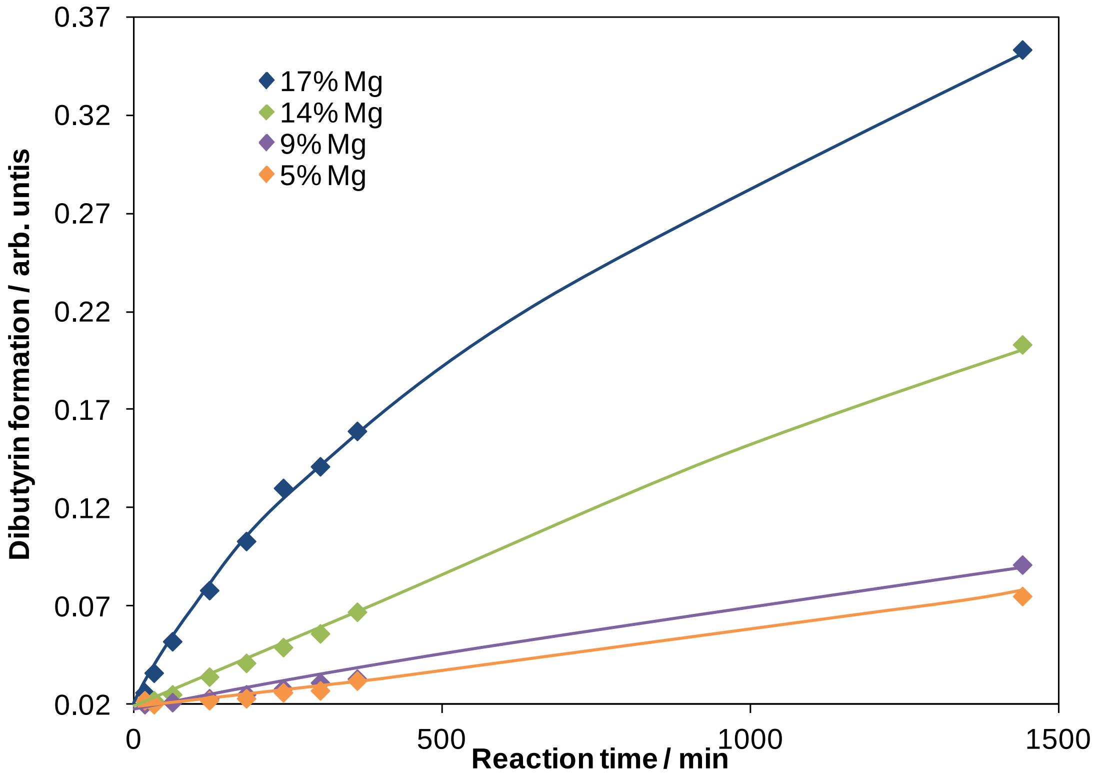

Figure 4.18. Intermediate dibutyrin formation over time for the HT on alumina series during the transesterification of tributyrin.

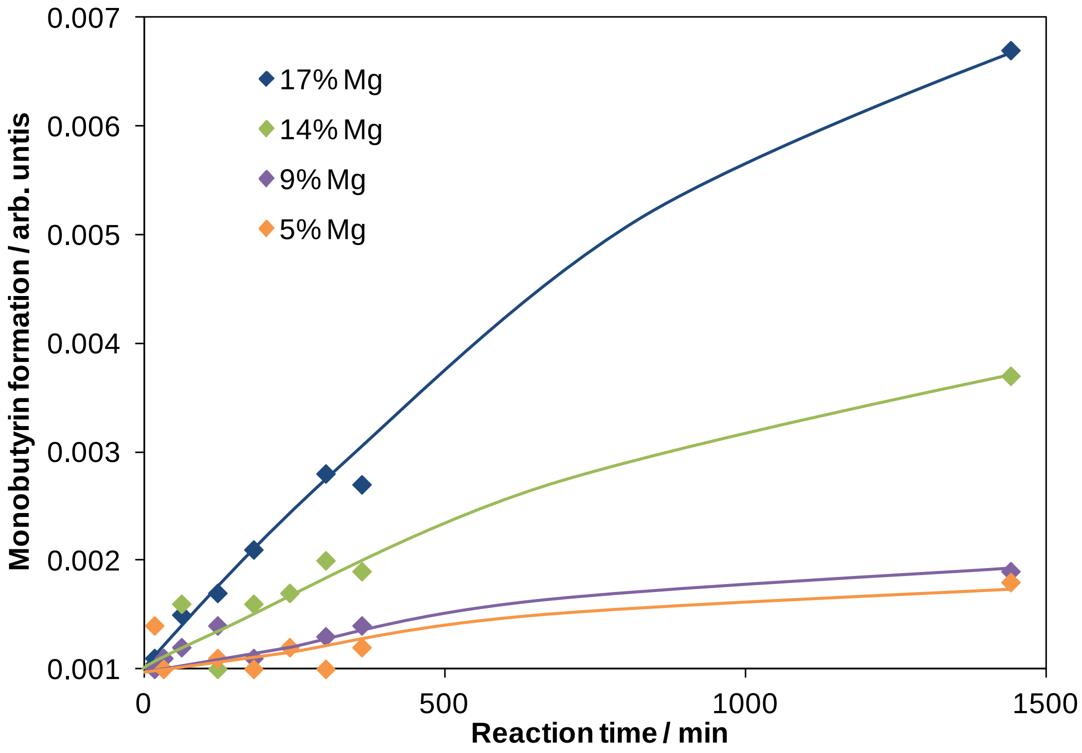

Figure 4.19. Intermediate monobutyrin formation over time for the HT on alumina series during the transesterification of tributyrin.

Table 4.9. Reaction data for the HT on alumina series compared to convHT for the transesterification of tributyrin.

Catalyst	Initial rate / mmol g^{-1} min^{-1}	TOF / min^{-1}	TAG conversion after 24 h / %	MB selectivity after 24 h / %
5% Mg	0.15+/- 0.01	19.01	12.6 +/- 1.5	6.8 +/- 1.5
9 % Mg	0.21 +/- 0.03	19.67	13.6 +/- 1.5	7.7 +/- 1.5
14 % Mg	0.40 +/- 0.02	19.42	18.9 +/- 1.5	14.4 +/- 1.5
17 % Mg	0.66 +/- 0.03	18.22	25.1 +/- 1.5	19.8 +/- 1.5
ConvHT	0.78 +/- 0.01	5.49	42.1 +/- 1.5	43.0 +/- 1.5
MacroHT	2.18 +/- 0.02	17.06	65.0 +/- 1.5	43.4 +/- 1.5

The initial rate increases across the series with increasing Mg content. However, the TOF values, when normalised to base site density, remain fairly constant across the series. This suggests that the strength of the base sites remain the same across the series of the materials, which supports the earlier characterisation data showing that the Mg:Al ratio remains constant across the series, with just the amount of hydrotalcite material and number of base sites increasing.

Although the overall conversions, and therefore selectivities, are lower than for the convHT, this is due to the low number of base sites due to the presence of the alumina support. When the TOF values, activity normalised to base sites, are compared, the hydrotalcites on alumina greatly outperform the convHT. The materials have the same stoichiometry and very similar base site strength, therefore any activity enhancement for the HT on alumina catalysts compared to convHT must be due to greater base site accessibility. The HT on alumina catalysts will have large voids on the open alumina surface between crystallite islands, removing the diffusion limitations observed for the convHT. The HT on alumina catalysts also have a much greater crystallinity and surface area due to being formed on the high surface area alumina support. Therefore there will be a much larger number of readily accessible hydroxide anions at the edge sites of the hydrotalcites.

4.2.2.2 Tricaprylin transesterification (C8 chain TAG)

The series of hydrotalcites on alumina were then tested in the transesterification of tricaprylin, a C8 chain length triglyceride. The tricaprylin conversion, methyl caprylate (MC) formation and intermediate formation profiles can be seen in **Figures 4.20-4.22.** The reaction data is reported in **Table 4.10**.

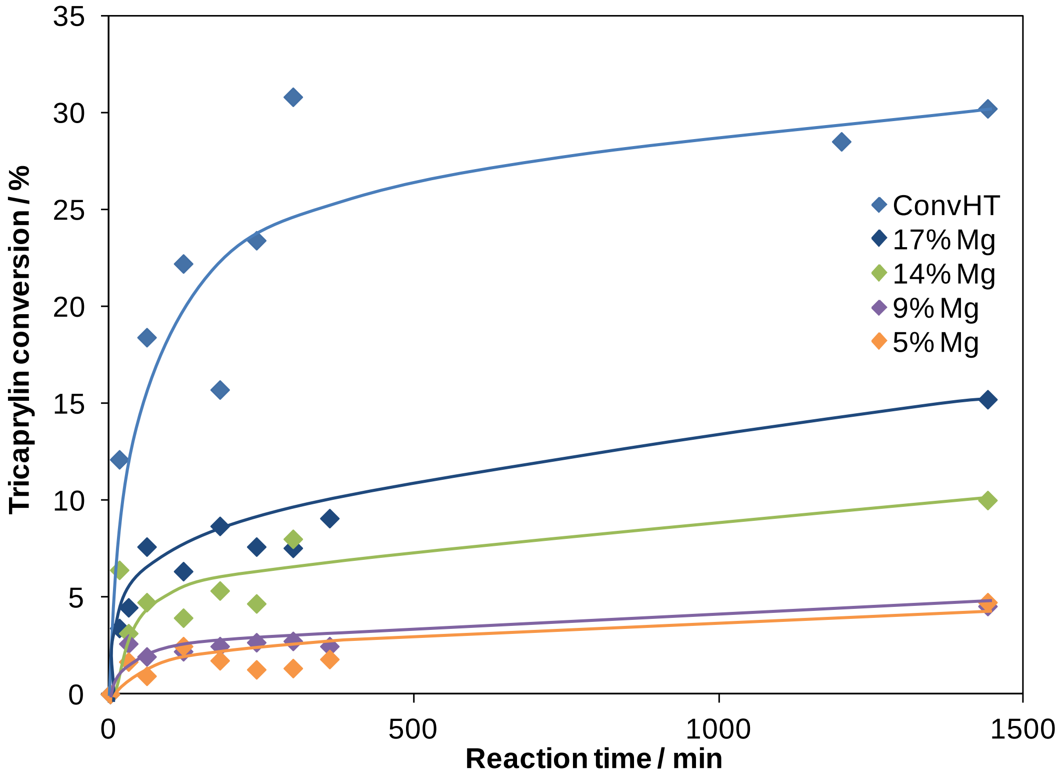

Figure 4.20. Reaction profiles showing tricaprylin transesterification over time for the HT on alumina series. The convHT profile has been shown for comparison.

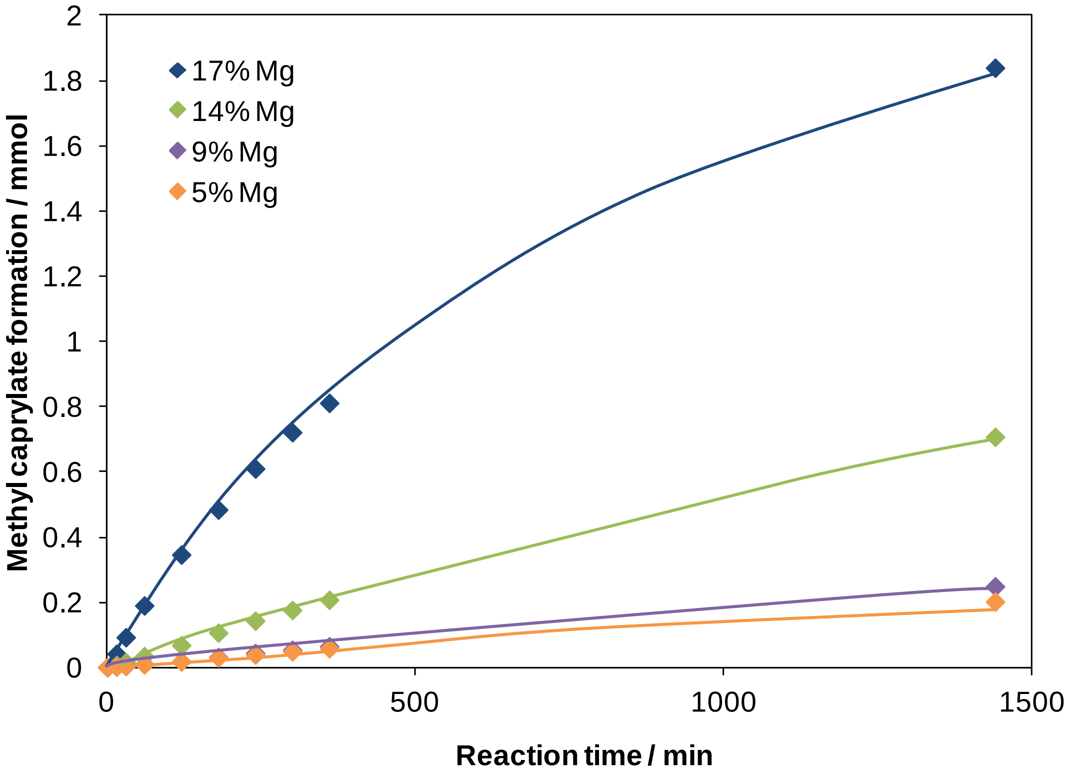

Figure 4.21. Methyl caprylate formation over time for the HT on alumina series during the transesterification of tricaprylin.

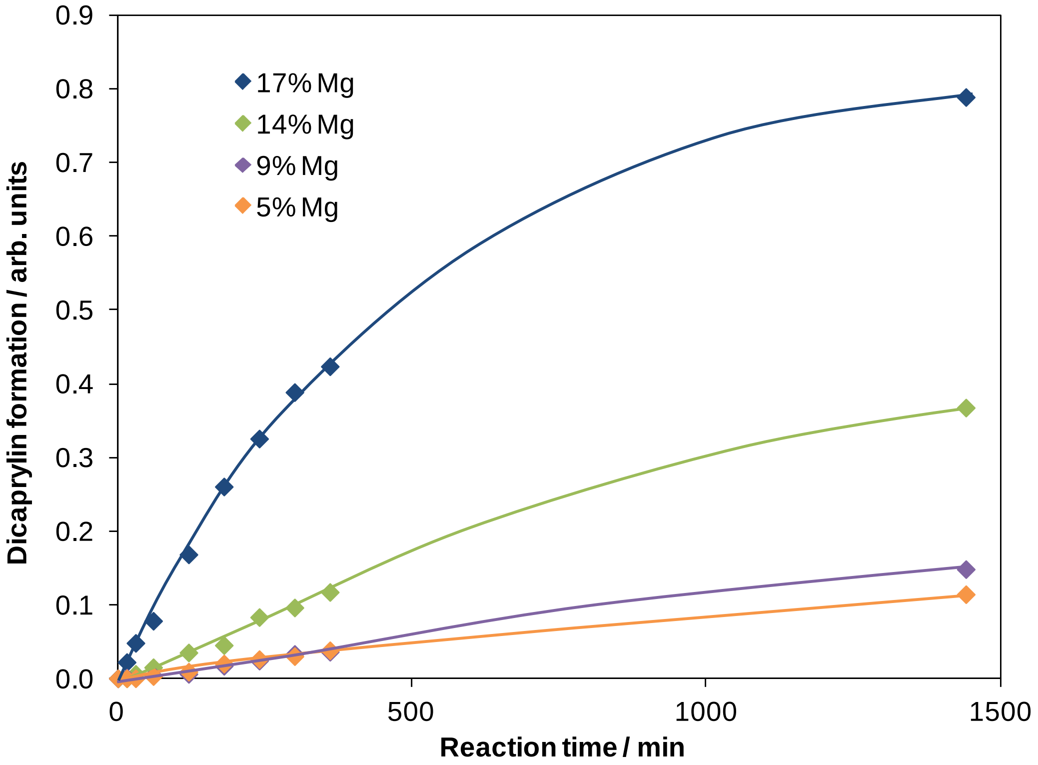

Figure 4.22. Intermediate dicaprylin formation over time for the HT on alumina series during the transesterification of tricaprylin.

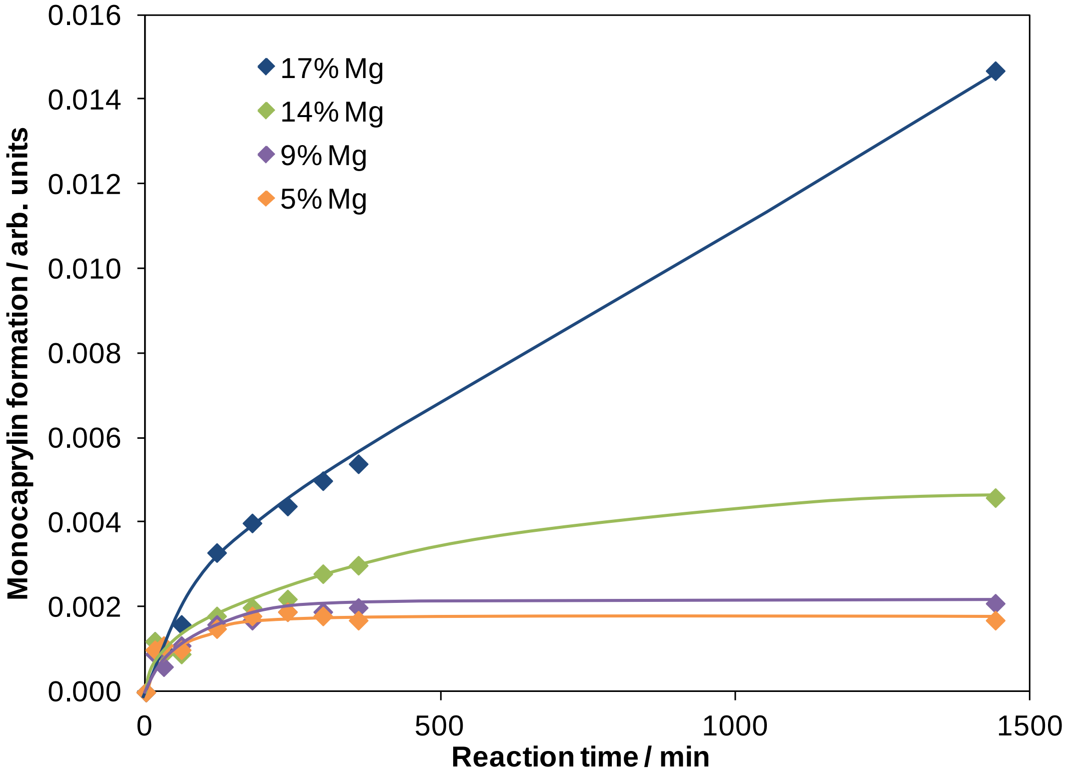

Figure 4.23. Intermediate monocaprylin formation over time for the HT on alumina series during the transesterification of tricaprylin.

Table 4.10. Reaction data for the HT on alumina series and convHT for the transesterification of tricaprylin.

Catalyst	Initial rate / mmol g^{-1} min^{-1}	TOF / min^{-1}	TAG conversion after 24 h / %	MC selectivity after 24 h / %
5% Mg	0.10 +/- 0.02	8.73	4.7 +/- 1.5	14.2 +/- 1.5
9 % Mg	0.16 +/- 0.03	9.93	4.5 +/- 1.5	18.0 +/- 1.5
14 % Mg	0.30 +/- 0.05	9.66	10.0 +/- 1.5	23.6 +/- 1.5
17 % Mg	0.49 +/- 0.09	9.05	15.2 +/- 1.5	40.4 +/- 1.5
ConvHT	0.42 +/- 0.13	2.98	30.2 +/- 1.5	54.3 +/- 1.5
MacroHT	1.33 +/- 0.09	10.43	50.7 +/- 1.5	55.7 +/- 1.5

Again, the TOF values are very similar across the HT on alumina series, and are still about three times greater than for the convHT. However, on moving from a C4 to a C8 chain triglyceride, the TOF values have decreased for the HT on alumina series, as for the convHT, due to the slower movement, and decreased solubility in methanol, of the bulkier TAG.

The selectivity to methyl caprylate has increased for the HT on alumina series compared to the selectivity values to methyl butyrate in the C4 transesterification. The intermediate DAG and MAG molecules will be smaller than the tricaprylin, therefore will move faster and react faster. This will not be as obvious for the less bulky C4 TAG. For the C8, a greater proportion of FAME is produced for each molecule of TAG converted than for C4.

4.2.2.3 Triolein Transesterification (C18 chain TAG)

Due to the low number of base sites in the two lowest Mg loading HT on alumina samples, and therefore the very low percentage conversions, only the 14 wt% Mg and 17 wt% Mg catalysts were tested in the triolein transesterification, in order to obtain accurate results. The triolein conversion and methyl oleate formation profiles can be seen in **Figure 4.24** and **Figure 4.25.** The reaction data is reported in **Table 4.11**.

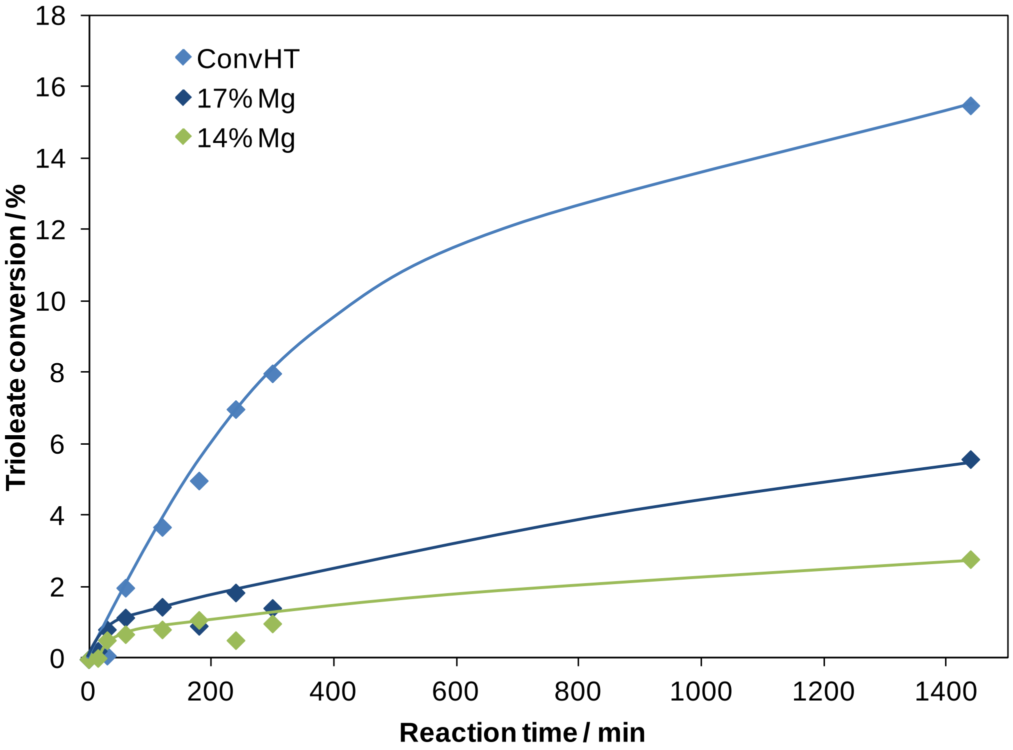

Figure 4.24. Reaction profiles showing triolein transesterification over time for the HT on alumina series, with the convHT profile included for comparison.

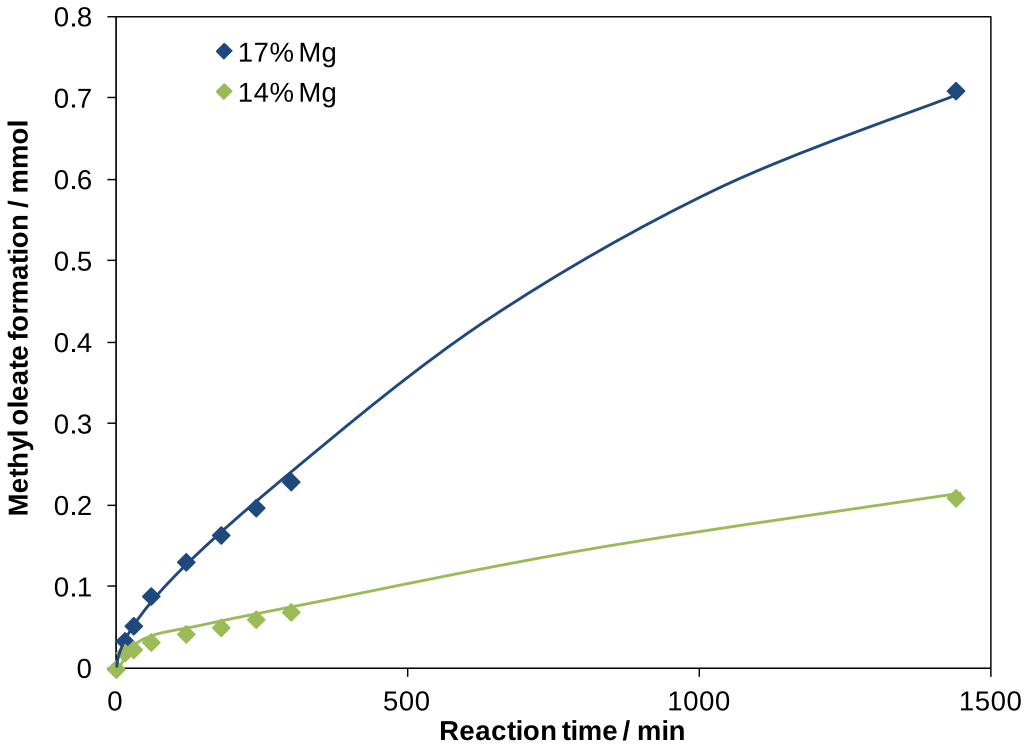

Figure 4.26. Methyl oleate formation over time for the HT on alumina series during the transesterification of triolein.

Table 4.11. Reaction data for the HT on alumina series and convHT in the transesterification of triolein.

Catalyst	Initial rate / mmol g^{-1} min^{-1}	TOF / min^{-1}	TAG conversion after 24 h/%	FAME selectivity after 24 h / %
14 % Mg	0.024 +/- 0.002	1.16	2.8 +/- 1.5	26 +/- 1.5
17 % Mg	0.042 +/- 0.004	1.15	5.6 +/- 1.5	42 +/- 1.5
ConvHT	0.026 +/- 0.01	0.18	15.5 +/- 1.5	67 +/- 1.5
MacroHT	0.22 +/- 0.006	1.73	26.1 +/- 1.5	73 +/- 1.5

Again, there has been a large decrease in TOF on moving to the bulkiest triglyceride. The TOF values for the C18 triglyceride are only 10 % of those for the C4, due to the general decrease in rate of diffusion of the bulky TAG through the reaction mixture to the catalyst. However, the catalysts are still much more active than those of the conventional hydrotalcite, and the decrease in TOF is less for the HT on alumina samples than it is for the convHT. The effect of easier access through the voids to the greater number of hydroxide base sites at crystallite edge sites for the HT on alumina catalysts becomes more noticeable for the reactions with the greatest diffusion limitations.

4.2.2.4 Comparison of TOF values

Figure 4.26 shows a plot of TOF values for the HT on alumina series for the varying chain length triglyceride transesterifications. The TOF values for both the convHT and macroHT can also be observed on the chart.

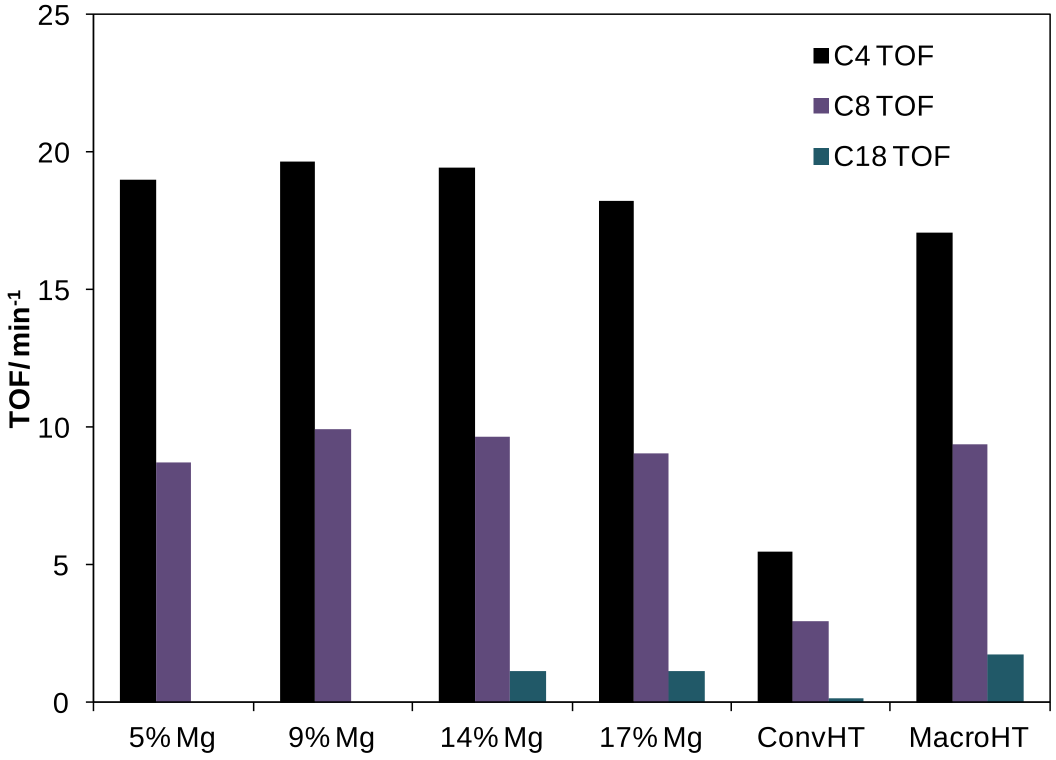

Figure 4.26. Chart showing TOF values for the HT on alumina series compared to the convHT and macroHT samples in varying chain length triglyceride transesterifications. The 5% and 9% Mg catalysts were not measured for the C18 transesterification.

The activities of the HT on alumina series and the macroHT series are very similar, producing virtually identical TOFs across a series of TAG chain length screenings. As discussed in **Chapter 3**, the macroHT has no mass transfer limitations and the base sites are readily accessible to the TAGs which is why it outperforms the convHT.

The same observation can therefore be made about the HT on alumina series. The HT crystallites are sat on the large, open space of the alumina surface, with large pores between the HT crystallites. Unlike the convHT, where a lot of the base sites are deep in the bulk of the material and inaccessible to TAGs, for the HT on alumina series the HT material is all at the surface and much more easily accessible.

The decrease in TOF on moving from C4 to C18 is due to the bulkier triglycerides moving more slowly, as well as being less soluble in methanol, and are therefore reacting more slowly.

4.2.2.5 Triglyceride conversion versus FAME selectivity

Figure 4.27 shows a plot of conversion versus selectivity for the 14 wt% and 17 wt% Mg HT on alumina catalysts as well as convHT and macroHT in varying chain length TAG transesterifications.

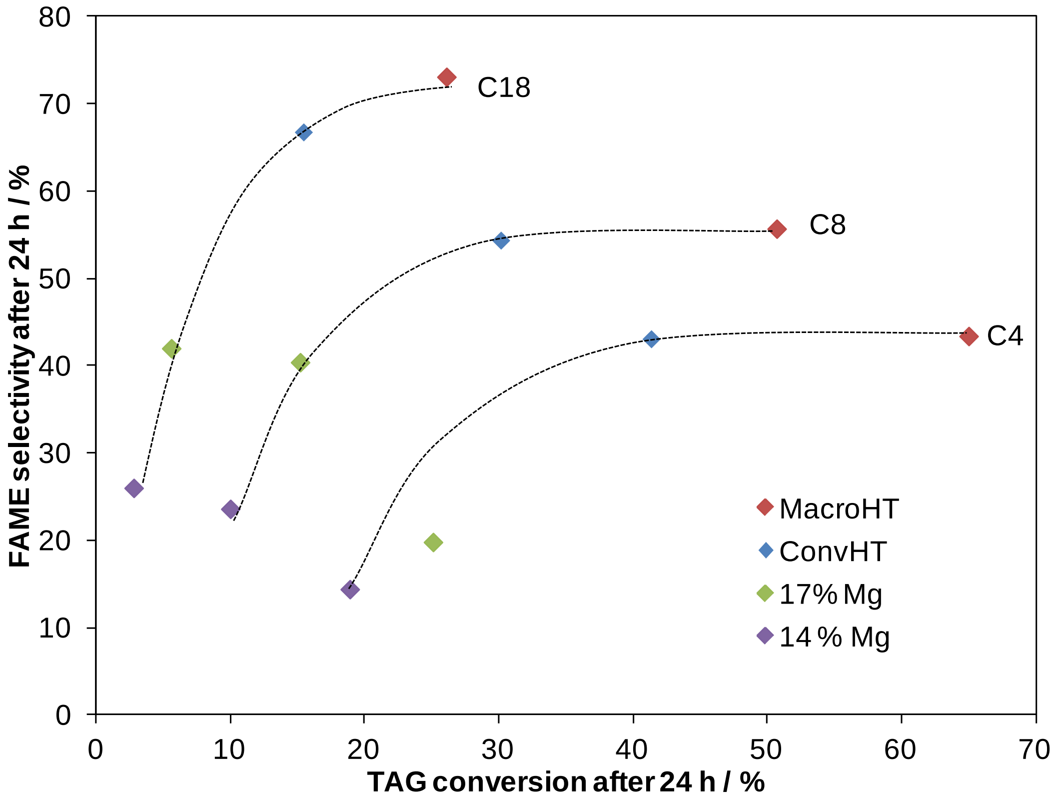

Figure 4.27. Plot of TAG conversion versus FAME selectivity after a 24 hour reaction for convHT, macroHT, and the 14 wt% Mg and 17 wt% Mg HT on alumina catalysts in varying TAG chain length transesterification reactions.

For each TAG a trend of increasing FAME selectivity with increasing catalyst conversion is observed. The lines of best fit start to level off above about 40 % conversion. The side product of FAME production is glycerol, which over time starts to block some of the active sites and slow down the reaction. By observing the reaction profiles it can be seen that after a few hours the rate of conversion becomes much slower and almost levels off. Therefore the macroHT catalyst may have a faster initial rate and convert more TAG quickly at the start of a reaction, however as glycerol production builds up, FAME production will slow down more quickly than for convHT, meaning that the overall selectivity after 24 hours is not much higher than for the convHT.

For each catalyst, on moving to longer chain length bulkier TAGs, with slower diffusion and decreased solubility in methanol, the conversion of the TAG decreases. However, on observing **Figure 4.27**, it can be seen that although conversion decreases, the selectivity to FAME actually increases. As the TAG chain length increases the corresponding DAGs become much less soluble in methanol. For example, diolein is much less soluble than dibutyrin in methanol, and also diffuses much more slowly. Therefore, once it reaches the pores of the catalyst and the active sites, it is less likely to leave as quickly and so further reactions can occur and higher FAME selectivities are achieved.

4.2.3 Spent catalyst characterisation

Characterisation was carried out on the series of HT on alumina catalysts, after recovery from a 24 hour C4 transesterification reaction, in order to determine information about how use in a reaction affects the structure and composition of the materials. After filtration from the reaction mixture, the catalysts were dried in a vacuum oven before being analysed using EDX, XRD and XPS.

4.2.3.1 EDX

The bulk Mg:Al ratios and Mg weight percentages for the spent catalysts compared to those of the fresh are reported in **Table 4.12**.

Table 4.12. Bulk Mg:Al ratios and Mg wt% values obtained for both fresh and spent HT on alumina catalysts via EDX analysis.

Bulk Mg content fresh catalyst series / wt%	Bulk Mg content spent catalyst series / wt%	Bulk Mg:Al ratio - fresh	Bulk Mg:Al ratio - spent
5.1 +/- 0.4	6.7 +/- 0.6	0.16:1	0.20:1
9.2 +/- 0.5	11.8 +/- 3.5	0.30:1	0.44:1
14.2 +/- 0.7	15.6 +/- 4.9	0.62:1	0.79:1
16.7 +/- 0.4	18.0 +/- 2.3	0.80:1	0.90:1

The bulk Mg:Al ratio is very similar in both sets of materials, therefore there is no evidence of magnesium leaching into solution during reaction.

4.2.3.2 XRD

The powder XRD diffraction patterns for the spent series of HT on alumina materials can be seen in **Figure 4.28**. The crystallite sizes, interlayer spacings, and lattice parameters for the series are reported in **Table 4.13**, along with the Mg:Al ratios extrapolated from the graph in **Figure 4.4** using lattice parameters.

Table 4.13. Crystallite sizes, interlayer spacings and lattice parameters for the spent HT on alumina series as determined via analysis of the XRD powder diffraction patterns.

Catalyst	Volume average crystallite size / nm	Interlayer spacing, *d* / nm	Lattice Parameter, *a* / Å	Mg:Al ratio extrapolated from **Fig.4.2**.
5% Mg-spent	25.8 +/- 2.1	0.75 +/- 0.01	3.043	1.60:1
9 % Mg-spent	19.0 +/- 1.5	0.76 +/- 0.01	3.044	1.66:1
14 % Mg-spent	32.7 +/- 2.6	0.76 +/- 0.01	3.046	1.79:1
17 % Mg-spent	26.8 +/- 2.3	0.76 +/- 0.01	3.047	1.87:1

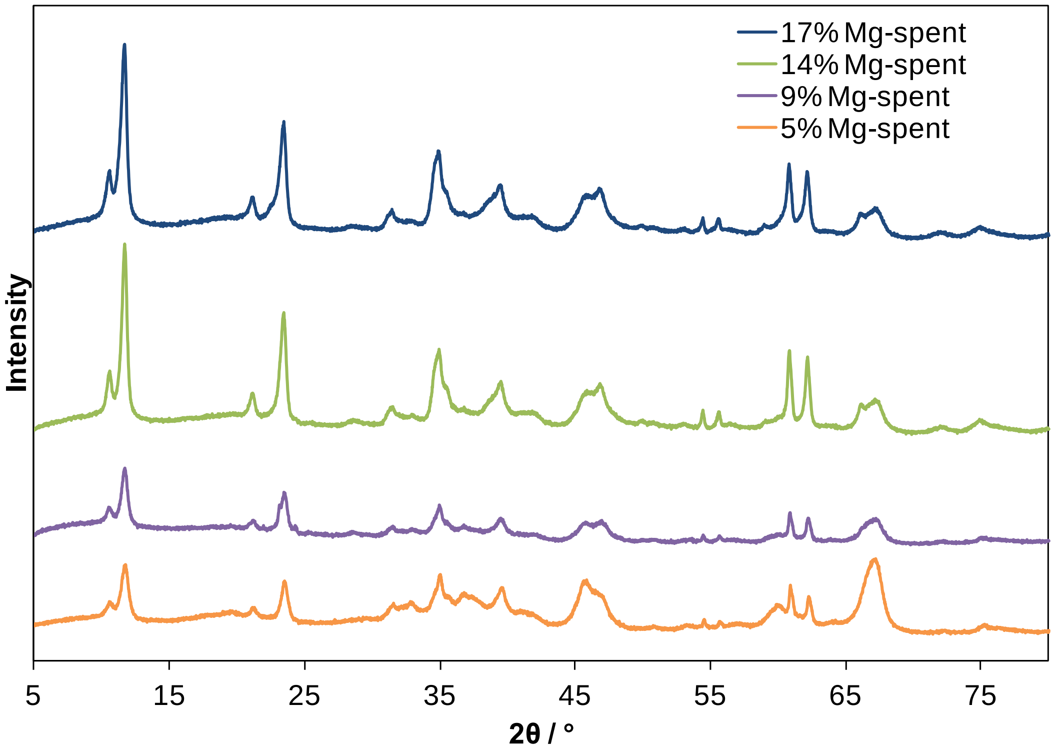

Figure 4.28. XRD analysis of the HT on alumina series after recovery from a 24h tributyrin transesterification reaction.

The spent XRD profiles all still show the characteristic hydrotalcite patterns. The hydrotalcite crystallite sizes have decreased slightly after a catalytic reaction meaning some of the ordering has been lost. However, the crystalline structure is still very ordered on the alumina surface. The interlayer spacings remain consistent with those of a hydrotalcite. The lattice parameter has decreased slightly. Therefore, when Vegard's law is applied, there is a decrease in bulk Mg:Al ratio after a 24 hour reaction. EDX has already shown that there is no loss of magnesium, and therefore this would indicate the incorporation of further aluminium into the hydrotalcite during the reaction.

Figure 4.29 shows plots of hydrotalcite XRD peak intensities and alumina XRD peak intensities for the fresh and spent HT on alumina series.

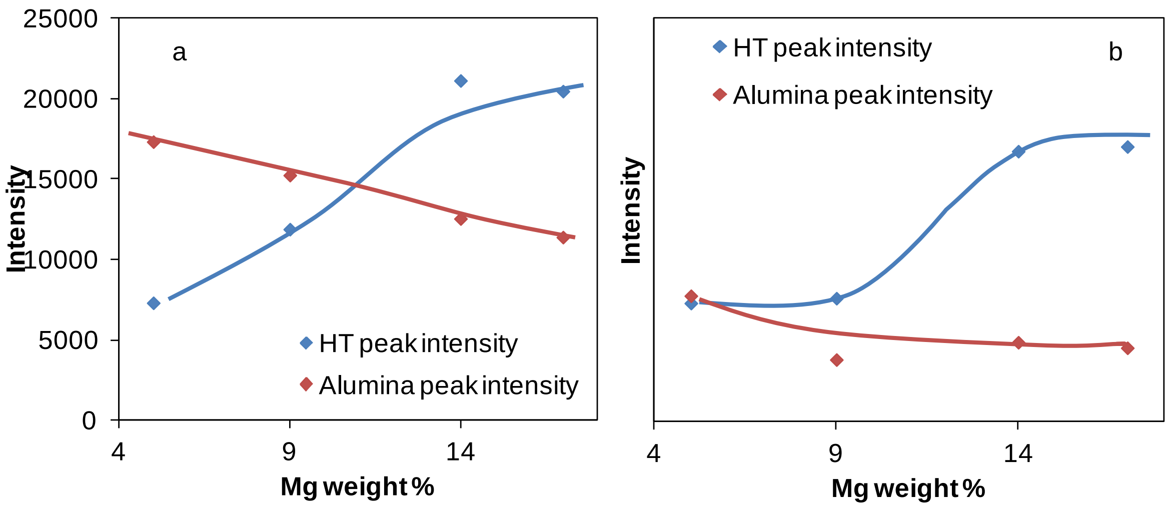

Figure 4.29. Plot showing hydrotalcite and alumina XRD peak intensities over Mg wt% for a) the fresh HT on alumina series and b) the spent HT on alumina series. The *y* axis is set to the same numerical scale in both plots.

The ratio of hydrotalcite: alumina peak intensities has increased greatly in the spent catalyst series, again giving evidence for further aluminium incorporation from alumina into the hydrotalcite crystallites.

4.2.3.3 XPS

XPS analysis was carried out on the spent series of materials. XP spectra for the Mg 2s regions comparing the fresh and spent set of catalysts can be seen in **Figure 4.30.**

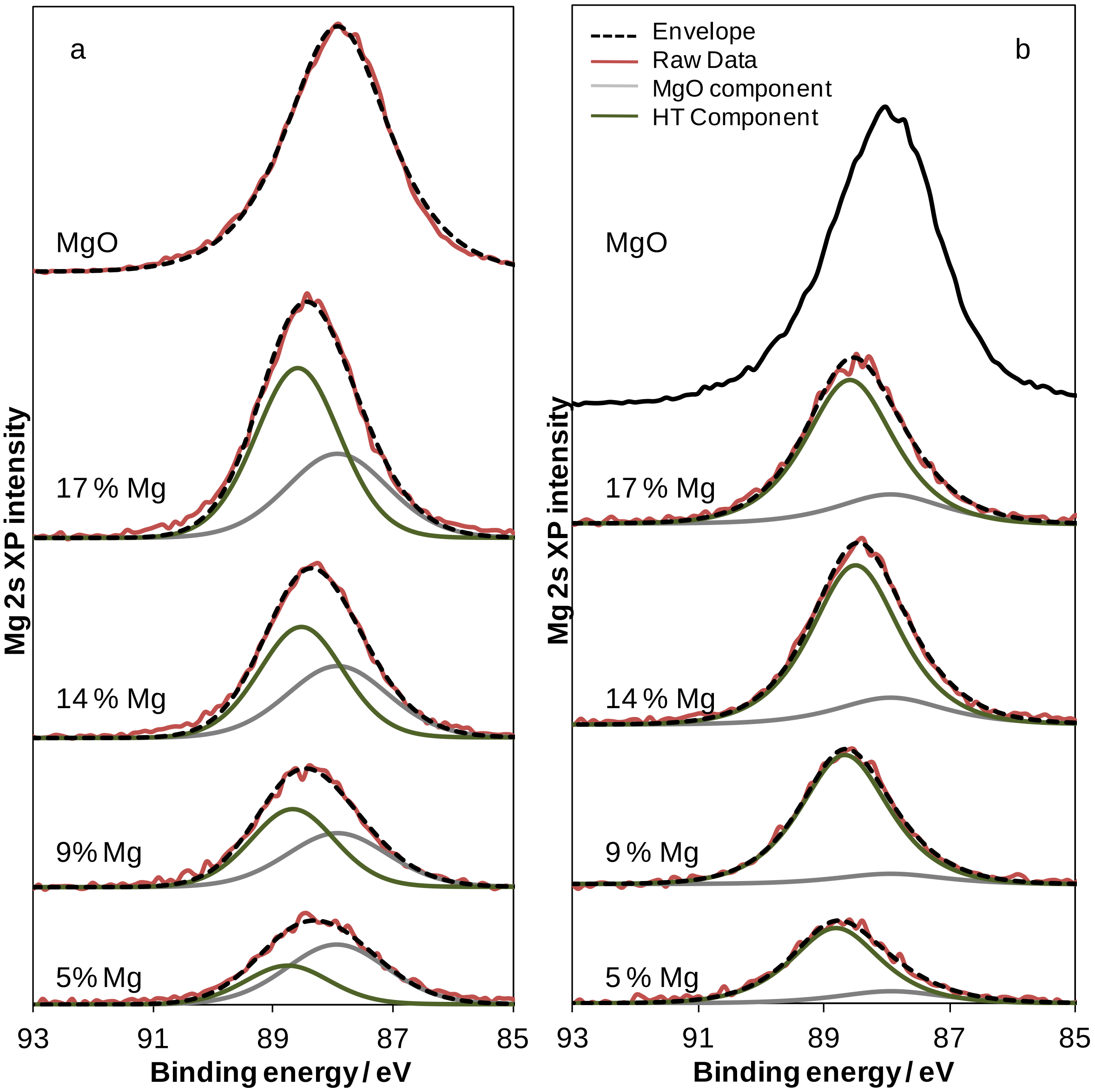

Figure 4.30. XP spectra showing the Mg 2s chemical environments for a) the fresh HT on alumina series and b) the spent HT on alumina catalyst series.

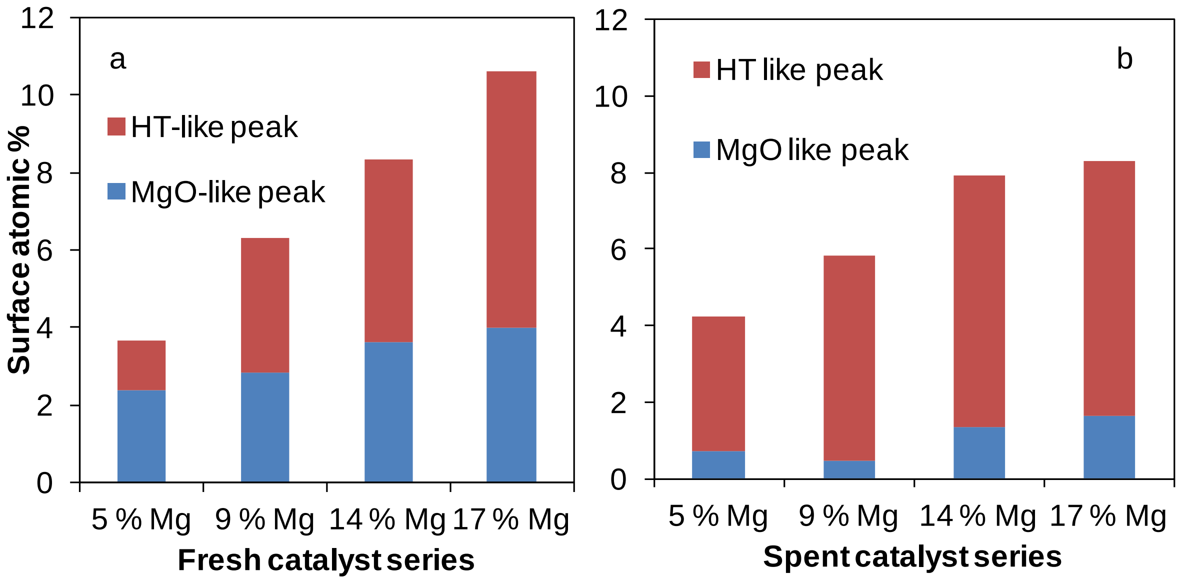

Figure 4.31. Bar chart indicating atomic percentages of surface Mg found as hydrotalcite and MgO in a) the fresh HT on alumina series and b) the spent HT on alumina series.

Figure 4.31 shows the proportion of the surface Mg found as MgO and as hydrotalcite for the spent materials taken from the XP spectra, alongside the results for the fresh materials. The amount of Mg on the surface has not changed greatly, however the proportion of the Mg found as hydrotalcite has increased noticeably, indicating that there has been some rearrangement of the material during the reaction to incorporate more magnesium into the hydrotalcite structure. The reaction conditions may have allowed for further hydrothermal treatment to form hydrotalcite from the areas of MgO on the alumina surface, incorporating more Mg into the hydrotalcite structure.

The XP spectra comparing the Al 2p chemical environments for the fresh and spent series of catalysts can be seen in **Figure 4.32**.

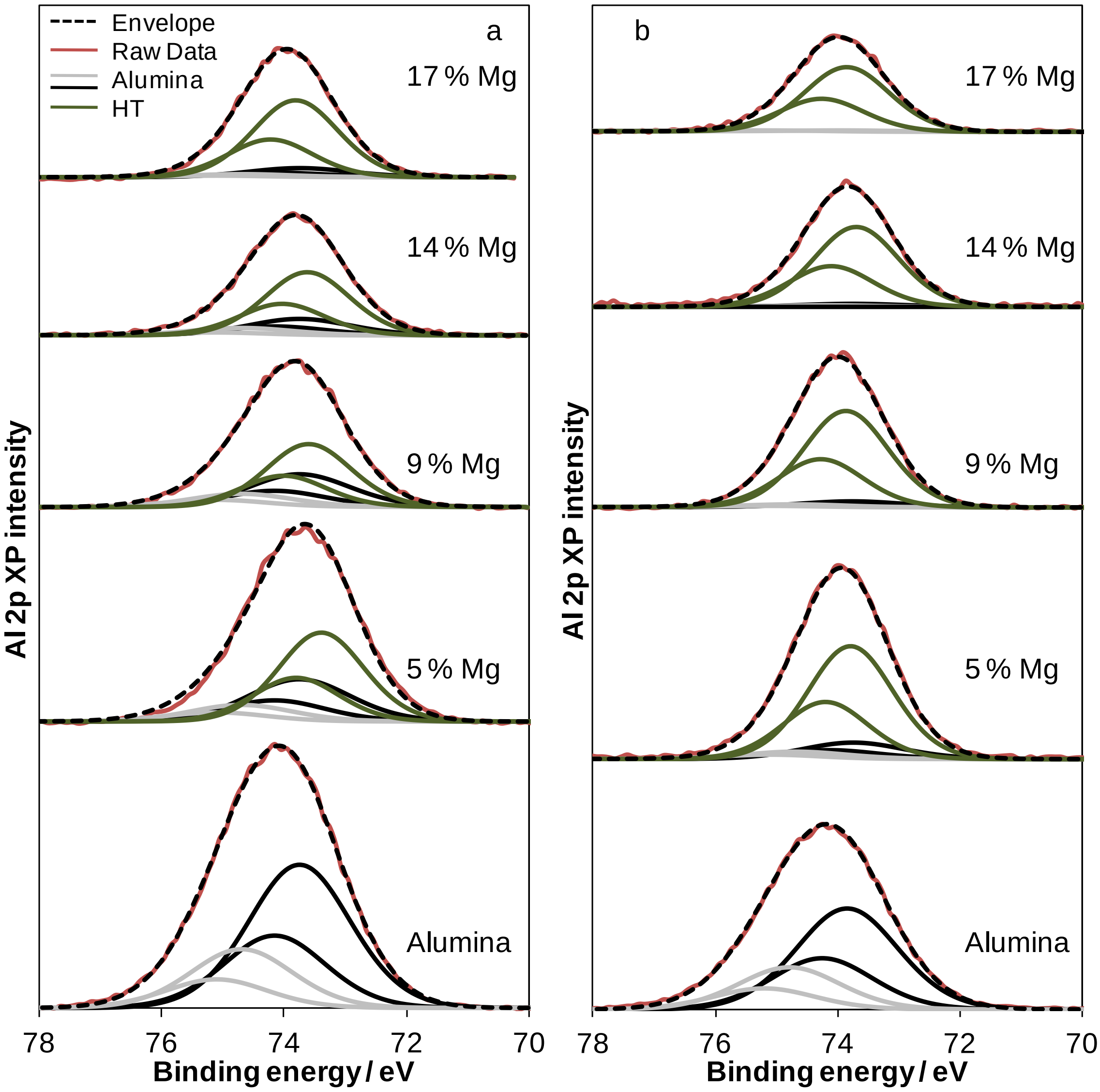

Figure 4.32. XP spectra showing the Al 2p chemical environments for a) the fresh HT on alumina series and b) the spent HT on alumina catalyst series.

Figure 4.33 shows the proportion of surface Al found as alumina or HT for the spent and fresh HT on alumina catalyst series.

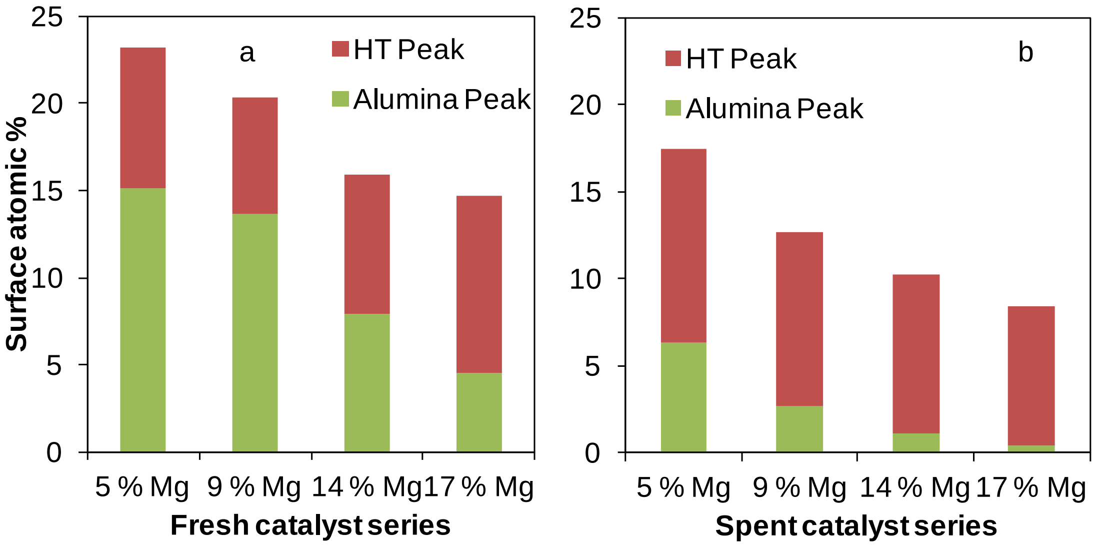

Figure 4.33. Bar chart indicating atomic percentages of surface Al found as hydrotalcite and alumina in a) the fresh HT on alumina series and b) the spent HT on alumina series.

A much greater proportion of the surface Al is now found as hydrotalcite, rather than alumina. This supports the earlier theory that during reaction conditions there is further ion exchange of both Al and Mg from the mixed oxides into hydrotalcite. The much greater supply of Al cations from the bulk alumina accounts for the decrease in bulk Mg:Al ratio observed through analysis of the XRD lattice parameters.

The raw XPS data and fittings for the O 1s regions of the fresh versus spent HT on alumina series can be seen in **Figure 4.34.** Two peaks have been fitted, one at lower binding energies due to mixed oxides and a higher binding energy peak accounting for oxygen found as hydroxide in the HT layered structure and interlayer anions. The amount of oxide surface material has decreased for the three lowest Mg loading samples, and has stayed the same for the highest Mg loading. Whilst there is still a lot of alumina at the surface, as is the case for the lower Mg loading samples, more alumina will rearrange to form hydrotalcite, therefore causing this greater difference in the fresh and spent oxide components at lower Mg loadings.

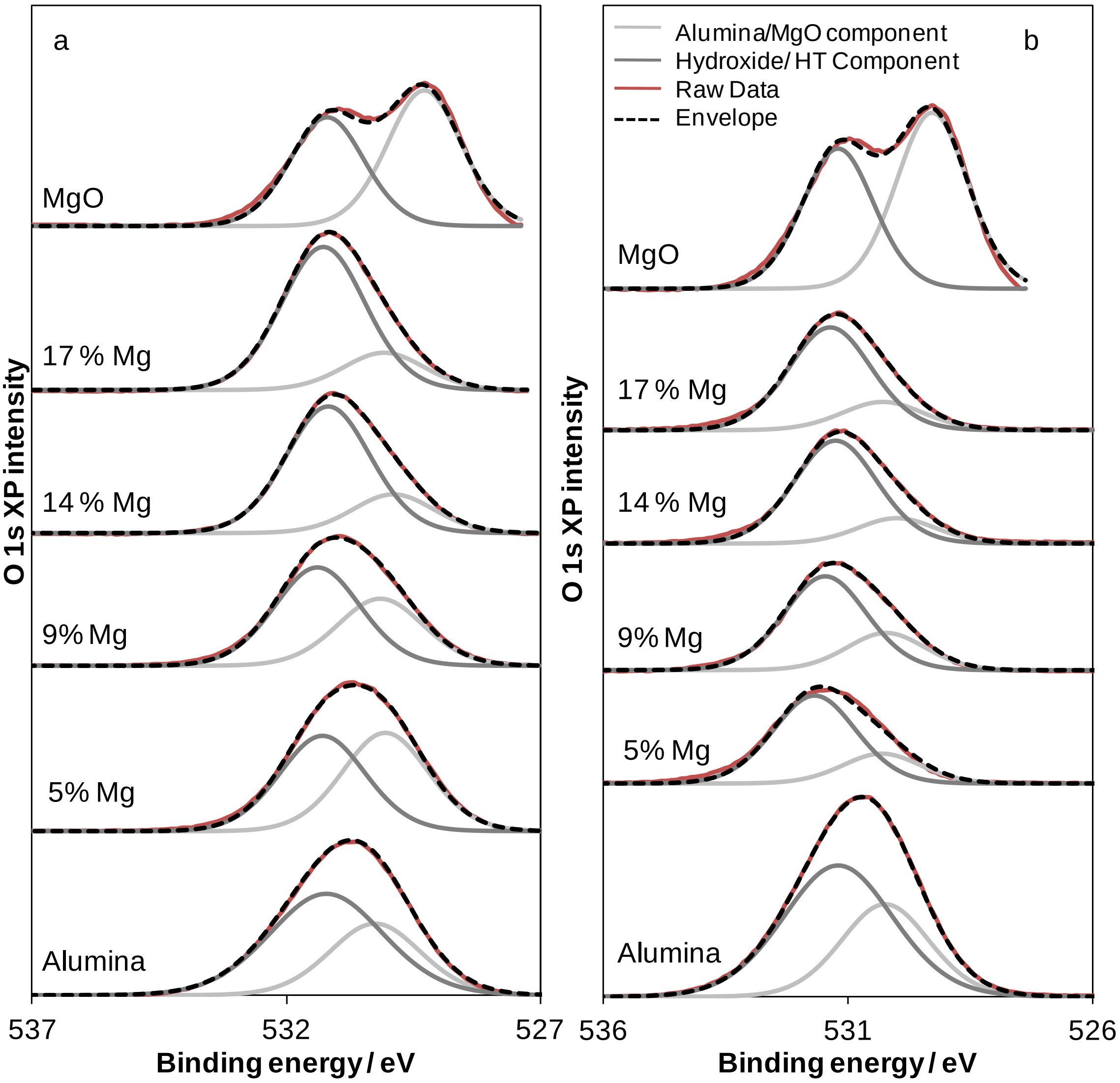

Figure 4.34. XP spectra showing the O 1s chemical environments for a) the fresh HT on alumina series and b) the spent HT on alumina catalyst series.

Figure 4.35 shows the C 1s XP spectra for both the fresh and spent HT on alumina series. The atomic percentages of carbon in the fresh and spent series are reported in **Table 4.15**. A new carbon component has appeared at binding energy 285.5 eV. This is assigned to the butyric acid anion, as this binding energy is associated with organic acids.[38] Therefore butyric acid, which forms as a side product during the transesterification reaction, is blocking the active sites by binding to the hydroxide anions. This effect could cause catalyst deactivation on re-use without a further calcination procedure. The carbon content increases across the series of spent catalysts, as the amount of binding organic content increases with increasing hydrotalcite content and hydroxide anions.

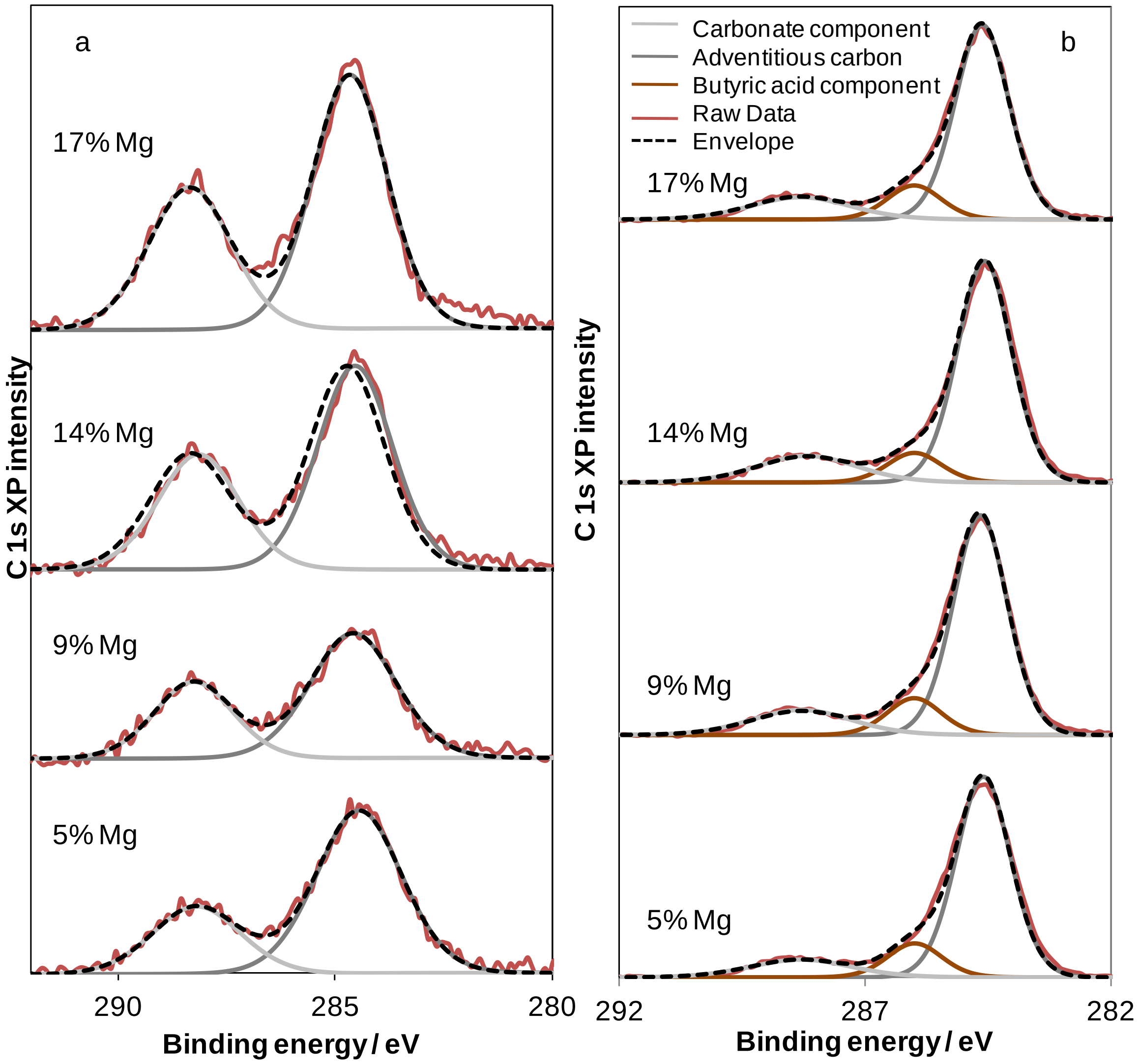

Figure 4.35. XP spectra showing the C 1s chemical environments for a) the fresh HT on alumina series and b) the spent HT on alumina catalyst series.

Table 4.15. Atomic percentages of carbon in the fresh and spent HT on alumina series, determined via XPS analysis.

Catalyst	Fresh carbonate content / surface at%	Spent carbonate content / surface at%
5 % Mg	1.72 +/- 0.05	3.09 +/- 0.08
9 % Mg	2.05 +/- 0.06	3.74 +/- 0.10
14 % Mg	3.30 +/- 0.09	4.28 +/- 0.12
17 % Mg	3.69 +/- 0.10	4.35 +/- 0.12

4.3 Conclusions

A series of hydrotalcites on alumina with varying Mg weight percentages have been prepared via magnesium methoxide impregnation onto an alumina surface, followed by calcination and a hydrothermal treatment. This demonstrates a novel and environmentally friendly way of preparing supported hydrotalcites, without the requirement of ammonia, alkali or nitrates. The materials were characterised and the hydrotalcite layer found to be highly crystalline, with an Mg:Al ratio of 2:1, the most stable hydrotalcite crystalline structure. With increasing Mg impregnation, the quantity of hydrotalcite on the alumina increased, but the composition remained constant.

In the transesterification reaction of varying chain length TAGs, the catalysts all vastly outperformed the convHT with matching Mg:Al ratio. Preparing hydrotalcites on the alumina surface leads to areas of ordered hydrotalcite crystallites in-between large voids on a high surface area support, and removes the mass transport limitations observed for the convHT. This can be confirmed by comparing the TOF values to those of the macroHT, the macropore "super highways" of which remove diffusion limitations for the TAGs. The very comparable TOF values across the series of TAG chain lengths suggests the same ability of TAGs to reach the hydrotalcite active sites when the catalysts are supported on alumina. The TOF enhancement is at its greatest for the bulkiest TAG when diffusion to reach the active sites of the convHT becomes the most difficult. These HT on alumina catalysts may offer a cost advantage compared to the macroHT, as no sacrificial template is required, saving chemical resources and energy.

It would be interesting to prepare hydrotalcites in this manner using meso-macroporous alumina to examine the activity of these catalysts. However, meso-macroporous alumina is not a very stable bulk support at the high temperatures required for hydrotalcite formation. Silica is a stable support material and Al can be grafted onto silica, as reported in the literature.[39] Therefore, a hydrotalcite could be prepared on Al-SBA-15 and Al-meso-macroporous (MM) SBA-15.[40] This should allow the formation of a catalyst with the enhanced crystallinity and surface area of the HT on alumina, along with the macropore super-highways observed for the macroHT and may further enhance the catalytic activity. Chapter 5 will examine this theory in more detail.

4.4 References

1. C. M. A. Parlett, D. W. Bruce, N. S. Hondow, A. F. Lee and K. Wilson, *ACS Catalysis*, 2011, **1**, 636-640.
2. J. M. Campelo, A. F. Lee, R. Luque, D. Luna, J. M. Marinas and A. A. Romero, *Chemistry – A European Journal*, 2008, **14**, 5988-5995.
3. N. Zheng and G. D. Stucky, *Journal of the American Chemical Society*, 2006, **128**, 14278-14280.
4. D.-e. Jiang, B. Zhao, Y. Xie, G. Pan, G. Ran and E. Min, *Applied Catalysis A: General*, 2001, **219**, 69-78.
5. H. Tsuji, F. Yagi, H. Hattori and H. Kita, *Journal of Catalysis*, 1994, **148**, 759-770.
6. *BASF AG UK Patent 1,462,059-60*, 1973.
7. E. Geraud, V. Prevot, J. Ghanbaja and F. Leroux, *Chemistry of Materials*, 2006, **18**, 238-240.
8. E. B. M. Doesburg, G. Hakvoort, H. Schaper and L. L. Vanreijen, *Applied Catalysis*, 1983, **7**, 85-90.
9. T. W. Kim, M. Sahimi and T. T. Tsotsis, *Industrial & Engineering Chemistry Research*, 2008, **47**, 9127-9132.
10. Y. P. Chang, Y. C. Chen, P. H. Chang and S. Y. Chen, *ChemSusChem*, 2012, **5**, 1249-1257.
11. T. W. Kim, M. Sahimi and T. T. Tsotsis, *Industrial & Engineering Chemistry Research*, 2009, **48**, 5794-5801.
12. D. P. Debecker, E. M. Gaigneaux and G. Busca, *Chem.-Eur. J.*, 2009, **15**, 3920-3935.
13. T. Lopez, P. Bosch, E. Ramos, R. Gomez, O. Novaro, D. Acosta and F. Figueras, *Langmuir*, 1996, **12**, 189-192.
14. M. R. Othman and J. Kim, *J. Sol-Gel Sci. Technol.*, 2008, **47**, 274-282.
15. J. S. Valente, E. Lima, J. A. Toledo-Antonio, M. A. Cortes-Jacome, L. Lartundo-Rojas, R. Montiel and J. Prince, *J. Phys. Chem. C*, 2010, **114**, 2089-2099.
16. U. Constantino, F. Marmottini, M. Nocchetti and R. Vivani, *European Journal of Inorganic Chemistry*, 1998, 1439-1446.
17. J. M. Oh, S. H. Hwang and J. H. Choy, *Solid State Ionics*, 2002, **151**, 285-291.
18. Z. P. Xu and G. Q. Lu, *Chemistry of Materials*, 2005, **17**, 1055-1062.
19. S. Mitchell, T. Biswick, W. Jones, G. WIlliams and D. O'Hare, *Green Chemistry*, 2007, **9**, 373-378.
20. Y. Z. Xi and R. J. Davis, *Journal of Catalysis*, 2009, **268**, 307-317.
21. D. G. Cantrell, L. J. Gillie, A. F. Lee and K. Wilson, *Applied Catalysis A: General*, 2005, **287**, 183-190.
22. J. J. Woodford, J.-P. Dacquin, K. Wilson and A. F. Lee, *Energy & Environmental Science*, 2012, **5**, 6145-6150.
23. V. Grewe, K. Dahlmann, S. Matthes and W. Steinbrecht, *Atmospheric Environment*, 2012, **59**, 102-107.
24. F. Cavani, F. Trifiro and A. Vaccari, *Catalysis Today*, 1991, **11**, 173-291.
25. G. Gutierrez, A. Taga and B. Johansson, *Physical Review, Serie 3. B - Condensed Matter*, 2002, **65**, 012101/-012101-012101/-012104.
26. P. Scherrer, *Nachr. Ges. Wiss. Göttingen* 1918, **26**, 98-100.

27. M. R. Othman, Z. Helwani, Martunus and W. J. N. Fernando, *Applied Organometallic Chemistry*, 2009, **23**, 335-346.
28. V. Rives, *Materials Chemistry and Physics*, 2002, **75**, 19-25.
29. S. Miyata, *Clay Clay Min.*, 1983, **31**, 305-311.
30. A. R. Denton and N. W. Ashcroft, *Phys. Rev. A*, 1991, **43**, 3161-3164.
31. H. Pfeiffer, L. Martinez-dIcruz, E. Lima, J. Flores, M. A. Vera and J. S. Valente, *J. Phys. Chem. C*, 2010, **114**, 8485-8492.
32. H. C. Greenwell, P. J. Holliman, W. Jones and B. V. Velasco, *Catalysis Today*, 2006, **114**, 397-402.
33. S. Abello, F. Medina, D. Tichit, J. Perez-Ramirez, J. C. Groen, J. E. Sueiras, P. Salagre and Y. Cesteros, *Chem.-Eur. J.*, 2005, **11**, 728-739.
34. R. Philipp and K. Fujimoto, *Journal of Physical Chemistry*, 1992, **96**, 9035-9038.
35. S. Abello, F. Medina, D. Tichit, J. Perez-Ramirez, X. Rodriguez, J. E. Sueiras, P. Salagre and Y. Cesteros, *Applied Catalysis A: General*, 2005, **281**, 191-198.
36. F. Kerkhof and J. A. Moulijn, *Journal of Physical Chemistry*, 1979, **83**, 1612-1619.
37. R. Allman and H. P. Jepsen, *Neues Jahrbuch fur Mineralogie, Monatsh efte*, 1969, 544.
38. D. Briggs and G. Beamson, *Analytical Chemistry*, 1992, **64**, 1729-1736.
39. M. V. Landau, E. Dafa, M. L. Kaliya, T. Sen and M. Herskowitz, *Microporous and Mesoporous Materials*, 2001, **49**, 65-81.
40. D. Zhao, J. Feng, Q. Huo, N. Melosh, G. H. Fredrickson, B. F. Chmelka and G. D. Stucky, *Science*, 1998, **279**, 548-552.

Chapter 5

Hydrotalcites supported on mesoporous and macro-mesoporous silica

5.1 Introduction

SBA-15 is a mesoporous silica sieve with uniform hexagonal mesopores.[1, 2] It has a narrow pore size distribution, with a tuneable pore diameter of between 5 and 30 nm.[3, 4] An example TEM image illustrating the structure of the mesopores in SBA-15 can be seen below in **Figure 5.1**. Its high surface area, high hydrothermal stability, and easy preparation[5] render it a very useful catalyst support.[6-10] For example, silica has been functionalised with sulfonic acid in literature,[11, 12] transforming the material into an active solid acid catalyst. However, its properties also render SBA-15 suitable for different applications such as heavy metal sorbents,[13] selective sorbents for protein,[14] advanced optical materials,[15] or as templates for Pt nanowires.[16, 17]

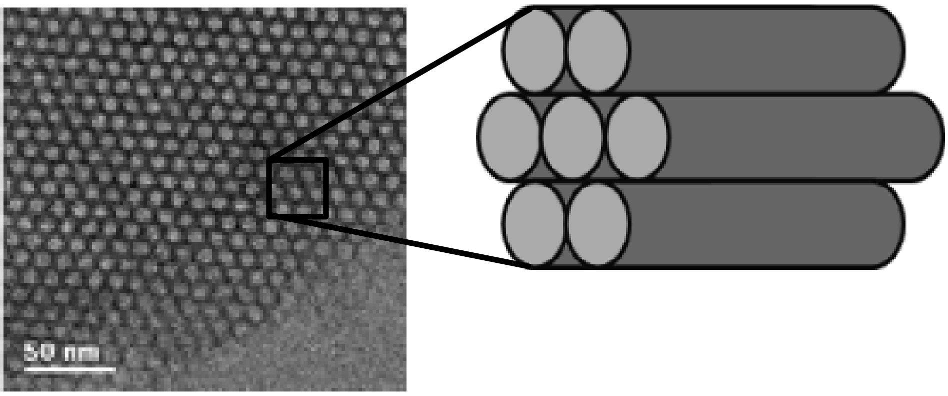

Figure 5.1. TEM image of SBA-15,[18] the hexagonal pore arrangement is illustrated.

There has been lots of interest in literature surrounding the grafting of a layer of alumina onto silica.[19-21] Alumina grafted silica, (referred to in this chapter as Al-SBA-15) has been used as a catalyst support to immobilise heteropolyacids,[22] or for supporting alkali metals.[23] The ability to prepare an aluminium grafted SBA-15 (Al-SBA-15) led to the idea of carrying out Mg grafting onto a prepared Al-SBA-15 material, followed by calcination and a hydrothermal treatment, in order to prepare hydrotalcite on silica in a similar way to the hydrotalcites on alumina examined in **Chapter 4.**

Previously in literature, alumina and MgO have been directly grafted onto the surface of the silica to form a hydrotalcite-like calcined mixed oxide.[24] However, the approach used in this chapter will be a novel route to hydrotalcite on silica, and will also involve the formation of rehydrated hydrotalcite intercalated with hydroxide anions, the species active for the transesterification of triglycerides. This will be the first report on the use of hydrotalcite supported on silica as a catalyst in the biodiesel synthesis reaction.

Sulfonic acid functionalised mesoporous SBA-15 materials have shown activity in the synthesis of biodiesel.[25, 26] The mesopore size is close to that of a TAG (~ 5 nm) and so mass-transport limitations have an effect on the activity of these catalysts. Recent work within the research group led to the development of a route to meso-macroporous silica using polystyrene bead templating.[27] This meso-macroporous material showed enhanced activity in triglyceride transesterification to form FAME when compared to mesoporous silica. It is anticipated that the same mass transport diffusion limitations will be seen in this work when using hydrotalcite grafted onto mesoporous silica. Diffusion through the mesopores for hydrotalcite on mesoporous SBA-15 will be slow, particularly for the larger, bulkier TAGs. Therefore, a hydrotalcite will also be prepared on alumina grafted meso-macroporous SBA-15 (Al-MMSBA-15). The macropore "super-highways" incorporated into the meso-macroporous material should allow for fast diffusion and should generate an active supported hydrotalcite catalyst.

The aim in this chapter is to prepare a thin layer of hydrotalcite supported on mesoporous SBA-15 and meso-macroporous SBA-15, via a novel magnesium methoxide grafting, calcination and hydrothermal treatment route. The materials will be fully characterised to determine how the hydrotalcite forms on the silica, and to gather information about the stoichiometry and crystal structure of the materials. The two catalysts will then be tested in the transesterification of varying chain length triglycerides from the model C4 chain length TAG tributyrin, up to the C18 chain length TAG triolein, the main component of olive oil, a real biodiesel feedstock. The activities of the catalysts will be examined and compared with each other as well as with the bulk conventional and macroporous hydrotalcites. It is anticipated that the macropore super highways in the meso-macroporous catalyst will remove diffusion limitations associated with the bulky TAGs and therefore improve the activity of the hydrotalcite on meso-macroporous SBA-15 (HT-MMSBA-15) compared to the hydrotalcite prepared on mesoporous SBA-15 (HT-SBA-15), as seen for macroHT versus convHT. The activities compared to their bulk counterparts will be examined for any enhancements in activity or stability due to the thin layer of hydrotalcite on a silica support.

5.2 Results and discussion

A hydrotalcite layer on both mesoporous SBA-15 and meso-macroporous SBA-15 (MMSBA-15) was prepared via Mg methoxide impregnation onto alumina grafted silicas (Al-SBA-15 and Al-MMSBA-15), followed by a calcination and hydrothermal treatment. The resulting materials, HT-SBA-15 and HT-MMSBA15 respectively, were fully characterised before being tested as catalysts in the transesterification of triglycerides.

5.2.1 Characterisation of Al-SBA-15 and Al-MMSBA-15

Before hydrotalcite preparation could commence on silica, the parent SBA-15 and MMSBA-15 supports were first prepared, before grafting an alumina multilayer onto them both using the method of Landau and co-workers.[19] The starting meso-macroporous SBA-15 (MMSBA-15) was prepared using the method published by Dhainaut and co-workers.[27] The pure mesoporous SBA-15 was prepared using the method of Zhao and co-workers.[28]

The grafting procedure was repeated four times on each parent silica, in order to obtain an alumina multi-layer on the silica surface. Characterisation was carried out after each grafting to examine the change in the parent silica on alumina addition. The properties of the final Al-SBA-15 and Al-MMSBA-15 after four graftings were then also determined. In the materials reported on in this chapter, the MMSBA-15 and alumina grafted MMSBA-15 were prepared by Christopher Parlett, and used with his permission.

5.2.1.1. Low angle XRD

Low angle XRD indicates the presence of long range ordering of the mesopores, as observed in SBA-15 and MMSBA-15.[29] **Figure 5.2** and **Figure 5.3** show the low angle XRD profiles for SBA-15 and MMSBA-15 respectively, as-prepared and after each of the four Al graftings.

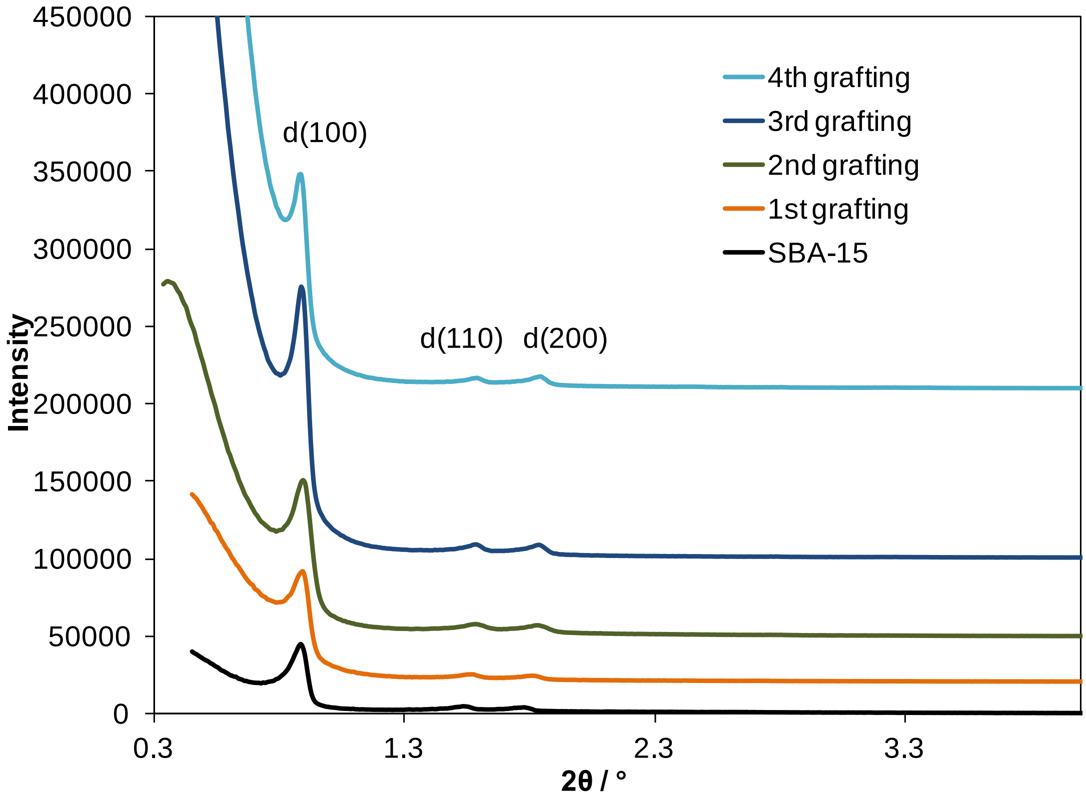

Figure 5.2. Low angle XRD profiles showing long range ordering of mesopores for SBA-15 and Al-SBA-15 after each successive Al grafting.

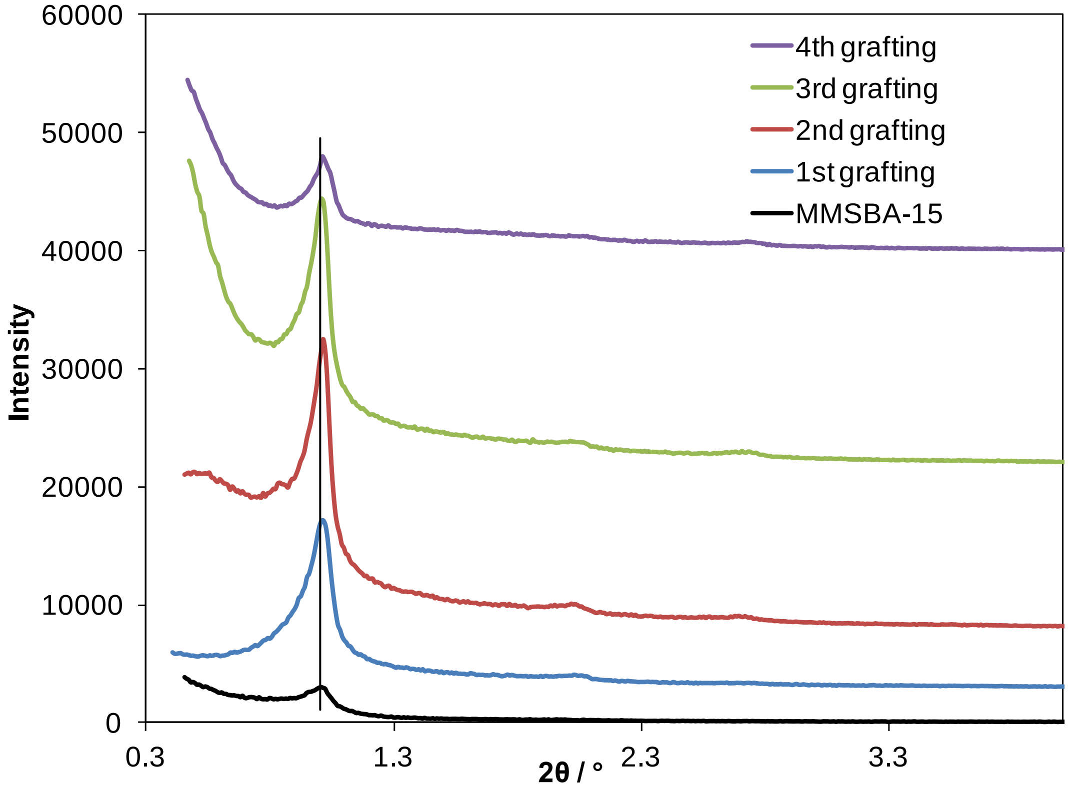

Figure 5.3. Low angle XRD profiles showing long range ordering of mesopores for MMSBA-15 and Al-MMSBA-15 after each successive Al grafting.

There are three peaks visible in the low angle XRD spectra for SBA-15 and its grafted materials, which can be indexed as the (100), (110), and (200) reflections, associated with the *P6mm* space group for hexagonal arrangement of mesoporous channels.[28, 30] The incorporation of the macropores causes the d(110) and d(200) peaks to shift to higher angles, which corresponds to a contraction in the mesopore lattice parameter observed on macropore incorporation.[27] This contraction is assigned to the curvature of the mesopore channels as they form around the polystyrene bead template during the synthesis due to the strong electrostatic interactions between the polystyrene beads, block co-polymer and silica precursor.[27]

Even after four Al graftings, long range hexagonal mesopore order can be observed in both the Al-SBA-15 and Al-MMSBA-15. The intensity of the peaks is not as high for the meso-macroporous SBA-15 materials because the macropores in the material break up the long range mesopore order periodically.

5.2.1.2 N_2 porosimetry

N_2 adsorption-desorption isotherms for SBA-15, as-prepared and after each of the four alumina graftings can be observed in **Figure 5.4**. The BJH pore size distributions[31] for each of these materials can also be observed in **Figure 5.5**. **Table 5.1** reports on the BET surface areas, BJH total pore volumes and BJH average pore diameters, along with the micropore volumes and surface areas for SBA-15 as-prepared and after each Al grafting.

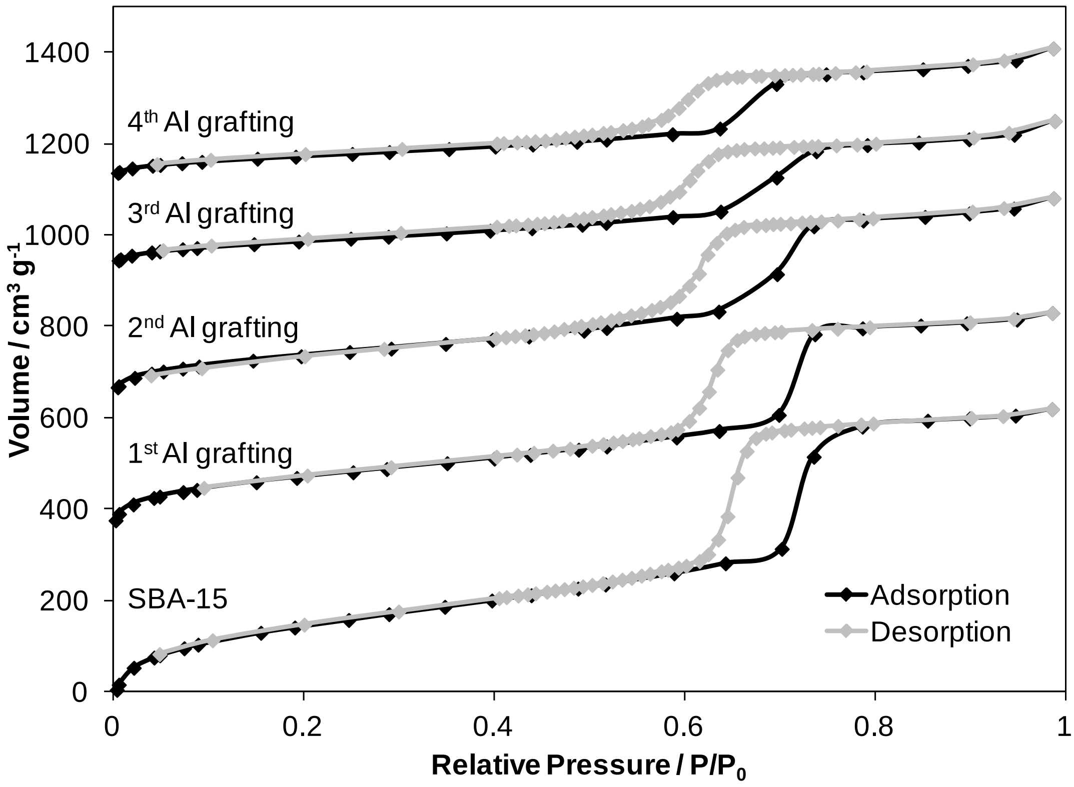

Figure 5.4. N_2 adsorption-desorption isotherms taken after each Al grafting onto SBA-15. The isotherms are offset for clarity.

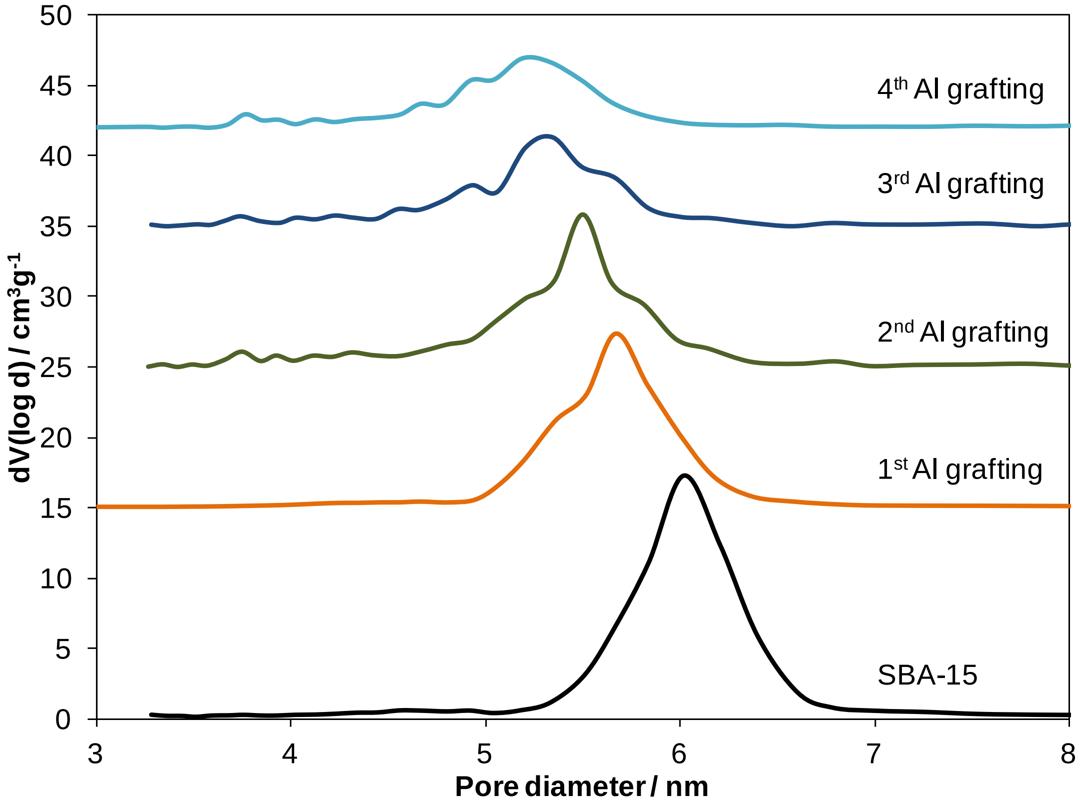

Figure 5.5. BJH pore size distribution plots for each Al grafting onto SBA-15, offset for clarity.

Table 5.1. Surface area, total pore volumes and average pore diameters for each Al grafting on SBA-15, as determined by N_2 porosimetry.

Grafting	BET surface area / m^2g^{-1}	BJH mesopore volume/ cm^3g^{-1}	Average BJH mesopore diameter / nm	Micropore volume / cm^3g^{-1}	Micropore surface area / m^2g^{-1}
SBA-15	923 +/- 92	0.96 +/- 0.03	6.02 +/- 0.19	0.143	297 +/- 30
1st Al graft	613 +/- 61	0.77 +/- 0.02	5.67 +/- 0.16	0.066	154 +/- 15
2nd Al graft	489 +/- 49	0.70 +/- 0.02	5.50 +/- 0.15	0.030	74 +/- 7
3rd Al graft	312 +/- 31	0.50 +/- 0.01	5.35 +/- 0.15	0.014	37 +/- 4
4th Al graft	262 +/- 26	0.45 +/- 0.01	5.19 +/- 0.15	0.005	14 +/- 1

The average mesopore diameter and total mesopore volume decreases after each grafting as a thicker layer of alumina forms on the silica. This can be observed visually in **Figure 5.5**, and is shown in **Table 5.1**. However, after four graftings the material is still mesoporous, and although the overall volume has halved, the average diameter is still over 5 nm. This decrease in mesopore volume has a large effect on surface area, which drops 3.5 fold over the course of the four graftings. These results show that more alumina is grafting to the surface during each cycle. The micropores of the SBA-15 are also filled with alumina as their volume and surface area drop to almost zero over the course of the 4 graftings.

N_2 adsorption-desorption isotherms for MM-SBA-15, as-prepared and after each of the four alumina graftings can be observed in **Figure 5.6**. The BJH pore size distributions for each of these materials can also be observed in **Figure 5.7**. **Table 5.2** reports on the BET surface areas, BJH total pore volumes and BJH average pore diameters for MMSBA-15, as-prepared and after each Al grafting, as well as micropore volumes and surface areas. This analysis was carried out by Christopher Parlett.

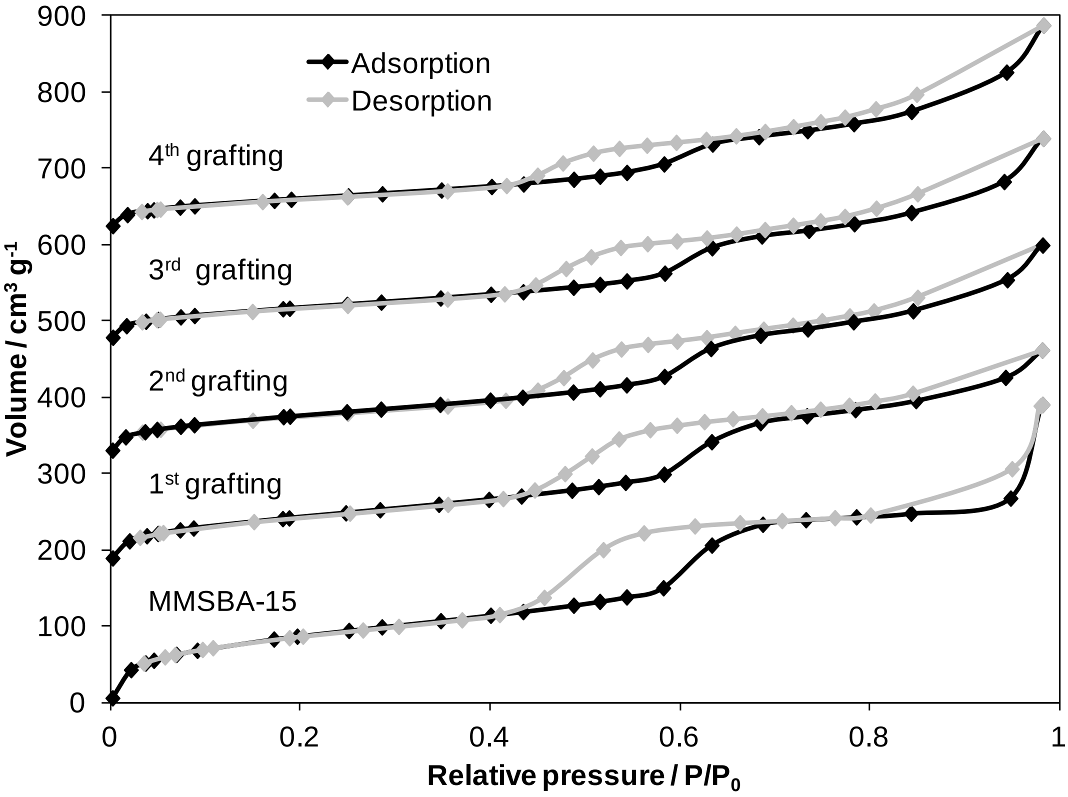

Figure 5.6. N_2 adsorption-desorption isotherms taken after each Al grafting onto MMSBA-15. The isotherms are offset for clarity.

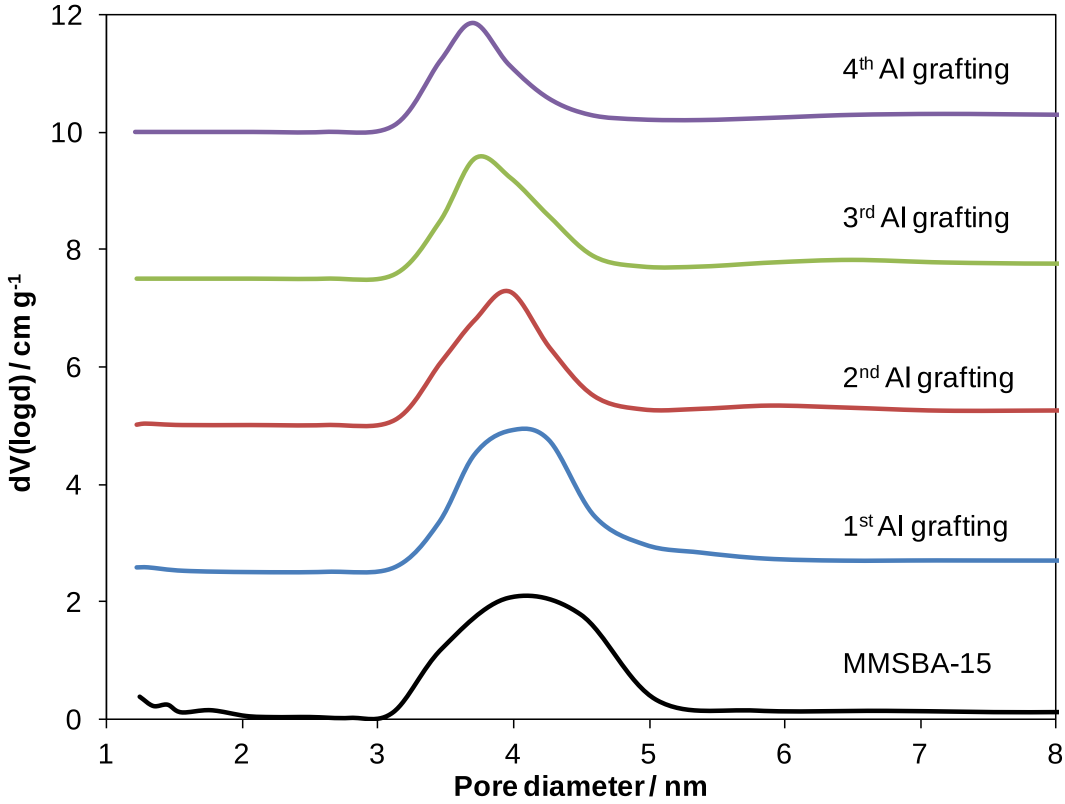

Figure 5.7. BJH pore size distribution plots for each Al grafting onto MMSBA-15, offset for clarity.

Table 5.2. Surface area, total pore volumes and average pore diameters for each Al grafting on MM-SBA-15, as determined by N_2 porosimetry.

Grafting	BET surface area / $m^2 g^{-1}$	Total BJH mesopore volume/ cm^3g^{-1}	Average BJH mesopore diameter / nm	Micropore volume / cm^3g^{-1}	Micropore surface area / m^2g^{-1}
MMSBA-15	473 +/- 47	0.66 +/- 0.09	3.94 +/- 0.52	0.079	166 +/- 17
1st Al graft	332 +/- 33	0.48 +/- 0.03	3.97 +/- 0.28	0.024	58 +/- 5.8
2nd Al graft	271 +/- 27	0.47 +/- 0.04	3.97 +/- 0.30	0.013	33 +/- 3.3
3rd Al graft	240 +/- 24	0.46 +/- 0.03	3.71 +/- 0.26	0.007	19.3 +/- 1.9
4th Al graft	201 +/- 20	0.45 +/- 0.03	3.71 +/- 0.27	0.004	13.5 +/- 1.4

In the case of the meso-macroporous SBA-15, in each isotherm, visually a mesopore and macropore region can be observed. The decrease in surface area is not as great, with a 2.2 fold decrease over the course of the graftings. There is also a much smaller drop in total mesopore volume and average mesopore diameter. It is therefore likely that some of the alumina is grafting to the walls of the macropores, as there will be fast diffusion of the alumina precursors to these regions of the MM-SBA-15. Therefore, less alumina will form within the mesopores causing less impact on surface area. The majority of the micropores are also filled with alumina, as for the HT-SBA-15 materials.

5.2.1.3 XPS

XPS analysis was carried out on the final alumina grafted silicas after four graftings. **Figure 5.8** compares the Al 2p and Si 2p chemical environments for Al-SBA-15 and Al-MMSBA-15. **Table 5.3** reports on the surface Al:Si atomic ratios and Al weight percentages for the two materials.

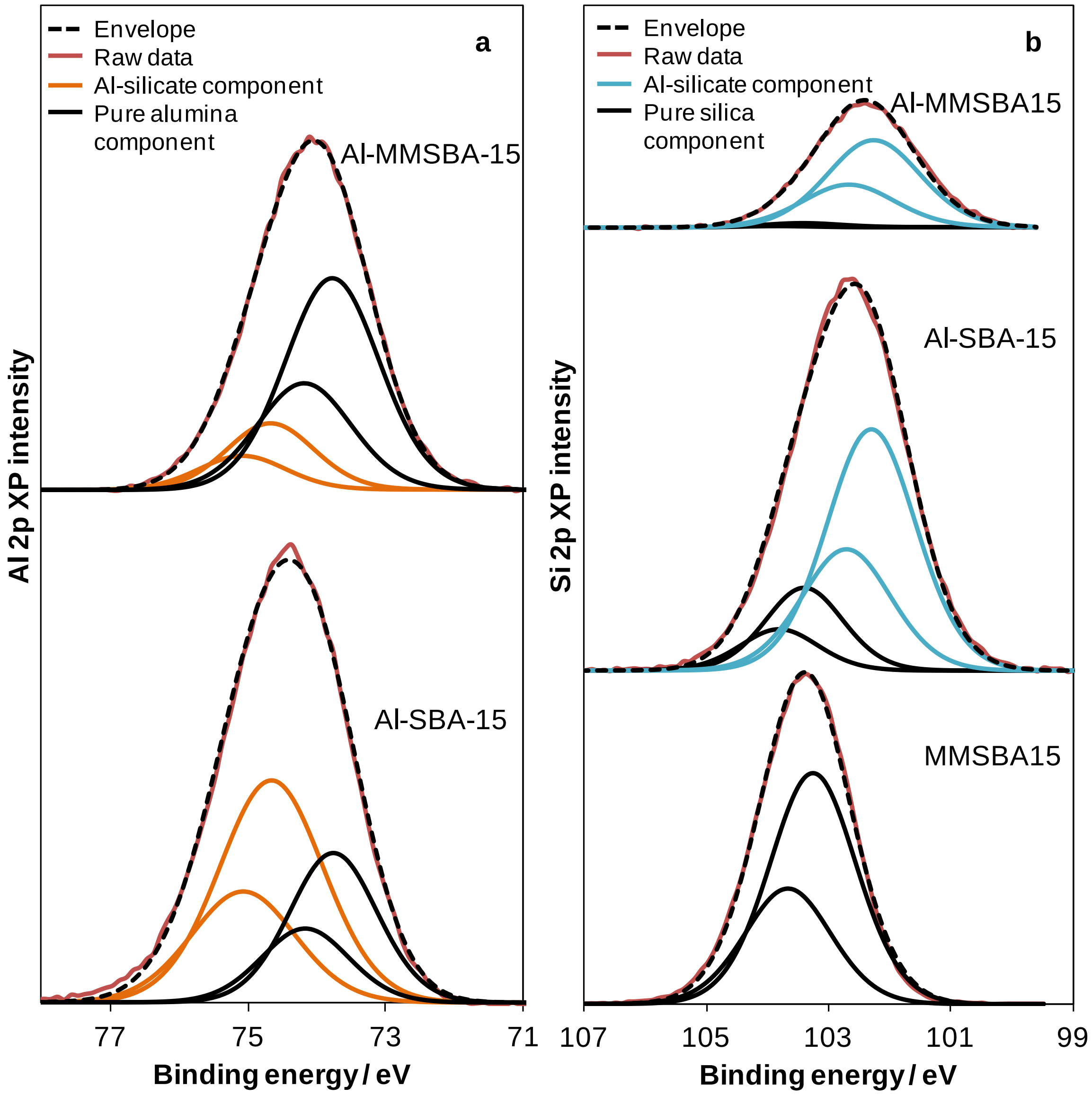

Figure 5.8. XPS spectra comparing a) the Al 2p and b) the Si 2p chemical environments for both Al-SBA-15 and Al-MMSBA-15 after 4 Al graftings. For the Si 2p region, a pure MM-SBA-15 is shown for comparison.

Table 5.3. Atomic ratios and weight percentages for Al-SBA-15 and Al-MMSBA-15, as determined via XPS analysis.

	Al:Si atomic ratio	Al content / wt%
Al-SBA-15	1.51:1 +/- 0.04	17.21 +/- 0.47
Al-MMSBA-15	3.54:1 +/- 0.10	22.25 +/- 0.61

The Al:Si ratio is twice as high for Al-MMSBA-15 as for Al-SBA-15. The same mass of alumina is added in both cases, however the difference in surface area of the two starting supports determines this difference. The crystal structure of α-alumina has a rhombohedral primitive cell consisting of 10 atoms, 4 aluminium and 6 oxygen, as shown below in **Figure 5.9**.

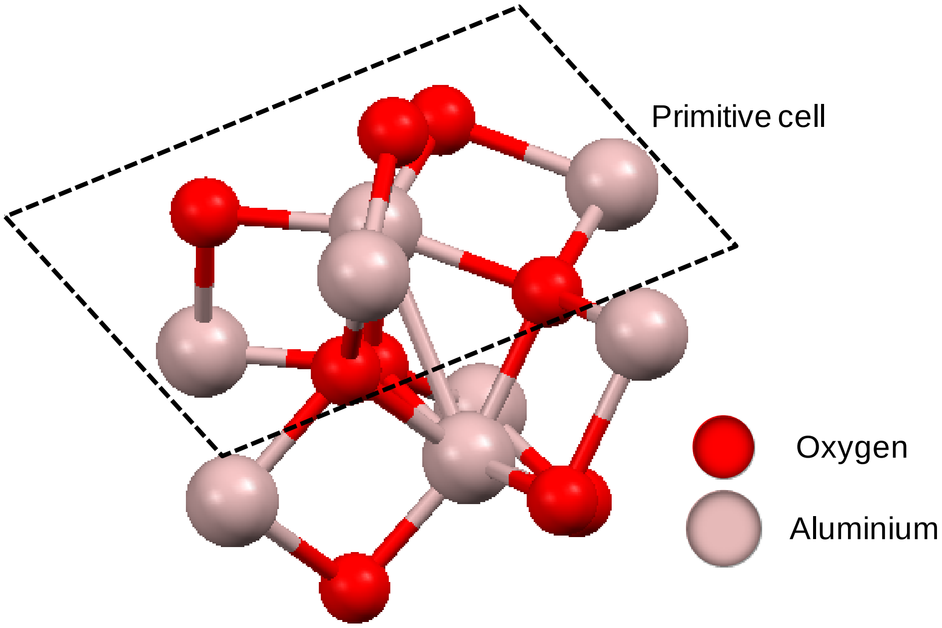

Figure 5.9. Crystal structure of α-alumina.[32] The primitive cell used to calculate monolayer formation is labelled.

The dimensions of the cell are 5.128 Å × 5.128 Å × 5.128 Å. Therefore, 4 Al atoms are required for every 5.128 $Å^2$ on the surface of silica, in order to form a monolayer of bulk α-alumina, one unit cell deep. Using the surface area of MM-SBA-15 and SBA-15 in calculations, for each grafting of SBA-15 theoretically 2.5 monolayers of bulk-like α-alumina could be formed. This increases to 4.9 for the MMSBA-15. Assuming all alumina grafts to the silica surfaces in both cases this would result in a 1.9 fold difference in layer thickness after four graftings. This almost accounts for the 2.3 fold difference observed in the surface Al:Si ratio. There will be attenuation of the silica and interface alumina signals which will affect the observed ratio slightly.

The difference in intensity between pure alumina and the alumina bound to silica can be used to determine how many monolayers of alumina have bound to the silica and therefore how successful the grafting process was. The alumina signal intensity at the interface with silica is attenuated by the surface alumina layer. The degree of attenuation is calculated using the equation shown below (**Equation 5.1**).

$$\frac{Alumina\ signal\ at\ interface}{Alumina\ signal\ at\ surface} = e^{-\left[\frac{(number\ of\ layers \times layer\ thickness)}{(\lambda_{Al} \times \cos 42)}\right]}$$ **Equation 5.1**[33]

When the layer thickness of 5.1 Å determined above is put into the equation, the alumina interface signal is found to be attenuated to 75 % under an alumina surface layer.

From **Figure 5.8**, for the Al-MMSBA-15, the intensity of pure alumina compared to alumina at the interface is 3.4:1. Taking into account the attenuation of the interface signal this difference in intensities becomes 2.6:1. With one monolayer at the interface, this means that there is in total 3.6 monolayers of alumina grafted to the MMSBA-15, out of a possible 19.6. Therefore, there is an 18.4 % success rate when grafting alumina onto MMSBA-15. For the SBA-15, the ratio of surface to interface alumina = 0.55:1 from **Figure 5.8**. Therefore, as only 55% of the interface is being attenuated, after this is factored in, the ratio of surface to interface becomes 0.7:1. Therefore there are 1.7 monolayers of alumina on the SBA-15, out of a possible 10, giving a 17 % grafting success rate. Therefore, although there may be a slight decrease in the rate of diffusion of the alumina precursors through the mesopores of the SBA-15, compared to the macropore channels of the MMSBA-15, overall the alumina grafts with the same success to both supports.

The layer thickness determined via XPS analysis can be compared with the shrinkage in mesopore diameter via porosimetry. For the SBA-15, after four graftings there is a 0.83 nm drop in mesopore diameter, suggesting an alumina layer which is 4.15 Å thick. This would suggest that 0.8 monolayers of alumina have grafted to the mesopores, a value lower than the 1.7 monolayers calculated via XPS, however XRD has also shown that the micropores are filled with alumina, so this may account for the difference in these values.

For the MMSBA-15, there is a much smaller drop in mesopore diameter of 0.23 nm, suggesting a layer of alumina 2.3 Å thick, equivalent to 0.45 monolayers, in comparison to the 3.6 monolayers calculated via XPS. This much greater difference between XPS and porosimetry measurements not seen for SBA-15, suggests that there is alumina grafted to the macropores of the Al-MMSBA-15.

5.2.2 Characterisation of HT-SBA-15 and HT-MMSBA-15

After Mg impregnation onto Al-SBA-15 and Al-MMSBA-15, followed by calcination and a hydrothermal treatment, the resultant HT-SBA-15 and HT-MMSBA-15 samples were characterised using XRD, N_2 porosimetry, SEM, EDX, TGA, XPS and CO_2 TPD in order to determine the structure, stoichiometry and basicity of the hydrotalcite layers.

5.2.2.1 XRD

Powder XRD diffraction patterns for both HT-SBA-15 and HT-MMSBA-15 were obtained and are compared to the patterns for convHT and brucite below in **Figure 5.10**. The crystallite sizes, interlayer spacings, lattice parameters and Mg:Al ratios determined using Vegard's law are reported in **Table 5.4**.

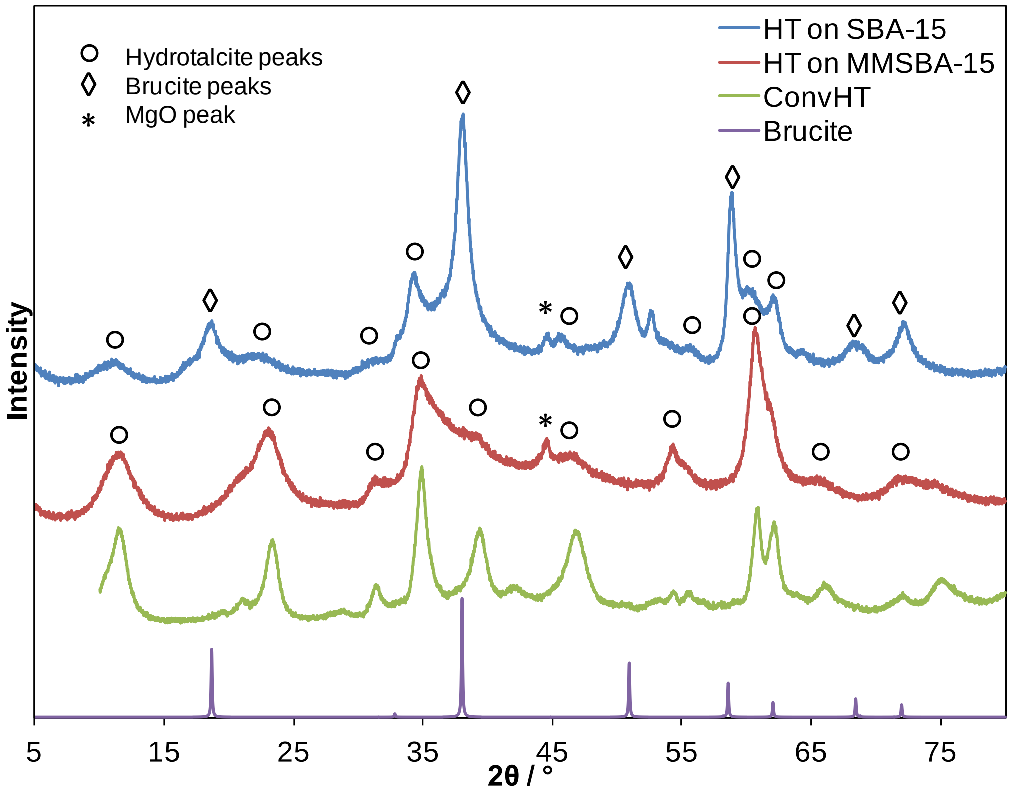

Figure 5.10. XRD profiles for HT-SBA-15 and HT-MMSBA-15 with profiles for convHT and brucite[34] shown for comparison.

Table 5.4. Crystallite sizes, interlayer spacings and lattice parameters for HT-SBA-15, HT-MMSBA-15, convHT and 17% Mg HT on alumina; as determined via analysis of the XRD patterns.

Catalyst	Volume average crystallite size / nm	Interlayer spacing, *d* / nm	Lattice Parameter, *a* / Å	Mg:Al ratio
HT-SBA-15	1.64 +/- 0.13 Brucite-7.08+/-0.57	0.81 +/- 0.01	3.082 +/- 0.01	3.91:1[a]
HT-MMSBA-15	1.18 +/- 0.10	0.76 +/- 0.01	3.053 +/- 0.01	2.21:1[a]
ConvHT	6.2 +/- 0.50	0.77 +/- 0.01	3.049 +/- 0.01	1.95:1
17% Mg HT on alumina	31 +/- 2.5	0.77 +/- 0.01	3.051 +/- 0.01	2.08:1[a]

[a] Determined from lattice parameter using Vegard's Law.[35]

The HT-MMSBA-15 sample shows a diffraction pattern very similar to that of the bulk convHT, with the broader peaks indicating smaller crystallite sizes. However, whilst hydrotalcite peaks can be indexed for HT-SBA-15, there is also a crystalline brucite phase present within the material. The narrow mesopores of the SBA-15, particularly after alumina grafting, may have made diffusion and dispersion of the magnesium methoxide through the material more difficult and much slower than for MMSBA-15. This may have resulted in some of the magnesium added during the synthesis of HT-SBA-15 being unable to graft to the alumina surface, forming brucite instead. It is quite likely that this brucite is separate non-grafted crystallites, although it may possibly be due to Mg grafted to pure silica, forming brucite on hydrothermal treatment.

The hydrotalcite crystallite sizes, determined using the Scherrer equation,[36] are much smaller for the HT-MMSBA-15 and HT-SBA-15 samples than for the bulk hydrotalcite and the 17 wt% Mg HT on alumina material. This indicates that the hydrotalcite structure is less ordered in the silica grafted materials. Alumina used in the generation of the hydrotalcite structure is a thin layer, already grafted to silica. Therefore the rearrangement of these atoms to form larger crystallites of hydrotalcite is not as easy as for the HT on bulk alumina, and this may be the reason smaller crystallites form.

Whilst the HT-MMSBA-15 sample has a similar Mg:Al ratio to that of the convHT and macroHT, the HT-SBA-15 sample has a higher Mg:Al ratio. Again, the most likely reason for this is that Mg could not diffuse quickly enough through the mesoporous support to reach all of the alumina (there is still a large amount of pure alumina in the HT-SBA-15 sample as discussed later in the XPS characterisation section 5.2.2.6). Therefore more Mg will have grafted to certain areas of accessible alumina, forcing the Mg:Al ratio up. The interlayer spacing is larger for the HT-SBA-15, as the higher Mg:Al ratio means there is less positive charge in the brucite-like layers, therefore there is a weaker electrostatic interaction between the brucite-like layer and the intercalating hydroxide anions.[37]

5.2.2.2 N_2 porosimetry

N_2 porosimetry adsorption-desorption isotherms for HT-SBA-15 compared to Al-SBA-15 and convHT can be observed in **Figure 5.11**. The BJH pore size distributions for HT-SBA-15 compared to the parent Al-SBA-15 are shown in **Figure 5.12**. The BET surface area, along with the BJH total pore volume and average pore diameter for HT-SBA-15 are reported in **Table 5.5**.

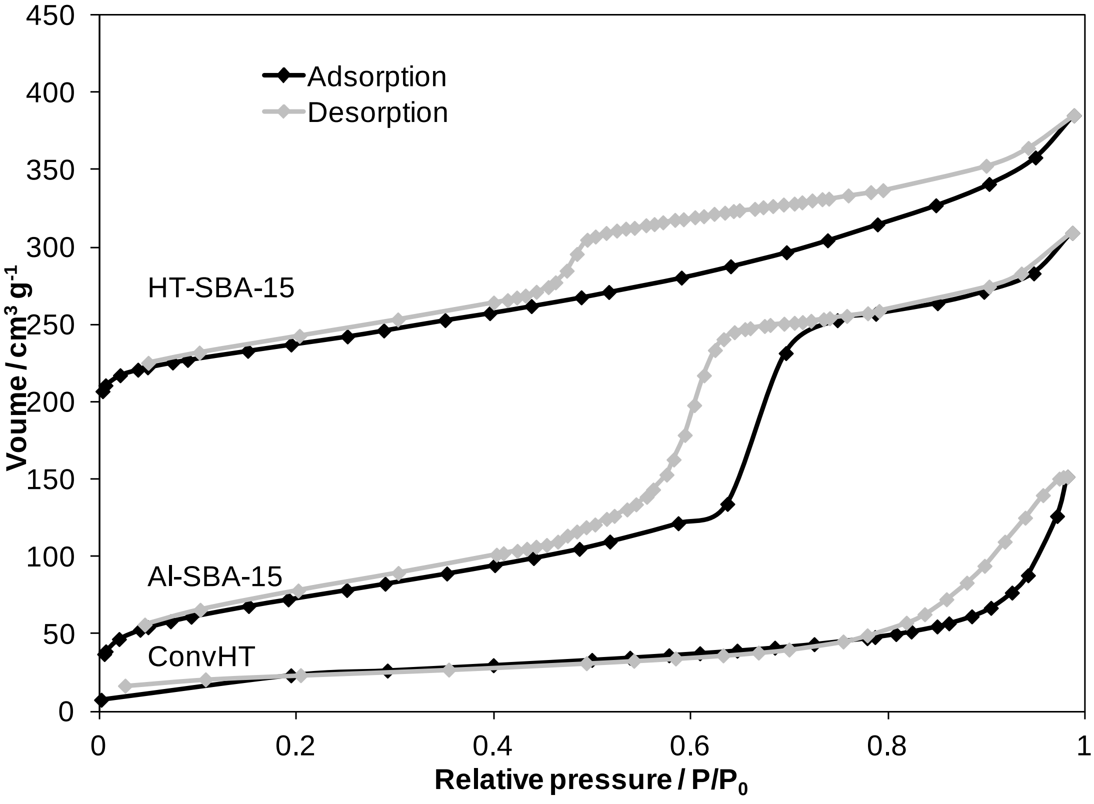

Figure 5.11. N_2 adsorption-desorption isotherms for Al-SBA-15, HT-SBA-15 and convHT. The isotherms have been offset for clarity.

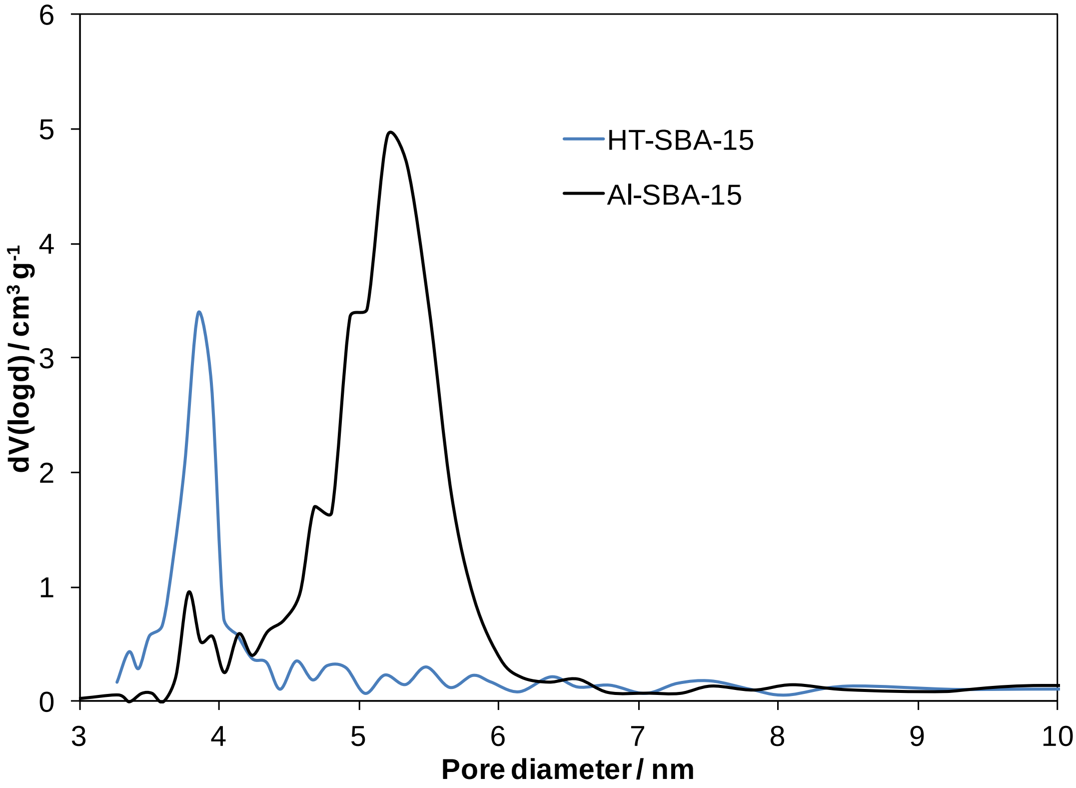

Figure 5.12. BJH pore size distributions for Al-SBA-15 and HT-SBA-15.

Table 5.5. BET surface areas, BJH total pore volumes and average pore diameter for HT-SBA-15 and Al-SBA-15, as determined by N_2 porosimetry.

	BET surface area / m^2 g^{-1}	Total BJH pore volume / cm^3 g^{-1}	Average BJH pore diameter / nm
Al-SBA-15	262 +/- 26	0.45 +/- 0.01	5.19 +/- 0.15
HT-SBA-15	205 +/- 21	0.25 +/- 0.007	3.84 +/- 0.10

There is a dramatic decrease in the mesopore size distribution for SBA-15 after hydrotalcite preparation. The addition of magnesium and the subsequent transformation to hydrotalcite and brucite has caused the mesopore volume to half and the average mesopore diameter has decreased from 5 nm to less than 2 nm. This can also be observed when comparing the isotherms in **Figure 5.11**, as the mesopore region is much smaller for the HT-SBA-15.

The N_2 adsorption-desorption isotherms for HT-MMSBA-15 compared to the parent Al-MMSBA-15 and macroHT are shown in **Figure 5.13**. The BJH pore size distributions for HT-MMSBA-15 compared to Al-MMSBA-15 can be seen in **Figure 5.14**. **Table 5.6** reports on the BET surface area, BJH total pore volume and BJH average pore diameter for HT-MMSBA-15.

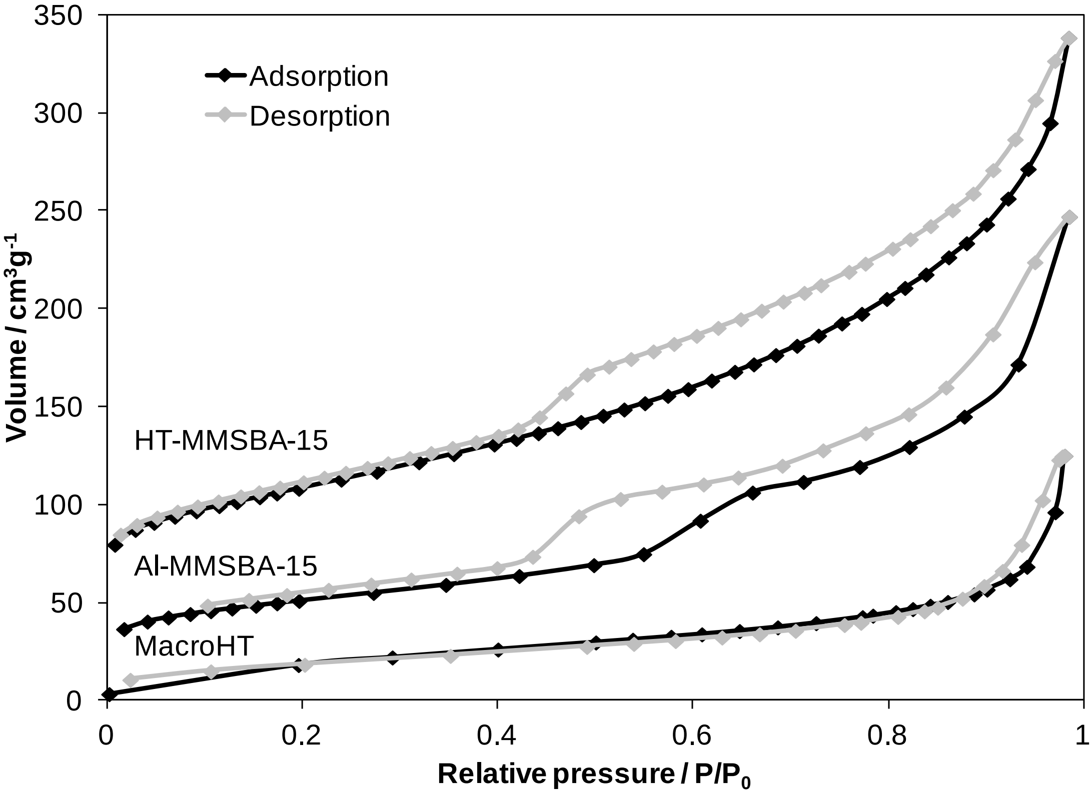

Figure 5.13. N_2 adsorption-desorption isotherms for Al-MMSBA-15, HT-MMSBA-15 and macroHT. The isotherms have been offset for clarity.

A mesopore and macropore region can still be observed in the isotherm after Mg grafting, although the definition is not as clear as for Al-MMSBA-15.

Table 5.6. BET surface areas, BJH total pore volumes and average pore diameter for HT-MMSBA-15 and Al-MMSBA-15, as determined by N_2 porosimetry.

	BET surface area / m^2 g^{-1}	Total BJH pore volume / cm^3 g^{-1}	Average BJH pore diameter / nm
Al-MMSBA-15	201 +/- 20	0.45 +/- 0.03	3.71 +/- 0.27
HT-MMSBA-15	246 +/- 25	0.47 +/- 0.03	3.66 +/- 0.21

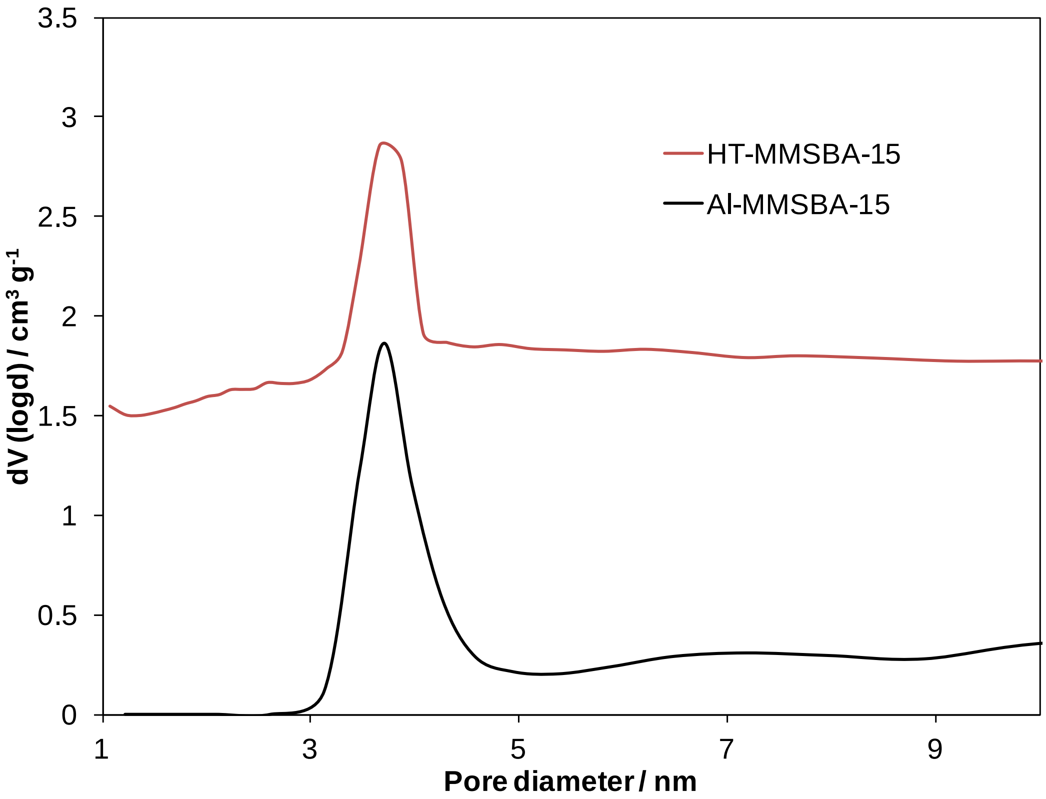

Figure 5.14. BJH pore size distributions for Al-MMSBA-15 and HT-MMSBA-15.

For the meso-macro material, after Mg grafting there has been virtually no change to the mesopore volume or diameter. Again, as seen for the Al grafting stage this suggests that the majority of the Mg grafting has occurred within the macropore walls, where diffusion is easiest. In contrast to the results for the HT-SBA-15 material there has actually been an increase in the overall BET surface area after the hydrotalcite preparation. This could be due to crystallite islands of hydrotalcite forming on the macropore walls, adding to the overall surface area.

5.2.2.3 SEM

Figure 5.15 shows an example SEM image of the HT-MMSBA-15 sample, showing the presence of macropores throughout the material. When preliminary experiments were carried out using meso-macroporous alumina as a support for hydrotalcite grafting, the hydrothermal treatment caused the macroporous structure of the alumina to collapse. In the case of Al-MMSBA-15, the hydrotalcite preparation, in particular the hydrothermal treatment, has not caused any collapse in the macroporous structure. This, along with the presence of mesopores shown through porosimetry, justifies the use of silica as a support for hydrotalcite preparation, due to its stability in water at high temperatures.

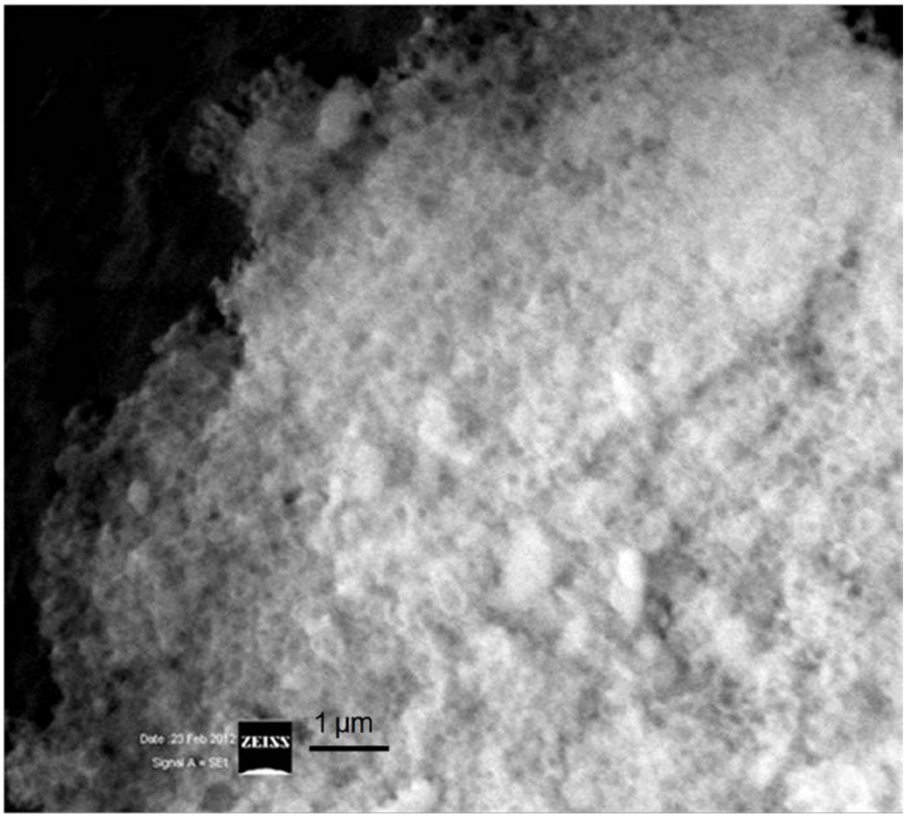

Figure 5.15. SEM image of HT-MMSBA-15, showing the presence of macropores throughout the structure.

5.2.2.4 EDX

EDX analysis was carried out on both HT-SBA-15 and HT-MMSBA-15. The bulk Mg:Al ratios, Mg:Si ratios and Mg weight percentage values are reported in **Table 5.7.**

Table 5.7. Bulk atomic ratios and Mg weight percent values for HT-SBA-15 and HT-MMSBA-15 as determined via EDX analysis.

	Bulk Mg:Al ratio	Bulk Mg:Si ratio	Mg content / wt%	Bulk Mg:Al HT ratio[a]
HT-SBA-15	5.31:1 +/- 0.16	2.94:1+/- 0.03	34.55 +/- 0.34	3.91:1
HT-MMSBA-15	2.48:1 +/- 0.03	2.54:1 +/- 0.10	19.79 +/- 2.06	2.21:1

[a] As determined from Vegard's law using XRD determined lattice parameters

The bulk Mg:Al ratio is twice as large for the HT-SBA-15 as for the HT-MMSBA-15. During the Al graftings the same amount of Al was grafted onto the two supports, resulting in similar Al wt% values, as shown in **Table 5.3**. However, the amount of Mg added was calculated based on the surface layer and area of Al, and not the total multilayer thickness. Therefore the difference in bulk Mg:Al ratio reflects this, with a difference equal to the difference in thickness of the alumina layer for each support, a factor of 2.1.

This again is reflected in the bulk Mg wt% of the two materials. More Mg was added to the Al-SBA-15, in order to allow the formation of the same amount of surface hydrotalcite across the greater surface area of the material.

When comparing the bulk Mg:Al ratios with the bulk hydrotalcite Mg:Al ratios determined via Vegard's law from XRD (section 5.2.2.1), the HT-MMSBA-15 values are in good agreement. For the HT-SBA-15 the bulk Mg:Al ratio is higher at 5.31:1 than the 3.9:1 Mg:Al HT ratio. This is due to the presence of brucite within the HT-SBA-15 structure. This difference in Mg:Al ratio can be used to estimate the weight percent of brucite within the material. For each mole of hydrotalcite there is 1.4 mole of brucite present, taking into account the difference between the 3.91:1 and 5.31:1 Mg:Al ratios. Using the molecular masses for both brucite and hydrotalcite, the mass of 1.4 mol and 1 mole of each material respectively comes to 81.7 g for brucite, and 604 g for hydrotalcite. Therefore, for each gram of material, 13.5 wt% is due to brucite.

5.2.2.5 TGA

TGA analysis was carried out on both HT-SBA-15 and HT-MMSBA-15 materials. The TGA profiles, compared to that of macroHT can be seen in **Figure 5.16**. The percentage weight loss values for different temperature regions are reported in **Table 5.8**.

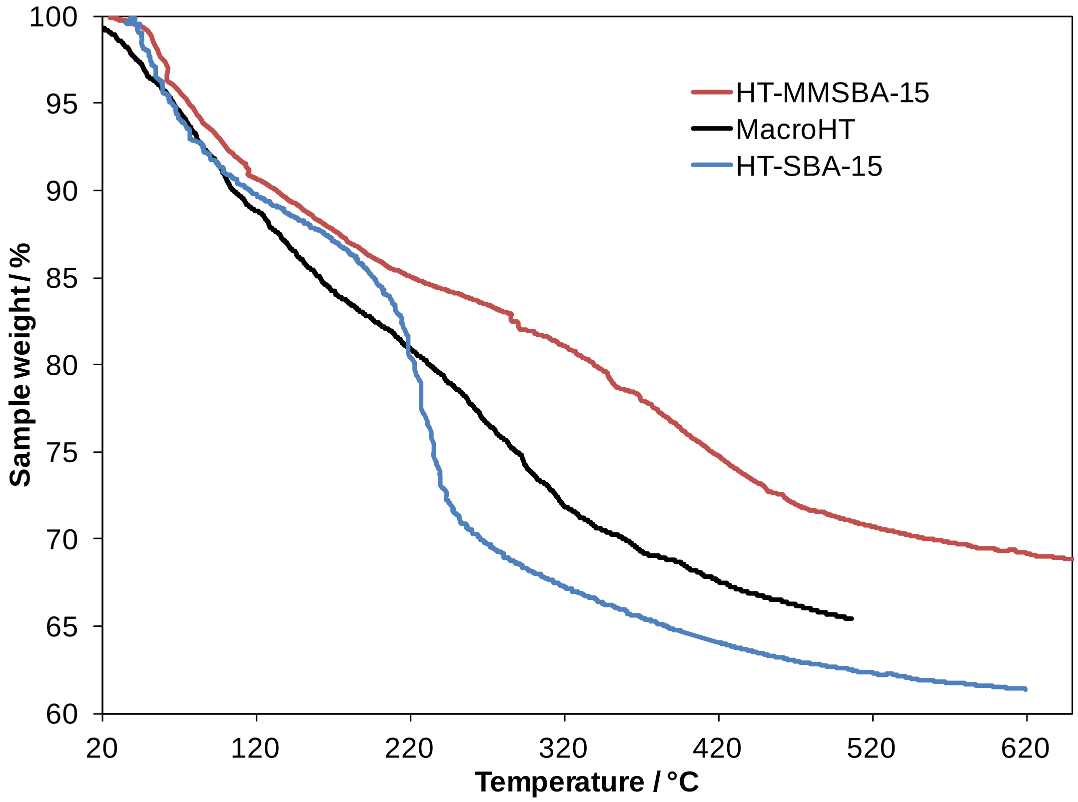

Figure 5.16. TGA profiles for HT-SBA-15 and HT-MMSBA-15, compared to macroHT.

Table 5.8. Percentage weight losses during TGA analysis for HT-SBA-15, HT-MMSBA-15 and macroHT.

Catalyst	Weight loss between 70 and 220 ºC / %	Weight loss between 250 and 350 ºC / %
HT-SBA-15	13.7 +/- 0.1	14.8 +/- 0.1
HT-MMSBA-15	10.7 +/- 0.1	5.0 +/- 0.1
MacroHT	13.6 +/- 0.1	8.2 +/- 0.1

The profiles for macroHT and HT-MMSBA-15 follow a similar pattern. There is a smaller overall weight loss for HT-MMSBA-15 due to the presence of the silica support and therefore the smaller overall weight percentage of hydrotalcite. However, the weight losses occur at the characteristic hydrotalcite regions; with weight loss between 70 and 220 ºC due to the loss of interlayer water and water molecules adsorbed to the hydrotalcite surface,[38] and weight loss between 250 and 350 ºC attributed to hydroxide anions in the brucite-like layers.[39] The HT-SBA-15 shows a much steeper weight loss between 250 and 350 ºC. This larger drop confirms the presence of significant amounts of brucite within the material. When calculating the percentage weight loss expected in the brucite region for the hydrotalcite in HT-SBA-15, based on the weight losses normalised to hydrotalcite metal wt% for both macroHT and HT-MMSBA-15, a value of 3.5 % is obtained. Therefore 11.3 wt % of the material is due to the hydroxide in $Mg(OH)_2$. This works out to 20 weight % of the material consisting of brucite, a bit higher than the value determined via EDX. It can however be deduced that there is a proportion of the material in the HT-SBA-15 sample between 13 and 20 wt% which is due to brucite.

5.2.2.6 XPS

XPS analysis was carried out for both HT-SBA-15 and HT-MMSBA-15. **Figure 5.17** shows the Al 2p chemical environments for HT-SBA-15 and HT-MMSBA-15, along with those of their alumina grafted silica parent supports.

In both cases, after Mg grafting, calcination and a hydrothermal treatment, some of the alumina at the surface is now present as hydrotalcite. For HT-SBA-15, 10.4 % of the alumina present is found as hydrotalcite. For HT-MMSBA-15, this value is much higher at 51.1 % of the surface alumina.

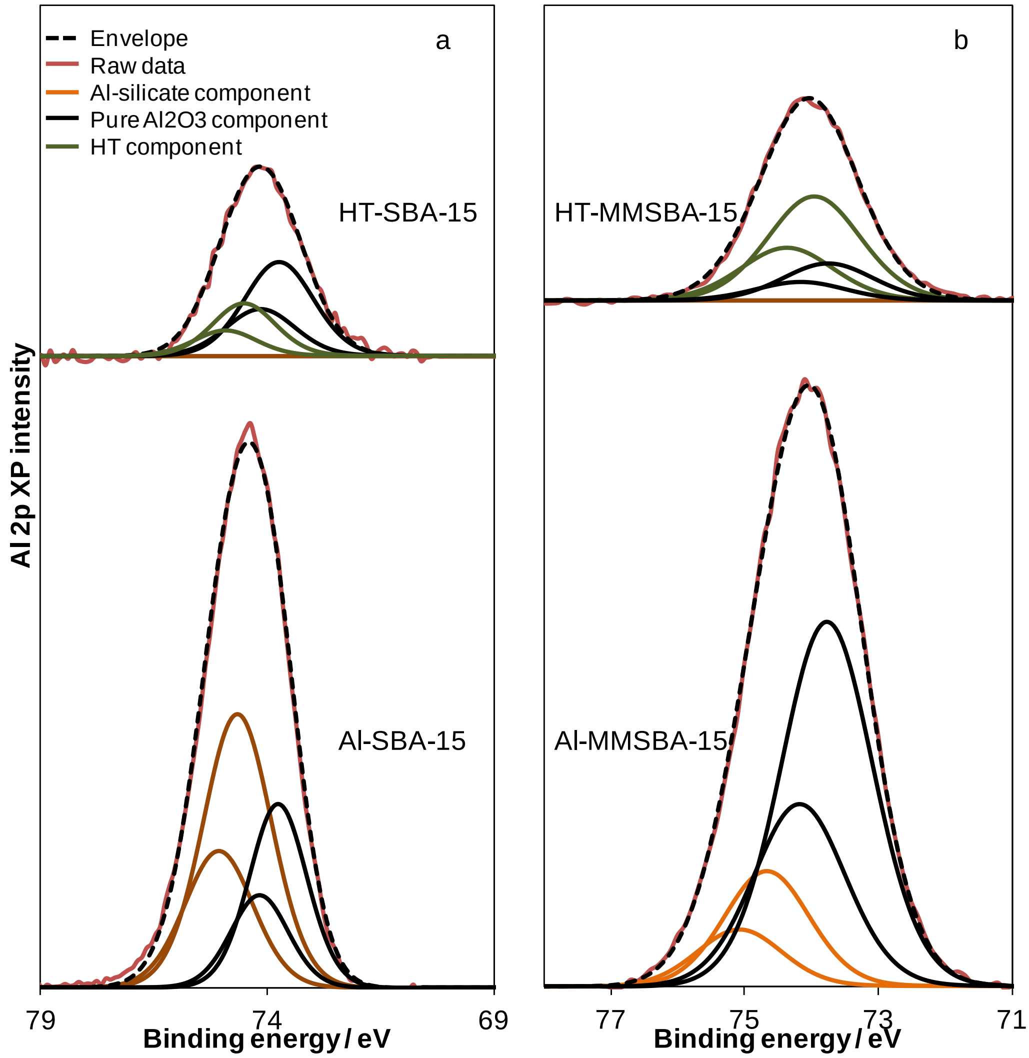

Figure 5.17. XP spectra showing the Al 2p chemical environments for a) HT-SBA-15 and the parent Al-grafted support and b) HT-MMSBA-15 and its parent Al grafted support.

The Si 2p chemical environments for HT-SBA-15 compared to Al-SBA-15, as well as HT-MMSBA-15 compared to Al-MMSBA-15 can be seen in **Figure 5.18a** and **b** respectively.

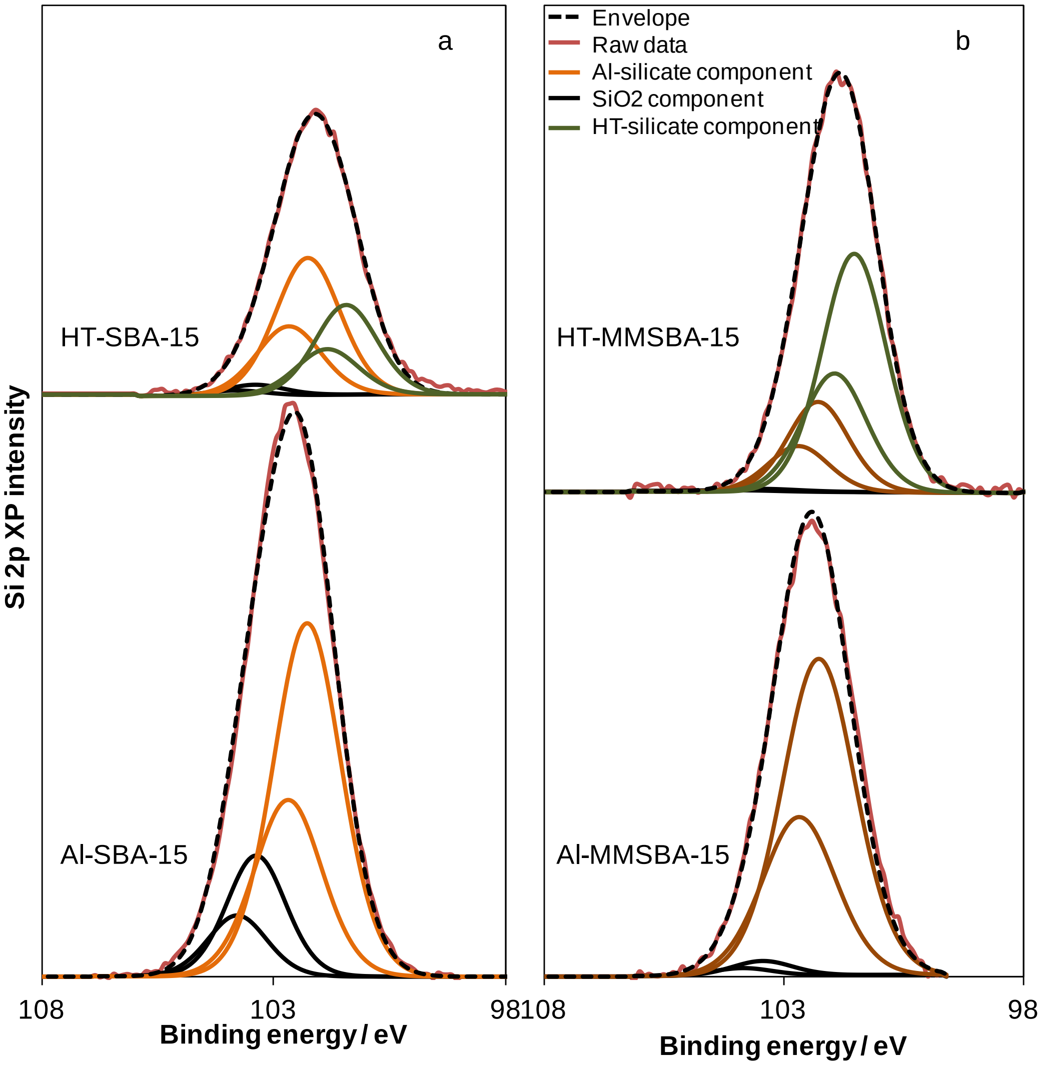

Figure 5.18. XP spectra showing the Si 2p chemical environments for a) HT-SBA-15 and its parent Al grafted support and b) HT-MMSBA-15 and its parent Al grafted support.

Again, after the hydrotalcite preparation, there has been a shift to lower binding energies for both of the Si 2p peaks, suggesting the silica is bound to a species with higher electron density than alumina, such as Mg^{2+} containing hydrotalcite. 19.1 % of the silica is bound to a hydrotalcite species at the surface of HT-SBA-15, whereas 52.3% of the silica at the HT-MMSBA-15 surface is adjacent to hydrotalcite. The binding energy of the hydrotalcite component is very similar for both HT-SBA-15 and HT-MMSBA-15. This suggests that the brucite is not bound to the silica in HT-SBA-15, as this would shift the peak to lower binding energy. It is therefore more likely that the brucite is found as separate crystallites.

Figure 5.19 shows the Mg 2s chemical environments for HT-SBA-15 and HT-MMSBA-15.

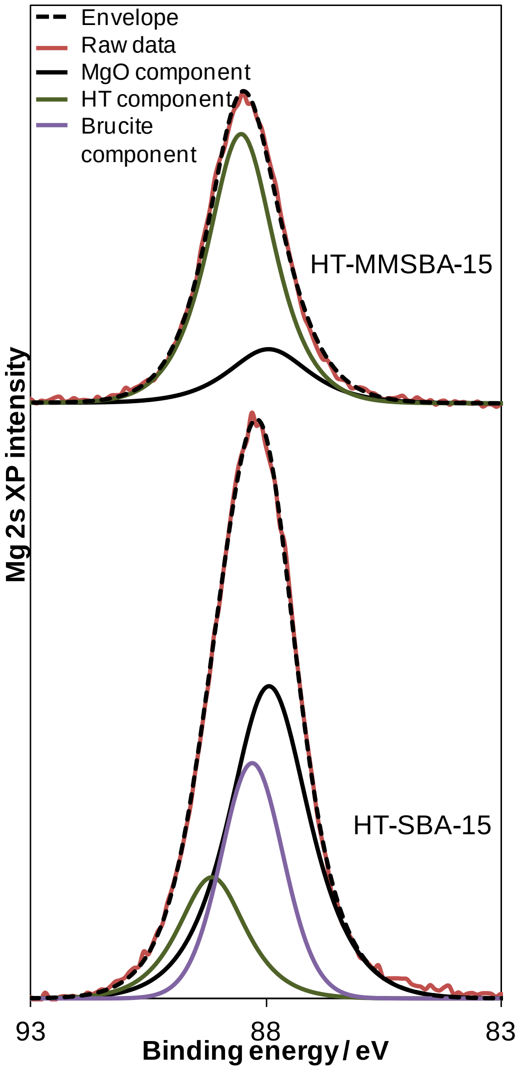

Figure 5.19. XP spectra showing the Mg 2s chemical environments for HT-SBA-15 and HT-MMSBA-15.

The HT-SBA-15 has an extra component fitted at binding energy 88.3 eV, which corresponds to that of brucite.[40] **Table 5.9** reports on the surface HT Mg:Al ratios, Mg and hydrotalcite weight percentages, and HT:Si ratios for the two materials, as determined via XPS analysis.

Table 5.9. Atomic ratios and weight percentages as determined via XPS analysis of HT-SBA-15 and HT-MMSBA-15.

Catalyst	Surface HT Mg:Al ratio	Surface Mg / wt%	Surface HT Mg / wt%	HT:Si ratio
HT-SBA-15	5.0:1 +/- 0.14	22.3 +/- 0.61	2.96 +/- 0.08	0.45:1 +/- 0.01
HT-MMSBA-15	2.6:1 +/- 0.07	16.7 +/- 0.46	7.68 +/- 0.21	2.3:1 +/- 0.06
17 % Mg HT on alumina	0.66:1 +/- 0.02	15.2 +/- 0.42	9.51 +/- 0.26	-

The Mg:Al hydrotalcite ratio is higher for HT-SBA-15 than for HT-MMSBA-15. However, less overall Mg found at the surface of the HT-SBA-15 is bound in hydrotalcite. As previously discussed, this is attributed to poor diffusion of the Mg methoxide during the impregnation and the presence of brucite.

Whilst for the HT-MMSBA-15 sample, the Mg wt% at the surface is comparable to that of the bulk, the lower Mg wt% for HT-SBA-15 when analysing the surface would suggest bulk brucite crystallites are present, and that the brucite is not grafted to the SBA-15. The presence of separate brucite crystallites should not affect the activity of the HT-SBA-15 material which is being analysed, other than decreasing the base site density of the material.

5.2.2.7 CO_2 TPD

CO_2 TPD analysis was carried out for HT-SBA-15 and HT-MMSBA-15, after saturating the samples with CO_2 using pulse chemisorption. The CO_2 desorption profiles as recorded by following the CO_2 signal in mass spectrometry can be seen in **Figure 5.20.** A profile for MgO has been included for reference. The base site densities and peak maxima temperature have been reported in **Table 5.10**. The values for macroHT have been included as a comparison.

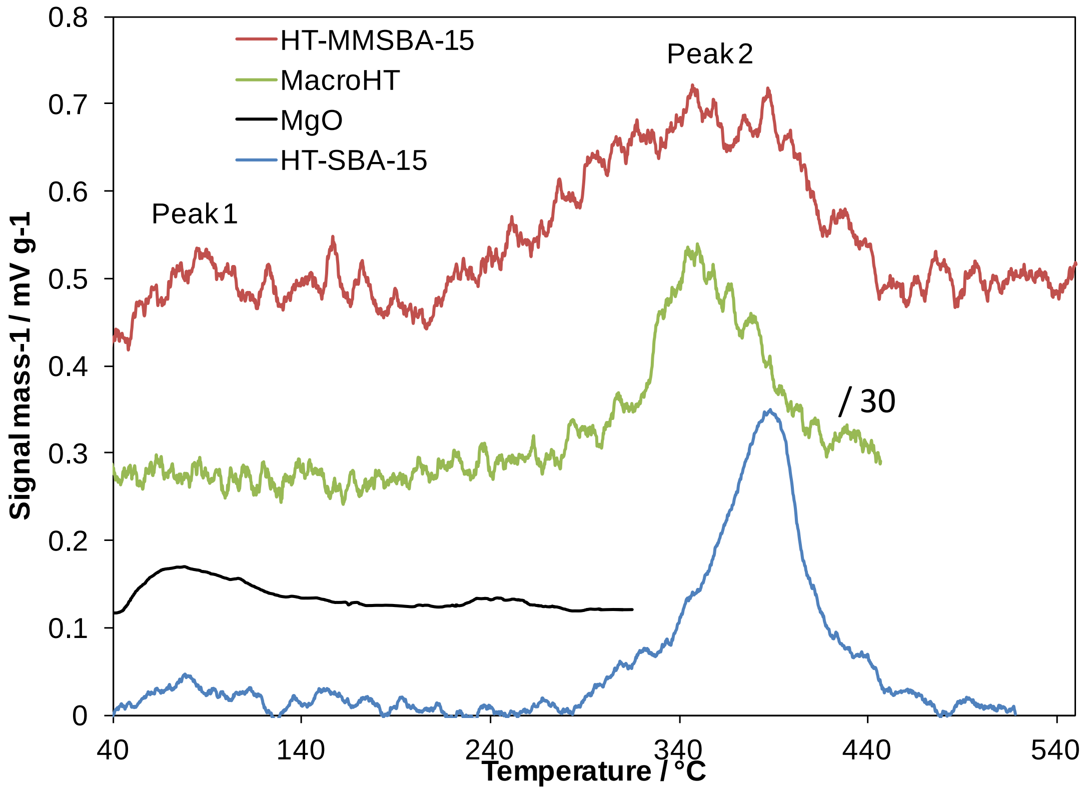

Figure 5.20. CO_2 TPD desorption profiles for HT-SBA-15 and HT-MMSBA-15. The profiles for MgO and macroHT (scaled down by a factor of 30) have been added for comparison.

Table 5.10. Base site densities and desorption peak maximum temperatures for HT-SBA-15, HT-MMSBA-15 and macroHT as a comparison.

Catalyst	Peak 1 base site density / g^{-1}	Peak 1 max. temp[a]. / ºC	Peak 2 base site density / g^{-1}	Peak 2 max. temp[a]. / ºC	Total base site density / g^{-1}	Total base site density / m^2	Total base site density /Mg atom
HT-SBA-15	3.5×10^{17}	78.2	3.9×10^{18}	388.0	4.2×10^{18}	2.1×10^{12}	0.5×10^{-3}
HT-MMSBA-15	1.3×10^{18}	84.2	5.1×10^{18}	346.9	6.4×10^{18}	2.6×10^{12}	1.3×10^{-3}
MacroHT	-	-	7.7×10^{19}	349.7	7.7×10^{19}	9.1×10^{17}	17.3×10^{-3}

[a] Measurement error +/- 0.2 ºC

Both of the HT-SBA-15 and HT-MMSBA-15 catalysts have a low temperature peak associated with MgO base sites, which is not seen for macroHT. The grafting method may mean that some MgO grafts to silica where it is not encapsulated by hydrotalcite as for macroHT, providing some accessible weak base sites.

The HT-SBA-15 profile has a higher maximum desorption peak temperature due to the higher Mg:Al ratio in the hydrotalcite, meaning the charge balancing anions are not held as tightly in the interlayer space due to lower charge density in the layers, making them more basic than for the other two catalysts.

Both the HT-SBA-15 and the HT-MMSBA-15 samples have much lower base site densities than the bulk macroHT, due to the presence of the support in both cases. However, even when normalised to Mg atom the macroHT has a greater base site density. More of the Mg atoms are found in hydrotalcite for the macroHT, with less forming oxides or brucite. The conventional preparation is still the most efficient way of preparing the most hydrotalcite for the quantity of Mg added.

The base site density for HT-SBA-15 is about 75 % that of the HT-MMSBA-15. This is due to the presence of brucite, with its lack of interlayer anions or overall basicity, along with the smaller amount, albeit much more strongly basic, of hydrotalcite formed in the material. The HT-MMSBA-15 has a broad desorption profile, with some CO_2 desorbing at higher temperature, suggesting varying base site strengths, possibly due to areas of the material with higher Mg:Al ratio than others.

5.2.3 Transesterification of triglycerides

The HT-SBA-15 and HT-MMSBA-15 were tested as catalysts in the transesterification of triglycerides to form FAME, the reaction used to synthesise biodiesel. Briefly, 50 mg of catalyst was added to 10 mmol of triglyceride, using a 30:1 methanol: oil ratio. Butanol was also used as a co-solvent to help solubilise the longer chained triglycerides. The reactions were carried out at 60 ºC and aliquots were removed from the reaction at various time intervals and analysed using a GC, in order to plot triglyceride conversion and FAME formation over 24 hours. The TAG chain length was varied from C4 up to C18, a real oil component and the main constituent of olive oil, to examine the effect on activity for each catalyst. In this way, the effect of the macroporous structure on accessibility to TAGs could be examined.

5.2.3.1 Tributyrin transesterification

The HT-SBA-15 and HT-MMSBA-15 catalysts were tested in the transesterification of tributyrin, a short chained C4 triglyceride. The tributyrin conversion profile, along with the methyl butyrate and intermediate formation profiles can be seen below in **Figures 5.21 - 5.24**. The reaction data is reported in **Table 5.11.**

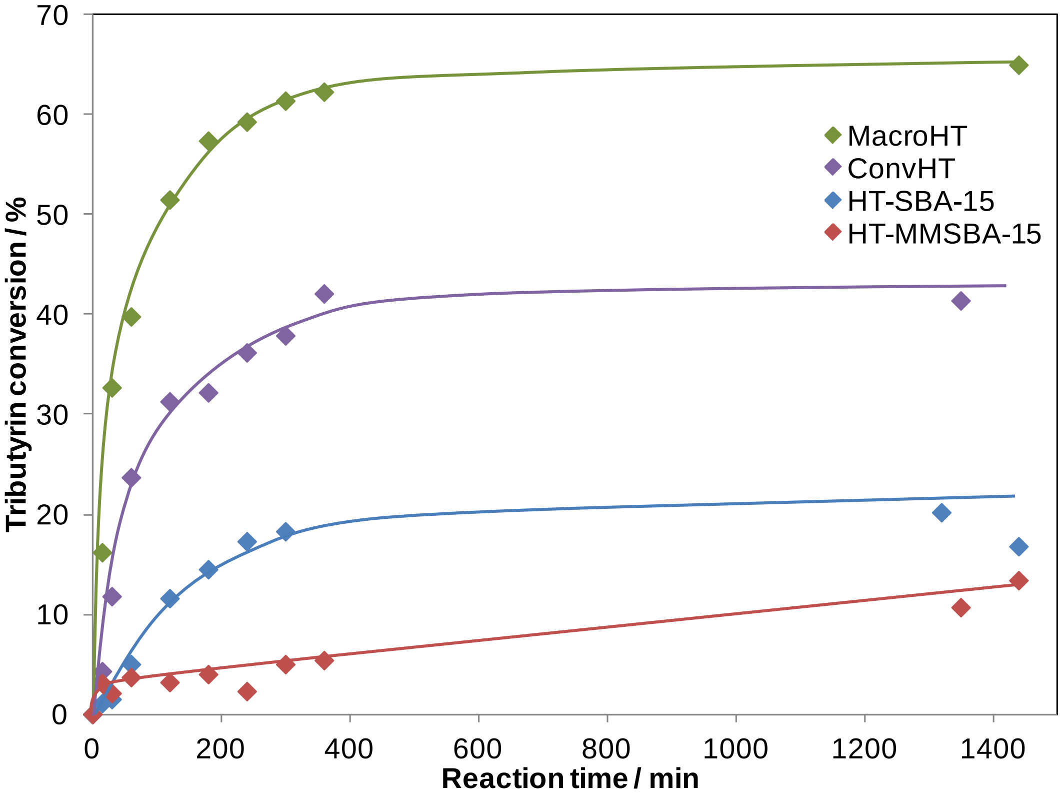

Figure 5.21. Reaction profiles showing tributyrin transesterification over time for HT-SBA-15 and HT-MMSBA-15, with convHT and macroHT shown for comparison.

Table 5.11. Reaction data for HT-SBA-15 and HT-MMSBA-15 in the transesterification of tributyrin. The data for convHT and macroHT has been shown for comparison.

Catalyst	Initial rate / mmol g^{-1} min^{-1}	TOF / min^{-1}	TAG conversion after 24 h / %	MB selectivity after 24h / %
HT-SBA-15	0.15 +/- 0.01	21.95	16.8 +/- 1.5	68.7 +/- 1.5
HT-MMSBA-15	0.19 +/- 0.05	18.31	13.4 +/- 1.5	32.5 +/- 1.5
ConvHT	0.78 +/- 0.01	5.49	42.1 +/- 1.5	43 +/- 1.5
MacroHT	2.18 +/- 0.02	17.06	65.0 +/- 1.5	43 +/- 1.5

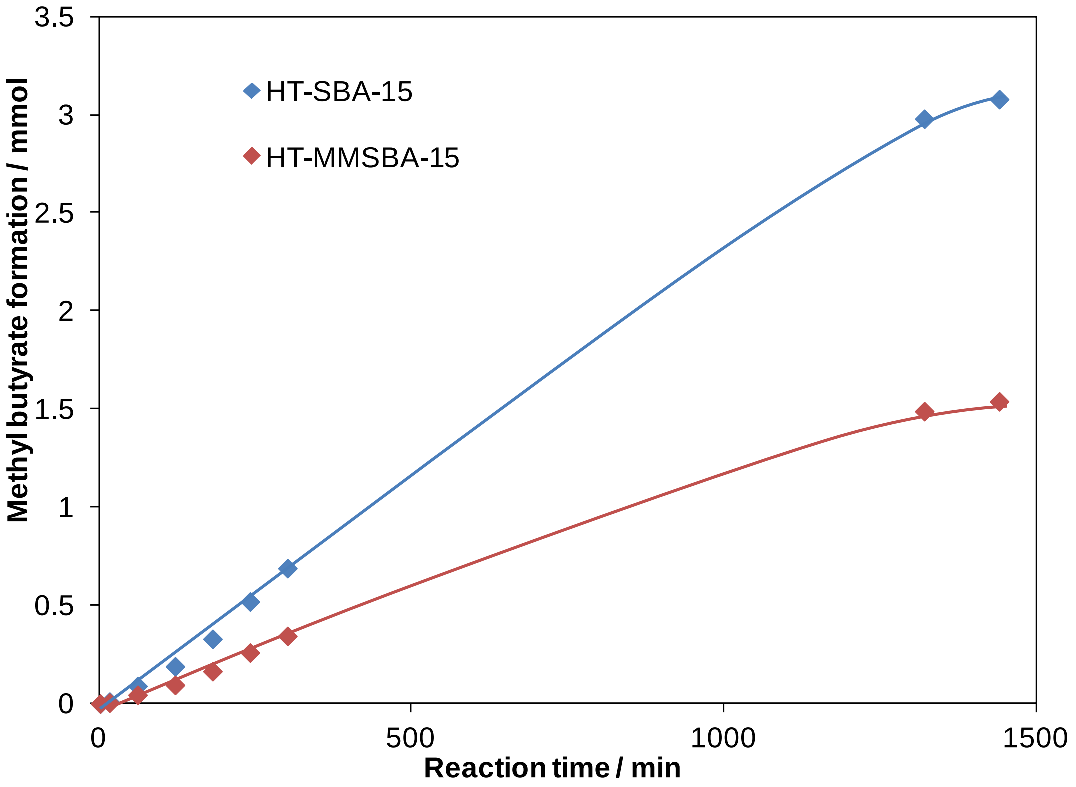

Figure 5.22. Methyl butyrate formation over time for HT-SBA-15 and HT-MMSBA-15 during the transesterification of tributyrin.

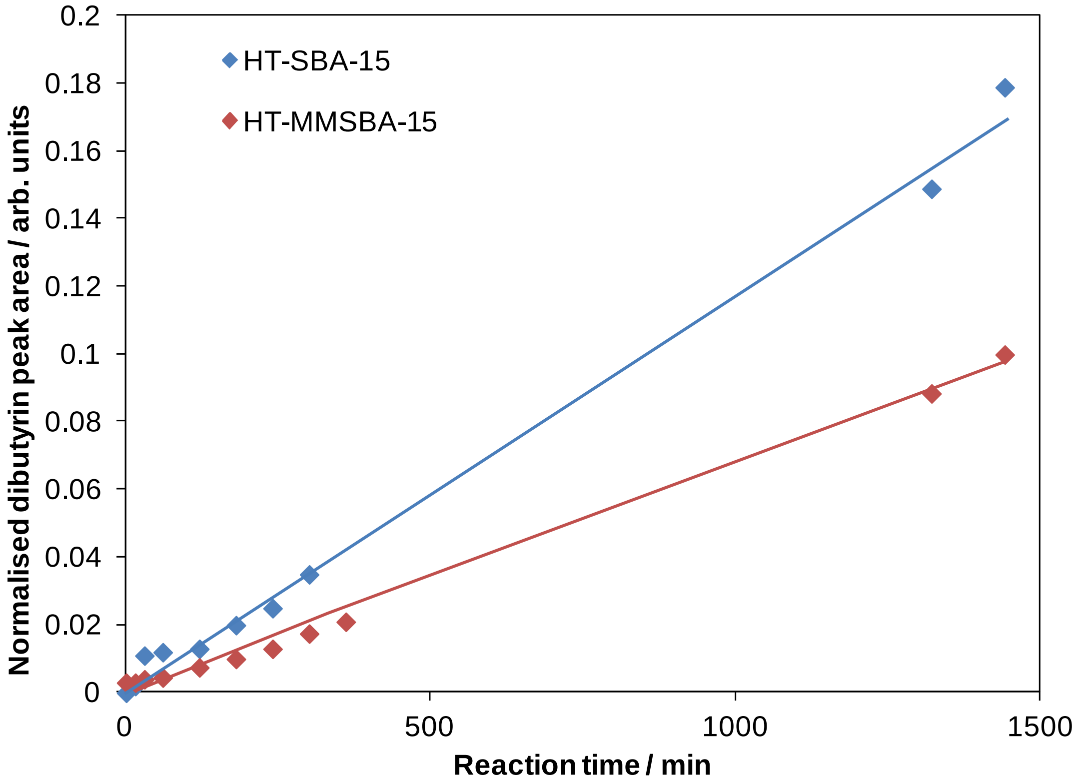

Figure 5.23. Intermediate dibutyrin formation over time for HT-SBA-15 and HT-MMSBA-15 during the transesterification of tributyrin

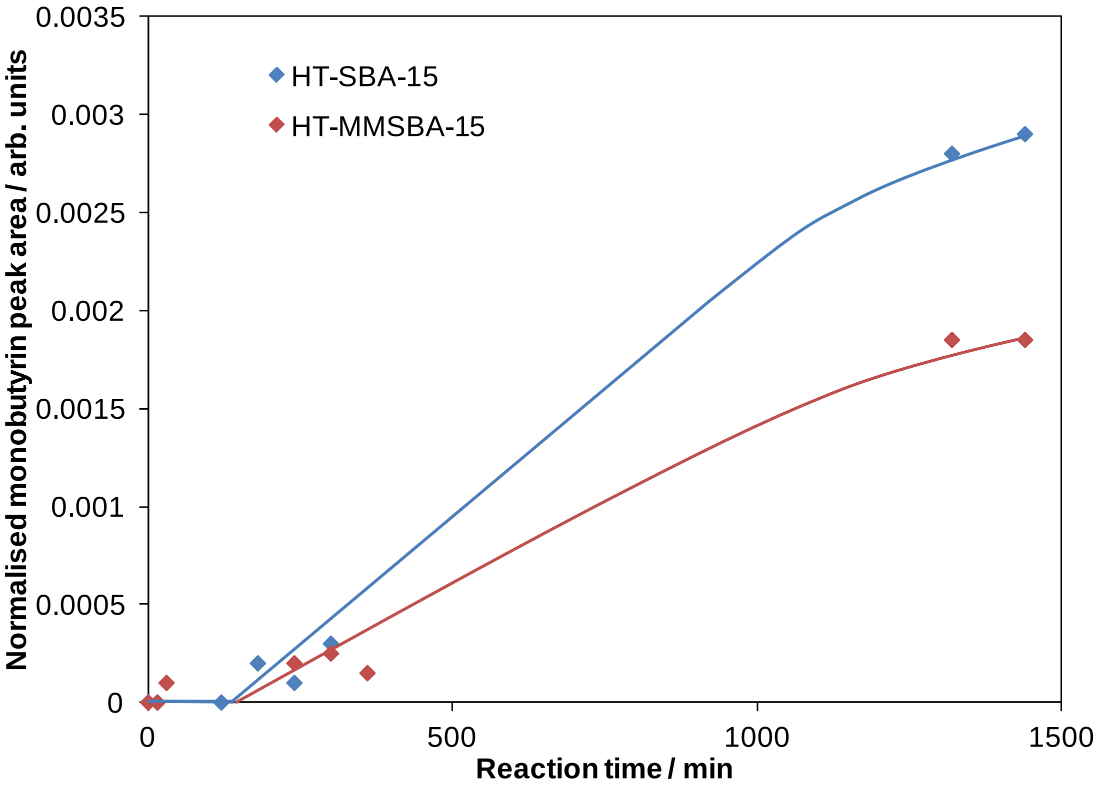

Figure 5.24. Intermediate monobutyrin formation over time for HT-SBA-15 and HT-MMSBA-15 during the transesterification of tributyrin

The HT-SBA-15 shows the highest TOF when normalised to base site density. The high Mg:Al ratio of the hydrotalcite present means that even though there are not as many base sites, the number of reactions per base site is highest. In this reaction there are the least diffusion limitations, and so the catalyst outperforms both the macroHT and HT-MMSBA-15.

The HT-MMSBA-15 and macroHT have similar stoichiometry and therefore the TOF values are very similar, associated with a 2:1 Mg:Al HT without diffusion limitations transesterifying a C4 chain length TAG. The overall conversion is lower due to the lack of base sites in the HT-MMSBA-15.

5.2.3.1.a Contribution of brucite to HT-SBA-15 activity

In order to determine whether the brucite present in the HT-SBA-15 sample was contributing to the activity of the catalyst, some pure brucite was synthesised, in the same way as for a conventional hydrotalcite, without the addition of any aluminium precursor. The structure was confirmed using powder XRD analysis, and CO_2 pulse chemisorption was also carried out to determine base site density.

The pure brucite sample was tested in the transesterification of tributyrin, under the same conditions as for the HT-SBA-15 sample. The reaction profile compared to that of HT-SBA-15 can be seen below in **Figure 5.25**, with the reaction data reported in **Table 5.12**.

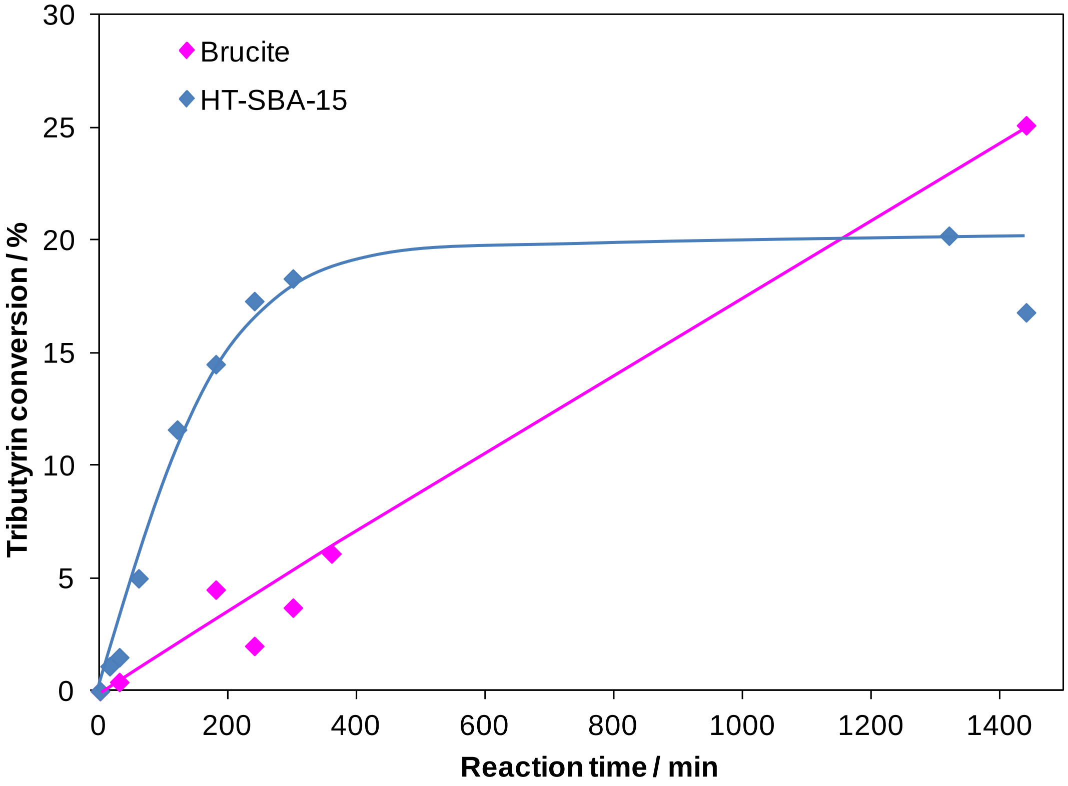

Figure 5.25. Reaction profiles showing tributyrin transesterification over time for HT-SBA-15 and pure brucite.

Table 5.12. Reaction data for HT-SBA-15 and brucite in the transesterification of tributyrin.

Catalyst	Initial rate / mmol g^{-1} min^{-1}	Number of base sites in 50 mg	TOF / min^{-1}	TAG conversion after 24 h / %
HT-SBA-15	0.15 +/- 0.01	2.11×10^{17}	21.95	16.8 +/- 1.5
Brucite	0.024 +/- 0.006	1.77×10^{18}	0.41	25.1 +/- 1.5

The profile shape is very different for that of a pure hydrotalcite catalyst, as there is not the same deactivation seen due to replacement of the interlayer hydroxide anions by butyric acid anions. Although the overall conversion is higher after 24 hours when pure brucite is used as the catalyst, the initial rate is much lower, and the TOF value calculated using the base site density of brucite is 50 times slower than for HT-SBA-15. Therefore, while brucite does show activity as a catalyst in the transesterification of tributyrin, and the brucite component of the HT-SBA-15 may well be contributing to its overall activity, this is not why the high TOF values are observed. Instead, the profile shape is due to the hydrotalcite base sites, and the high TOF value most likely due to the high Mg:Al hydrotalcite ratio.

5.2.3.2 Trilaurin transesterification

The HT-SBA-15 and HT-MMSBA-15 catalysts were then tested in the transesterification of trilaurin, a C12 chain length triglyceride. The trilaurin conversion profiles and methyl laurate formation profiles can be seen in **Figure 5.26** and **Figure 5.27** respectively. The reaction data is reported in **Table 5.13**.

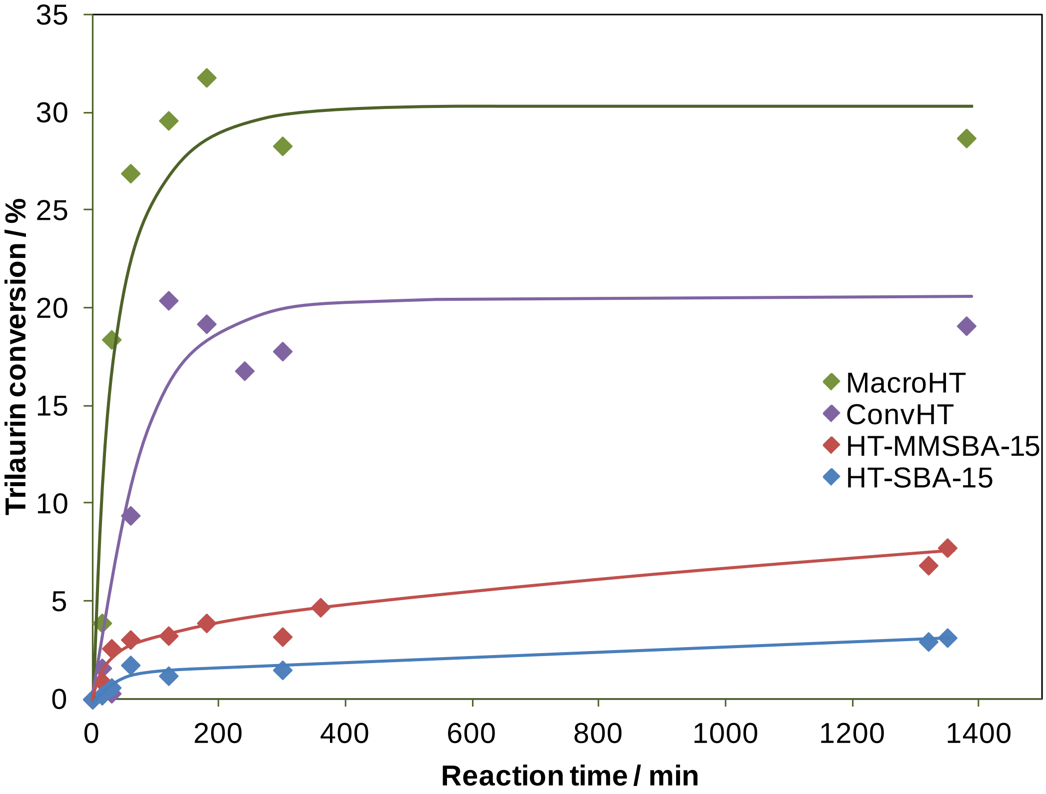

Figure 5.26. Reaction profiles showing trilaurin transesterification over time for HT-SBA-15 and HT-MMSBA-15, with convHT and macroHT shown for comparison.

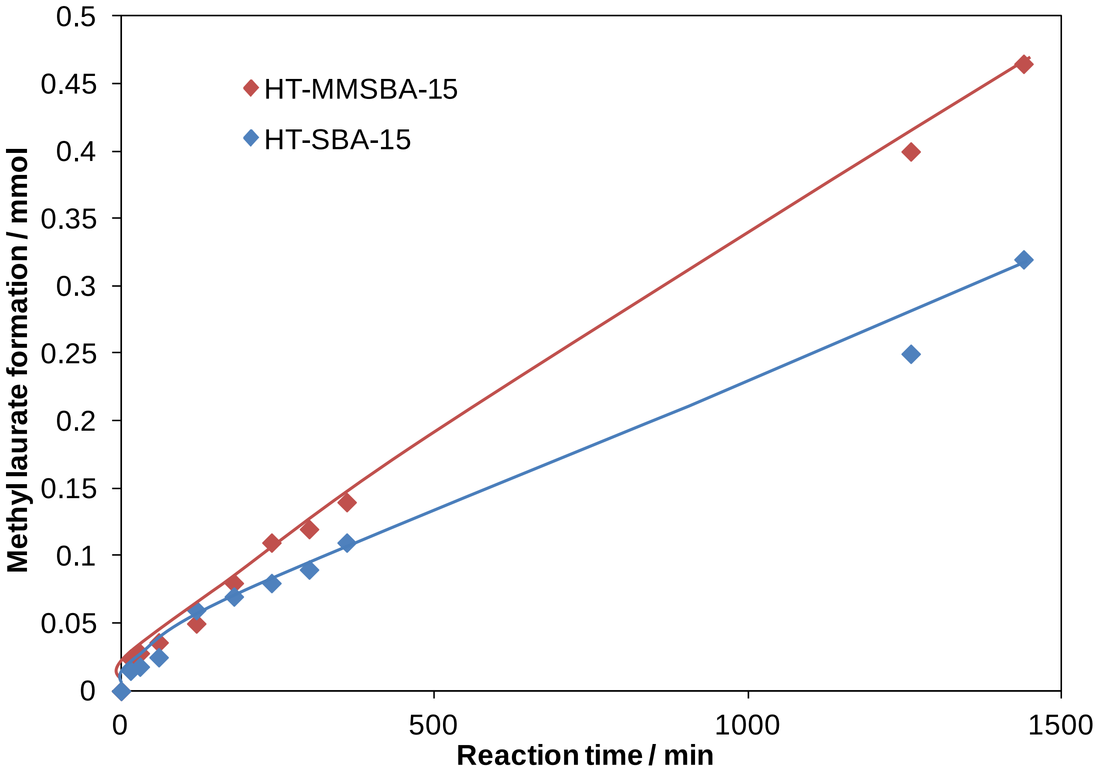

Figure 5.27. Methyl laurate formation over time for HT-SBA-15 and HT-MMSBA-15 during the transesterification of trilaurin

Table 5.13. Reaction data for HT-SBA-15 and HT-MMSBA-15 in the transesterification of trilaurin. The data for convHT and macroHT has been shown for comparison.

Catalyst	Initial rate / mmol g^{-1} min^{-1}	TOF / min^{-1}	TAG conversion after 24 hours / %	ML selectivity after 24h / %
HT-SBA-15	0.054 +/- 0.02	7.41	3.2 +/- 1.5	33.7 +/- 1.5
HT-MMSBA-15	0.10 +/- 0.02	9.62	7.8 +/- 1.5	20.0 +/- 1.5
ConvHT	0.26 +/- 0.05	1.83	19.1 +/- 1.5	54.5 +/- 1.5
MacroHT	0.94 +/- 0.07	7.37	28.7 +/- 1.5	57.2 +/- 1.5

In the transesterification of the C12 chain length triglyceride, trilaurin, the activity of the HT-SBA-15 catalyst has decreased 3 fold, resulting in a lower TOF than for HT-MMSBA-15, which has only decreased by a factor of two. There will always be a certain decrease in activity on moving to a longer chained triglyceride even when there are no diffusion limitations, as shown previously for macroHT and the HT on alumina series, due to the slower rate of movement, and decreased solubility of the triglyceride. The TOF values for HT-MMSBA-15 and macroHT have decreased by a similar amount on moving from C4 to C12, suggesting that the macropore channels in the HT-MMSBA-15 are acting in the same way as for the macroHT and removing diffusion limitations associated with the larger TAG reaching the active site. The TOF is slightly higher for the HT-MMSBA-15 due to the slightly higher Mg:Al ratio.

The HT-SBA-15 and convHT have both decreased by a similar amount, suggesting that diffusion limitations are an issue for both catalysts. The small mesopores of the HT-SBA-15, already partially filled with the HT and mixed oxides, make diffusion of the bulkier C12 TAG to the active sites difficult and slow. Although the stronger base sites mean the material still outperforms the 2:1 Mg:Al convHT, the decrease in TOF is equivalent.

5.2.3.3 Triolein transesterification

The HT-SBA-15 and HT-MMSBA-15 catalysts were tested in the transesterification of glyceryl trioleate, a C18 chain length TAG. **Figure 5.28** and **Figure 5.29** show the triolein conversion and FAME production profiles for the two catalysts respectively, and the reaction data is reported in **Table 5.14**.

Table 5.14. Reaction data for HT-SBA-15 and HT-MMSBA-15 in the transesterification of triolein. The data for convHT and macroHT has been shown for comparison.

Catalyst	Initial rate / mmol g^{-1} min^{-1}	TOF / min^{-1}	TAG conversion after 24 hours / %	MO selectivity after 24h / %
HT-SBA-15	0.006	0.86	0.5 +/- 1.5	23.5 +/- 1.5
HT-MMSBA-15	0.04 +/- 0.006	3.58	2.6 +/- 1.5	6.5 +/- 1.5
ConvHT	0.026 +/- 0.01	0.18	15.5 +/- 1.5	66.7 +/- 1.5
MacroHT	0.22 +/- 0.006	1.73	26.1 +/- 1.5	73.1 +/- 1.5

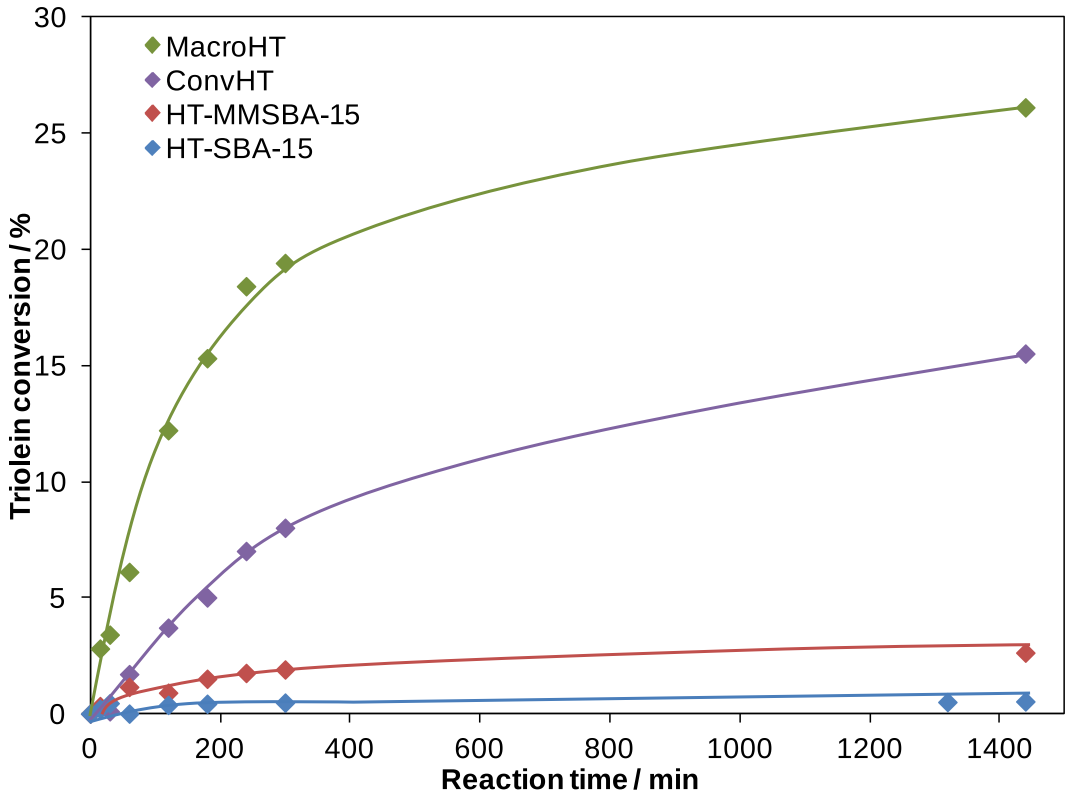

Figure 5.28. Reaction profiles showing triolein transesterification over time for HT-SBA-15 and HT-MMSBA-15, with convHT and macroHT shown for comparison.

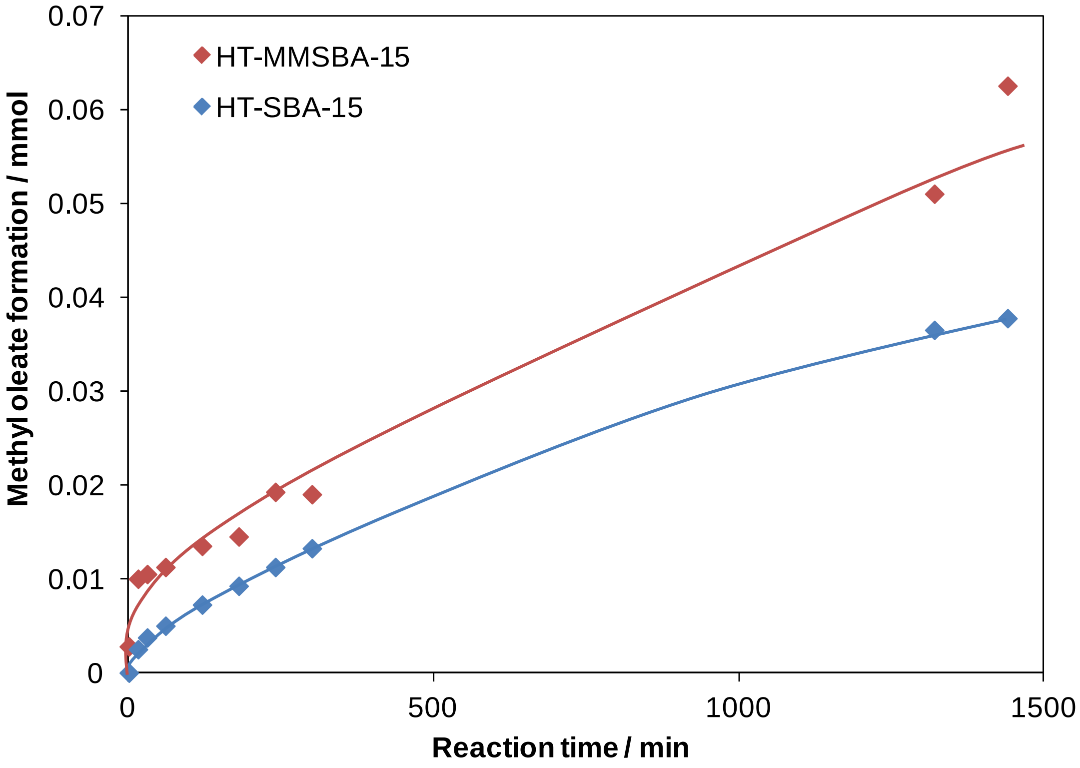

Figure 5.29. Methyl oleate formation over time for HT-SBA-15 and HT-MMSBA-15 during the transesterification of triolein.

Again, the TOF values for HT-SBA-15 and convHT have decreased by a factor of 8.6 and 10 respectively on moving to the largest, bulkiest triglyceride. The rate of diffusion through the bulk hydrotalcite, or the small mesopores of the silica, to reach the hydrotalcite base sites, is very slow. For the macroHT this decrease is a factor of 4, and for the HT-MMSBA15, only 2.7. The HT-MMSBA-15 outperforms the macroHT due to the presence of the macropores, along with the thin layer of hydrotalcite on the silica support meaning there are a greater number of the hydrotalcite base sites accessible to the TAGs.

5.2.3.4 Comparison of selectivities

For the HT-SBA-15 and HT-MMSBA-15, the highest FAME selectivities are seen for the shortest chain length C4 triglyceride, and the selectivities decrease as the chain length increases and conversion decreases, as illustrated in **Figure 5.30**. This is the opposite effect seen for all previous catalysts, the convHT, macroHT and the HT on alumina series. It is a pattern normally observed for surface reactions, when the less soluble TAGS cannot spend longer within the pores of the catalysts causing an increase in FAME selectivity, as previously hypothesised. It could be the case that because less hydrotalcite forms on the material, the layer is much thinner and therefore the less soluble TAGS cannot diffuse so far into the bulk of the microporous hydrotalcite, removing this favourable FAME formation at higher TAG chain length.

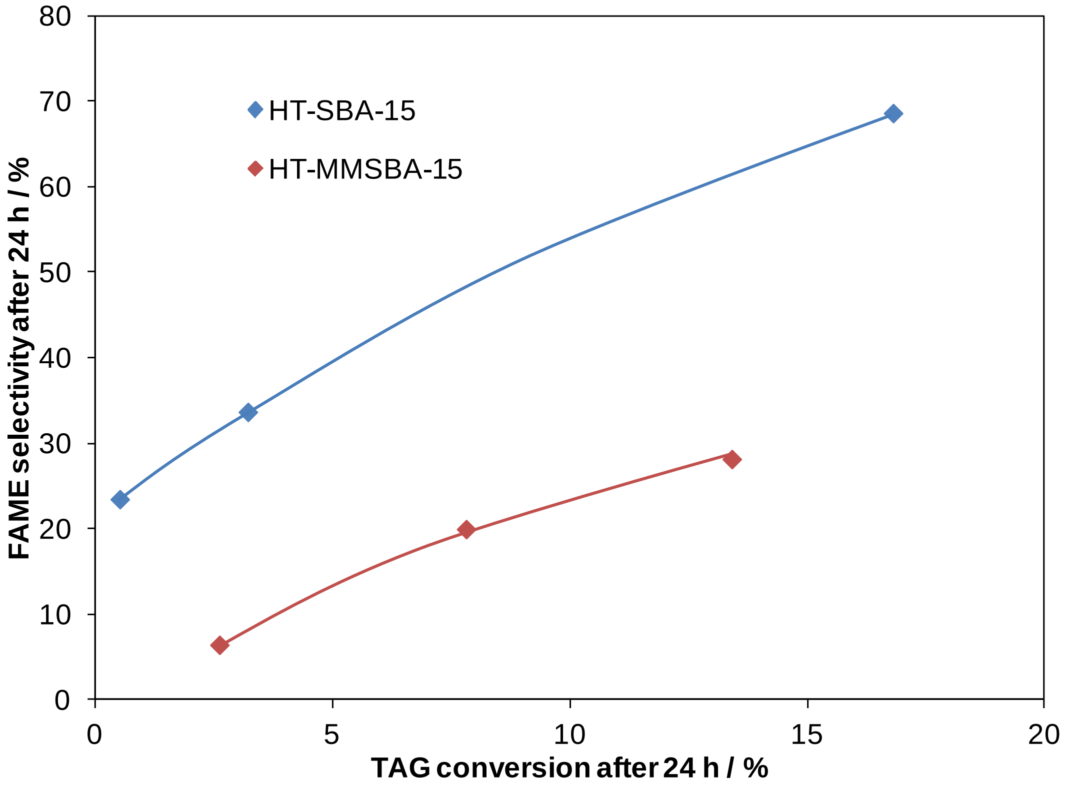

Figure 5.30. Plot showing TAG conversion versus FAME selectivity for HT-SBA-15 and HT-MMSBA-15, in the transesterification of varying chain length triglycerides.

5.2.3.5 Comparison of TOF values

Figure 5.31 compares the TOF values for HT-SBA-15, HT-MMSBA-15 and the bulk convHT and macroHT samples in the transesterification reactions of varying chain length triglycerides.

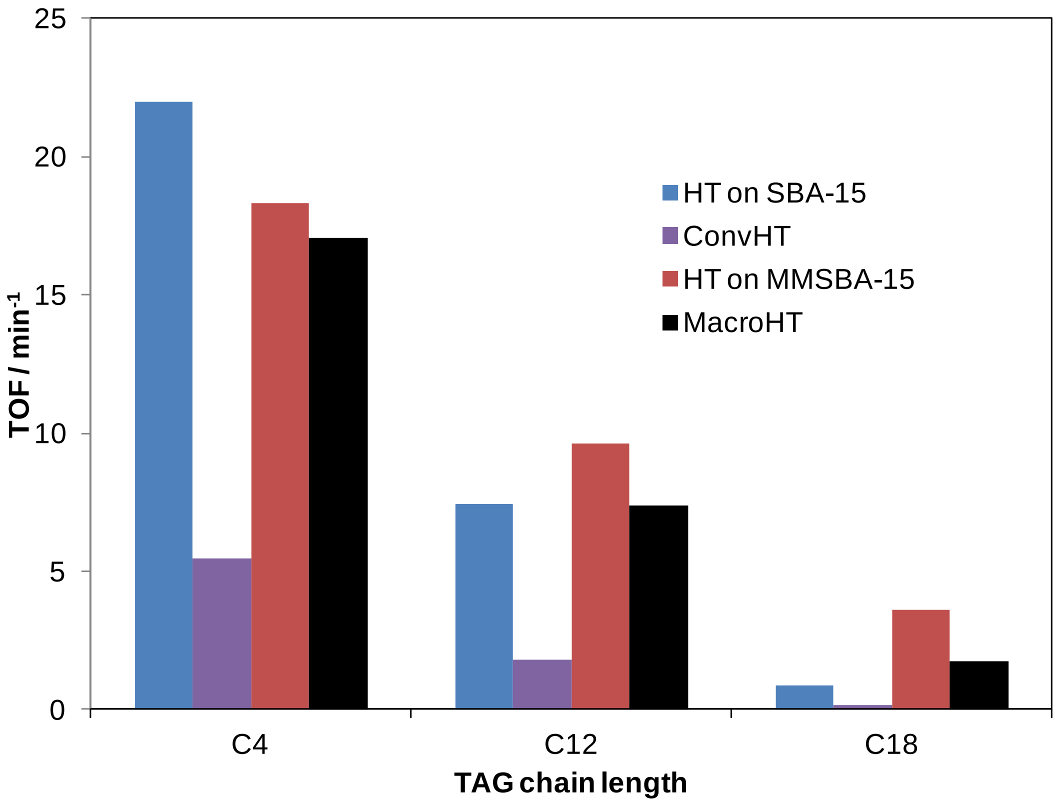

Figure 5.31. Bar chart comparing TOF values for HT-SBA-15 and HT-MMSBA-15 compared to the bulk convHT and macroHT catalysts in the transesterification of varying chain length triglycerides from C4 to C18.

The HT-SBA-15 has the highest TOF in the transesterification of a C4 chain triglyceride where there are the least diffusion limitations. This is due to the increased base site strength due to the high Mg:Al ratio formed during the synthesis.

The TOF values for the macroHT and HT-MMSBA-15 catalysts are very similar, the slightly higher value for HT-MMSBA-15 due to the slightly higher Mg:Al ratio of the hydrotalcite in this case, along with the greater accessibility of hydrotalcite base sites due to the thin layer on the silica support.

On moving to the C12 TAG chain length, the TOF values for the convHT and HT-SBA-15 decrease three fold due to poor diffusion of the bulkier TAG through the micropores/mesopores to reach the active sites. The HT-MMSBA-15 TOF decreases by the same amount as the macroHT, as would be expected for a macroporous 2:1 Mg:Al hydrotalcite without diffusion limitations transesterifying a slower, less soluble triglyceride.

For both the convHT and HT-SBA-15 catalysts, the TOF values on moving from C12 to a C18 TAG chain length decrease around 10 fold. This is a huge decrease compared to the 2.7 fold and 4 fold decreases observed for the HT-MMSBA-15 and macroHT respectively. Therefore, it is not just the slower movement of the bulkier TAGs causing the decrease in TOF for convHT and HT-SBA-15 but a lack of accessibility of the base sites to the bulkier molecules. Although the HT-SBA-15 outperforms the convHT due to its basicity, in terms of accessibility, they are similar in that they lose the same proportion of their activity when the TOF chain length increases.

The HT-MMSBA-15 and macroHT catalysts, which have similar stoichiometry and therefore can be directly compared, show similar activity for each TAG chain length. There are no diffusion limitations for the TAGs and so the TOF values are much greater than for convHT at longer chain lengths. The higher TOF values for the HT-MMSBA-15 may be due to the slightly higher Mg:Al ratio and greater accessibility of the hydrotalcite base sites in the thin hydrotalcite layers.

5.2.4 Reusability of HT-SBA-15 and HT-MMSBA-15

Characterisation was carried out on HT-SBA-15 and HT-MMSBA-15 after recovery from a 24 hour tributyrin reaction. Reactions were then run on the spent catalysts. For the HT-MMSAB-15 the catalyst was run straight after recovery. For the HT-SBA-15 the spent material was first re-calcined and rehydrated to reactivate it, before being tested in a further C4 transesterification reaction.

5.2.4.1 Spent catalyst characterisation

XPS analysis was carried out on the spent catalysts. **Figure 5.32** shows the Al 2p XP spectra for both fresh and spent a) HT-SBA-15 and b) HT-MMSBA-15. In both cases the proportion of alumina found as hydrotalcite has increased in the spent catalysts when compared to fresh. This suggests that under reaction conditions, further ion exchange of alumina into the hydrotalcite is occurring, as discussed in Chapter 4.

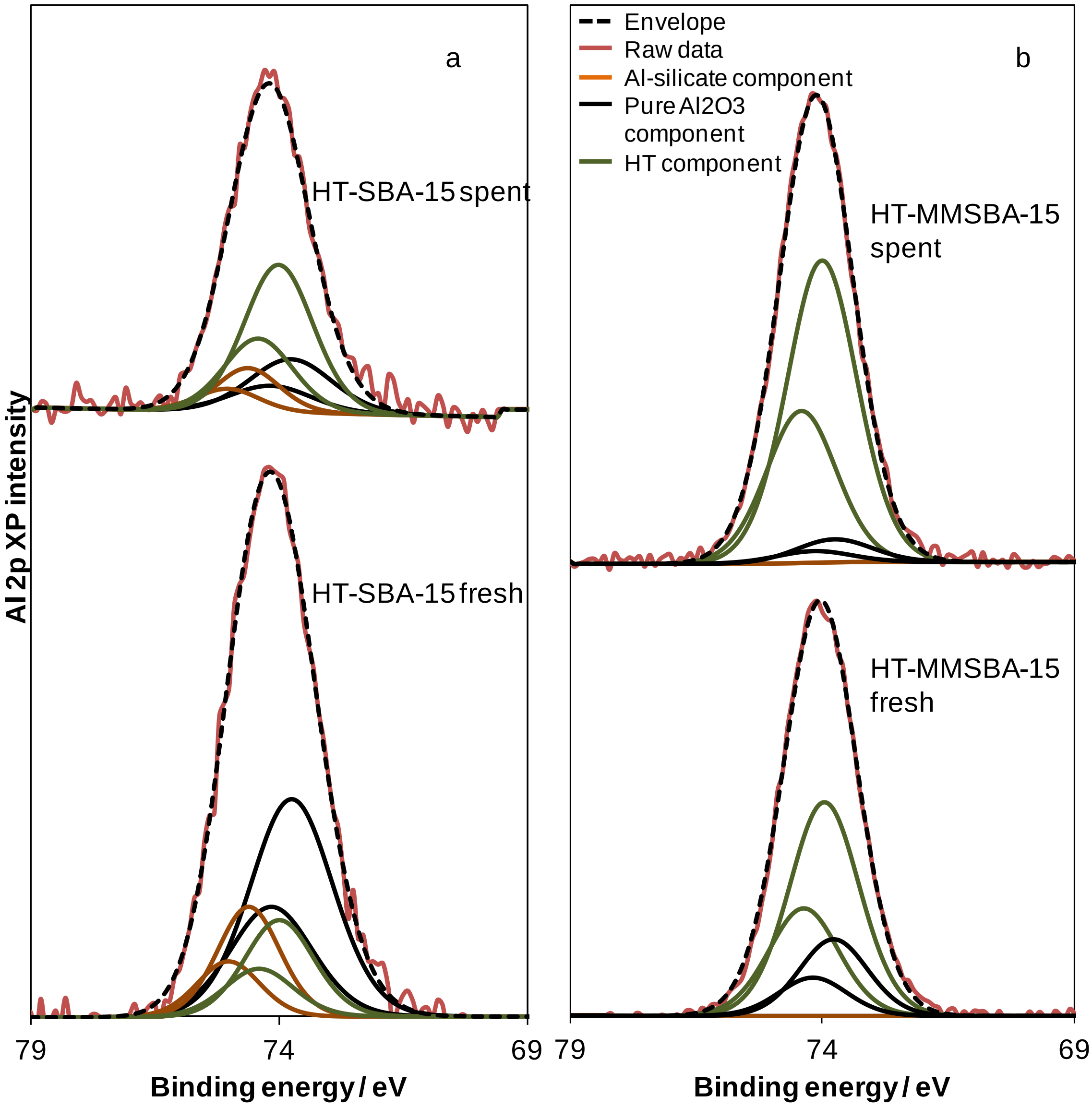

Figure 5.32. XP spectra showing the Al 2p chemical environments for a) HT-SBA-15 fresh and spent and b) HT-MMSBA-15 fresh and spent.

Figure 5.33 shows the Si 2p XP spectra for both fresh and spent a) HT-SBA-15 and b) HT-MMSBA-15. In both cases, the spent profiles show more silica bound to a hydrotalcite species than for the fresh catalysts, which gives more evidence for Al incorporation during reaction, forming a greater amount of hydrotalcite on the silica surface, with a lower Mg:Al ratio.

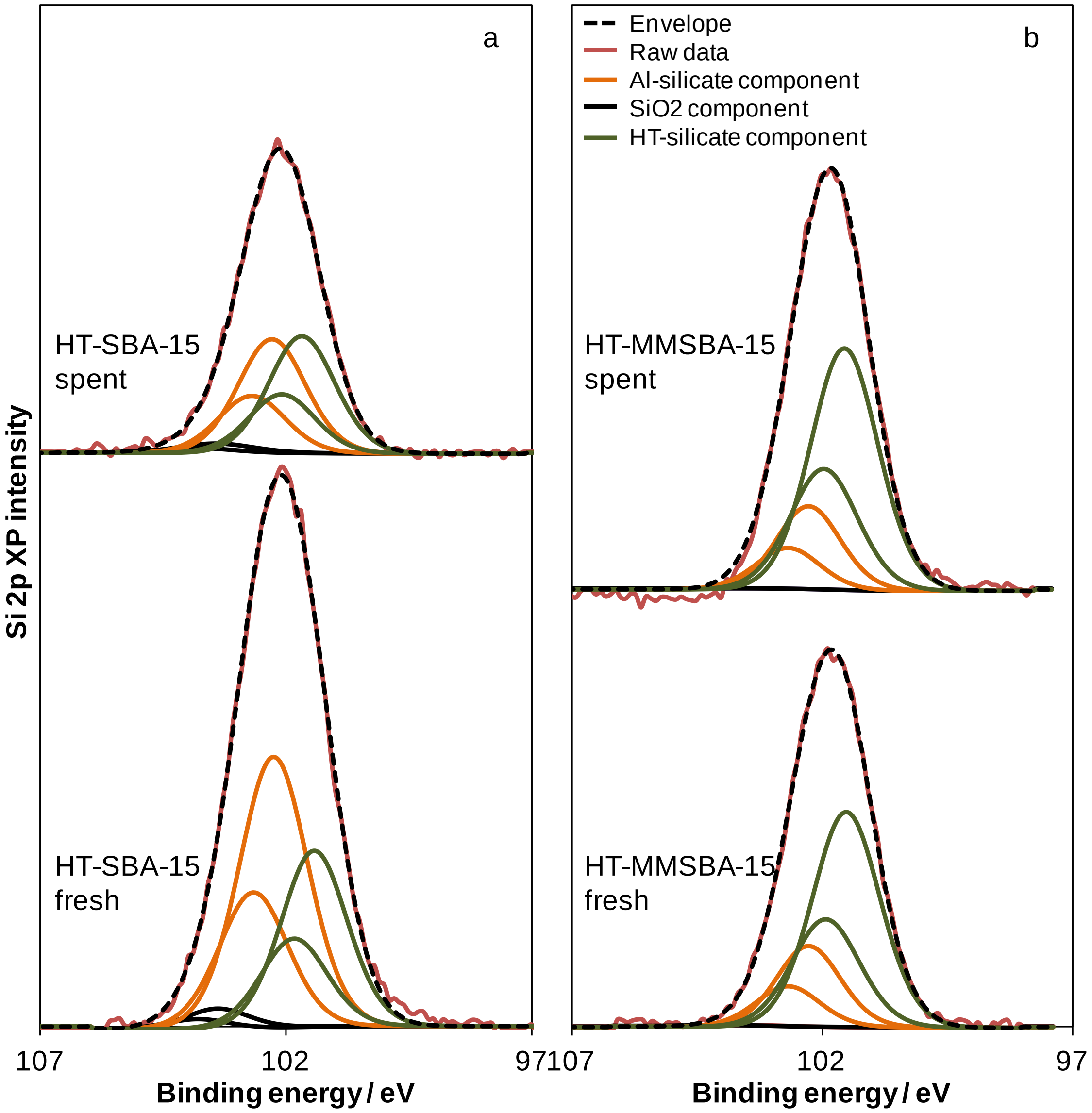

Figure 5.33. XP spectra showing the Si 2p chemical environments for a) HT-SBA-15 fresh and spent and b) HT-MMSBA-15 fresh and spent.

Figure 5.34 shows the Mg 2s XP spectra for both fresh and spent a) HT-SBA-15 and b) HT-MMSBA-15. **Table 5.15** reports on the metal weight percentages and ratios determined from XPS analysis, for both fresh and spent catalysts.

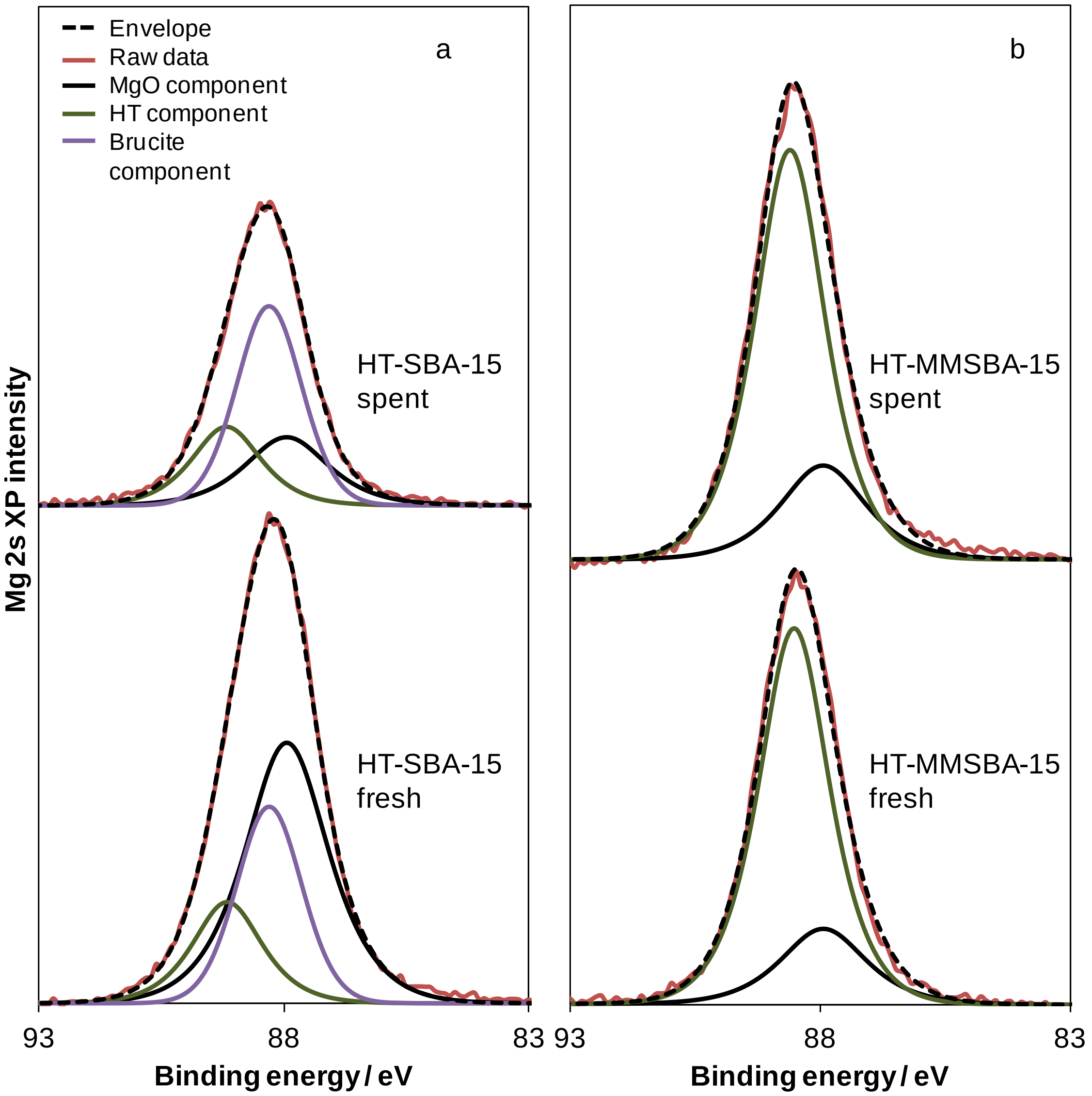

Figure 5.34. XP spectra showing the Mg 2s chemical environments for a) HT-SBA-15 fresh and spent and b) HT-MMSBA-15 fresh and spent.

Table 5.15. Atomic and weight percent ratios for the different constituents of HT-SBA-15 and HT-MMSBA-15 both fresh and spent, as determined via XPS analysis.

Catalyst	Surface HT Mg:Al ratio	Mg content / wt%	HT content / wt%	HT:Si ratio	Al_2O_3 content / wt%
HT-SBA-15-fresh	5.0:1	22.3 +/- 0.6	4.7 +/- 0.1	0.45:1	4.7 +/-0.1
HT-SBA-15 spent	2.7:1	21.1 +/- 0.6	7.0 +/- 0.2	0.54:1	2.48+/-0.07
HT-MMSBA-15 fresh	2.6:1	16.7 +/- 0.5	19.2 +/- 0.5	2.03:1	5.5 +/- 0.2
HT-MMSBA-15 spent	1.5:1	16.2 +/- 0.4	21.7 +/- 0.6	2.52:1	2.01+/-0.06

After 24 hours under reaction conditions the Mg wt% has not altered for either catalyst, showing that it does not leach from the surface. The HT Mg:Al ratio has decreased significantly after reaction for both cases. This, coupled with the increase in HT metal weight and HT:Si ratio, and the decrease in alumina wt% all gives evidence to the theory that under reaction conditions further hydrothermal treatment occurs allowing more ion exchange of alumina into the hydrotalcite, forming more hydrotalcite with a lower Mg:Al ratio.

Figure 5.35 shows the C 1s XP spectra for both fresh and spent a) HT-SBA-15 and b) HT-MMSBA-15. **Table 5.16** reports on the carbon content for the fresh and spent catalysts.

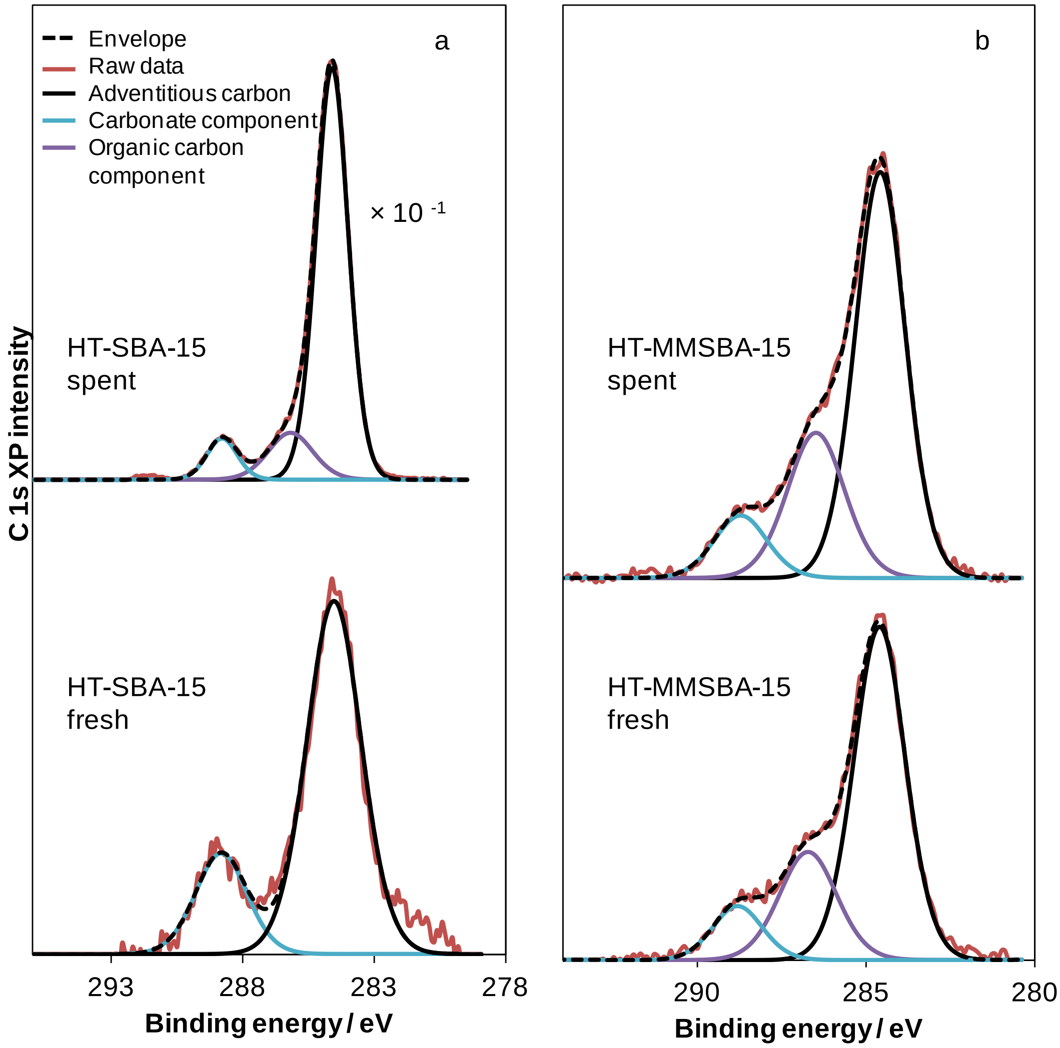

Figure 5.35. XP spectra showing the C 1s chemical environments for a) HT-SBA-15 fresh and spent and b) HT-MMSBA-15 fresh and spent.

Table 5.16. Atomic percentages of carbon for HT-SBA-15 and HT-MMSBA-15, both fresh and spent, as determined via XPS analysis.

Catalyst	Carbonate content / surface at%	Other organic carbon content / surface at %
HT-SBA-15-fresh	1.36 +/- 0.04	-
HT-SBA-15 spent	3.21 +/- 0.09	5.31 +/- 0.15
HT-MMSBA-15 fresh	1.53 +/- 0.04	3.62 +/- 0.10
HT-MMSBA-15 spent	1.64 +/- 0.05	4.12 +/- 0.11

The fresh HT-MMSBA-15 sample has 3.62 at% organic carbon content. It is most likely that this is due to a small amount of the polystyrene bead template used in the synthesis of the macroporous material, which has not fully burnt out during the calcination.

When looking at these results there is a large difference between the carbon adsorption of the two catalysts. There is a much larger amount of carbon on the HT-SBA-15 after reaction than for HT-MMSBA-15, an increase of 7.16 at% for HT-SBA-15 compared to 0.61 at% for HT-MMSBA-15. This difference is probably due to the difference in accessibility between the two catalysts. As TAG molecules move into the mesopore channels, it is harder to diffuse back out and they may become trapped within the channels. Whereas when there are large macropore super-highways running through the material, the organic material can diffuse quickly away from the catalyst active sites.

5.2.4.2 Recycle tests

The spent HT-SBA-15 was filtered from the C4 TAG transesterification reaction mixture after 24 hours and dried under vacuum before being calcined and treated hydrothermally under the same conditions as for the fresh catalyst. This reactivated material was the tested as a catalyst in another tributyrin transesterification reaction. The reaction profiles for both fresh and reactivated HT-SBA-15 can be seen in **Figure 5.36**. The methyl butyrate product formation profiles for the two catalysts have been plotted in **Figure 5.37**. **Table 5.17** reports on the reaction data for each catalyst.

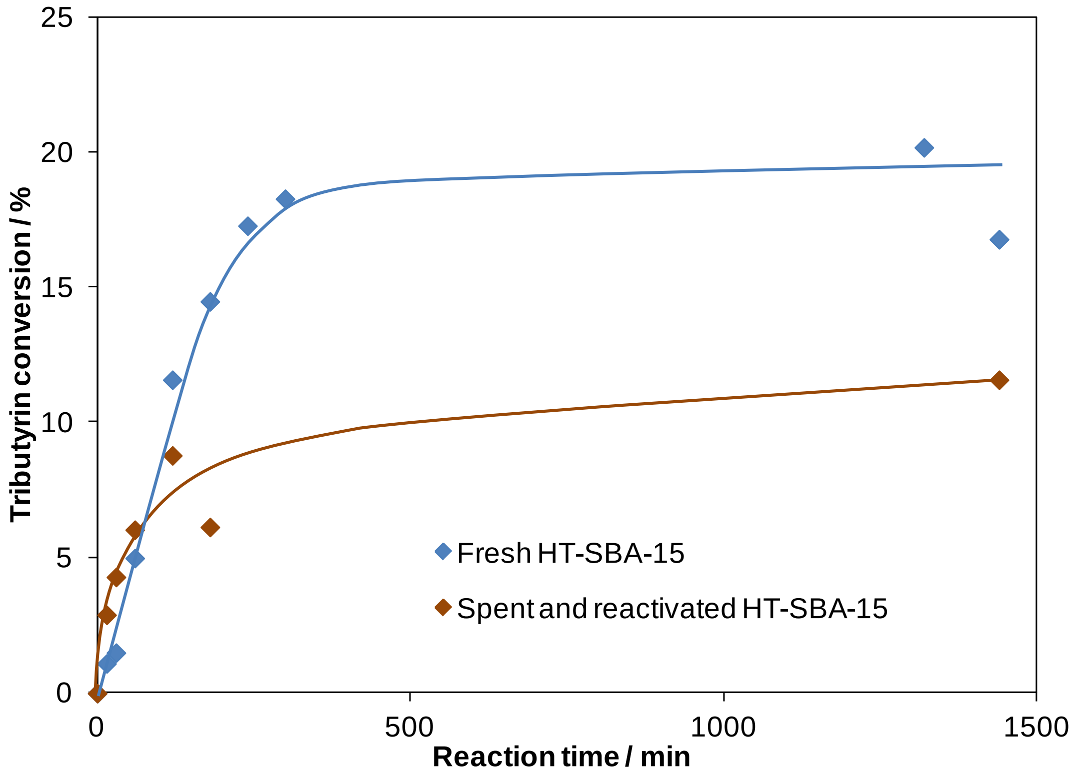

Figure 5.36. Triglyceride conversion for fresh versus spent-reactivated HT-SBA-15 during the transesterification of tributyrin.

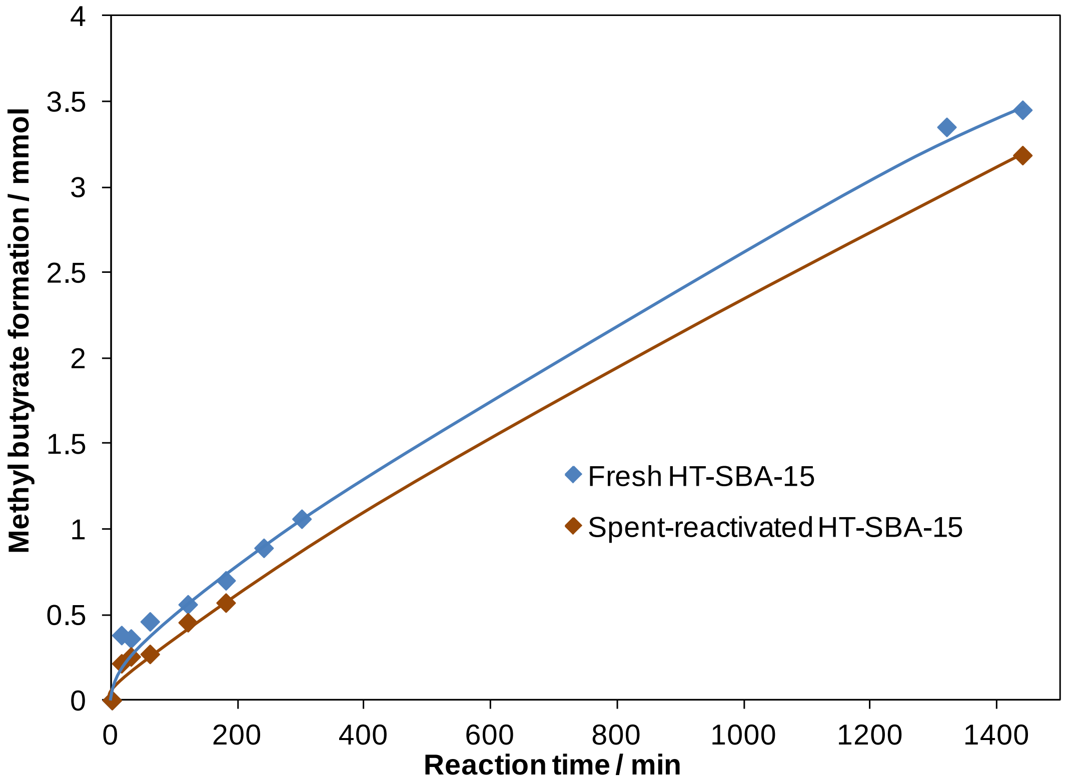

Figure 5.37. Methyl butyrate formation profiles for both fresh and spent-reactivated HT-SBA-5 during the transesterification of tributyrin.

Table 5.17. Reaction data for HT-SBA-15 both fresh and spent-reactivated in the transesterification of tributyrin

Catalyst	Initial rate / mmol g^{-1} min^{-1}	TOF / min^{-1}	TAG conversion after 24 hours / %	MB selectivity after 24h / %
HT-SBA-15 fresh	0.15 +/- 0.01	21.95	16.8 +/- 1.5	68.7 +/- 1.5
HT-SBA-15 Spent-reactivated	0.23 +/- 0.01	32.80	11.6 +/- 1.5	91.7 +/- 1.5

The initial rate of the reactivated HT-SBA-15 is actually faster than the fresh material. However, the catalyst deactivates more quickly and so the overall conversion is lower. From XPS analysis it has been established that there is a greater amount of hydrotalcite in the material, albeit with a lower Mg:Al ratio, and so it is likely that if base site titration had been carried out on the reactivated material, this would show a higher base site density and therefore the TOF value would be calculated as lower than it is now, possibly comparable to the fresh catalyst.

As the HT-SBA-15 material has been shown to be prone to adsorb butyric acid and organic carbon content, the faster rate may mean this deactivation occurs more quickly, hence the lower conversion.

The spent HT-MMSBA-15 was recovered from a tributyrin transesterification reaction after 24 hours by filtration, before drying in a vacuum oven. The spent catalyst was then immediately re-used in a further tributyrin transesterification reaction without any treatment to see how much of the activity has been retained. The reaction profiles showing tributyrin transesterification over time for both fresh and spent HT-MMSBA-15 can be seen below in **Figure 5.38**. The methyl butyrate formation profiles for each catalyst have been plotted in **Figure 5.39**. **Table 5.18** reports the reaction data for the two catalysts.

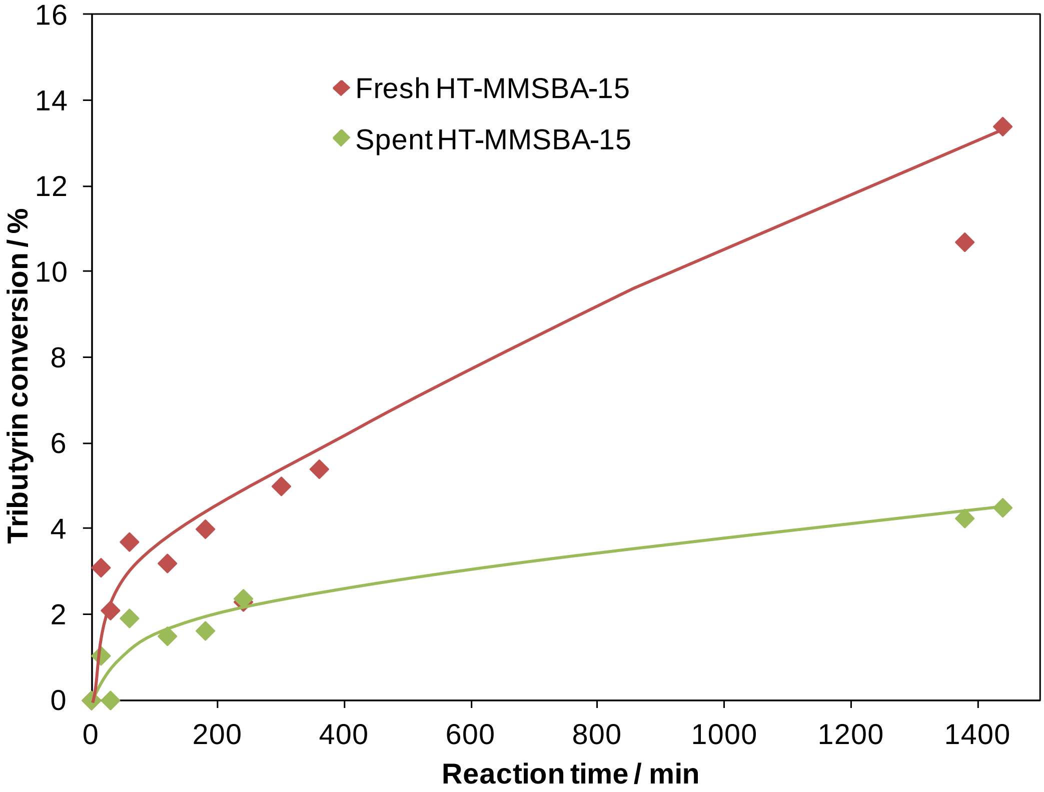

Figure 5.38. Triglyceride conversion for fresh versus spent HT-MMSBA-15 during the transesterification of tributyrin.

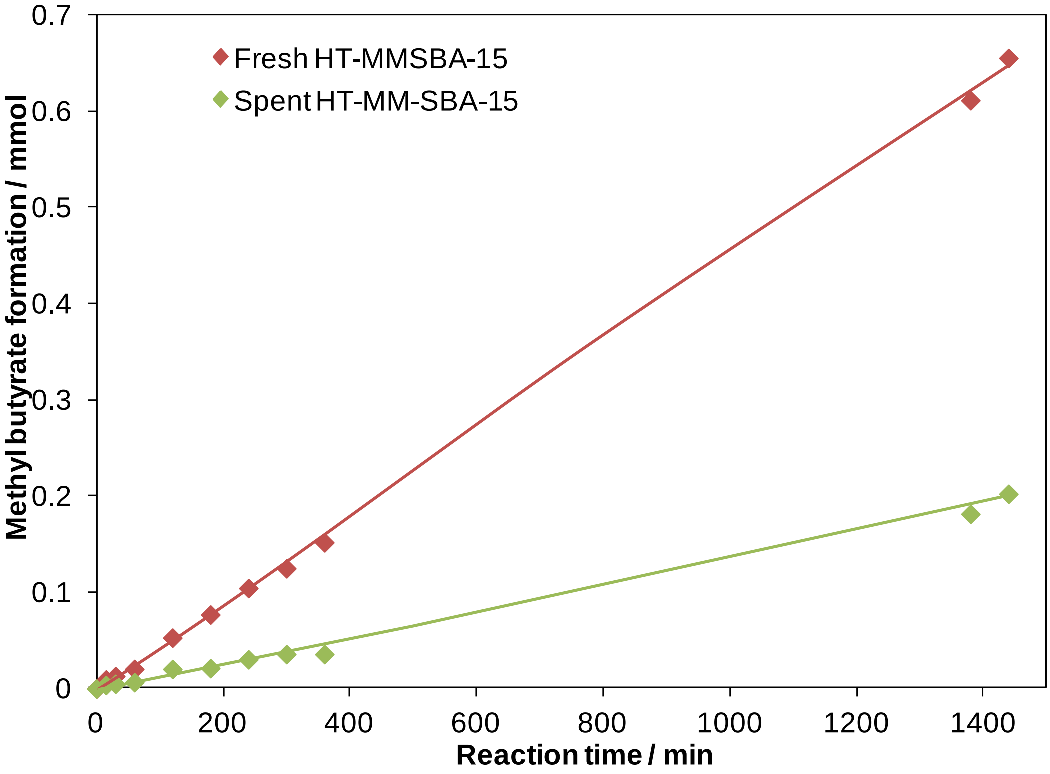

Figure 5.39. Methyl butyrate formation profiles for fresh and spent HT-MMSBA-15 during the transesterification of tributyrin.

Table 5.18. Reaction data for HT-MMSBA-15 both fresh and spent in the transesterification of tributyrin

Catalyst	Initial rate / mmol g^{-1} min^{-1}	TOF / min^{-1}	TAG conversion after 24 hours / %	MB selectivity after 24h / %
HT-MMSBA-15 fresh	0.19 +/- 0.05	18.31	13.4 +/- 1.5	32.5 +/- 1.5
HT-MMSBA-15 spent	0.068 +/- 0.004	6.41	4.5 +/- 1.5	12.4 +/- 1.5

With no re-activation treatment at all, the HT-MMSBA-15 retains 35 % of its initial TOF value, a result far superior to that of macroHT, which completely deactivates after one reaction. Not only does the spent HT-MMSBA-15 contain less adsorbed carbon, but the extra hydrotalcite formation occurring during the reaction will have helped to combat any catalyst deactivation.

5.3 Conclusions

Hydrotalcite has been successfully grafted onto the surface of both a mesoporous SBA-15 and a meso-macroporous SBA-15, using a novel preparation method. Al-SBA-15 and Al-MMSBA-15 were prepared using the method of Landau and co-workers[19] and characterised. Mg methoxide impregnation was then carried out onto the Al-SBA-15 surface, followed by calcination and a hydrothermal treatment, in order to form hydrotalcite on the silica surface.

Characterisation of the materials showed the grafting to be much more successful on the Al-MMSBA-15 surface due to better diffusion of the Mg methoxide through the macropore channels allowing greater metal dispersion, although both materials showed a hydrotalcite crystalline phase present. For HT-SBA-15 there was a significant amount of un-grafted brucite present due to poor metal dispersion. The Mg:Al ratio of the hydrotalcite formed on HT-SBA-15 was also greater than for HT-MMSBA-15.

The two materials were tested as catalysts in the transesterification of triglycerides to form biodiesel. Whilst the HT-SBA-15 showed superior activity in the transesterification of tributyrin due to its greater base site strength; accessibility issues became apparent on moving to longer chained triglycerides, as the activity dropped at a much faster rate than for macroHT where there are no diffusion limitations, and at a similar rate to the diffusion limited convHT. Therefore, the HT-SBA-15 catalyst showed no advantages over bulk convHT in terms of accessibility, but purely through the difference in stoichiometry. The higher activity over the few base sites present due to the higher Mg:Al ratio. However, if more Mg could be forced into the convHT during the preparation, possibly via enhanced pH, the activity of the convHT could also be enhanced, without the requirement of the silica support and the extra preparation steps involved.

On moving from short chain to long chain triglycerides, the HT-MMSBA-15 vastly outperforms the HT-SBA-15 due to the ease of accessibility of the bulky TAGs through the macropore superhighways to reach the catalyst active sites.

The HT-MMSBA-15, which had a directly comparable stoichiometry to the macroHT, showed similar activity to macroHT in the transesterification of varying chain length triglycerides. Slightly more activity was retained on increasing triglyceride chain length, possibly due to the combination of a thin surface HT layer, along with macropore superhighways. The main advantage over the macroHT comes when examining the spent catalyst. The stability and method of preparation of the HT means that on direct re-use, instead of the complete deactivation observed for macroHT, 35% of the HT-MMSBA-15 catalyst's activity remains. On reactivation, the activity may be recovered, as shown for the HT-SBA-15, and the catalyst may prove to be useful for several runs, making it promising as an industrial catalyst for biodiesel synthesis.

5.4 References

1. N. A. Melosh, P. Davidson and B. F. Chmelka, *Journal of the American Chemical Society*, 2000, **122**, 823-829.
2. M. Imperor-Clerc, P. Davidson and A. Davidson, *Journal of the American Chemical Society*, 2000, **122**, 11925-11933.
3. J. P. Thielemann, F. Girgsdies, R. Schlögl and C. Hess, *Beilstein J Nanotechnol*, 2011, **2**, 110-118.
4. Z. Luan, E. M. Maes, P. A. W. van der Heide, D. Zhao, R. S. Czernuszewicz and L. Kevan, *Chemistry of Materials*, 1999, **11**, 3680-3686.
5. A. Galarneau, H. Cambon, F. Di Renzo and F. Fajula, *Langmuir*, 2001, **17**, 8328-8335.
6. Z. Kónya, E. Molnar, G. Tasi, K. Niesz, G. Somorjai and I. Kiricsi, *Catal Lett*, 2007, **113**, 19-28.
7. M. Zhao, T. L. Church and A. T. Harris, *Applied Catalysis B: Environmental*, 2011, **101**, 522-530.
8. C.-H. Tu, A.-Q. Wang, M.-Y. Zheng, X.-D. Wang and T. Zhang, *Applied Catalysis A: General*, 2006, **297**, 40-47.
9. S. Jin Bae, S.-W. Kim, T. Hyeon and B. Moon Kim, *Chemical Communications*, 2000, **0**, 31-32.
10. X. Feng, M. Yan, T. Zhang, Y. Liu and M. Bao, *Green Chemistry*, 2010, **12**, 1758-1766.
11. D. Margolese, J. A. Melero, S. C. Christiansen, B. F. Chmelka and G. D. Stucky, *Chemistry of Materials*, 2000, **12**, 2448-2459.
12. S. S. Reddy, B. D. Raju, V. S. Kumar, A. H. Padmasri, S. Narayanan and K. S. R. Rao, *Catalysis Communications*, 2007, **8**, 261-266.
13. A. M. Liu, K. Hidajat, S. Kawi and D. Y. Zhao, *Chemical Communications*, 2000, **0**, 1145-1146.
14. Y.-J. Han, G. D. Stucky and A. Butler, *Journal of the American Chemical Society*, 1999, **121**, 9897-9898.
15. P. Yang, G. Wirnsberger, H. C. Huang, S. R. Cordero, M. D. McGehee, B. Scott, T. Deng, G. M. Whitesides, B. F. Chmelka, S. K. Buratto and G. D. Stucky, *Science*, 2000, **287**, 465-467.
16. Y.-J. Han, J. M. Kim and G. D. Stucky, *Chemistry of Materials*, 2000, **12**, 2068-2069.
17. R. Ryoo, C. H. Ko, M. Kruk, V. Antochshuk and M. Jaroniec, *The Journal of Physical Chemistry B*, 2000, **104**, 11465-11471.
18. Sujandi, S.-E. Park, D.-S. Han, S.-C. Han, M.-J. Jin and T. Ohsuna, *Chemical Communications*, 2006, **0**, 4131-4133.
19. M. V. Landau, E. Dafa, M. L. Kaliya, T. Sen and M. Herskowitz, *Microporous and Mesoporous Materials*, 2001, **49**, 65-81.
20. R. N. Kerber, A. Kermagoret, E. Callens, P. Florian, D. Massiot, A. Lesage, C. Copéret, F. Delbecq, X. Rozanska and P. Sautet, *Journal of the American Chemical Society*, 2012, **134**, 6767-6775.
21. Y. H. Liu, H. P. Lin and C. Y. Mou, *Journal of the Chinese Chemical Society*, 2005, **52**, 717-720.
22. P. Madhusudhan Rao, A. Wolfson, M. V. Landau and M. Herskowitz, *Catalysis Communications*, 2004, **5**, 327-331.

23. A. Zukal, J. Mayerova and J. Cejka, *Physical Chemistry Chemical Physics*, 2010, **12**, 5240-5247.
24. A. Ji, L. Y. Shi, Y. Cao and Y. Wang, in *Studies in Surface Science and Catalysis*, eds. S. Abdelhamid and J. Mietek, Elsevier, 2005, vol. Volume 156, pp. 917-924.
25. J. A. Melero, L. F. Bautista, G. Morales, J. Iglesias and R. Sánchez-Vázquez, *Chemical Engineering Journal*, 2010, **161**, 323-331.
26. M. A. Jackson, I. K. Mbaraka and B. H. Shanks, *Applied Catalysis A: General*, 2006, **310**, 48-53.
27. J. Dhainaut, J. P. Dacquin, A. F. Lee and K. Wilson, *Green Chemistry*, 2010, **12**, 296-303.
28. D. Zhao, J. Feng, Q. Huo, N. Melosh, G. H. Fredrickson, B. F. Chmelka and G. D. Stucky, *Science*, 1998, **279**, 548-552.
29. A. Y. Khodakov, V. L. Zholobenko, R. Bechara and D. Durand, *Microporous and Mesoporous Materials*, 2005, **79**, 29-39.
30. J. J. Chiu, D. J. Pine, S. T. Bishop and B. F. Chmelka, *Journal of Catalysis*, 2004, **221**, 400-412.
31. E. P. Barrett, L. G. Joyner and P. P. Halenda, *Journal of the American Chemical Society*, 1951, **73**, 373-380.
32. E. N. Maslen, V. A. Streltsov, N. R. Streltsova, N. Ishizawa and Y. Satow, *Acta Crystallographica Section B*, 1993, **49**, 973-980.
33. P. J. Cumpson and M. P. Seah, *Surface and Interface Analysis,* 1997, **25**, 430-446.
34. A. V. G. Chizmeshya, M. J. McKelvy, R. Sharma, R. W. Carpenter and H. Bearat, *Materials Chemistry and Physics*, 2003, **77**, 416-425.
35. A. R. Denton and N. W. Ashcroft, *Phys. Rev. A*, 1991, **43**, 3161-3164.
36. P. Scherrer, *Nachr. Ges. Wiss. Göttingen* 1918, **26**, 98-100.
37. G. W. Brindley and S. Kikkawa, *American Mineralogist*, 1979, **64**, 836-843.
38. H. C. Greenwell, P. J. Holliman, W. Jones and B. V. Velasco, *Catalysis Today*, 2006, **114**, 397-402.
39. S. Abello, F. Medina, D. Tichit, J. Perez-Ramirez, J. C. Groen, J. E. Sueiras, P. Salagre and Y. Cesteros, *Chemistry-a European Journal*, 2005, **11**, 728-739.
40. D. E. Haycock, D. S. Urch, C. J. Nicholls and M. Kasrai, *Journal of the Chemical Society-Dalton Transactions*, 1978, 1791-1796.

Chapter 6

Cs-promoted MgO nanocatalysts

6.1 Introduction

Magnesium oxide, along with other alkaline earth oxides, is basic in nature and has shown activity as a catalyst in various reactions such as methane activation[1] and ketone dehydrogenation.[2] MgO has also been reported as an active catalyst in the transesterification of plant oils to form biodiesel.[3-5]

Figure 6.1 shows the three most common surface terminations for an MgO crystal, the (100), (110) and (111) planes.

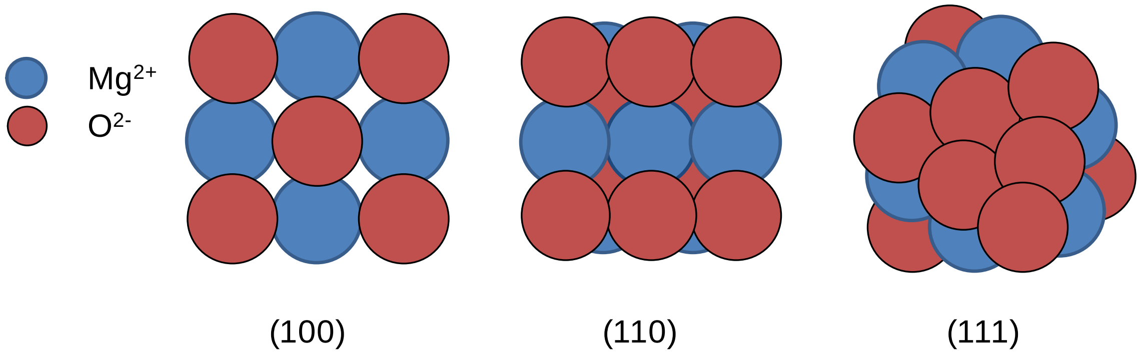

Figure 6.1. Diagram showing the most common MgO surface terminations.

The surface termination dramatically affects the Lewis basicity of the MgO. The (111) surface is the least energetically stable, and has a net dipole moment due to the alternating O^{2-} and Mg^{2+} layers. The O^{2-} layer is thermodynamically favoured on exposure to air,[6] and therefore this is the most electron rich surface. The (110) and (100) surfaces consist of Mg^{2+}-O^{2-} pairs, however the surface energy is higher for the (110) surface, due to relaxation of the Mg-O interatomic distances.[7] The higher the number of exposed (111) planes, the more basic the MgO crystal.

Reconstruction of the magnesium oxide surface during annealing can result in defects[8] where there are lower co-ordinate anion sites such as corner, step or edge sites. These sites are more polarisable and more likely to donate electrons than the stoichiometric sites, and therefore these defects also contribute to the basicity and catalytic activity of magnesium oxide.

Doping alkaline earth oxides with alkali metals offers a route to achieving even greater catalytic activity, through the resulting enhancement of surface basic properties.[9] Promotion by lithium has been well studied, and is postulated to occur via Li^+ incorporation into the oxide lattice generating $[Li^+O^-]$ ion pairs and oxygen vacancies, which show superior catalytic activity and selectivity for reactions including oxidative methane coupling.[10, 11] The introduction of alkali ions into the oxide lattice is thought to induce significant morphological changes, favouring more polarisable low coordination step and corner sites.[10] It has been suggested that Li^+ dopants subsequently preferentially coordinate to these highly active corner and step sites upon thermal processing, limiting the enhancement of the basicity.[9] Larger alkali cations are predicted unable to coordinate to these sites due to their greater ionic radii, leaving them available for reaction.[12, 13] Instead, they can donate electrons to the magnesium oxide lattice, which are trapped at oxygen vacancies, giving rise to electron rich sites, called F-centres. This effect is illustrated in **Figure 6.2**, the smaller Li^+ cation coordinates to the edge O^{2-} anions and removes basic sites, whereas the larger Na^+ cation does not.

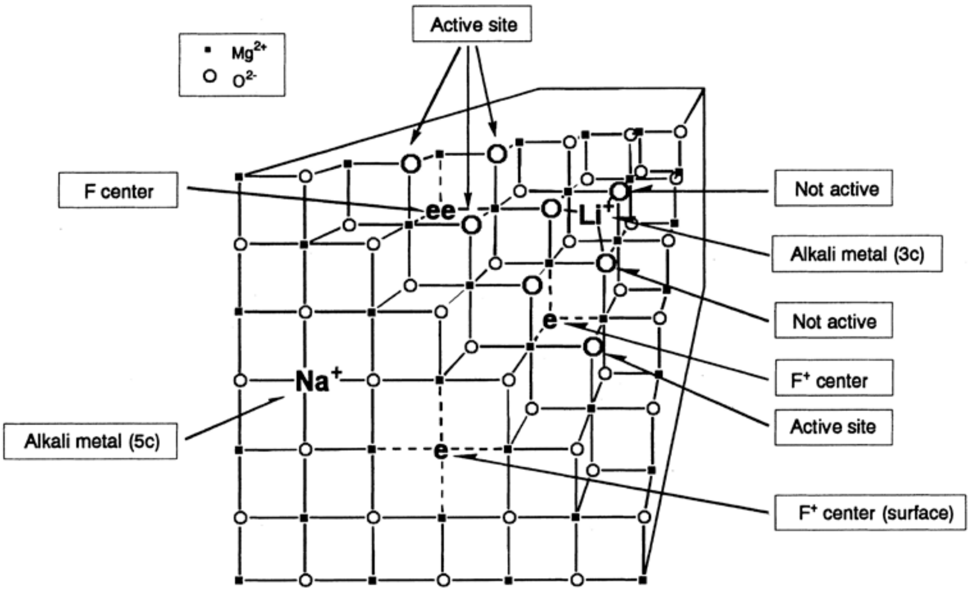

Figure 6.2. Diagram illustrating how doping MgO with varying alkali ions of varying radii can effect basicity , taken from Matsuhashi and co-workers.[13]

Montero and co-workers recently reported on the enhanced catalytic activity of MgO in the transesterification of tributyrin via Cs-doping using a co-precipitation method.[14] The nature of the active phase and why such enhancement was seen was not clear.

This chapter focuses on the transesterification of longer chained, bulkier triglycerides and real oils using Cs-MgO as a catalyst to determine whether the activity enhancement observed for a model C4 chained TAG is transferrable to a real biodiesel reaction.

EXAFS analysis is used to determine the nature of the active site in the Cs-MgO catalyst, in an attempt to uncover why such enhancement is observed in catalytic activity on doping NanoMgO with caesium.

6.2 Results and discussion

The Cs-MgO was prepared by Janine Montero using a co-precipitation method as described in **Chapter 2**. Before using the material in this study it was calcined at 500 ºC for 5 hours in O_2 along with the commercial NanoMgO, calcined to give NanoMgO-500. Commercial NanoMgO was used throughout this study as the commercial production method is the same as that used to synthesise the material in the laboratory, and previous characterisation carried out by Janine Montero had found there to be no difference in the physicochemical properties of commercial versus synthesised NanoMgO.

Characterisation on the fresh catalysts had already been reported on in the thesis of Janine Montero, as well as a paper by Montero and co-workers,[14] but has been included here for completeness. The materials were tested as catalysts in the transesterification of varying chain length TAGs from C4 up to the real oil feedstock olive oil. The active site for the Cs-MgO catalyst was investigated using EXAFS analysis.

6.2.1 Characterisation of Cs-MgO

The initial characterisation of the Cs-MgO material reported in this section was carried out by Janine Montero and is reported in her thesis. The XRD and CO_2 desorption profiles are shown, and a table lists the other physicochemical properties investigated, as determined via N_2 porosimetry and EDX.

6.2.1.1 XRD

Figure 6.3 shows the XRD profiles for NanoMgO-500 and Cs-MgO. The indexed reflections for nanoMgO-500 are assigned to the periclase form of MgO.[15] The Cs-MgO sample shows these same MgO reflections, as well as the presence of a new phase with peaks in the region of $2\theta = 10\text{-}35^\circ$. The phase cannot be assigned to caesium only compounds such as CsOH,[16] Cs_2CO_3[17]or $CsOCH_3$.[18] It is therefore assigned to a mixed Cs/Mg carbonate phase, based upon its similarity to the powder XRD pattern simulated for the $Cs_2Mg(CO_3)_2$ structure reported by Zheng and co-workers.[19]

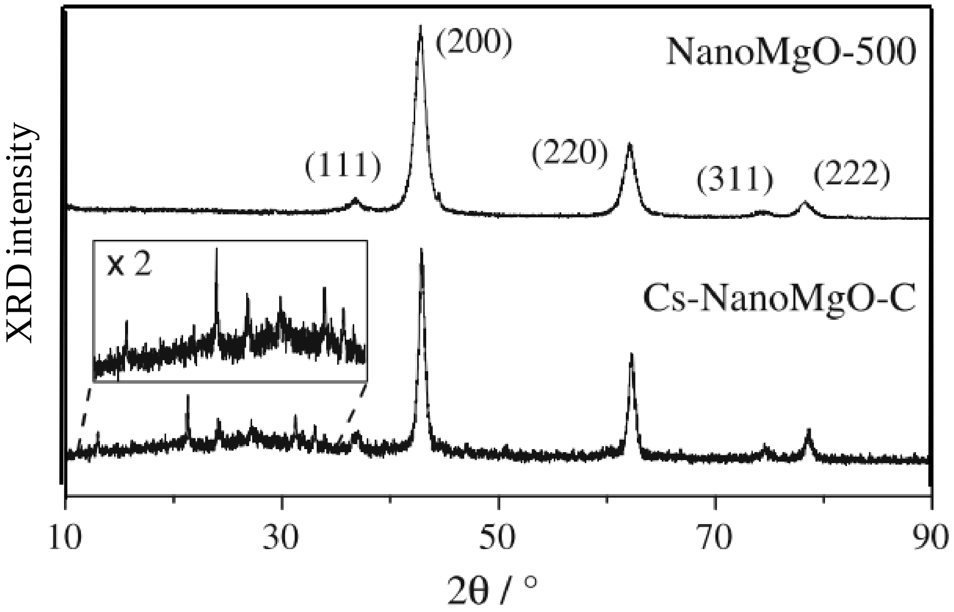

Figure 6.3. XRD profile comparing Cs-MgO and NanoMgO-500. A new, unidentified phase is present in the profile for Cs-MgO.

6.2.1.2 Base site titration

CO_2 pulse chemisorption was carried out for both Cs-MgO and NanoMgO-500. **Figure 6.4** shows the subsequent CO_2 desorption profiles. The base site densities and physicochemical properties for both catalysts are reported in **Table 6.1**.

The surface area of the Cs-MgO is only 30 % that of the NanoMgO-500, yet the Cs doped material has a 46 % greater surface base site density than the NanoMgO-500.

Cs-MgO has a Cs content of 26.4 wt% (equivalent to 1.95 mmol Cs per g Cs-MgO), corresponding to an empirical Cs:Mg molar ratio of 1:9.5. Therefore, this increase in base site density is only ~4% of that expected from a simple cumulative effect of surface doping Cs^+ onto MgO, particularly as XRD shows the Cs-Mg phase co-existing with nanoparticulate MgO, meaning any Cs-Mg phase formed will have a higher Cs:Mg ratio than that predicted from the empirical composition above. Therefore, it can be assumed that much of the Cs is locked up within the bulk of a compound.

As can be observed in **Figure 6.4**, doping the NanoMgO-500 with Cs has generated a large number of new weak - medium strength base sites. This may be due to the formation of additional defect centres on the surface, most likely due to the presence of the new mixed Cs/Mg carbonate phase. However, there are no new strong base sites generated via Cs-doping. Auger parameter analysis, a new methodology demonstrated by Montero and co-workers[18] as a sensitive basicity probe for NanoMgO, revealed enhanced surface polarisability compared to the NanoMgO-500, which would explain the enhanced catalytic activity observed for the C4 transesterification reaction.

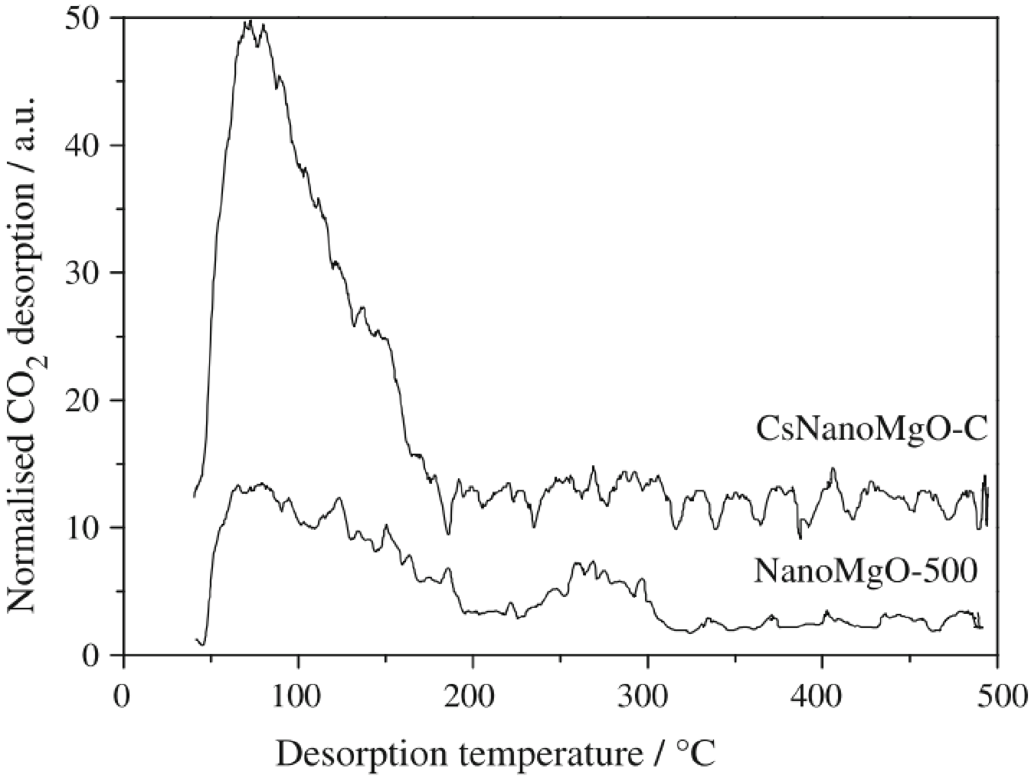

Figure 6.4. CO_2 desorption profiles for Cs-MgO and NanoMgO-500.

Table 6.1. Physicochemical properties for Cs-MgO and NanoMgO-500.

Sample	Cs content[a] / wt %	BET Surface area[b] / m^2 g^{-1}	Crystallite diameter[c] / nm	Base site loading / mmol g^{-1}	Base site density / molecules m^{-2}
NanoMgO	-	250 +/ 25	8 +/- 2.2	0.540	1.3×10^{18}
Cs-MgO	26.4 +/- 7.9	70 +/- 7	17.5 +/- 5.3	0.219	1.9×10^{18}

[a] Determined via XPS analysis [b] Determined via N_2 porosimetry [c]Mean size from TEM

6.2.2 Transesterification of triglycerides

The Cs-MgO and NanoMgO-500 samples were tested as catalysts in the transesterification of triglycerides to form FAME, the reaction used to synthesise biodiesel, as described in **Chapter 2**. Briefly, 50 mg of catalyst was added to 10 mmol of triglyceride, using a 30:1 methanol: oil ratio. Butanol was also used as a co-solvent throughout to help solubilise the longer chained triglycerides. The reactions were carried out at 60 ºC and aliquots were removed from the reaction at various time intervals and analysed using a GC, in order to plot triglyceride conversion and FAME formation over 24 hours.

Previous work by Janine Montero had shown the enhancement of activity for the transesterification of tributyrin when using Cs-MgO as a catalyst compared to NanoMgO-500 or the homogeneous Cs_2CO_3, indicating a strong synergy between the Cs and Mg components of the Cs-MgO.[14] However, no catalytic tests had been trialled with longer chained TAGS or real-oil feedstocks to examine the effect of increasing TAG chain length on TOF enhancement via Cs-MgO. In these tests the triglyceride chain length was varied from C4 up to olive oil, a real plant oil biodiesel feedstock.

6.2.2.1 Tributyrin transesterification

Although the Cs-MgO sample had previously been tested as a catalyst in the tributyrin transesterification, this test was repeated in under the same conditions as for all of the longer chained TAG reactions for continuity. Butanol was used as a co-solvent as it is required to solubilise longer chained TAGs in methanol. The tributyrin conversion profile, along with the methyl butyrate and intermediate formation profiles can be seen below in **Figures 6.5-6.8**. The reaction data is reported in **Table 6.2**.

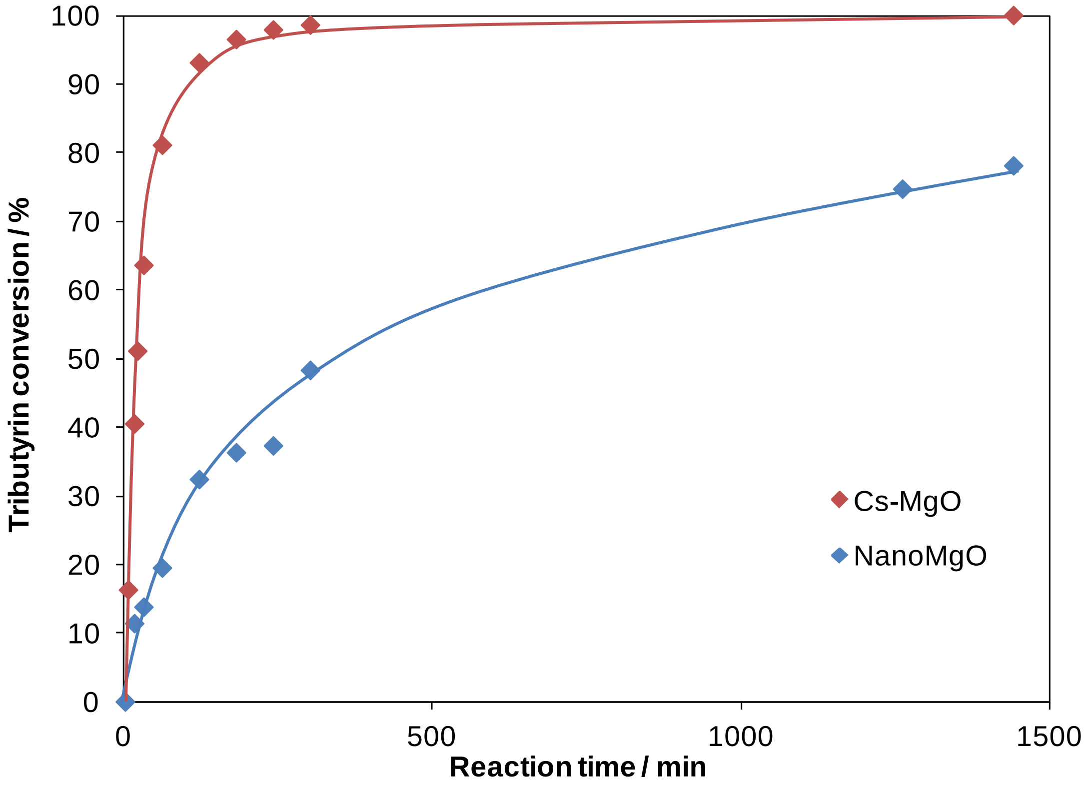

Figure 6.5. Reaction profiles showing tributyrin transesterification over time for Cs-MgO and NanoMgO-500.

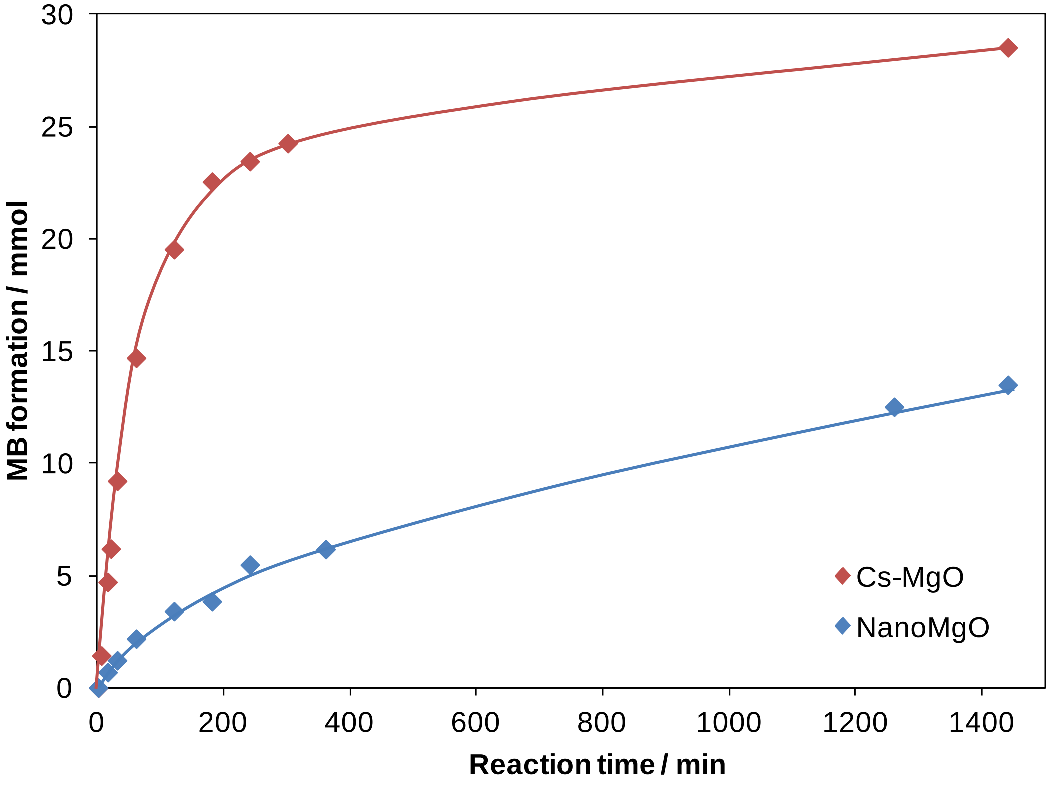

Figure 6.6. Methyl butyrate formation over time for Cs-MgO and NanoMgO-500 during the transesterification of tributyrin.

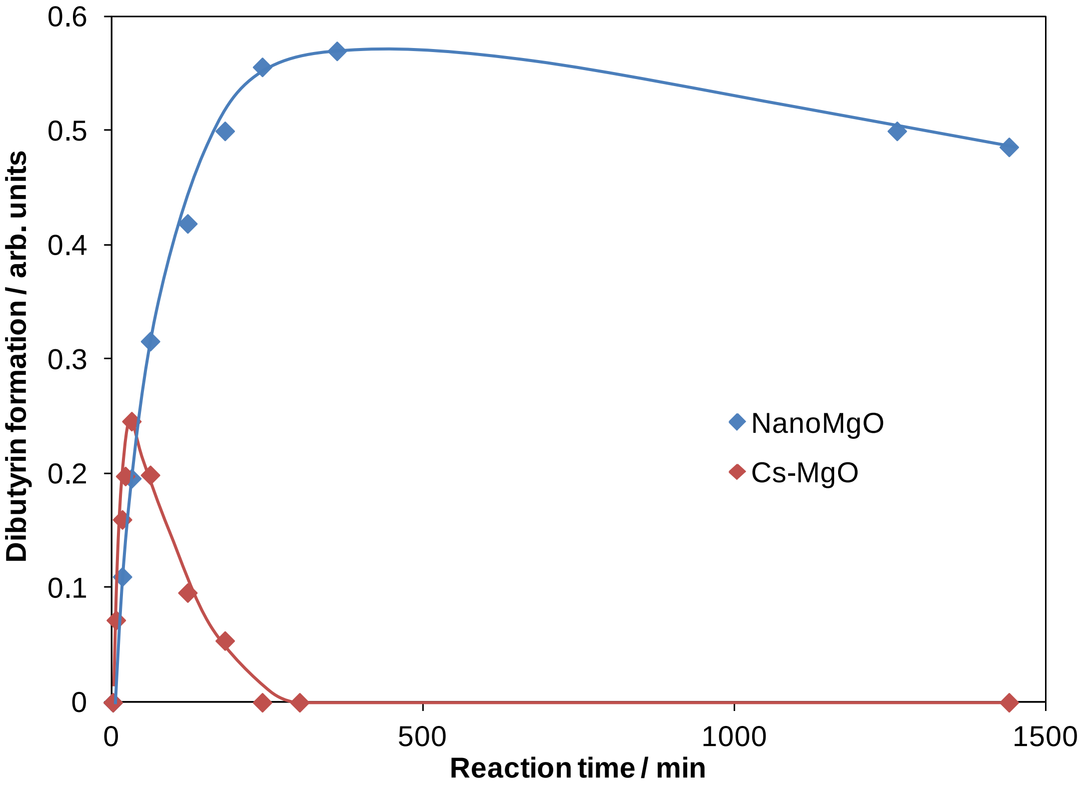

Figure 6.7. Intermediate dibutyrin formation over time for Cs-MgO and NanoMgO-500 during the transesterification of tributyrin.

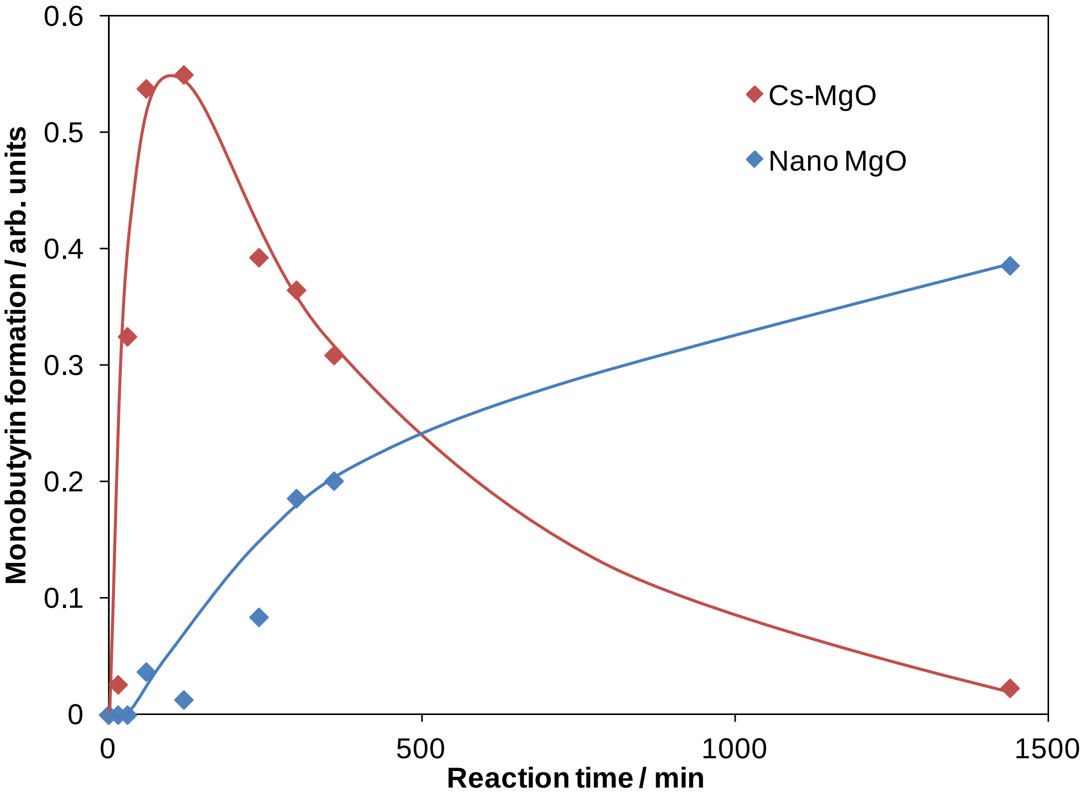

Figure 6.8. Intermediate monobutyrin formation over time for Cs-MgO and NanoMgO-500 during the transesterification of tributyrin.

Table 6.2. Reaction data for Cs-MgO and NanoMgO-500 as catalysts in the transesterification of tributyrin.

Catalyst	Initial rate / mmol g^{-1} min^{-1}	TOF / min^{-1}	C4 TAG conversion after 24 h / %	MB selectivity after 24 h / %
Cs-MgO	5.26 /- 0.25	24.1	100 +/- 1.5	95.1 +/- 1.5
NanoMgO	0.74 +/- 0.04	1.4	77.3 +/- 1.5	58.2 +/- 1.5

As previously reported, the Cs-MgO vastly outperforms the NanoMgO-500 sample. The TOF value for Cs-MgO is 17 times faster than for NanoMgO-500, and 100 % of the TAG is converted for the Cs-MgO before 24 hours, with almost 100 % selectivity to the methyl butyrate FAME product. The greater surface polarisability and basicity of the Cs-doped material due to the extra defect sites has dramatically enhanced the catalytic activity when compared to NanoMgO-500.

6.2.2.2 Tricaprylin transesterification

The two catalysts were then tested in the transesterification of the longer chained C8 TAG tricaprylin. The tricaprylin conversion profiles, along with the methyl caprylate and intermediate formation profiles can be seen below in **Figures 6.9-6.12**. The reaction data is reported in **Table 6.3**.

Table 6.3. Reaction data for Cs-MgO and NanoMgO-500 in the transesterification of tricaprylin.

Catalyst	Initial rate / mmol min^{-1} g^{-1}	TOF / min^{-1}	C8 TAG conversion after 24 h / %	MC selectivity after 24 h / %
Cs-MgO	4.60 +/- 0.30	21.1	100.0 +/- 1.5	83.2 +/- 1.5
Nano MgO	0.62 +/- 0.05	1.2	61.4 +/- 1.5	54.9 +/- 1.5

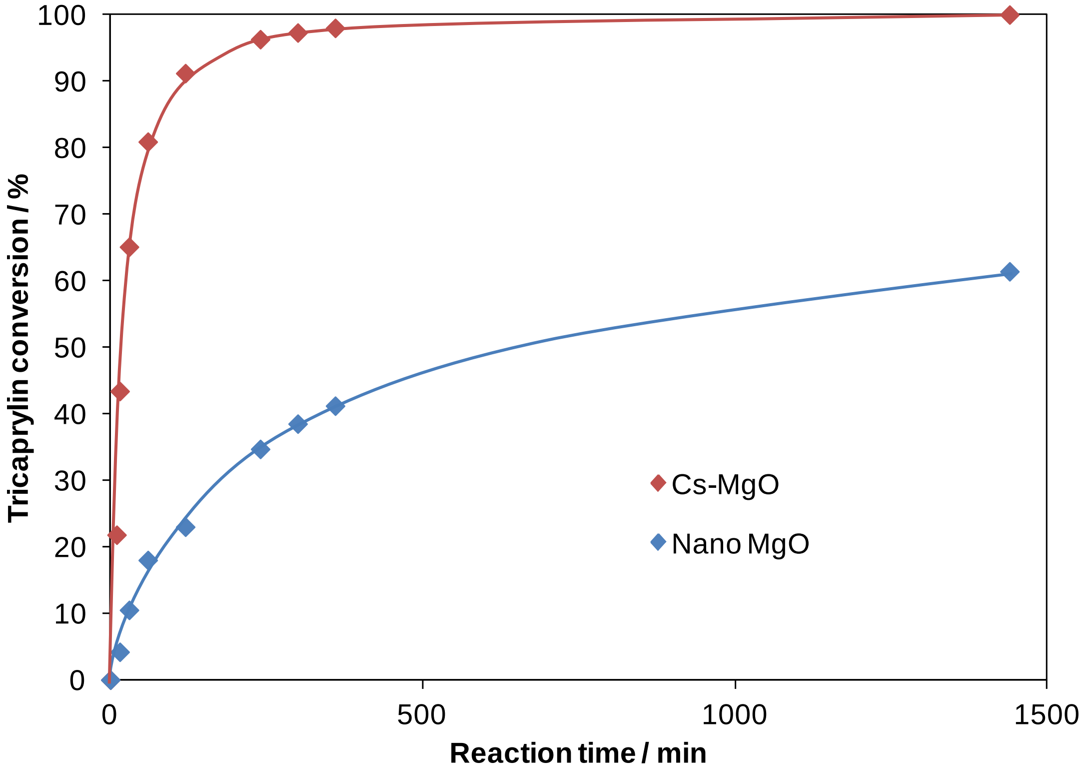

Figure 6.9. Reaction profiles showing tricaprylin transesterification over time for Cs-MgO and NanoMgO-500.

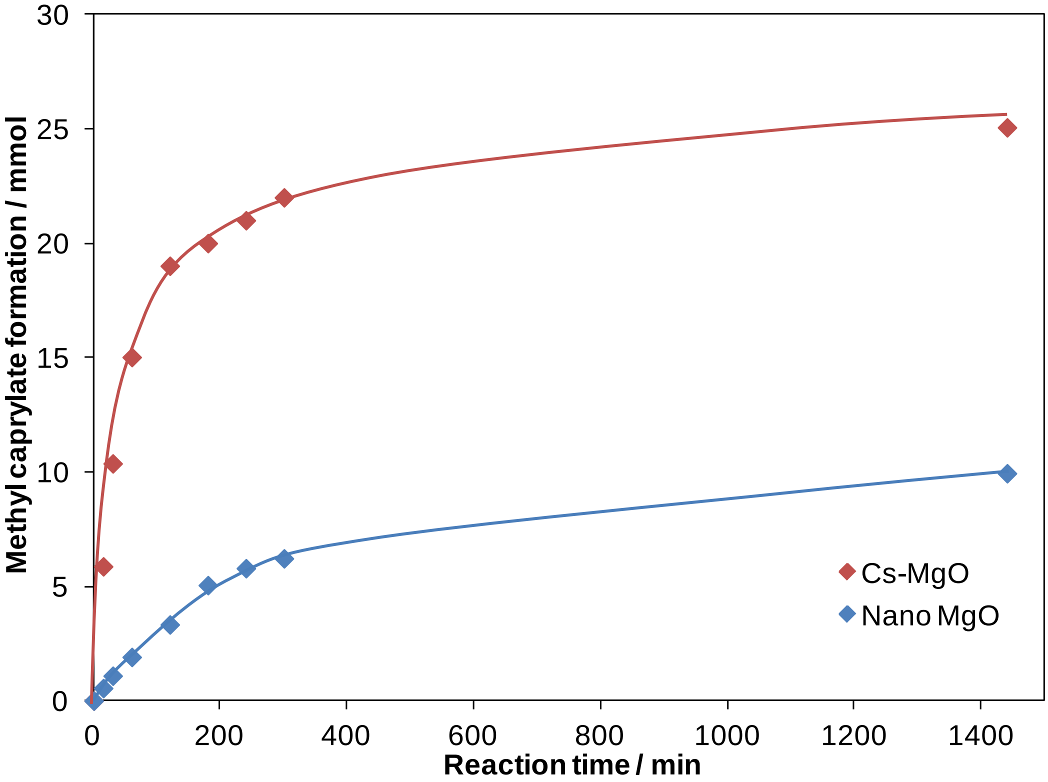

Figure 6.10. Methyl caprylate formation over time for Cs-MgO and NanoMgO-500 during the transesterification of tricaprylin.

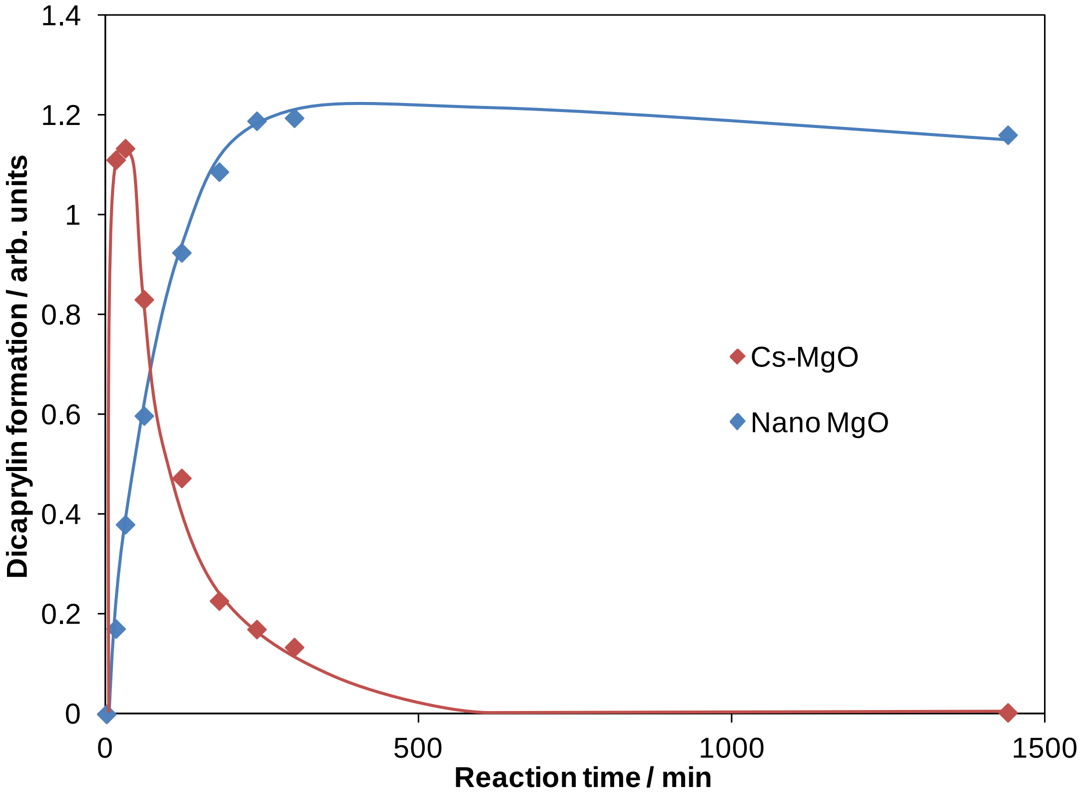

Figure 6.11. Intermediate dicaprylin formation over time for Cs-MgO and NanoMgO-500 during the transesterification of tricaprylin.

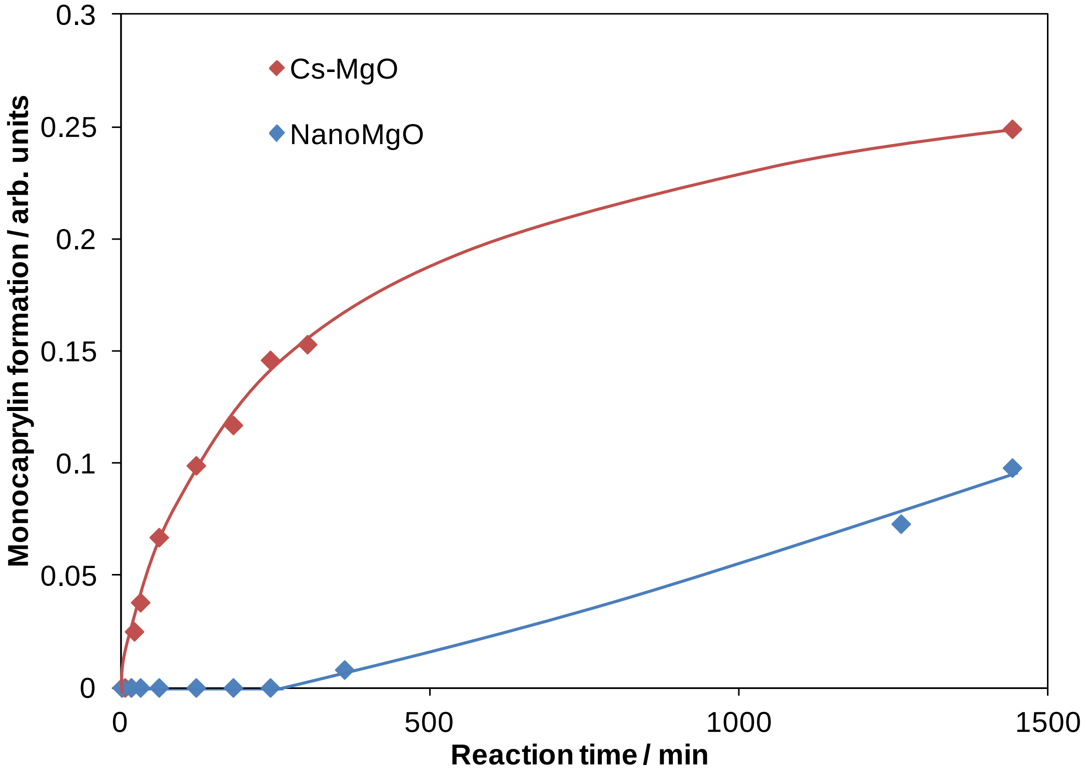

Figure 6.12. Intermediate monocaprylin formation over time for Cs-MgO and NanoMgO-500 during the transesterification of tricaprylin.

Again, a dramatic TOF enhancement is observed for Cs-MgO compared to NanoMgO-500. The initial rates have dropped for both catalysts, due to the slower diffusion of the longer chained TAG through the bulk medium, and decreased solubility of the TAG. However, the relative enhancement is equal to that of the C4 TAG. This is what would be expected for a non-porous nanocrystalline catalyst. The reaction occurs at the surface so the base sites are equally accessible to the TAGs for both catalysts, and so, unlike the macroHT versus convHT, there is no increased TOF enhancement on increasing TAG bulk due to increased diffusion rates for Cs-MgO versus NanoMgO-500.

6.2.2.3 Trilaurin transesterification

Cs-MgO and NanoMgO-500 were tested in the transesterification of the C12 chain length TAG, trilaurin. The trilaurin conversion profiles, methyl laurate and intermediate formation profiles can be seen in **Figures 6.13-6.16**. The reaction data is reported in **Table 6.4**.

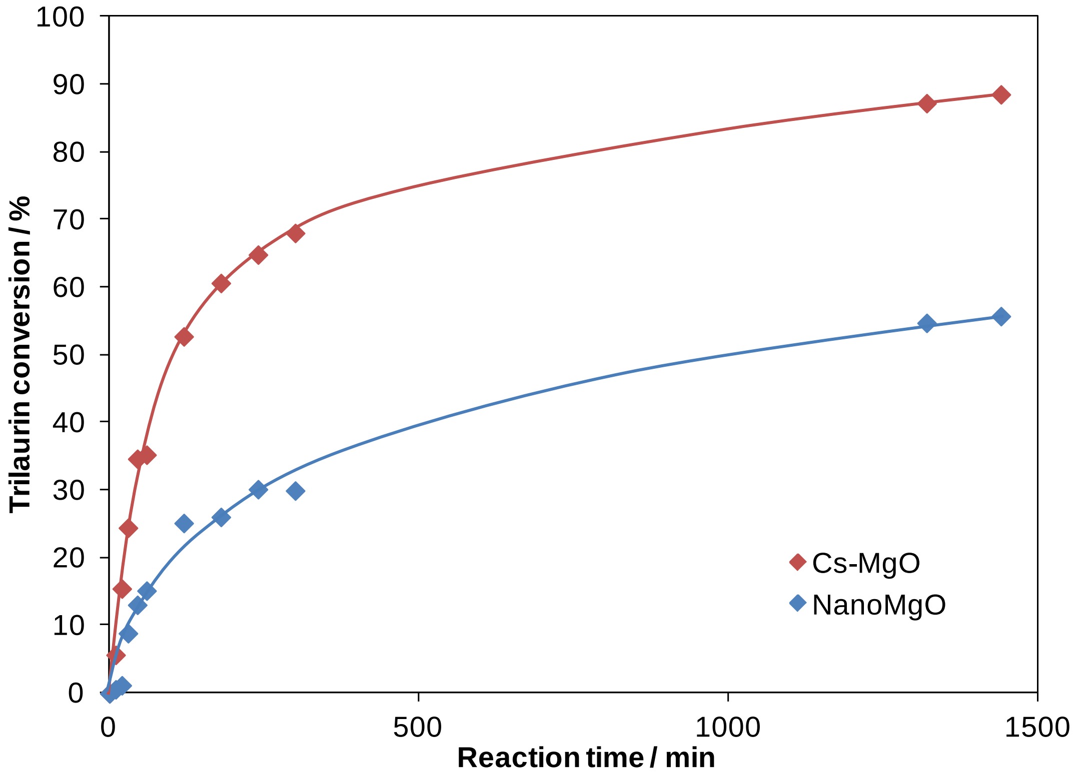

Figure 6.13. Reaction profiles showing trilaurin transesterification over time for Cs-MgO and NanoMgO-500.

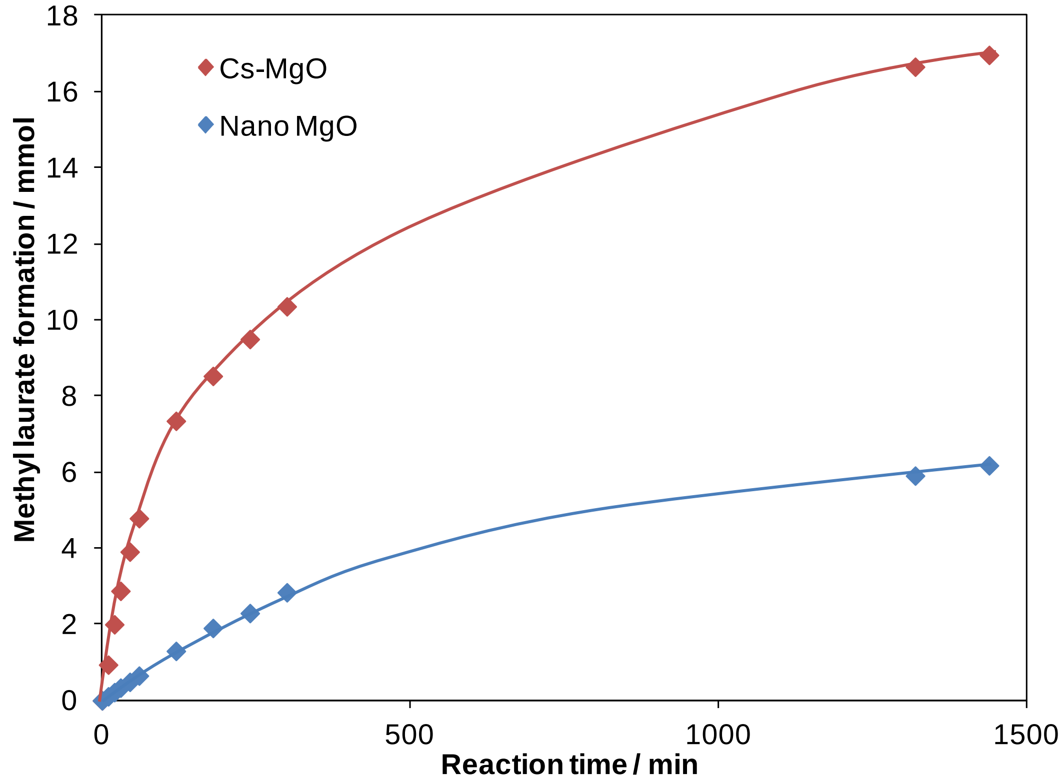

Figure 6.14. Methyl laurate product formation over time for Cs-MgO and NanoMgO-500 during the transesterification of trilaurin.

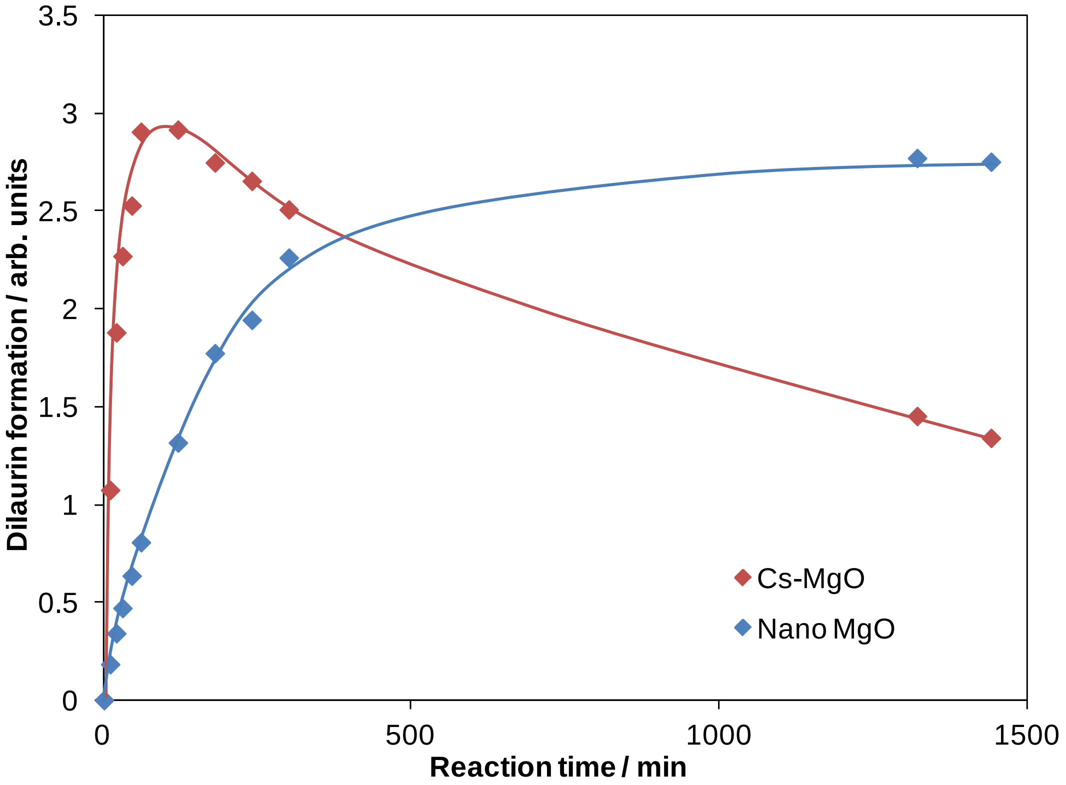

Figure 6.15. Intermediate dilaurin formation over time for Cs-MgO and NanoMgO-500 during the transesterification of trilaurin.

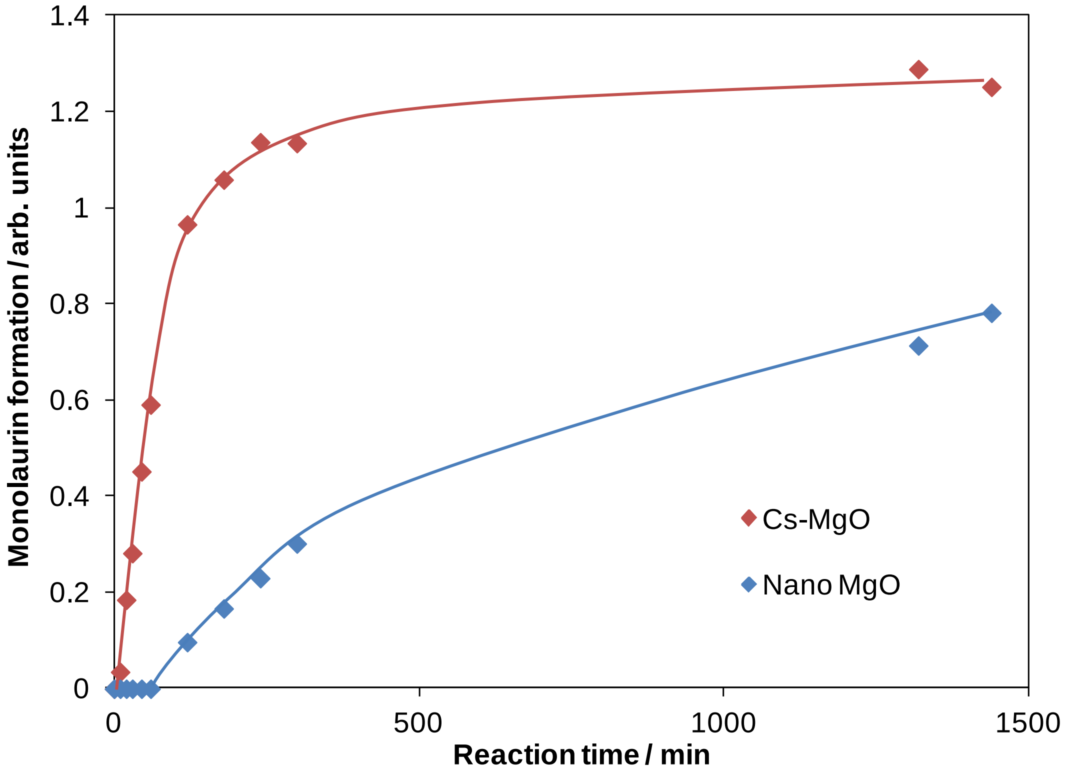

Figure 6.16. Intermediate monolaurin formation over time for Cs-MgO and NanoMgO-500 during the transesterification of trilaurin.

Table 6.4. Reaction data for Cs-MgO and NanoMgO-500 in the transesterification of trilaurin.

Catalyst	Initial rate / mmol min^{-1} g^{-1}	TOF / min^{-1}	Trilaurin conversion after 24 h / %	ML selectivity after 24 h / %
Cs-MgO	2.18 +/- 0.11	10.0	89.0 +/- 1.5	61.7 +/- 1.5
Nano MgO	0.42 +/- 0.12	0.79	54.2 +/- 1.5	39.4 +/- 1.5

Again, there is a significant TOF enhancement via Cs-MgO compared to NanoMgO-500. The TAG conversions and FAME selectivities have once again decreased compared to the shorter chained C8 TAG transesterification, but the overall enhancement via Cs-MgO is still comparable to the C4 and C8 reactions.

6.2.2.4 Olive Oil transesterification

The Cs-MgO and NanoMgO-500 catalysts were tested in the transesterification of olive oil, a real oil feedstock. The triolein conversion profiles and methyl oleate product formation profiles can be seen below in **Figure 6.17** and **Figure 6.18** respectively. The conversion profile for the second most prevalent triglyceride, oleic-oleic-palmitic (OOP), compared to that of triolein over Cs-MgO is shown in **Figure 6.19**. The reaction data is reported in **Table 6.5**.

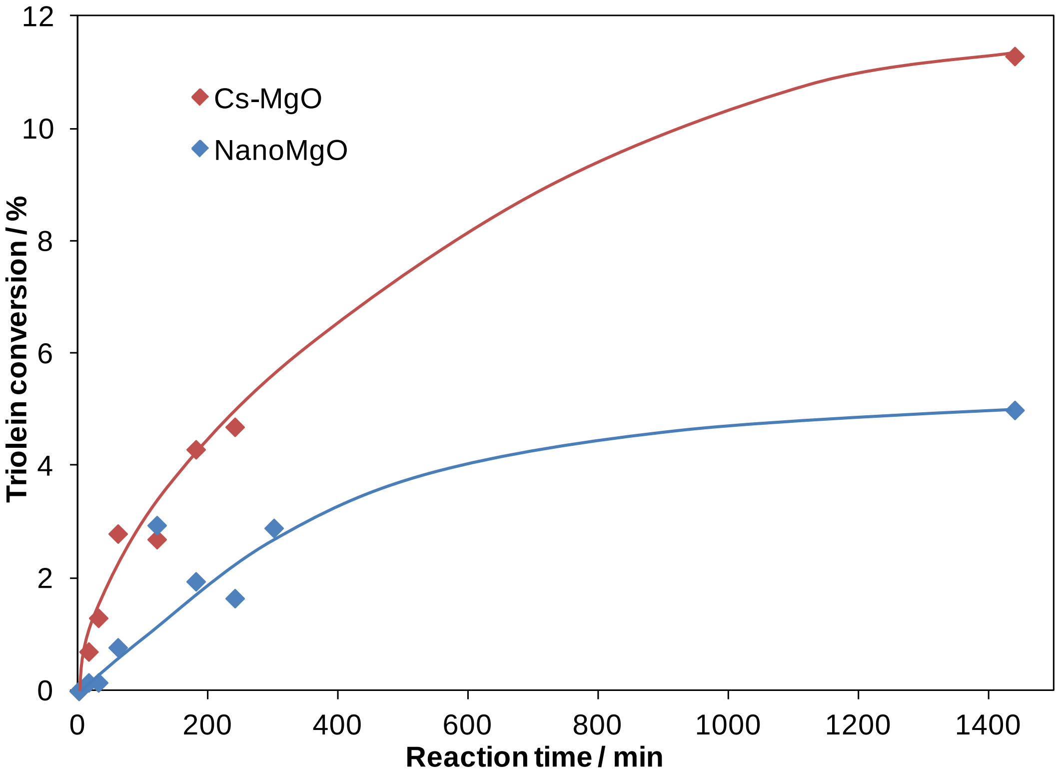

Figure 6.17. Reaction profiles showing the transesterification of triolein for Cs-MgO and NanoMgO-500 during the transesterification of olive oil.

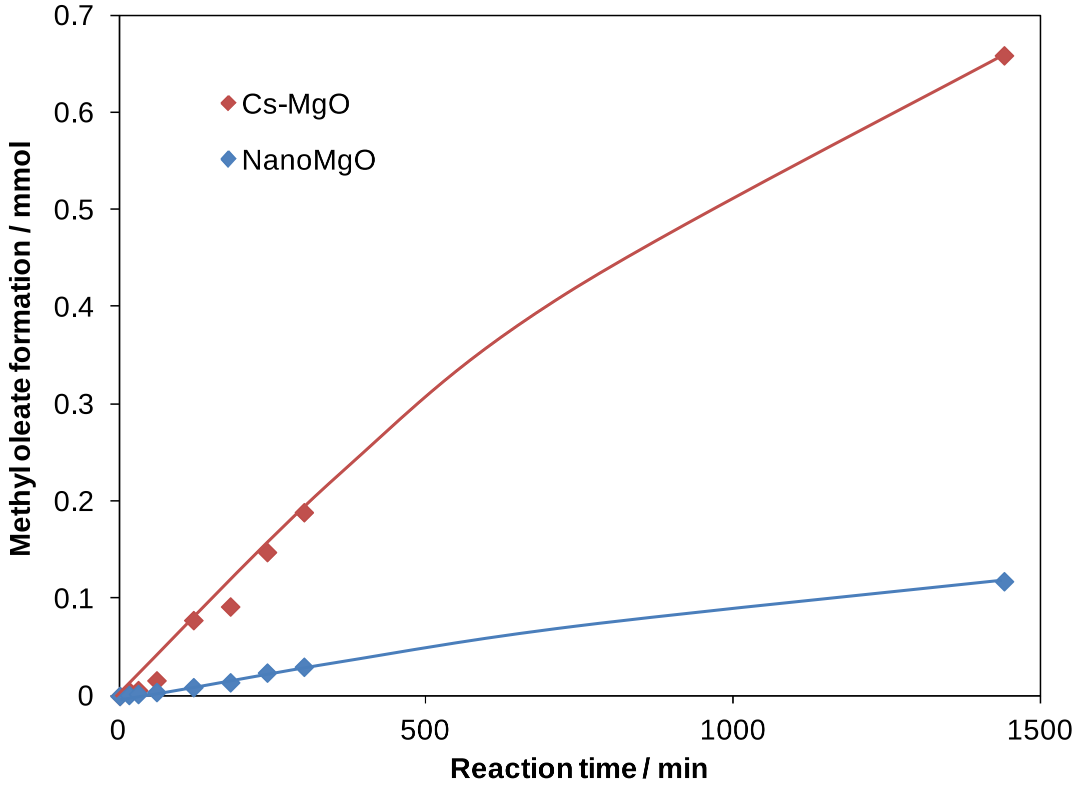

Figure 6.18. Methyl oleate product formation profiles for Cs-MgO and NanoMgO-500 during the transesterification of olive oil.

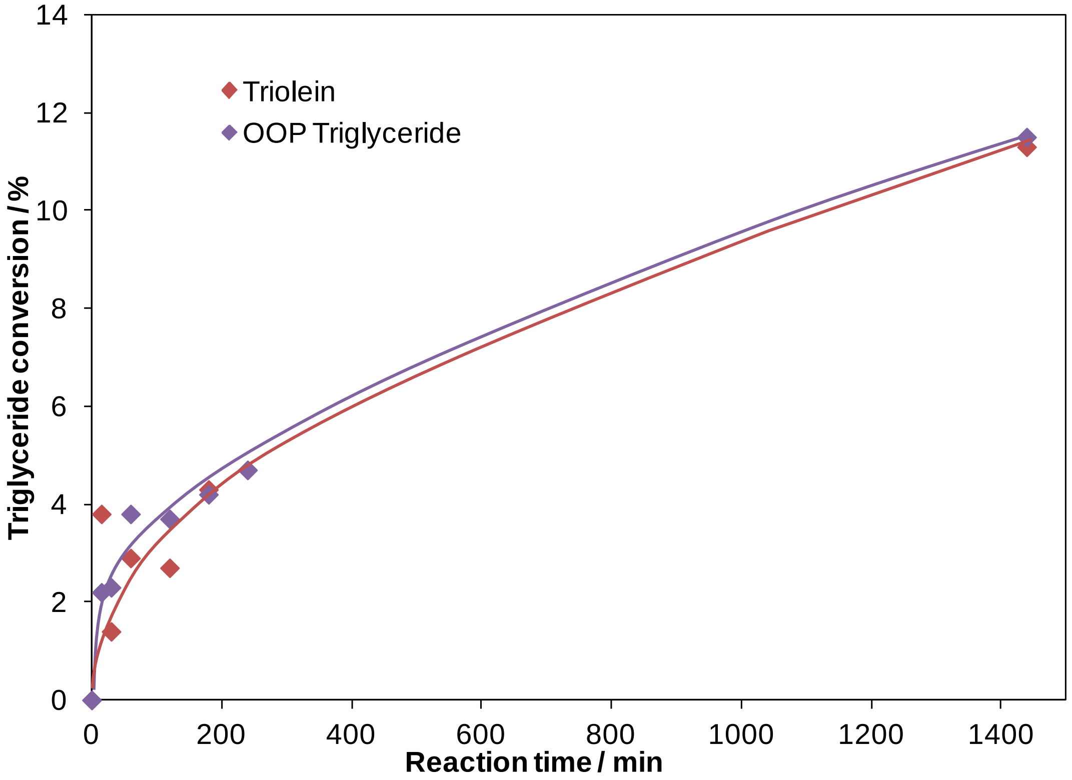

Figure 6.19. Conversion profiles for the two main triglycerides in olive oil over Cs-MgO, showing similarity in initial rates and overall conversions of the two.

Table 6.5. Reaction data for Cs-MgO and NanoMgO-500 in the transesterification of olive oil.

	Cs-MgO	NanoMgO-500
Triolein conversion initial rate / mmol g^{-1} min^{-1}	0.058 +/- 0.01	0.011 +/- 0.02
OOP triglyceride initial rate / mmol g^{-1} min^{-1}	0.070 +/- 0.04	0.012 +/- 0.02
Overall initial rate / mmol g^{-1} min^{-1}	0.13 +/- 0.05	0.023 +/- 0.04
TOF / min^{-1}	0.7	0.04
Triolein conversion after 24 h / %	11.3 +/- 1.5	5.0 +/- 1.5
MO selectivity after 24 h / %	19.3 +/- 1.5	7.6 +/- 1.5

The overall reaction rates are much slower for this bulky real oil in the case of both catalysts. The conversion of both the triolein and the second most prevalent TAG (believed to be the oleic-oleic palmitic (OOP) triglyceride) were followed and the rate and overall conversions found to be very similar for both, as shown in **Figure 6.19**. For the TOF calculations it was assumed that the olive oil was only made up of these two components in a 1:1 ratio of triolein: OOP, therefore the catalysts were transesterifying 5 mmol of each. However, due to the similar initial rates and conversions in both cases, the TOF value would not change significantly if this ratio was altered. Methyl oleate formation was also followed. The selectivity to methyl oleate was calculated in terms of total triglyceride conversion in both cases.

The formation of butyl esters was followed and under these low temperature conditions found to be negligible, accounting for < 0.5% of the total methyl ester formed during transesterification, which may reflect the lower adsorption strength of butanol relative to methanol[20] in conjunction with our low butanol: methanol ratios.

6.2.2.4.a Olive Oil transesterification at high pressure

In order to examine the performance of Cs-MgO under more realistic operating conditions, a reaction was carried out at 90 ºC, in a high pressure flask. Under these conditions, only 25 wt% butanol was required to solubilise the olive oil. The wt% of catalyst added to the reaction was increased from 0.05 wt% for all previous reactions, to 2.5 wt%, a value more in line with other literature tests (**Table 6.7**). Due to carrying out the reaction under pressure, samples were only taken at 3 hours and at 24 hours, to avoid depressurising the system too frequently. The results can be seen below in **Table 6.6**. The TOF value for the high pressure reaction was calculated assuming a linear rate up to the first point at 3 hours. There is a great improvement in the overall conversions and TOF values when the reaction conditions are altered to be more realistic. Therefore, this catalyst does show real promise industrially for biodiesel synthesis, as even for a real oil, high conversions can be quite easily achieved during the transesterification reaction.

Table 6.6. Reaction data for Cs-MgO in the transesterification of olive oil, under varying reaction conditions.

	Triolein conversion after 3h / %	Triolein conversion after 24h / %	TOF / min^{-1}	MO selectivity after 24h / %
Cs-MgO at 60 ºC	4.2 +/- 1.5	11.6 +/- 1.5	0.70	22.3 +/- 1.5
Cs-MgO at 90 ºC	31.5 +/- 1.5	92.1 +/- 1.5	1.60	78.4 +/- 1.5

6.2.2.5 Cs leaching

In order to examine whether or not Cs leaching had occurred during transesterification reactions using Cs-MgO as the catalyst, XPS analysis was carried out on a spent Cs-MgO sample recovered after 24 hours as a catalyst in the transesterification of tributyrin, in order to compare the Cs content to that of the fresh material, as discussed earlier in the characterisation section. EDX analysis was also carried out to compare fresh and spent Cs-MgO. The results can be seen in **Table 6.7.**

Table 6.7. Cs content of fresh and spent Cs-MgO, as determined via EDX and XPS analysis.

	XPS Cs content / wt%	EDX Cs content / wt%
Cs-MgO fresh	26.4 +/- 7.9	13.9 +/- 4.1
Cs-MgO spent	3.1 +/- 0.9	3.5 +/- 1.5

It can be observed from the results that there is a significant loss of Cs from the catalyst during reaction. It can therefore be concluded that leaching does occur from the Cs-

MgO during reaction. This may well affect the reusability of the catalyst as removal of the Cs will most likely lead to deactivation.

It is worth noting that during her PhD research, Janine Montero carried out a leach test, in which the Cs-MgO material was mixed with a known volume of methanol, the solvent used for transesterification, under the same conditions as for a typical reaction. After 24 h in contact with the alcohol, the catalyst was filtered off and the leachate was recovered after centrifuging to remove any traces of the solid oxide. Transesterification reactions were then performed over the methanolic leachate, which gave 90 % tributyrin conversion after 24 hours. It is therefore apparent that a quantity of homogeneous and catalytically active species is present in the methanol leachate, However, this level of TAG conversion is still below that recorded for the fresh material. Janine Montero also tested Cs_2CO_3 as a homogeneous catalyst comparison during the transesterification of tributyrin. The Cs-MgO sample reaches 100 % tributyrin conversion almost as fast as caesium carbonate, which operates via a homogeneous mechanism, with associated benefits of excellent mixing between the catalytic species and reactants. It should be emphasised that only 13.2 mg of caesium is present in the 50 mg Cs-MgO sample, compared with 40.8 mg of caesium in same mass of the homogeneous carbonate comparison. Therefore, the excellent activity observed for Cs-MgO cannot be ascribed solely to leached Cs.

6.2.2.6 Comparison of TOF values

Figure 6.20 shows the TOF values for the Cs-MgO and NanoMgO-500 catalysts as a function of TAG chain length for C4-C18 oils.

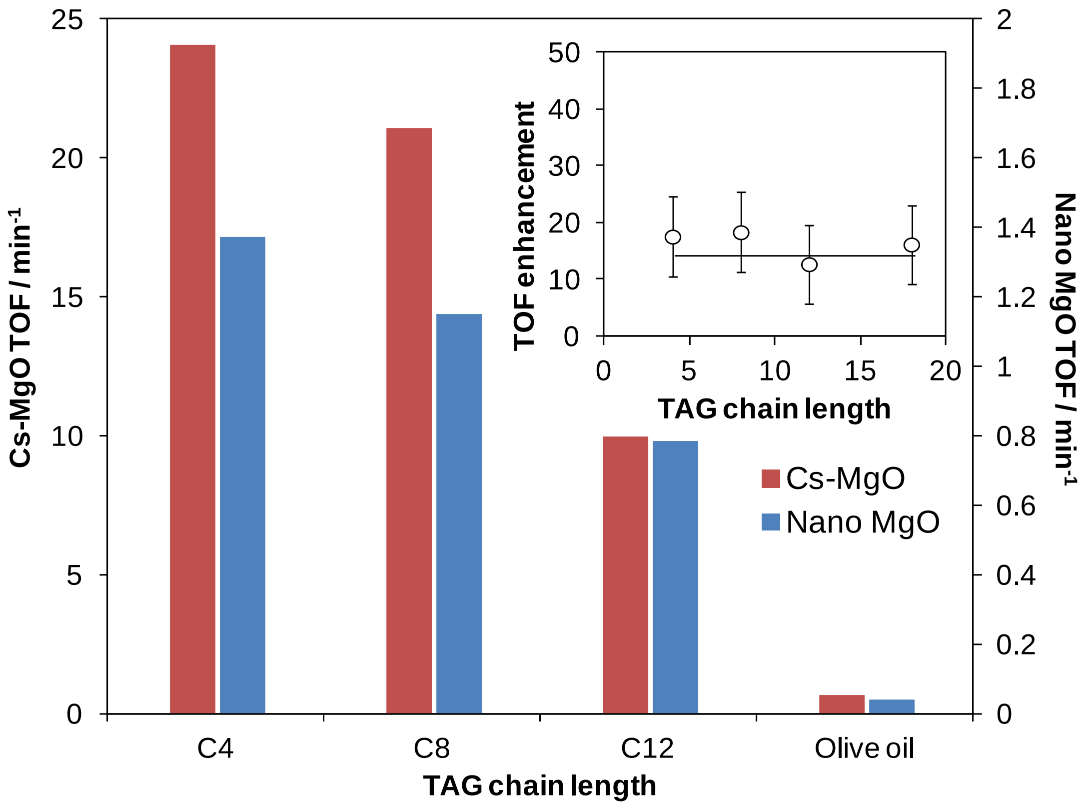

Figure 6.20. Initial TOFs for C4-C18 TAG transesterification by methanol over Cs-MgO versus NanoMgO-500 catalysts at 60 ºC. Inset shows Cs-promotion is independent of fatty acid chain length.

The Cs-MgO TOFs are all an order of magnitude greater than those of NanoMgO-500, reflecting their enhanced surface polarisability and thus basicity, as shown earlier via CO_2 TPD (section 6.2.1.2). It is important to note that the relative rate enhancements arising from Cs-doping are independent of TAG chain length, as the inset graph shows. This is what would be expected for non-porous nanocrystalline catalysts, as each TAG can reach the base sites of Cs-MgO as easily as for NanoMgO-500, and so any TOF enhancement is purely due to basicity, rather than any increased rate of diffusion discussed for the hydrotalcites in previous chapters.

There is an overall decrease in TOF on increasing TAG chain length. The measured TOFs are a convolution of intrinsic surface reaction and mass-transport kinetics. DFT calculations suggest that the activation barrier for transesterification is invariant of fatty acid chain length,[21] therefore such decreases are most likely due to falling oil solubility and slower diffusion through the bulk medium for the larger TAGs, as observed in **Chapters 3** and **4**. Steric effects associated with the bulkier triglycerides will also affect base site accessibility. Kinetic modelling[22, 23] suggests that triglyceride adsorption is the rate-limiting step in MgO catalysed transesterification, facilitating the attack of the ester species by pre-activated MeO^- species.[24, 25] **Figure 6.21** illustrates this transesterification mechanism.

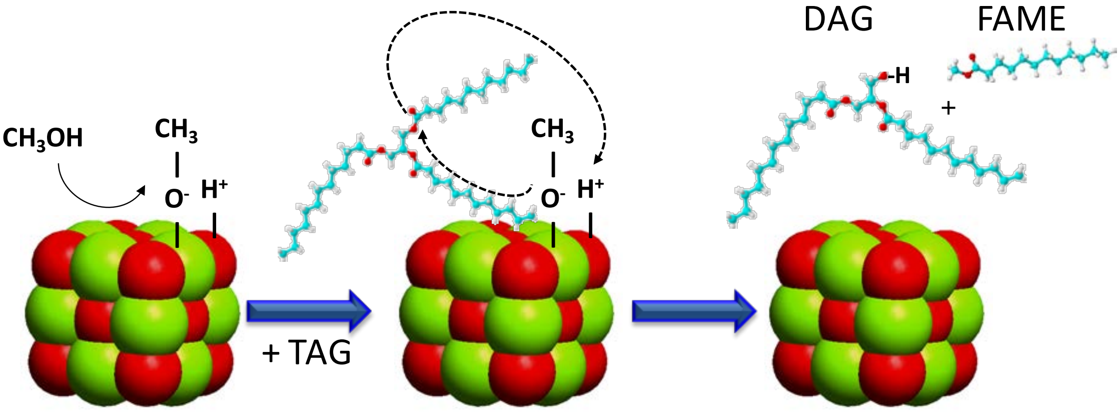

Figure 6.21. Langmuir-Hinshelwood mechanism of solid base catalysed TAG transesterification illustrating sterically hindered nucleophilic attack of adsorbed methoxy anion on the ester function of bulky oils.

Therefore, increased TAG chain length is anticipated to lower the TOF due to the steric hindrance and slower rate-limiting step. Although the TOF values for olive oil appear very low, it is interesting to note that the activity of Cs-MgO in olive oil transesterification compares very favourably with literature values for other solid acids and bases, examples of which can be seen in **Table 6.8**. When operating under mild conditions (60-80 °C) with catalyst loadings of 0.1-6 wt%, typical TOFs for the transesterification of real oils range between 0.0014-1.68 min^{-1}, hence the Cs-MgO TOF of 0.57 min^{-1} using only 0.05 wt% catalyst evidences excellent performance. Olive oil transesterification under more realistic operating conditions of 90 °C and 2.5 wt% catalyst significantly increase both the TOF and 24 h TAG conversion to 1.6 min^{-1} and 93 % respectively, comparable to the best commercial heterogeneous catalysts, demonstrating the potential of Cs-MgO for FAME production from real oils.

Table 6.8. Summary of literature reactivity data for solid acid and base catalysed triglyceride transesterification.

Reference	**Catalyst**	**TAG**	**Conditions**	**TOF / min^{-1}**	**TAG conversion / %**
Solid Acid Catalysts					
Lopez et al.[26]	Sulfate modified zirconia	Triacetin	6:1 methanol: oil, 60ºC, 2 wt% catalyst	2.29	57 after 8 h
Dhainaut et al.[27]	RSO_3H SBA-15	Tricaprylin	30:1 methanol: oil, 60 ºC, 1 wt% catalyst	0.05	2.1 after 6 h
Dhainaut et al.[27]	RSO_3H MM-SBA-4	Tricaprylin	30:1 methanol: oil, 60 ºC, 1 wt% catalyst	0.13	2.4 after 6 h
Dacquin et al.[28]	RSO_3H SBA-15-14	Triolein	30:1 methanol: oil, 60 ºC, 1 wt% catalyst, 30 wt% butanol to solubilise TAG	0.018	0.3 after 6 h
Xu et al.[29]	$H_3PW_{12}O_{40}/Ta_2O_5$-3.6	Tripalmitin	90:1 methanol: oil, 65ºC, 2 wt% catalyst	1.19	38.4 after 6 h
Xu et al.[29]	$H_3PW_{12}O_{40}$/SBA-15-10.9	Tripalmitin	90:1 methanol: oil, 65ºC, 2 wt% catalyst	0.29	9.8 after 6 h
Solid Base Catalysts					
Xi et al.[30]	2:1 Mg:Al HT	Tributyrin	3:1 methanol: oil , 60 ºC, 4.6 wt % catalyst	3.11	82.3 after 20 h
Umdu et al.[31]	60% CaO/Al_2O_3	Sunflower oil	9:1 methanol: oil, 50ºC, 6 wt% catalyst	1.68	80 after 4 h
Georgogianni et al[32]	Mg/MCM-41	Rapeseed oil	10:1 methanol: oil, 60ºC, 0.1 wt% catalyst	0.0075[a]	85 after 24 h
Georgogianni et al[32].	2:1 Mg:Al HT	Rapeseed oil	10:1 methanol: oil, 60ºC, 0.1 wt% catalyst	0.0014[a]	97 after 24 h
Hamad et al[33]	3:1 Mg:Al HT	Rapeseed oil	18:1 ethanol : oil, 79ºC, 0.04 wt% catalyst	0.033	6 after 5 h
Hamad et al.[33]	ZrOCs	Rapeseed oil	18:1 ethanol : oil, 79ºC, 0.04 wt% catalyst	0.77	64 after 5 h
Woodford et al.[34]	2:1 Mg:Al HT	Olive oil	30:1 methanol:oil[b],60ºC, 0.05 wt% catalyst	0.15	5 after 24 h
This work	Cs-MgO	Olive Oil	30:1 methanol:oil[b],60ºC, 0.05 wt% catalyst	0.57	11 after 24 h
This work	Cs-MgO	Olive Oil	30:1 methanol: oil 90ºC, 2.8 wt% catalyst 25 wt% butanol to solubilise TAG	1.60[c]	93 after 24 h

[a]Calculated after 24 h; [b]30 wt% butanol added to solubilise TAG, [c]Calculated after 3h, 31.5 % triolein conversion

6.2.2.7 FAME selectivity versus TAG conversion

Figure 6.22 shows a plot of FAME selectivity over TAG conversion after 24 hours for all of the transesterification reactions carried out by Cs-MgO and NanoMgO-500.

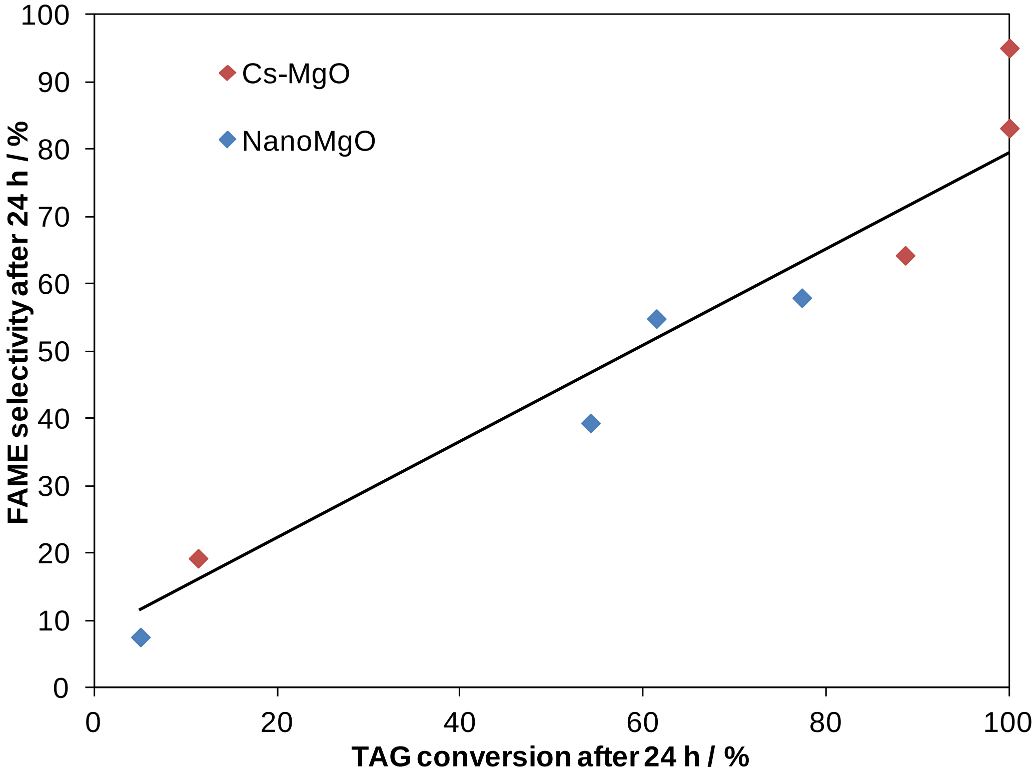

Figure 6.22. Plot of FAME selectivity over TAG conversion after 24 hour reaction in varying chain length TAG transesterifications for Cs-MgO and NanoMgO-500.

Transesterification to the desired product increases with conversion, due to more transesterification reactions occurring more quickly and therefore more DAG and MAG molecules being converted.

For bulk, porous hydrotalcites, as the TAG chain length increases, selectivity to FAME increases, even though there is slower conversion. This is assigned to the faster moving DAG and MAG molecules diffusing through the bulk more easily to reach the active sites, an effect which becomes more noticeable with increased TAG chain length.

For the nano-particulate, non-porous Cs-MgO and NanoMgO, the nucleophilic attack may be less sterically hindered for DAG and MAG and therefore these reactions may occur faster. However, relatively, for each TOF this increased rate of attack of DAG and MAG over TAG will remain the same, as there is no bulk catalyst to diffuse through to reach the active sites and no diffusion limitations. Therefore no FAME selectivity enhancement is observed on increasing TAG chain length.

6.2.3 EXAFS Analysis

XAS analysis was carried out on the Cs-MgO sample at the Diamond Light Source as described in **Chapter 2**. **Figure 6.23** compares the XANES regions of the Cs-MgO catalyst both before and after calcination with CsOH, Cs_2CO_3 and CsCl reference compounds.

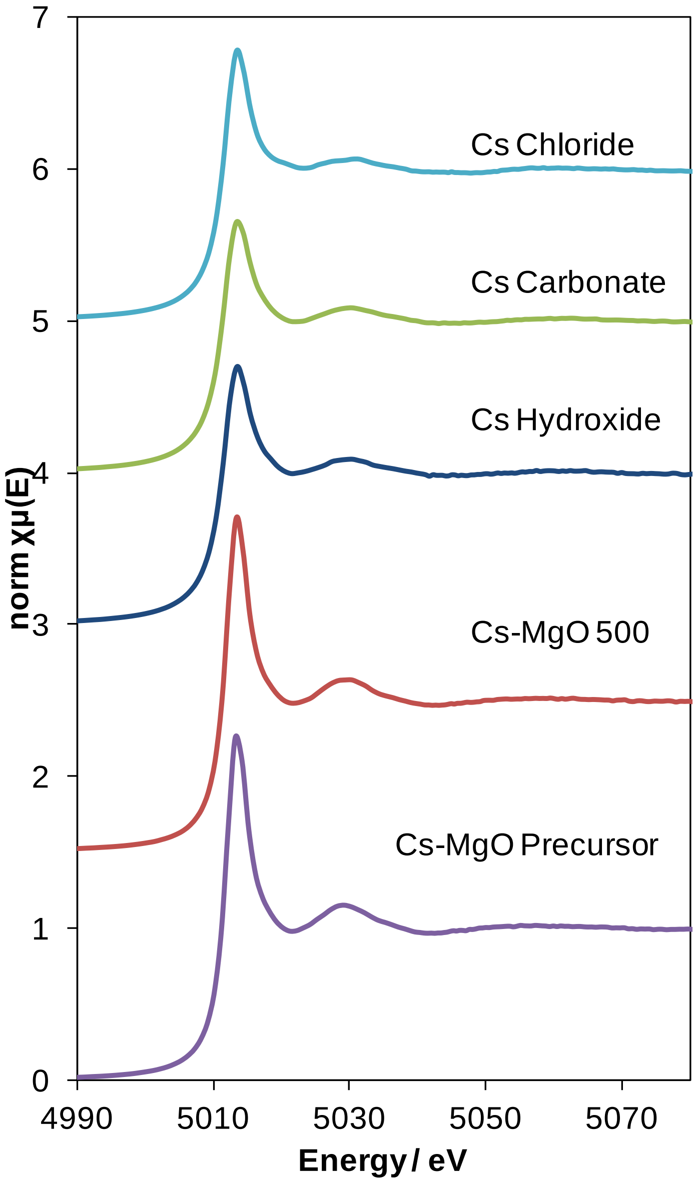

Figure 6.23. Cs L_{III}-edge XANES of Cs-MgO catalyst and Cs reference compounds.

The white line intensity of Cs-MgO is significantly greater than the standards, consistent with Cs in a high oxidation state, associated with strong electron donation to oxygen neighbours and the resultant genesis of strong base sites. Strong Cs electron donation and the parallel creation of O_2^- superoxide radical anions has been reported over dehydrated polycrystalline MgO.[35]

The corresponding EXAFS data were tested against potential model Cs structures. The chi-squared spectra and Fourier Transform radial distribution functions for Cs-MgO when fitted against Cs_2CO_3, Cs_2O, CsOH and $Cs_2Mg(CO_3)_2(H_2O)_4$ can be seen in **Figure 6.24** . The fit parameters are reported in **Table 6.9**.

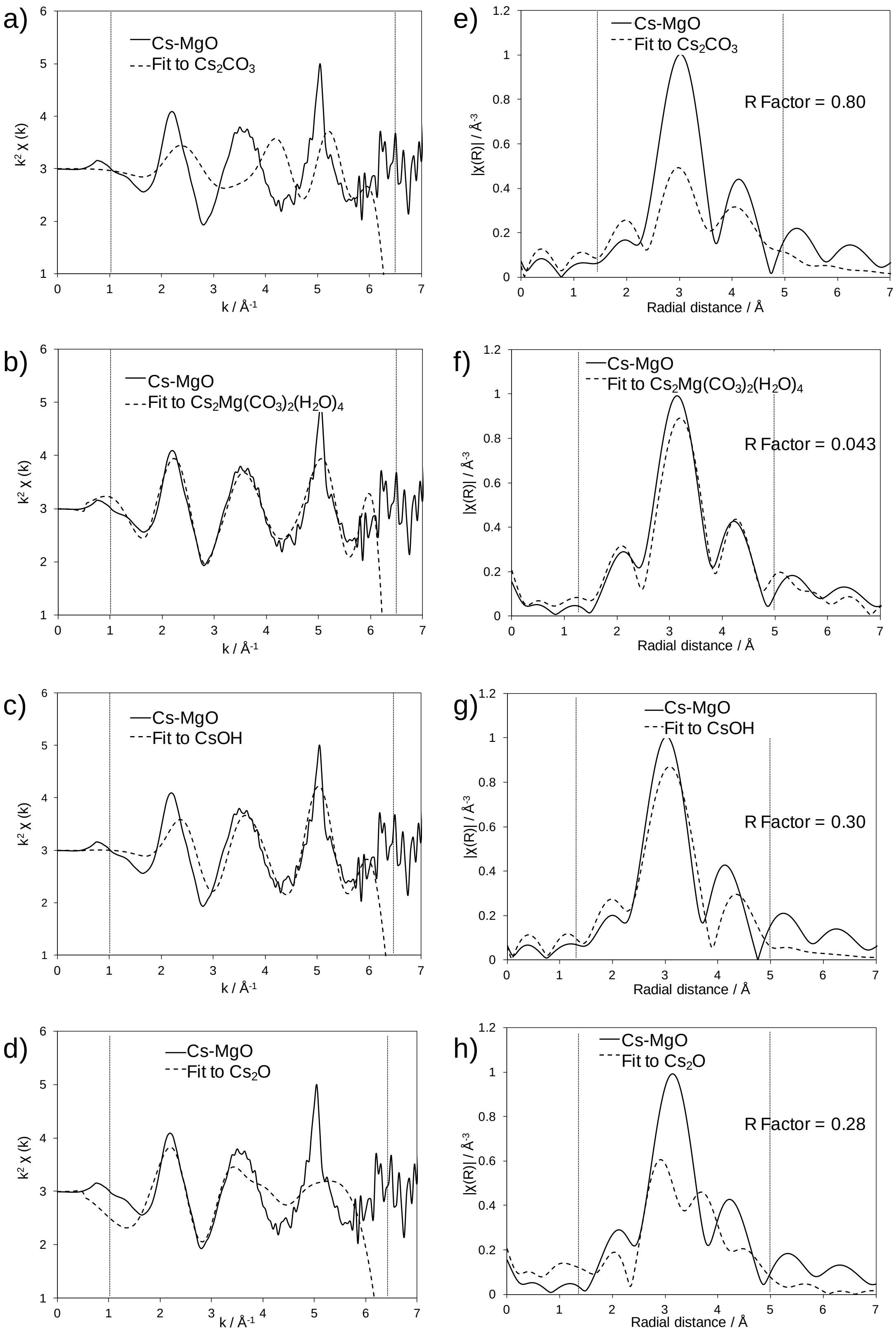

Figure 6.24. Cs L_{III}-edge EXAFS of k^2-weighted chi and Fourier Transforms for Cs-MgO fitted against (a,e) Cs_2CO_3, (b,f) CsOH, (c,g) Cs_2O and (d,h) $Cs_2Mg(CO_3)_2(H_2O)_4$ reference compounds.

Table 6.9. Fitting parameters for Cs L_{III}-edge EXAFS of Cs-MgO

Cs_2O	***Coordination number***					***Scattering distance / Å***					***Debye Waller / Å^2***				
R_{fac} = 0.25	***CN1 Cs-O***	***CN2 Cs-Cs***	***CN3 Cs-Cs***	***CN4 Cs-Cs***	***CN5 Cs-O***	***R1 Cs-O***	***R2 Cs-Cs***	***R3 Cs-Cs***	***R4 Cs-Cs***	***R5 Cs-O***	***σ1 Cs-O***	***σ2 Cs-Cs***	***σ3 Cs-Cs***	***σ4 Cs-Cs***	***σ5 Cs-O***
Model	*3*	*3*	*3*	*6*	*1*	*2.86*	*3.83*	*4.19*	*4.26*	*4.86*					
Fit	*1.02*	*1.02*	*1.02*	*2.04*	*0.34*	*2.81*	*3.78*	*4.14*	*4.21*	*4.81*	*0.084*	*0.085*	*0.253*	*0.205*	*0.048*

CsOH	***Coordination number***							***Scattering distance / Å***							***Debye Waller / Å^2***						
R_{fac} = 0.69	***CN1 Cs-O***	***CN2 Cs-O***	***CN3 Cs-O***	***CN4 Cs-Cs***	***CN5 Cs-Cs***	***CN6 Cs-Cs***	***CN7 Cs-Cs***	***R1 Cs-O***	***R2 Cs-O***	***R3 Cs-O***	***R4 Cs-Cs***	***R5 Cs-Cs***	***R6 Cs-Cs***	***R7 Cs-Cs***	***σ1 Cs-O***	***σ2 Cs-O***	***σ3 Cs-O***	***σ4 Cs-Cs***	***σ5 Cs-Cs***	***σ6 Cs-Cs***	***σ7 Cs-Cs***
Model	*1*	*4*	*2*	*2*	*4*	*2*	*2*	*2.94*	*3.15*	*3.75*	*4.05*	*4.10*	*4.35*	*4.52*							
Fit	*0.98*	*3.92*	*1.96*	*1.96*	*3.92*	*1.96*	*1.96*	*3.13*	*3.34*	*3.94*	*4.23*	*4.29*	*4.54*	*4.70*	*0.036*	*0.058*	*1.827*	*0.029*	*0.055*	*0.025*	*0.023*

Cs_2CO_3	***Coordination number***											
R_{fac} = 0.49	***CN1 Cs-O***	***CN2 Cs-O***	***CN3 Cs-O***	***CN4 Cs-C***	***CN5 Cs-O***	***CN6 Cs-C***	***CN7 Cs-O***	***CN 8 Cs-Cs***	***CN 9 Cs-C***	***CN 10 Cs-Cs***	***CN 11 Cs-Cs***	***CN 12 Cs-O***
Model	*1*	*1*	*2*	*1*	*1*	*1*	*2*	*1*	*1*	*1*	*1*	*1*
Fit	*0.59*	*0.59*	*1.18*	*0.59*	*0.59*	*0.59*	*1.18*	*0.59*	*0.59*	*0.59*	*0.59*	*0.59*
	Scattering distance / Å											
	R1	***R2***	***R3***	***R4***	***R5***	***R6***	***R7***	***R8***	***R9***	***R10***	***R11***	***R12***
Model	*2.71*	*2.88*	*3.04*	*3.27*	*3.41*	*3.55*	*3.87*	*3.84*	*3.87*	*3.96*	*4.03*	*4.08*
Fit	*2.86*	*2.91*	*3.07*	*3.30*	*3.44*	*3.58*	*3.90*	*3.87*	*3.90*	*3.99*	*4.06*	*4.11*
	Debye Waller / Å^2											
	σ1	***σ2***	***σ3***	***σ4***	***σ5***	***σ6***	***σ7***	***σ8***	***σ9***	***σ10***	***σ11***	***σ12***
Fit	*0.01*	*0.01*	*0.01*	*0.01*	*0.01*	*0.01*	*0.01*	*0.01*	*0.01*	*0.01*	*0.01*	*0.01*

$Cs_2Mg(CO_3)_2(H_2O)_4$	***Coordination number***											
R_{fac} = 0.043	***CN1 Cs-O***	***CN2 Cs-O***	***CN3 Cs-O***	***CN4 Cs-O***	***CN5 Cs-O***	***CN6 Cs-O***	***CN7 Cs-O***	***CN 8 Cs-Mg***	***CN 9 Cs-Mg***	***CN 10 Cs-Cs***	***CN 11[a] Cs-C***	***CN 12[a] Cs-O***
Model	*3*	*1*	*1*	*2*	*1*	*1*	*1*	*1*	*1*	*2*	*4*	*7*
Fit	*2.76*	*0.92*	*0.92*	*1.84*	*0.92*	*1.84*	*0.92*	*0.92*	*0.92*	*1.84*	*3.68*	*6.44*
	Scattering distance / Å											
	R1	***R2***	***R3***	***R4***	***R5***	***R6***	***R7***	***R8***	***R9***	***R10***	***R11***	***R12***
Model	*3.07*	*3.09*	*3.17*	*3.29*	*3.39*	*3.49*	*3.64*	*3.87*	*4.15*	*4.55*	*3.8*	*4.6*
Fit	*3.10*	*3.12*	*3.20*	*3.32*	*3.42*	*3.52*	*3.67*	*3.90*	*4.18*	*4.58*	*3.83*	*4.63*
	Debye Waller / Å^2											
	σ1	***σ2***	***σ3***	***σ4***	***σ5***	***σ6***	***σ7***	***σ8***	***σ9***	***σ10***	***σ11***	***σ12***
Fit	*0.009*	*0.009*	*0.005*	*0.005*	*0.005*	*0.006*	*0.007*	*0.009*	*0.007*	*0.016*	*0.21*[a]	*0.25*[a]

[a] Average coordination for next shell carbonate taken to simplify fit, hence larger σ

Cs-MgO exhibits a strong first shell at 3.1 Å, consistent with Cs-O interatomic scattering.[36, 37] From observing **Figure 6.24** it can be observed that there is a poor fit to the Cs-O co-ordination shell of Cs_2CO_3. When CsOH is used as a reference compound, better agreement is obtained to the first shell of Cs-MgO. However, the second shell observed for the Cs-MgO at 4.3 Å is inconsistent with pure CsOH.

The Cs-O shell for Cs_2O does not give a good fit to the Cs-MgO sample, and so the Cs-MgO shell cannot be attributed to this phase. Cs-MgO was then fitted against $Cs_2Mg(CO_3)_2(H_2O)_4$, the structure of which can be seen in **Figure 6.25**.

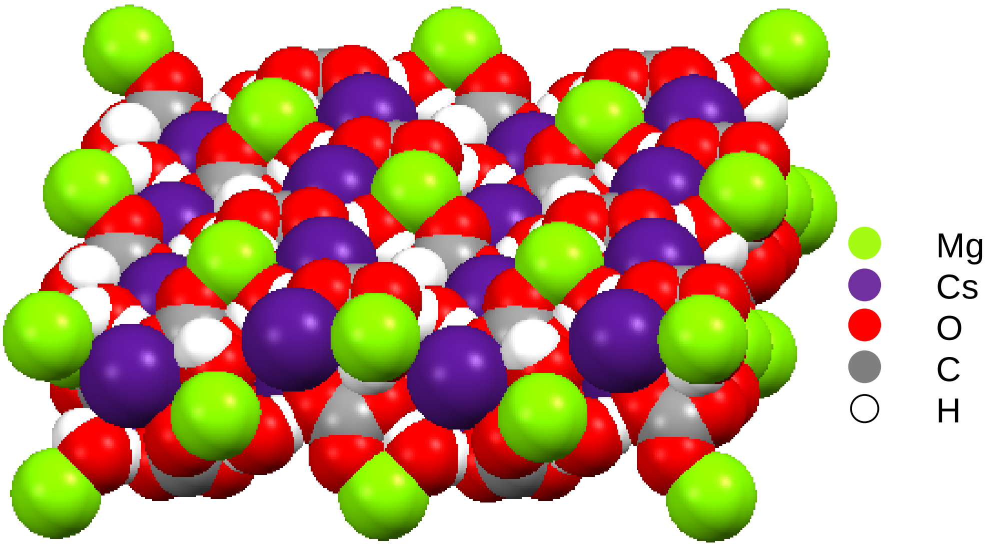

Figure 6.25. Space filling structure of $Cs_2Mg(CO_3)_2(H_2O)_4$.

Cs-MgO shows an excellent fit to $Cs_2Mg(CO_3)_2(H_2O)_4$, evidencing a Cs-Mg scattering shell at around 4 Å. From this result it can be concluded that there is a well defined, intimately mixed Cs/Mg phase present, as inferred from powder XRD (section 6.2.1.1). Formation of this new $Cs_2Mg(CO_3)_2(H_2O)_4$ active phase is due to the co-precipitation synthetic route employed to prepare Cs-MgO. Intimate contact between Cs and Mg is therefore very important to achieve the high catalytic activities for TAG transesterification.

6.3 Conclusions

Cs promoted MgO nanoparticles have been prepared using a sol-gel co precipitation technique and characterised. A new phase was observed in the XRD pattern of Cs-MgO, which was postulated to be a mixed Cs/Mg carbonate phase. The Cs-MgO showed an enhanced surface base site density and polarisability to the NanoMgO-500. Cs doping was thought to have introduced a greater number of defect sites on the MgO surface due to the creation of the new Cs/Mg phase.

Cs-MgO was tested in the transesterification of C4-C12 chain length model triglycerides, as well as olive oil, and showed good catalytic activity. Doping with Cs gives an order of magnitude enhancement in TOF for the transesterification of TAGs compared to NanoMgO. However, FAME yield remains a strong function of TAG size, with activity towards the bulky triolein component of olive oil approximately twenty times slower than for pure tributyrin. The selectivity to FAME increased with conversion for both NanoMgO-500 and Cs-MgO across the TAG transesterification reactions.

Ex-situ XAS was used to investigate the nature of the catalytically active phase in Cs-MgO. In EXAFS fitting, Cs-MgO showed excellent agreement to $Cs_2Mg(CO_3)_2(H_2O)_4$. It can therefore be concluded that a new mixed Cs/Mg phase is present, in the form of $Cs_2Mg(CO_3)_2(H_2O)_4$ nanocrystallites. EXAFS revealed the presence of highly electron deficient Cs atoms, indicative of strong charge transfer to superoxide anion surface base sites, located within $Cs_2Mg(CO_3)_2(H_2O)_4$ nanocrystallites. This study has revealed that it is the intimate mixing of Cs and Mg which is important in achieving the high catalytic activities observed.

6.4 References

1. D. J. Driscoll, W. Martir, J. X. Wang and J. H. Lunsford, *Journal of the American Chemical Society*, 1985, **107**, 58-63.
2. M. Glinski, J. Kijenski, J. Gibka and J. Gora, *Reaction Kinetics and Catalysis Letters*, 1995, **56**, 121-127.
3. M. Verziu, B. Cojocaru, J. Hu, R. Richards, C. Ciuculescu, P. Filip and V. I. Parvulescu, *Green Chemistry*, 2008, **10**, 373-381.
4. A. Corma, S. Iborra, S. Miquel and J. Primo, *Journal of Catalysis*, 1998, **173**, 315-321.
5. J. M. Montero, D. R. Brown, P. L. Gai, A. F. Lee and K. Wilson, *Chemical Engineering Journal*, 2010, **161**, 332-339.
6. K. Zhu, J. Hu, C. Kuebel and R. Richards, *Angewandte Chemie-International Edition*, 2006, **45**, 7277-7281.
7. D. O. Scanlon, A. Walsh, B. J. Morgan, M. Nolan, J. Fearon and G. W. Watson, *Journal of Physical Chemistry C*, 2007, **111**, 7971-7979.
8. G. Pacchioni, *Solid State Sciences*, 2000, **2**, 161-179.
9. T. Berger, J. Schuh, M. Sterrer, O. Diwald and E. Knoezinger, *Journal of Catalysis*, 2007, **247**, 61-67.
10. J. S. J. Hargreaves, G. J. Hutchings, R. W. Joyner and C. J. Kiely, *Journal of Catalysis*, 1992, **135**, 576-595.
11. T. Ito, J. X. Wang, C. H. Lin and J. H. Lunsford, *Journal of the American Chemical Society*, 1985, **107**, 5062-5068.
12. E. Finazzi, C. Di Valentin, G. Pacchioni, M. Chiesa, E. Giamello, H. Gao, J. Lian, T. Risse and H.-J. Freund, *Chemistry-a European Journal*, 2008, **14**, 4404-4414.
13. H. Matsuhashi, M. Oikawa and K. Arata, *Langmuir*, 2000, **16**, 8201-8205.
14. J. M. Montero, K. Wilson and A. F. Lee, *Topics in Catalysis*, 2010, **53**, 737-745.
15. F. Cavani, F. Trifiro and A. Vaccari, *Catalysis Today*, 1991, **11**, 173-291.
16. Y. Xi and R. J. Davis, *Journal of Catalysis*, 2008, **254**, 190-197.
17. M. J. Kim, S. M. Park, D. R. Chang and G. Seo, *Fuel Processing Technology*, 2010, **91**, 618-624.
18. J. M. Montero, P. Gai, K. Wilson and A. F. Lee, *Green Chemistry*, 2009, **11**, 265-268.
19. Y. Q. Zheng and A. Adam, *Chemical Research in Chinese Universities*, 1999, **15**, 211-217.
20. M. Atteya and K. J. Klabunde, *Chemistry of Materials*, 1991, **3**, 182-187.
21. Y. Asakuma, K. Maeda, H. Kuramochi and K. Fukui, *Fuel*, 2009, **88**, 786-791.
22. T. Davison, C. Okoli, K. Wilson, A. F. Lee, A. Harvey, J. Woodford and J. Sadhukhan, *RSC Advances*, 2013.
23. A. Kapil, K. Wilson, A. F. Lee and J. Sadhukhan, *Industrial & Engineering Chemistry Research*, 2011, **50**, 4818-4830.
24. M. Kouzu, T. Kasuno, M. Tajika, Y. Sugimoto, S. Yamanaka and J. Hidaka, *Fuel*, 2008, **87**, 2798-2806.
25. Y. Xiao, L. Gao, G. Xiao and J. Lv, *Energy & Fuels*, 2010, **24**, 5829-5833.
26. D. E. Lopez, J. G. Goodwin, D. A. Bruce and E. Lotero, *Applied Catalysis a-General*, 2005, **295**, 97-105.
27. J. Dhainaut, J. P. Dacquin, A. F. Lee and K. Wilson, *Green Chemistry*, 2010, **12**, 296-303.

28. J. P. Dacquin, A. F. Lee, C. Pirez and K. Wilson, *Chemical Communications*, 2012, **48**, 212-214.
29. L. L. Xu, Y. H. Wang, X. Yang, X. D. Yu, Y. H. Guo and J. H. Clark, *Green Chemistry*, 2008, **10**, 746-755.
30. Y. Z. Xi and R. J. Davis, *Journal of Catalysis*, 2009, **268**, 307-317.
31. E. S. Umdu and E. Seker, *Bioresour. Technol.*, 2012, **106**, 178-181.
32. K. G. Georgogianni, A. K. Katsoulidis, P. J. Pomonis, G. Manos and M. G. Kontominas, *Fuel Processing Technology*, 2009, **90**, 1016-1022.
33. B. Hamad, A. Perard, F. Figueras, F. Rataboul, S. Prakash and N. Essayem, *Journal of Catalysis*, 2010, **269**, 1-4.
34. J. J. Woodford, J.-P. Dacquin, K. Wilson and A. F. Lee, *Energy & Environmental Science*, 2012, **5**, 6145-6150.
35. M. Chiesa, M. C. Paganini, E. Giamello and D. M. Murphy, *Journal of Physical Chemistry B*, 2001, **105**, 10457-10460.
36. B. C. Bostick, M. A. Vairavamurthy, K. G. Karthikeyan and J. Chorover, *Environmental Science & Technology*, 2002, **36**, 2670-2676.
37. M. Nakano, K. Kawamura and Y. Ichikawa, *Applied Clay Science*, 2003, **23**, 15-23.

Chapter 7

Conclusions and Future Work

7.1 Conclusions

This thesis has investigated several different types of solid base catalysts for triglyceride transesterification. In this chapter the best performing catalysts from each chapter will be compared, both in terms of activity and the cost of preparation, to determine which catalyst shows the highest efficiency overall and is therefore the most industrially viable for use in biodiesel synthesis.

7.1.1 Comparison of catalyst TOFs

The TOF values for the most active catalysts discussed in this thesis are compared for C4, C12 and C18 TAG transesterification reactions in **Figure 7.1**.

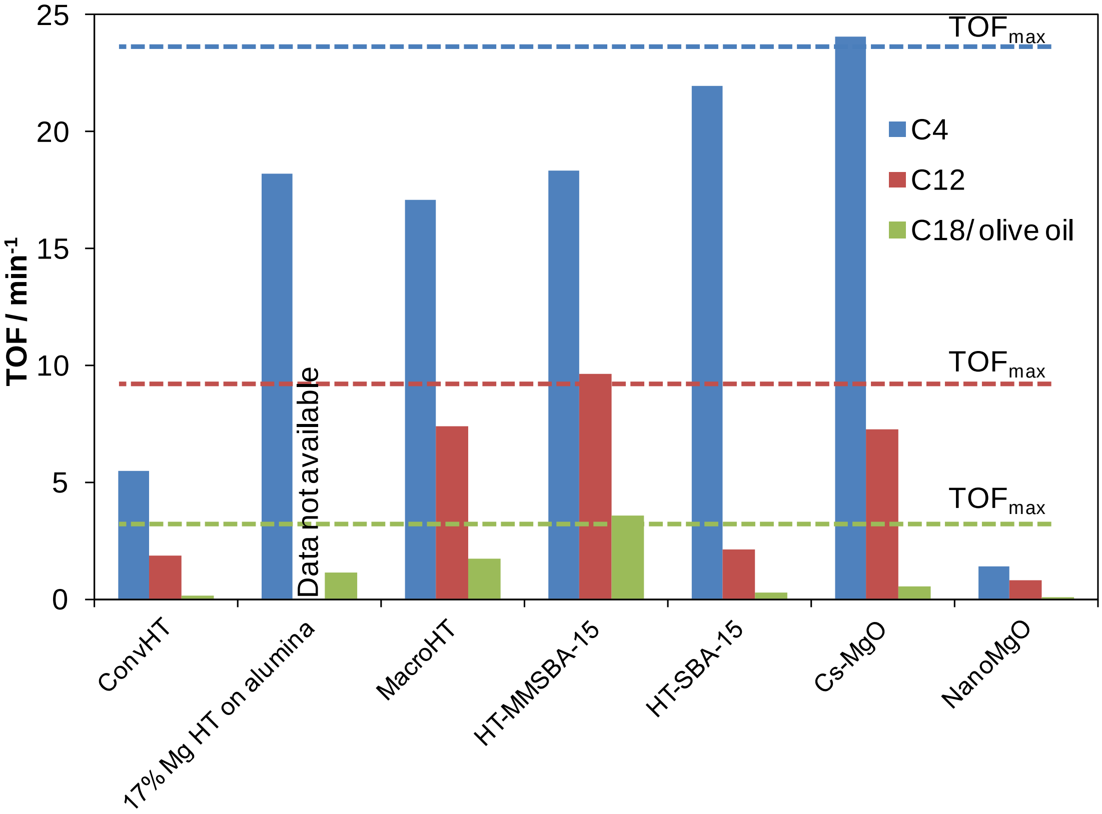

Figure 7.1. Comparison of TOF values in varying chain length triglyceride (C4, C12 and C18) transesterification reactions for the best performing catalysts from each chapter.

For the shortest chain, least sterically hindered and least diffusion limited TAG, tributyrin, the most active catalyst is the Cs-MgO, due to its high basicity. The HT-SBA-15, with its high Mg:Al ratio and greater basicity, also performs favourably. The three 2:1 Mg:Al hydrotalcites without diffusion limitations, HT-MMSBA-15, macroHT and 17% Mg HT on alumina all have similar TOFs, and the conventional microporous hydrotalcite, which has mass transport limitations, performs poorly when compared to these three catalysts. The NanoMgO has the lowest TOFs in all reactions.

On moving to the C12 TAG, the smallest drop in TOF values are seen for both macroHT and HT-MMSBA-15 as these two catalysts have no diffusion limitations for the large bulky TAGS, which can easily move down the macropore channels. The decrease in TOF observed is due to the slower movement of the TAG, and the decrease in solubility of the longer chained triglyceride in methanol. The HT-SBA-15 and convHT samples, which have mass transport limitations due to their smaller pore diameters, display an equal TOF decrease, much larger than for the macroporous materials. This larger decrease is also observed for Cs-MgO, where although the reaction is occurring at the catalyst surface, with increasing triglyceride chain length steric effects hinder bases site accessibility as the glycerol backbone of the TAG cannot get close enough to the small nanocrystallites.

For the bulkiest, C18 TAG transesterification, the real benefit of greater base site accessibility can be observed, as the macroporous materials, along with the thin coating of hydrotalcite on alumina, far outperform the other catalysts. The HT-MMSBA-15 has the highest overall TOF, due to its slightly higher Mg:Al ratio, along with the combination of the macropore super highways and thin hydrotalcite layer on the high surface area silica support providing a greater number of accessible hydrotalcite base sites at crystallite edges.

From this overall TOF comparison, the catalyst with the best TOF for bulky triglycerides like those used in the synthesis of biodiesel is the HT-MMSBA-15, followed closely by the macroHT and 17% Mg HT on alumina.

7.1.2 Comparison of catalyst activities

It is also important to compare overall catalyst activity, per gram of catalyst, when evaluating catalyst viability. The activities for the highest performing catalysts from this thesis in the transesterification of varying chain length triglycerides are compared below in **Figure 7.2**.

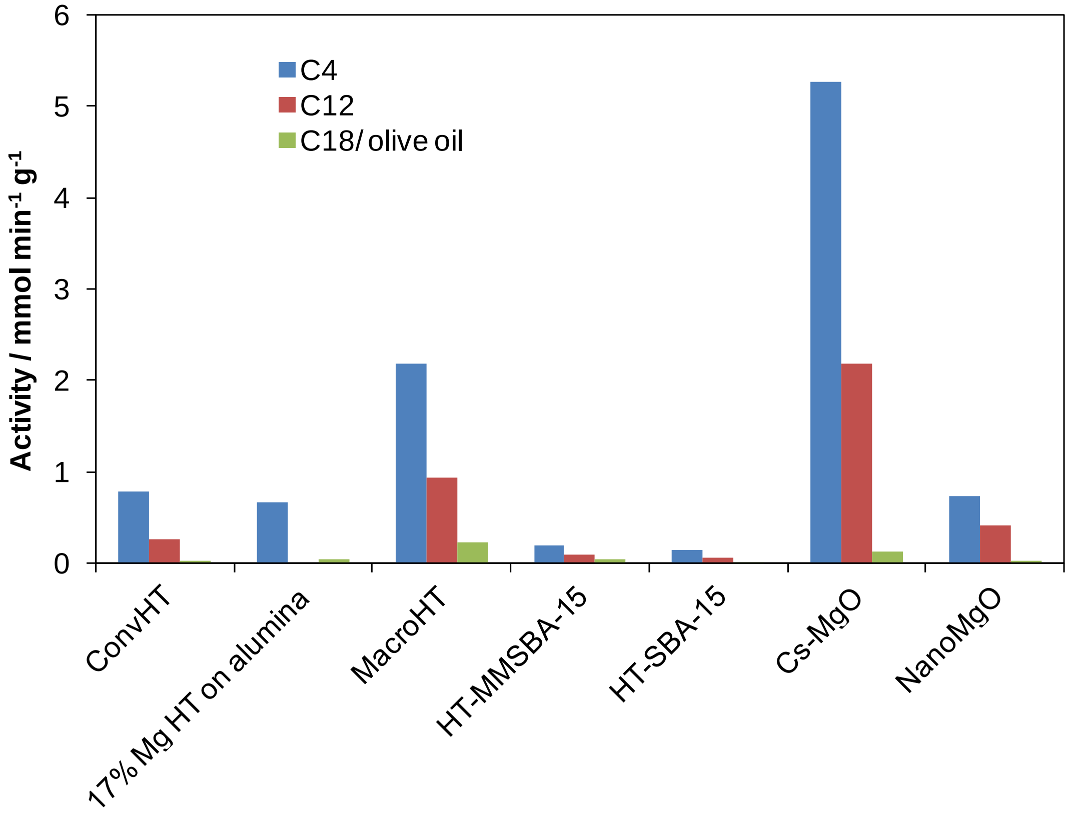

Figure 7.2. Comparison of activity values in varying chain length triglyceride (C4, C12 and C18) transesterification reactions for the best performing catalysts from each chapter.

As expected, the supported catalysts show the lowest activities per gram of catalyst, as the majority of the material is the support. The catalyst which far outperforms the rest at short triglyceride chain length is Cs-MgO. This is due to its high base site density after alkali doping. By C18 triglyceride chain length, steric effects associated with the Cs-MgO have caused a large decrease in activity for this catalyst, and it is the bulk macroHT which has the highest activity, due to the macropore channels allowing fast diffusion of the bulky triglycerides to the active catalyst sites, along with the high base site density.

7.1.3 Cost Analysis

In order to be able to compare the various catalysts more completely, the cost of preparing each catalyst should be considered, as this will have a large influence on its industrial viability. Therefore, a cost analysis was carried out testing each of the catalysts compared above, to determine which would be the most economically viable.

7.1.3.1 Chemical costs

Initially, the chemical costs involved in the preparation were compared for each catalyst. Whilst buying starting materials in bulk would bring the cost down dramatically, in order to make this test as fair as possible the prices for 100 g of each chemical, or as near as possible to this scale, were taken from the Sigma-Aldrich website on April 15th 2013. Solvents were costed on a 2.5 L basis, and liquids on a 1 L scale. Naturally, economies of scale dictate that prices would come down comparably for all catalysts if syntheses were scaled up to commercial levels.

The cost of methyl oleate production using the preceding catalysts was subsequently taken as the basis for price comparison of FAME manufacture, since the corresponding glyceryl trioleate would likely dominate any commercial bio-oil used for industrial biodiesel synthesis. Methyl oleate production is also the most dependent of the FAMEs investigated in this thesis upon catalyst selection. For Cs-MgO and NanoMgO, the limiting 24 h MO yields obtained during olive oil transesterification were chosen for comparison as catalytic data was not available for pure glyceryl trioleate transesterification. However, it should be noted that the results for olive oil and triolein transesterification over the convHT and macroHT catalysts from Chapter 3 were in any event very similar. For each catalyst, the chemical costs involved in preparing sufficient material to produce

5.72 mmol of methyl oleate after 24 h of reaction were calculated. 5.72 mmol was chosen as the production target since this represented the maximum productivity observed for any of the catalysts trialled (namely the macroHT). The following calculations were derived for MO yields obtained while testing all of the catalysts under the identical reaction conditions used throughout this thesis: 60 ºC; 30:1 methanol: oil ratio; 10 mmol triglyceride; and 50 mg catalyst. In order to simplify the overall calculation, it was assumed that all reactions were (and would continue to) operate in the absence of mass-transport limitations, such that doubling the mass of catalyst would double the resulting TAG conversion and MO yield. The results are listed in **Table 7.1**.

Table 7.1 Cost analysis for each catalyst based on methyl oleate formation.

Catalyst	Cost to prepare 1g of catalyst / £	Amount of catalyst required[a]/ g	Cost to produce 5.72 mmol MO / £
ConvHT	2.54	0.09	0.23
MacroHT	3.61	0.05	0.18
17% Mg HT on alumina	0.64	0.41	0.26
HT-SBA-15	28.23	8.18	230.92
HT-MMSBA-15	43.97	5.64	247.99
NanoMgO	5.65	2.12	11.98
Cs-MgO	5.46	0.37	2.02

[a] To produce 5.72 mmol MO after 24 h under reaction conditions as discussed

The best performing catalyst in this study is the bulk macroporous hydrotalcite, although the convHT and 17% Mg HT on alumina catalysts perform very similarly cost wise. The polystyrene bead sacrificial template is cheap to produce, and so the incorporation of macropores into the bulk hydrotalcite is not economically unfavourable, due to the significant rate enhancement it results in.

The cost of preparing 1g of Cs-MgO and NanoMgO is very similar. Due to the far greater activity of the Cs-MgO catalyst compared to the NanoMgO catalyst, the cost to produce 5.72 mmol of FAME is 6 times lower for the Cs-MgO. However, the Cs-MgO is still over 10 times more expensive than the macroHT.

By far the most expensive and least economical catalysts are the HT-SBA-15 and HT-MMSBA-15 catalysts. This is due to the preparation of the Al-grafted support, which requires 4 alumina grafting cycles each using large amounts of aluminium tri-sec butoxide and solvent. This is coupled with their low base site density, meaning that over 5 g of HT-MMSBA-15 is required to convert the same amount of triglyceride as 0.05 g of the bulk macroHT. Although the HT-MMSBA-15 catalyst shows the highest TOF values of all catalysts for the C18 TAG transesterification, even showing enhancement compared to the macroHT, this study has shown that in terms of industrially viable catalysts, the macroHT still far outperforms it.

If a more efficient route could be found to graft Al onto silica, then this catalyst could become economically viable. One possible option might be atomic layer deposition (ALD) or chemical vapour deposition (CVD) to graft a single monolayer of aluminium onto the silica support, using $AlCl_3$ as the aluminium precursor.[1] This would remove the need for organic solvents or co-factors. In literature, Kerãnen and co-workers[2] have prepared vanadium oxide on a silica support using ALD to deposit a thin vanadium layer, before carrying out an oxidative treatment.

7.1.3.2 Other cost factors

The above analysis only took chemical costs into the equation, and not any expensive processes used within the syntheses. The synthetic routes of the three most economical catalysts can be discussed, to determine whether any particular catalyst stands out as being substantially more expensive than the others to prepare.

The convHT and macroHT catalysts undergo the same preparation conditions, which involves holding at 60 ºC with stirring for 3 h. The preparation of the polystyrene bead template for the macroHT also requires a flow of nitrogen, as well as heat input to hold the mixture at 70 ºC for 15 h.

The preparation of the HT on alumina catalyst can be carried out at room temperature, however there are drying steps carried out in the vacuum oven, and the rotary evaporator is also used. In terms of preparation of an un-calcined material, the macroHT has the highest energy input of the three catalysts, when taking into account the polystyrene bead synthesis.

The calcination procedure is the same for all three of the catalysts. For the bulk convHT and macroHT the rehydration step is carried out at room temperature, however wet nitrogen is flowed over the catalysts for 48 h at 100 mL min^{-1}. Therefore, the rehydration requires 288 L of nitrogen (at a rough estimate around £5.21 worth of nitrogen). The HT on alumina catalyst does not require gases for rehydration, however the hydrothermal step involves stirring the sample in water at 125 ºC for 21 h. Although difficult to calculate exactly, the rehydration processes are fairly comparable in terms of their energy usage.

The macroHT has the highest energy input in its preparation when compared with convHT and HT on alumina, although in terms of chemical costs it is the cheapest of the three with regards to preparing 5.72 mmol of methyl oleate. It can be concluded that there are no particularly energy intensive processes to consider and none of the three catalysts far outweigh the other two in terms of overall cost.

7.1.3.3 Environmental impact of catalyst syntheses

It is also important to consider whether any of the various catalyst syntheses have a substantially higher cost to the environment than the others, as this could have implications when deciding on the best industrial catalyst.

The conventional and macroporous hydrotalcite syntheses require the use of metal nitrates as precursors. These nitrates are washed out at the end of the preparation before calcination and should therefore not be burnt out to form the greenhouse gas NO_x. However, it is very important that the aqueous washes containing the nitrates are disposed of correctly, as release through waste water systems into rivers can greatly accelerate eutrophication and decrease water quality. It would therefore potentially be possible to reduce the environmental impact of these syntheses by using an alternative metal salt in the co-precipitation route.

During the calcination procedure for each catalyst, either carbonate or methoxide are burnt out and CO_2 is released into the environment. However, the removal of the polystyrene bead template in the case of the macroHT and HT-MMSBA-15 catalysts will result in a larger proportion of CO_2 being released.

Higher chemical costs generally mean more extreme conditions, higher energy demands and greater environmental impact in order to prepare them. Therefore, in general. the catalysts with the higher starting chemical costs and greatest energy demands will also be the catalysts whose syntheses have the greatest detrimental effect on the environment.

7.1.4 Overall conclusions

Overall, when taking into account catalyst TOFs and costs involved in catalyst preparation, although the HT-MMSBA-15 catalyst has the greatest TOF value at C18 TAG chain length, it is not economically viable to prepare. Therefore the best catalyst for use industrially in the synthesis of biodiesel from this study, both economically and based on activity, would be the macroHT catalyst, followed closely by the 17% Mg HT on alumina catalyst.

7.2 Future work

It has been shown throughout this thesis that the incorporation of macropores into a material increases the accessibility of the base sites to bulky TAGS, enhancing the activity of the catalyst. However, the determination of the relative accessibility of base sites of the convHT and macroHT to the different chain length triglycerides still remains experimentally challenging to determine, as direct measurement of intrapore molecular diffusion coefficients is extremely difficult. The visualisation of meso versus macropore diffusion will remain an obstacle without further improvement in the spatial resolution of magnetic resonance imaging. Molecular dynamics simulation[3] and modelling studies[4, 5] are offering a short term solution to quantifying mass transport versus reaction kinetics in the catalysis of viscous bio-oil mixtures. It may be possible to use these techniques to compare the mass transport of the TAGs through the pore networks of the various catalysts studied in this thesis, to help aid the development of future catalysts.

The activity of the macroHT catalyst has already been enhanced compared to the convHT via the incorporation of macropores. However, it has also been shown that alkali metal doping enhances the basicity and activity of the MgO catalyst. By doping MgAl hydrotalcite with an alkali metal, it may be possible to enhance the activity of the macroHT even further.
Abello and co-workers[6] showed that doping MgAl hydrotalcites with Li, Na or K, either via direct impregnation or by not washing out the alkali used in the synthesis properly, improved the catalytic activity, however there was leaching into the reaction medium. It would be interesting to investigate altering the hydrotalcite co-precipitation method to incorporate Cs cations into the structure, as seen in **Chapter 6** with the co-precipitation of Cs-MgO. Through incorporation into the lattice structure the issue of leaching may be avoided. The resultant material could then be examined for its basicity and activity. The Cs may have formed a new phase within the hydrotalcite structure as seen for Cs-MgO, or it may simply withdraw less electron density away from the hydroxide anion Brønsted base sites, increasing their basicity.

Although not economically favourable, the HT-MMSBA-15 catalyst offers good stability and showed far better reusability without activation than the macroHT and convHT catalysts. In order to fully appreciate the benefit of this stability more run cycles with the spent catalyst need to be carried out, in order to examine how much of the catalytic activity remains after 4 or 5 reaction runs. There could then be further examination into the spent catalyst and any structural alterations after reaction. If there really is a vast improvement in catalyst lifetime and reusability compared to convHT and macroHT, then the economic issues in preparation of this material may be negated, or at least diminished.

Further characterisation could be carried out on the Cs-MgO catalyst via DRIFTS analysis. Methanol and methyl acetate adsorption experiments could be carried out in order to characterise the catalyst surface based on the vibrations of the methoxy species formed. The potential interactions of the various chemical species with the catalyst surface during a transesterification reaction could then be examined.

Tests with different real oil feedstocks such as *Jatropha Curcas* or algal oils need to be carried out with these catalysts to see how they perform with second generation, viable biodiesel feedstocks. Optimisation of the reaction conditions should be carried out, now that true kinetic data has been determined at these low conversions during low temperature reactions. It has already been shown in **Chapter 6**, that by increasing the temperature, the butanol: methanol ratio can be reduced and the activity of Cs-MgO can be dramatically enhanced for olive oil transesterification. Further tests into how these catalysts perform under more realistic reaction conditions need to be carried out. After further reusability tests, the catalysts could also be tested under scale up conditions on a fixed bed reactor. The initial studies into novel hierarchical solid base catalysts in this thesis have shown promise. With further work, the industrial viability of these catalysts for use in the synthesis of biodiesel can be more fully determined.

7.3 References

1. L. Catoire and M. T. Swihart, *Journal of the Electrochemical Society*, 2002, **149**, C261-C267.
2. J. Keränen, A. Auroux, S. Ek and L. Niinistö, *Applied Catalysis A: General*, 2002, **228**, 213-225.
3. J.-P. Dacquin, H. E. Cross, D. R. Brown, T. Duren, J. J. Williams, A. F. Lee and K. Wilson, *Green Chemistry*, 2010, **12**, 1383-1391.
4. A. Kapil, K. Wilson, A. F. Lee and J. Sadhukhan, *Industrial & Engineering Chemistry Research*, 2011, **50**, 4818-4830.
5. T. J. Davison, C. Okoli, K. Wilson, A. F. Lee, A. Harvey, J. Woodford and J. Sadhukhan, *RSC Advances*, 2013, **3**, 6226-6240.
6. S. Abelló, F. Medina, D. Tichit, J. Pérez-Ramírez, X. Rodríguez, J. E. Sueiras, P. Salagre and Y. Cesteros, *Applied Catalysis A: General*, 2005, **281**, 191-198.